ABSTRACT

Title of dissertation: ELECTRON TRANSPORT SIMULATIONS AND BAND STRUCTURE CALCULATIONS OF NEW MATERIALS FOR ELECTRONICS: SILICON CARBIDE AND CARBON NANOTUBES.

Gary Pennington, Doctor of Philosophy, 2003

Dissertation directed by: Professor Neil Goldsman
Department of Electrical Engineering

Silicon carbide (SiC) and carbon nanotubes (CNTs) are two materials which have promising potential in electronics. Due to its large bandgap and large thermal conductivity, SiC is targeted as a potential material for use in high-power high-temperature electronics. Carbon nanotubes are at the forefront of current research in nanoelectronics, and field-effect nanotube transistors have already been developed in research laboratories. The small dimensions of these materials suggests their possible use in densely packed CNT-integrated circuits. Carbon nanotubes also appear to have very large electron mobilities, and may have applications in high-speed electronic devices.

In this work the properties of the electronic structure and electron transport in

silicon carbide and in semiconducting zig-zag carbon nanotubes are studied. For SiC, a new method to calculate the bulk band structure is developed. The conduction band minimum is found to lie at the L and M points in the Brillouin zones of 4H and 6H-SiC respectively. The quasi-2D band structure of hexagonal SiC is also determined for a number of lattice orientations. Electron transport in SiC is investigated in the bulk and at the SiC/oxide interface. The dependence of transport on the lattice temperature, applied field, and crystal orientation is studied.

A methodology for semiclassical transport of electrons in semiconducting carbon nanotubes is also developed. Monte Carlo simulations predict large low-field mobilities ($0.4 - 13$ x$10^4 cm^2/Vs$) agreeing with experiments. The simulations also predict high electron drift velocities ($5X10^7 cm/s$) and negative differential resistance.

ELECTRON TRANSPORT SIMULATIONS AND BAND STRUCTURE CALCULATIONS OF NEW MATERIALS FOR ELECTRONICS: SILICON CARBIDE AND CARBON NANOTUBES

by

Gary Pennington

Dissertation submitted to the Faculty of the Graduate School of the
University of Maryland, College Park in partial fulfillment
of the requirements for the degree of
Doctor of Philosophy
2003

Advisory Committee:

Professor Neil Goldsman, Chair/Advisor
Professor Edward Ott
Professor Thomas Antonsen
Professor John Orloff
Professor Michael Fuhrer

ACKNOWLEDGEMENTS

First of all I would like to thank my research advisor, Dr. Neil Goldsman, for giving me the opportunity to work on number of very interesting topics. I thank him for his support and his willingness to let me learn and develop.

I would also like to thank Dr. Ed Ott, Dr. Thomas Antonsen, Dr. John Orloff, and Dr. Michael Fuhrer for serving on my dissertation committee.

I also wish to thank Dr. Skip Scozzie, Dr. James McGarrity, Dr. Barry McLean, Dr. Aivars Lelis, and Dr. Frank Crowne from the Army research laboratory whom I have had the good fortune to work with. I thank them for supporting my work.

I also wish to thank my fellow graduate students whom I have learned much from. I thank Akin Akturk, Zeynep Dilli, Dr. Stephen Powell, Dr. Chung-Kuang Huang, Dr. Zhiyi Han, Dr. Chung-Kai Lin, and Siddharth Potbhare.

TABLE OF CONTENTS

LIST OF TABLES

LIST OF FIGURES

Chapter 1

Introduction

Over the past four decades, no other invention has had a greater impact on our daily lives than the integrated circuit. So far this "microelectonics revolution" has been largely powered by silicon. During this time silicon has, to a great extent, continued to meet the need for smaller, faster, cheaper, more reliable, and diverse electronic circuits. It is although unlikely that silicon will continue to play such an encompassing role in microelectronics in the 21st century.

The material properties of silicon are not sufficient to meet todays technical demands in high-power high-temperature electronics. Materials, such as silicon carbide, with a larger band gap, a larger thermal conductivity, and a larger breakdown field, are now replacing silicon in these applications. The scaling limits of silicon MOSFETs are also rapidly approaching. To continue to produce increasingly faster

integrated circuits with progressively more computational power, researchers are investigating many new materials. One structure that has received considerable attention and shows significant promise is the carbon nanotube (CNT). This material is smaller enough to produce chips with 500 times as many transistor as is currently possible with silicon[1]. It is also likely that, for a given applied field, electrons within a CNTs will move faster than in silicon.

1.1 SiC in High-Power High-Temperature Electronics

Silicon carbide (SiC) is known to form a large number of similar polytypes which, except for the wurzite phase, exhibit a roughly linear bandgap variation[2, 3] as a function of increasing hexagonal content. The most interesting polytypes are hexagonal 4H-SiC and 6H-SiC since they have a very large bandgap and a high bulk drift velocity. Many of the material properties of SiC are well suited for electronic devices operating in the high-temperature, high-power regime. These are a large bandgap, a large thermal conductivity and a large breakdown field[4, 5, 6, 7, 8]. Furthermore, SiO_2 can be thermally grown on SiC, allowing for the production of SiC-MOSFETs and the use of planar fabrication methods[9].

In Table 1.1 we show a comparison of these material properties with those of Si. A large bandgap is useful in eliminating a number of breakdown mechanisms in power MOSFETs. These include leakage currents induced by the build-up of free

charges, and thermal runaway resulting from impact ionization processes. A large thermal conductivity is useful in eliminating device breakdown due to the formation of hot spots in the device. The large bandgap and large thermal conductivity of SiC is therefore ideal for power MOSFETs. Devices are expected to have fast switching speeds and low energy loss even at high temperatures. These properties offer a potential advantage over Si

Currently, the bright potential of SiC is limited by the small electron mobilities that are typically measured in the inversion layers of SiC MOSFETs [11, 12, 13, 14]. The likely cause is the large density of interface trap states that have been observed at the oxide-semiconductor interface[15, 16, 17, 18]. Since this density depends on the particular crystalline plane on which the oxide is grown, it may be possible to improve the problematic small inversion layer mobilities in SiC MOSFETs by altering the crystalline orientation. Indeed experiments on $(11\overline{2}0)$ oriented MOSFETs do show large improvements in the channel mobility[13]. In this case the crystal orientation was chosen to reduce the density of interface traps at the oxide interface, but the use of different SiC crystal planes is also useful in non-conventional MOSFETs such as UMOS devices. Such devices are easily fabricated and have potential applications in high-power electronics [19, 20].

1.2 Carbon Nanotubes in Electronics

Since the discovery[21] of carbon nanotubes (CNTs), interest in the potential applications of their electronic properties has continued to grow. These properties

vary with each tube's fundamental indices (n,m), which specify the diameter and wrapping angle as a graphene sheet is seamlessly wrapped into a CNT. As n and m vary, conduction ranges from metallic to semiconducting, with an inverse-diameter dependent bandgap of $\leq$ 1eV[22]. Furthermore, it has been shown experimentally that different types of CNTs may be seamlessly connected allowing contacts with widely varying conduction properties to be made within the same material[23, 24]. Doping of the tubes with donors and acceptors has been demonstrated,[25, 26] while metallic tubes have shown the capacity for large current densities and large thermal conductivities[27, 28]. These, and other, versatile electronic properties offer great hope for CNT-based nanoelectronics. Already important steps have been made. A variety of electronic devices operating at room temperature have been produced including field-effect transistors,[29, 119, 120] rectifying diodes and heterojunctions[121, 122, 123, 124, 125, 126, 127]. Recently logic circuits using both p and n doped CNT-based FETs[29] have shown promising experimental results. It is hoped that large arrays of nanotube transistors can be assembled into integrated circuits with 500 times the transistor density as in conventional Si[1].

The mobility of long semiconducting SWCNTs has recently been measured and values as large as 2x10$^4 cm^2/Vs$ [30] and 8x10$^4 cm^2/Vs$ [31], have been obtained. Such large values indicate that these nanotubes may have applications in high-mobility electronic devices. Carbon nanotubes may also find applications in supplementing already existing Si technology.

1.3 Motivation

The motivation of this dissertation is to study the electron transport properties of two potentially new materials for electronics, silicon carbide and carbon nanotubes. For SiC, the effects of the band structure, lattice temperature, and applied field on electron transport are investigated. For CNTs, a methodology for semiclassical transport is developed. This is used to understand and predict the properties of electron transport in carbon nanotubes.

1.4 Outline

The outline of this dissertation is as follows. In the Introduction a discussion of the general concepts of the Monte Carlo simulation of carrier transport is presented.

In Chapter 2, the band structure for a the 3C, 4H, and 6H polytypes of SiC is determined by employing a new model potential approach to the empirical pseudopotential method[32]. The results agree well with the available experimental data. The conduction band minimum of 4H is found at the M point and the conduction band minimum of 6H is found at the L point in the Brillouin zone. The exact location of the 6H minimum has still not been determined experimentally, but experiments do indicate that it lies along the M-L symmetry line.

In Chapter 3 the calculated bulk band structures are used within a full-band Monte Carlo simulation of electron transport in bulk 6H-SiC. Electron-phonon coupling constants are fit to experiments, and transport under high-field and high-temperature conditions is studied. The saturation velocity of 6H-SiC is found to

decrease linearly with increasing temperature, while it is determined that as many as 4 conduction bands and two band structure valleys contribute to electron transport at high fields.

In Chapter 4 surface band structure calculations are performed for different orientations of hexagonal SiC. The subband structure perpendicular to an oxide-SiC interface is determined self-consistently with the confining transverse potential. Investigations have been performed in the range of weak/strong inversion and high/low temperatures. The $(01\overline{1}0)$, $(11\overline{2}0)$, $(03\overline{3}8)$, and (0001) surfaces are compared for both 4H-SiC and 6H-SiC. Each orientation is characterized based on its 2-dimensional nature, its degree of anisotropy parallel to the oxide, and the spatial extent of mobile electrons from the oxide-semiconductor interface.

In Chapter 5, a surface Monte Carlo simulation of electron transport in a 4H-SiC MOS inversion layer is presented. The self-consistent inversion layer calculations of Chapter 4 are employed. The low-field inversion layer mobility for the (0001) orientation was found to increase linearly with increasing lattice temperature, in agreement with experiments. The simulated low-field mobility for $(11\overline{2}0)$ oriented 4H-SiC was much higher, due to a reduction in interface traps. In this case the mobility decreased with increasing temperature. These trends have also been observed in experiments on $(11\overline{2}0)$ oriented 4H-SiC MOSFETs.

In Chapter 6, current flow, considering a semiclassical electron-electric field interaction and electron scattering by acoustic and optical phonons, is studied in semiconducting zig-zag carbon nanotubes[33, 34]. The π-electronic band structure and the phonon spectrum of the nanotube are both calculated from graphene by the

zone-folding method. Scattering rates are calculated using first order perturbation theory and the deformation potential approximation, while the selection rules for the electron-phonon interaction are developed based on the conservation of crystal momentum. The steady state transport properties of electrons in small diameter nanotubes are simulated using the Monte Carlo method. Results show negative differential mobility, occurring at smaller threshold fields as the tube diameter increases. The peak drift velocity is also found to depend on the tube diameter, and reaches values as high as $5X10^7 cm/s$ in the largest tube considered with a diameter of $\cong 4.6nm$.

Results show large low-field mobilities of approximately $0.4 - 13$ x$10^4 cm^2/Vs$, which are consistent with experimental results[30, 31]. An analytical mobility model is introduced which reproduces the Monte Carlo simulations over a wide range of tube indices n. Such large mobility values indicate that these nanotubes may have applications in high-mobility electronic devices. Furthermore, recent theoretical results using the mobility model indicate that the transconductance of a silicon-based MOSFET can be enhanced if a CNT is inserted into the channel [35].

We will begin by introducing the general concepts at the core of the Monte Carlo method as applied to the simulation of carrier transport in semiconductors.

1.5 General Monte Carlo Method

The strength of the Monte Carlo method is the ability to accurately simulate physical phenomena using a very detailed computer simulation model. The method

reproduces the stochastic nature of many physical systems through the skillful use of random numbers. This method was first applied to electron transport in GaAs in the late 1960s[36, 37], and has since became an important tool in the study of carrier transport in semiconductors. In this section we will describe the general concepts of the Monte Carlo Method for electron transport in semiconductors (MCM)[38, 39, 40].

The MCM essentially solves the Boltzmann transport equation through a computer simulation of the dynamics of carrier transport. It relies on a semiclassical approach. Free carriers are treated as classical point-like particles, which in the absence of scattering, drift in an external field $\vec{F}$ according to Newton's equation of motion

$$\hbar \frac{d\vec{k}}{dt} = e\vec{F}. \tag{1.1}$$

For this approximation to be used, the length scale in the direction of $\vec{F}$ must be much larger than the size of the semiconductor unit cell in that direction. If this is true, then the carrier energy spectrum is approximately continuous in the electron wavevector, $\vec{k}$, and carriers can be described as point-like wavepackets.

Upon this classical picture, carrier scattering is included via quantum mechanics. Imperfections in the perfectly periodic lattice of the semiconductor, such as impurities or phonons, are described as small perturbations on the carrier energy spectrum. To first order this is described by "Fermi's Golden Rule"

$$\Gamma(\vec{k}, \vec{k'}) = \frac{2\pi}{\hbar} |H|^2 \delta\left(\varepsilon(\vec{k'}) - \varepsilon(\vec{k})\right), \tag{1.2}$$

where $\Gamma(\vec{k}, \vec{k'})$ is the rate at which a carrier scatters from an initial wavevector $\vec{k}$ to a

final wavevector $\vec{k'}$. Also included are H, the interaction energy between the carrier and the scattering imperfection, and ε, the wavevector-dependent carrier energy. Here the scattering events are considered as occurring instantaneously at a localized point in space. It is typically desirable to sum equation (1.2) over all possible final states in which case the rate, $\Gamma(\varepsilon(k))$, depends on the electron energy.

For simulations which are both time and space-independent, the transport properties of a collection of carriers can be found through the simulation of just one carrier. This is the general ergodic case we will focus on here. At the beginning of the Monte Carlo simulations of electron transport, the simulated electron is placed at the conduction band minimum. The steady-state results are however independent of the choice of initial state. The electron is then allowed to drift in the applied field according to equation (1.1), for a specified drift time T_d. This drift time is chosen so that it is always much smaller than the inverse of the scattering rate. After the drift, it is determined whether a scattering event will occur. To illustrate the method for this determination consider the example when the electron has an energy $\varepsilon(k)$ after the drift and may now be scattered by n different independent mechanisms. A flat random number $r1$ from 0 to 1 is generated. If

$$r1 < T_d \sum_{m=1}^{n} \Gamma^m(\varepsilon), \tag{1.3}$$

then a scattering events occurs. Otherwise the electron is allowed to drift again for a time T_d and the process repeats. In the case that equation (1.3) is satisfied, of the n scattering mechanisms, the one which scatters the electron must be determined. A second random number $r2$ is now generated. The event m' which scatters the

electron is then assigned by the relation

$$S_{m'-1} < r2 \leq S_{m'}, \tag{1.4}$$

where the partial sum S is defined according to

$$S_{m'} = \frac{\sum_{m=1}^{m'} \Gamma^m(\varepsilon(k))}{\sum_{m=1}^{n} \Gamma^m(\varepsilon(k))}. \tag{1.5}$$

Once the scattering event is determined, the final electron state after scattering is determined by stochastic methods. The particular method for this will depend on the particular scattering event that scatters the electron. This is constrained by requiring that the final state of the system, electron and scatterer, have the same energy and crystal momentum as the initial state of the system.

The simulation continues through a series of drifts and scattering events, until the convergence of the average electron velocity along the direction of the driving field. This is the drift velocity ϑ_d. This velocity can be determined in a number of ways. The first way is to find the drift velocity from the energy that the electron gains from the field during all the drifts. Summing up the change in energy during each and every drift, a result we will label as ΔE, the drift velocity can be determined by

$$\vartheta_d = \frac{\Delta E}{eFT_T}. \tag{1.6}$$

Here F is the driving electric field and T_T is the total simulation time. Another way to determine ϑ_d is to require that in the steady-state, the average total rate at which the simulated electron gains energy is zero. This requires the average rate that energy is gained from the field ($eF\vartheta_d$), be equal to the average rate that

	3C-SiC	**4H-SiC**	**6H-SiC**	**Si**
Bandgap (eV)	2.39	3.26	2.86	1.12
Bulk Electron Mobility (cm^2/Vs)	1000	600	300	1500
Saturation Velocity ($10^7 cm/s$)	2	2	2	1
Breakdown Field ($10^6 V/cm$)	2	3	3	1
Thermal Conductivity (W/Kcm)	4.9	4.9	4.9	1.5
Static Dielectric Constant	9.7	9.7	9.7	11.8

Table 1.1: Important physical properties of the SiC polytypes and Si[10]

energy is dissipated through scattering events (P_{sc}). The drift velocity can then be determined as

$$\vartheta_d = \frac{P_{sc}}{eF}. \tag{1.7}$$

It is useful to determine the convergence of the MCM simulations by tracking the convergence of the drift velocity calculated in a few different ways, such as in equations (1.6) and (1.7). When the drift velocity is accurately obtained, the results are similar. To calculate the mobility, the drift velocity is divided by the electric field F.

Chapter 2

Bulk Band Structure Calculations for SiC

The harsh environment of the electronics for which SiC is proposed, make knowledge of the bandstructure, especially near the conduction band minimum, important in determining electronic device characteristics. When applicable, the empirical pseudopotential method (EPM) is usually the method of choice for such work since it is computationally efficient and easily interpreted when compared to other methods such as density functional theory (DFT).[42] When calculating semiconductor properties which are influenced weakly by the deep core electronic states, such as the bandstructure close to the bandgap, the method is often highly accurate.[43] The weakness of the EPM is that it often relies heavily on the use of experimental data. Unfortunately, though useful for many diamond and zincblende phase semiconductors, the EPM is not as successful for lattice types with larger unit cells

since the number of form factor parameters that must be fit increases while the experimental data available generally decreases. The approach in these cases is to use the transferability of the pseudopotential and approximate the form factors by using those of a similar material. An important example is the success of using the same form factors for many direct band-gap materials that exist in both cubic and wurzite phases.[44] Due to differences in the density and magnitude of the reciprocal lattice vectors, the 3 diamond or 7 zincblende parameters are interpolated to obtain the 10 or 19 parameters needed for homopolar or heteropolar wurzite, respectively. For progressively larger unit cell phases, as in the polytypes of SiC, the number of form factors increases such that the zincblende form factors alone cannot provide the detail of the Fourier transform of the pseudopotential required.

The EPM has been successfully applied to the 3C zincblende phase of SiC[45, 46, 47] where there are at least 5 reliable experimental band energies[48, 49] to fit the 7 form factors needed. These studies did not however include a fitting to experimental effective masses which is important in determining transport properties. This is included as a nonlocal correction in this work. For 4H and 6H SiC roughly 30 form factors are needed while there is only one reliable experimental band energy[2] for each material. Due to the lack of experimental data, these form factors have, to our knowledge, never been characterized and published till now. We overcome the difficulty in fitting the form factors of 4H and 6H by using a model potential to represent the empirical pseudopotential. The use of a model potential is highly advantageous when working with large unit cells since the full potential can be calculated and fit to optical data using a limited number of parameters. By extending the nonlo-

cal Heine and Abarenkov model potential,[50] including the nonlocal screening of Animalu,[51, 52] for use in covalent and partially ionic semiconductors, and refitting one parameter, we found a model empirical pseudopotential that could accurately reproduce the experimental band energies of Si, SiC, and diamond around the band gap region. The limited number of fitting parameters in SiC , commensurate with the amount of experimental data available for the hexagonal polytypes, is the result of the use of transferable Si and C potentials. A local model potential is used for convenience which directly produces fitted form factors that can be used within the EPM. A nonlocal correction with one additional parameter is then added to fine tune the bandstructure, and is used to fit the effective masses of 3C and 4H. The correction is not used for 6H since the local potential alone gives good results for the effective masses.

2.1 HA Model Potential

By adding nonlocal screening to the Heine and Abarenkov potential, Heine and Animalu (HA) developed a model atomic potential which successfully predicted the long-wavelength form factors for many metals.[51, 52] The unscreened core potential was represented as a sum of angular-momentum-dependent square wells extending over a nonlocal core of radius R within which valence electrons interact with the core electrons. This radius turns out to be quite large, roughly 60-70% of the atomic radius in Si and C. The well depths, A_l, were each independently fit to the experimental energy levels of the corresponding free ions . Taking into account their

energy dependence, the metallic values were then obtained by extrapolating from the free ion energy to the corresponding equivalent energy relative to the Fermi level of the metal. An approximation to the metal values was thus obtained by fitting to atomic spectroscopic data. For simplicity, the square wells of the metallic core potential were then considered to be energy independent with the same radius, R, used for each.

The atomic potential is in general a sum over all l

$$V^a_{HA} = \sum_{l=0}^{l=\infty} \sum_{m=-l}^{m=l} V_l |lm><lm|. \tag{2.1}$$

The relevant members of the sum will only involve the l values of the unexcited valence and core electrons. HA argued that higher harmonics would produce pseudowavefunction nodes within the core. Such structure in the pseudowavefunction would be incompatible with the concepts of the pseudopotential method. Although others have questioned the theoretical significance of this approximation and have improved the model to eliminate it,[53] we retain it since it renders the model in a convenient form for fitting to experimental data. For Si and C, we will therefore not need to include members of the sum for $l > 1$. Based on the Phillips-Kleinman cancellation theorem,[54] these unnecessary angular-momentum components of the potential should all be roughly the same size. They can therefore all be removed from the sum by removing the $l = 2$ component as an average. The $l = 2$ well then forms the local potential. The final form of the Fourier transform of the atomic potential, indicating the wavevector and model parameter dependence of the various

terms, is

$$V^a_{HA}(\vec{q}) = \frac{B(q; A_2, R, Z)}{\epsilon_m(q)} + \sum_{l<2} \left[\frac{I(q; A_l - A_2, R)}{\epsilon_m(q)} + F(\vec{k}, \vec{G}; A_l - A_2, R) \right], \quad (2.2)$$

where the lattice and electron wavevectors are $\vec{q}$ and $\vec{k}$, respectively. The local, or $\vec{k}$ independent, bare potential B is constructed from a local approximation to the $l = 2$ square well, the potential due to the net core charge Z, and correlation and orthogonality hole corrections. F is the nonlocal bare core potential involving square wells of depth $\Delta A_l = A_l - A_2$ for each angular momentum considered. Hence, as previously discussed, only wells that differ in depth from A_2 will enter this term. The terms in Eq. (2.2) are given in greater detail in Appendix A.

HA screened the bare potentials by using Sham's[55] modification of the Hartree dielectric function appropriate for metals, ϵ_m, and included the screening of the non-local potentials through the term I. The "on Fermi sphere approximation" was used to take out the $\vec{k}$ dependence in F when appropriate. This involved setting $k = k_f$, the Fermi wavevector, and letting

$$|\vec{k} + \vec{q}| = \begin{cases} k_f & q \leq 2k_f \\ q - 2k_f & q > 2k_f \ . \end{cases} \quad (2.3)$$

This also takes care of the angular dependence of $\vec{k}$ since it enters F through the angle between $\vec{k}$ and $\vec{k} + \vec{q}$ which becomes

$$\theta_{\vec{k},\vec{k}+\vec{q}} = \begin{cases} 0 & q \leq 2k_f \\ \pi & q > 2k_f \ . \end{cases} \quad (2.4)$$

The "on Fermi sphere approximation" is used to construct a local atomic pseudopotential using simple average values for the electron energy and momentum.

These average values are used to obtain an average potential that no longer depends on the electron energy and wavevector.

2.2 Si and C Model Potentials

The Si and C local atomic potentials that will be used in SiC are constructed by fitting the HA model to the band energies of homopolar diamond-phase Si and C. First a number of changes are made to the HA potential in order convert it into a suitable form to represent the empirical pseudopotential of semiconductors. The metallic dielectric function in equation (2) must be replaced by one appropriate for semiconductors. For this we use the result of Penn[56]

$$\epsilon(q;E_g) = 1 + \frac{\left[\frac{\hbar\omega_p}{E_g}\right]^2 \left[1 - \frac{E_g}{4E_F}\right]}{\left[1 + \frac{E_F}{E_g}\left(\frac{q}{E_F}\right)^2 \sqrt{1 - \frac{E_g}{4E_F}}\right]^2}, \tag{2.5}$$

where E_F is the Fermi energy, ω_p the plasma frequency, and E_g is a band gap parameter determined by[57] the $q \to 0$ limit

$$E_g = \frac{\hbar\omega_p}{\sqrt{\epsilon(0) - 1}}. \tag{2.6}$$

The model potential must be adjusted at high q where the empirical pseudopotential is truncated. For semiconductors it has been shown that the potential may be suitably cut off at $3k_f$, yet damping should not interfere with the potential for lattice vectors less than $2k_f$.[58] We therefore damp the potential according to

$$V^a(\vec{k},\vec{q}) = V^a_{HA}(\vec{k},\vec{q}) e^{-\alpha\Theta(X)X}, \tag{2.7}$$

where $X(q) = \left(\frac{q}{2.2k_f} - 1\right)$ and

$$\Theta(X) = \begin{cases} 1 & X \geq 0 \\ 0 & X < 0 \ . \end{cases} \tag{2.8}$$

The damping factor α is adjusted so that the potential damps to zero for $q > 3k_f$, and the step function ensures that all truncation occurs after $q = 2.2k_f$, and therefore well after $2k_f$. Since the fitting parameter will be used to vary the potential in this region, this simple damping term is chosen so that no new fitting parameters are introduced. It also represents the diminishing importance of EPM form factors for $q > 2k_f$, which is roughly $q^2 > 12$ in reciprocal lattice vector units. For Si and diamond, the only form factor from the damped region occurs at $q^2 = 16$. Since this form factor is found not to improve the fit to experimental data in EPM studies of Si,[59] we do not include it. For diamond, however, it is needed.[61]

We also use the "on Fermi sphere" approximation to treat F locally as

$$F = F(q; A_l - A_2, R). \tag{2.9}$$

Only the square wells which differ significantly from the $l = 2$ well will be considered in order to limit the number of parameters in the model. These are the repulsive $l = 0$ well for Si and the attractive $l = 1$ well for C. This attractive well in C originates from the lack of core p states.

Following EPM theory[43], the crystal pseudopotential, V_p, can be represented as a sum over all reciprocal lattice vectors $\vec{G}$

$$V_p(\vec{r}) = \sum_{\vec{G}} V(\vec{G}) e^{i\vec{G}\cdot\vec{r}}, \tag{2.10}$$

where

$$V(\vec{G}) = \sum_{\alpha} S_{\alpha}(\vec{G}) V_{\alpha}^{a}(\vec{G}), \tag{2.11}$$

with the sum over each atomic species α present. For the diamond phase potential, there is only one species present, but we will keep the potential in a general form applicable to SiC as well. The structure factor is

$$S_{\alpha}(\vec{G}) = \frac{1}{n_{\alpha}} \sum_{\vec{\tau}_{\alpha}} e^{-i\vec{G}\cdot\vec{\tau}_{\alpha}}, \tag{2.12}$$

where n_{α} is the total number of atoms of species α in the unit cell and the sum is over the corresponding basis vectors, $\vec{\tau}_{\alpha}$, of these atoms. The atomic potential in Fourier space, represented in (7), is evaluated from the real space atomic pseudopotential according to

$$V_{\alpha}^{a}(\vec{G}) = \frac{1}{\Omega_{\alpha}} \int_{\Omega_{\alpha}} V_{\alpha}^{a}(\vec{r}) e^{-i\vec{G}\cdot\vec{r}} d^{3}r, \tag{2.13}$$

where Ω_{α} is the atomic volume and V_{α}^{a} is the atomic pseudopotential of species α. For diamond(A^N) or zinc-blende($A^N B^{8-N}$) phases, the Fourier transform of the pseudopotential is represented in terms of symmetric(V^S) and antisymmetric(V^A) parts

$$V(\vec{G}) = V^{S}(\vec{G}) cos(\vec{G}\cdot\vec{\tau}) + iV^{A}(\vec{G}) sin(\vec{G}\cdot\vec{\tau}), \tag{2.14}$$

where

$$\begin{aligned} V^{S}(\vec{G}) &= \frac{V_{A}(\vec{G}) + V_{B}(\vec{G})}{2} \\ V^{A}(\vec{G}) &= \frac{V_{A}(\vec{G}) - V_{B}(\vec{G})}{2}. \end{aligned} \tag{2.15}$$

For crystalline Si and C, the diamond-phase potential is then only the symmetric term

$$V(\vec{r}) = \sum_{\vec{G}} V(G) cos(\vec{G} \cdot \vec{\tau}) e^{i\vec{G}\cdot\vec{r}}. \tag{2.16}$$

With the exception of the C core radius R_C, which was chosen 4% less, the HA results were used for the first approximation of the model parameters. One fitting parameter, A_2, was then increased by 21% for C and decreased by less than 2% in Si, to fit to experiment. This parameter adjusts not only the local well but the nonlocal wells, treated locally here by the "on Fermi sphere approximation", since $\Delta A_l = A_l - A_2$. The refitting of A_2 can be interpreted as accounting for the difficulty in extrapolating the well depths from the free ion values to obtain those for the corresponding metal, in particular the choice of the free ion equivalent energy in the metal. Also, since A_2 should be one of the more energy-dependent parameters, its adjustment may account for the use of energy independent model parameters and a local approximation to the potential.

To calculate the bandstructure, we use a plane wave basis including all plane waves satisfying $(\vec{k} + \vec{G})^2 \leq 21$. This criteria is found to give convergence in diamond and zinc-blende semiconductor structures.[60] Convergence of the fitted band energies is found within .02 eV for Si and diamond using 125 plane waves for each material. The model potential and corresponding bandstructure of Si and diamond, are shown in Fig. 2.1- 2.4, while the model parameters used are given in Table 2.5. For Si, the model potential agrees closely with EPM form factors and subsequently agrees well with the experimental band energies in Table 2.2. There is less agree-

ment between the model potential and the EPM form factors for diamond, but the bandstructures[61] and band energies in Table 2.5 are similar. Close to the bandgap, the agreement with experiment is good. Several aspects of both the model and EPM diamond bandstructure[61], such as the lowest conduction bands around Γ and L, and the width of the valence bands, don't agree with experimental data.[61, 63, 64] This is most likely due to ignoring the strong nonlocality of the C potential. Since the motivation here is to obtain a local C potential that can be transferred into the SiC polytypes and is accurate around the bandgap, the potential is adequate.

2.3 SiC Model Potential

For SiC, it is desirable to use modifications of the homopolar diamond-phase Si and C potentials. By using such transferable potentials, a close approximation to the SiC potential may be obtained which can be further fit to experimental data by slightly adjusting a limited number of parameters. This is useful since band-energy data is limited for the hexagonal polytypes. For heteropolar materials the model potential must first be amended to incorporate the effects of charge transfer and screening once dissimilar nearest neighbors are introduced.

The partial ionic nature of bonds, resulting from charge transfer, is important in the determination of the bandstructure of heteropolar materials. This can readily be seen in the ionic gaps in the bandstructure of polar zincblende semiconductors. Charge transfer, fit to experimental band energies of many semiconductors in model calculations, has been shown[66] to approximately agree with the Phillips ionicity[67]

of these materials. This involved using a screened charge transfer that was added directly to the core charge of the individual atoms. These good results suggest a means of estimating and including charge transfer in the HA model. However, since the effects resulting from the bonding of C atoms to much larger Si atoms in SiC, are not accounted for in the Phillips ionicity, we cannot use it to estimate the charge exchange. An ionicity scale[68] based on the charge density asymmetry in the bonds can account for these size-effects. Considering the transferred charge in the valence difference, the asymmetry coefficient can be estimated as

$$g_{SiC} \simeq 1 - \frac{(Z_C - \Delta Z')}{4} = \frac{\Delta Z'}{4}, \tag{2.17}$$

allowing calculation of the charge transfer $\Delta Z'$. To obtain the screened charge transfer ΔZ, $\Delta Z'$ must be adjusted by the average value of the inverse dielectric constant

$$\Delta Z \simeq \frac{4 g_{SiC}}{\overline{\epsilon}_{SiC}} \simeq 1. \tag{2.18}$$

To include these effects in the model, a charge of $-\Delta Z$ is added to the net core charge of C and a charge of $+\Delta Z$ is added to the net core charge of Si. Since the core charge potential is contained in the local bare potential, the transferred charge will alter the potential according to

$$B(q; Z \pm \Delta Z) = B(q; Z) \mp \frac{8\pi \Delta Z}{\Omega q^2} cos(qR), \tag{2.19}$$

where Ω is the unit cell volume.

We also alter the homopolar potentials by screening each atom equivalently with the Penn dielectric function of SiC and by adding a nonlocal correction to the

C potential. This correction, F_C^{NL}, enters the potential through F_C according to

$$F_C = F_C^L(q; A_{C1} - A_{C2}, R_C) + F_C^{NL}(\vec{k}, \vec{q}; A_{C1}^{NL}, R_C). \tag{2.20}$$

A_{C1}^{NL} is the nonlocal $l = 1$ well depth which is used to fine tune the bandstructures, fitting the SiC effective masses, once the best fit local potential is obtained.

Once the homopolar potentials are renormalized with respect to the SiC unit cell volume Ω_{SiC}, we attain the effective atomic potentials transferable into SiC

$$V_{\text{eff}}^{Si} = \Bigg[\frac{B_{Si}(q; A_{Si2}, R_{Si}Z + \Delta Z) + I_{Si}(q; A_{Si0} - A_{Si2}, R_{Si})}{\epsilon_{SiC}(q)} + F_{Si}^L(q; A_{Si0} - A_{Si2}, R_{Si})\Bigg] \frac{\Omega_{Si}}{\Omega_{SiC}} e^{-\alpha_{Si}\Theta(X_{Si})X_{Si}}. \tag{2.21}$$

and

$$V_{\text{eff}}^{C} = \Bigg[\frac{B_C(q; A_{C2}, Z - \Delta Z, R_C) + I_C(q; A_{C1} - A_{C2}, R_C)}{\epsilon_{SiC}(q)} + F_C^L(q; A_{C1} - A_{C2}, R_C) + F_C^{NL}(\vec{k}, \vec{q}; A_{C1}^{NL}, R_C)\Bigg] \frac{\Omega_C}{\Omega_{SiC}} e^{-\alpha_C\Theta(X_C)X_C}. \tag{2.22}$$

The symmetric and antisymmetric potentials are then

$$V_A^S(\vec{q}) = \frac{[V_{\text{eff}}^{Si}(\vec{q}) \pm V_{\text{eff}}^{C}(\vec{q})]}{2}. \tag{2.23}$$

These can then be used along with the structure factor, with basis vector $\vec{\tau}$, to attain the full potential of 3C-SiC

$$V_{3C}(\vec{r}, \vec{k}) = \sum_{\vec{G}} \left[V^S(\vec{k}, \vec{G}) cos(\vec{G} \cdot \vec{\tau}) + iV^A(\vec{k}, \vec{G}) sin(\vec{G} \cdot \vec{\tau})\right] e^{i\vec{G}\cdot\vec{r}}. \tag{2.24}$$

For other polytypes considered an effective 3C-SiC potential is used and the basis atoms are placed in the perfect tetrahedron.[69] Deviations from these "ideal"

positions has been discovered[70], but is ignored here in light of the error involved in treating the potentials locally. Since the lattice spacing and the density of reciprocal lattice vectors differ from 3C, the model potential is evaluated at wave vectors and reciprocal lattice vectors represented in units of the corresponding 3C vectors. For a given polytype nH-SiC, this involves scaling by the ratio of lattice constants $\frac{a_{nH}}{a_{3C}}$. The form of the potential for the hexagonal polytypes considered is

$$V_{nH}(\vec{r},\vec{k}) = \sum_{\vec{G}} F_n(\vec{G}) \left[V^S(\vec{k'},\vec{G'}) cos(\frac{G_z u}{n}) + iV^A(\vec{k'},\vec{G'}) \sin(\frac{G_z u}{n}) \right] e^{i\vec{G}\cdot\vec{r}}, \quad (2.25)$$

where $\vec{k'}(\vec{G'}) = \frac{a_{nH}}{a_{3C}}\vec{k}(\vec{G})$ and $u = \left(\frac{a_{2H}}{c_{2H}}\right)^2$, the wurzite value. For 4H

$$F_4(\vec{G}) = \left[\frac{1 + 2cos(\vec{G}\cdot\vec{\tau}_{4H}) + e^{-\frac{iG_z}{2}}}{4} \right] \quad (2.26)$$

and for 6H

$$F_6(\vec{G}) = \left[\frac{1 + 2cos(\vec{G}\cdot\vec{\tau}_{6H}) + e^{-\frac{2iG_z}{3}}(1 + 2e^{\frac{iG_z}{4}} cos(\vec{G}\cdot\vec{\tau}_{6H} - \frac{G_z}{12}))}{6} \right], \quad (2.27)$$

with $\vec{\tau}_{nH} = (\frac{1}{3}, \frac{1}{3}, \frac{1}{n})$ in 3C direct lattice vector units.

For each of the SiC polytypes, the local model potential is used to produce form factors for $G^2 < 16$ in 3C reciprocal lattice vector units. This is accomplished by retaining all of the Si and C parameters in the model potentials as a first approximation and then varying A_2 of C slightly to fit to the band energies. In this way the large number of EPM form factors needed are obtained by adjustment of one model parameter only. To fit the effective masses the addition of the nonlocal correction to the C A_1 well is needed in 3C and 4H, such a correction was not needed for 6H. As for Si and diamond, a plane wave basis is used that includes the contribution of all plane waves satisfying $(\vec{k}+\vec{G})^2 \leq 21$ for 3C, and by analogy $(\vec{k}+\vec{G})^2(\frac{a_{3C}}{a_{nH}})^2 \leq 21$

for the hexagonal polytypes. These criteria are met with 125, 270, and 390 plane waves for 3C, 4H, and 6H respectively. Convergence is found to within .02 eV for the fitted band energies and effective masses.

Both the local and nonlocal fitting parameters adjust the core potential of the C atoms in SiC. This choice is made since the simplifications used in the model potential are expected to be less reliable for C. As previously discussed, this is evident from the diamond model bandstructure and is a consequence of the lack of $l = 1$ core states that produce a strong attractive well in the C core, allowing the valence electrons to occupy the core with greater ease. Except for the nonlocal correction, the dependence of the core potential on electron wavevector and energy is ignored in the model. The more the valence electrons test out the core, the less valid these approximations should be. Hence, it is the core potential of C that is adjusted in accordance with experimental data.

2.4 Results for SiC

In this section we discuss the results for the polytypes of SiC. The unit cell of each polytype is shown in Fig. 2.5. By varying A_{C2} by less than 3% from the fitted value for carbon and adding a charge transfer of $\Delta Z = 1$, we obtained good fits to experimental band energies of 3C, 4H, and 6H SiC using the local model potential. Nonlocal corrections were needed in 3C and 4H to fit the effective masses, along with a slight adjustment of the local parameter in 4H to retain the fitted band gap. The parameters used are shown in Table 2.5 and comparisons of the band energies

and effective masses with other methods and with experiment is given in Table 2.5 for 3C and in Table 2.5 for the hexagonal polytypes.

For 3C-SiC the local band structure in Fig. 2.6 and the calculated band energies agree well with EPM results[45, 46, 47] and experimental data.[48, 49] A band gap of 2.3eV at the X point is found. The effect of charge transfer is clearly shown in Fig. 2.10. The asymmetric potential agrees well with the EPM form factors once charge transfer is added. An exact fit of the tail of the potential is not expected since we have used V_{12}^{A}. The addition of charge transfer also changes the symmetrical potential, decreasing the q^2 point where the potential passes through zero and raising the maximum.

The transverse effective mass(X-W) calculated from the local 3C bandstructure, agrees well with experiment,[71] but the longitudinal effective mass(X-Γ) is somewhat higher. This is brought into agreement by adjusting the nonlocal correction and attaining a nonlocal bandstructure which, as seen if Fig. 2.6, is very similar to the local results. The valence bands are noticeably altered by the nonlocal term, especially along the K-X symmetry line, while except at the L point, the conduction bands appear relatively unaltered. The slight adjustment of the conduction bands by the nonlocal correction is enough to fit to the experimental effective masses. The improvement in the fit is given in Table 2.5. Agreement with experiment is slightly worse at the conduction band L point once the nonlocal term is included, but this is overshadowed by the benefits of improving the effective masses.

In 4H, the local potential was fit to the experimental bandgap[2] with an A_{C2} closer to the C value. A conduction band minimum or 3.20eV was found at the

M point of Fig. 2.7, agreeing with experiment. As obtained by other methods,[72] the splitting between the first two conduction bands at M was found to be about 0.1eV. Greater anisotropy is found in the effective masses than for 3C, with a large mass found along M-Γ, while smaller yet clearly distinct masses are found in the transverse directions. As seen in Table 2.5, it is expected from experiment that the bands should be flatter along M-K and much steeper along M-Γ. The other transverse mass in the M-L direction agrees reasonably with experiment.

The experimental values of $m_\perp$ and $m_\parallel$ in Table 2.5 were obtained by experiments[73] in which variations in the effective mass, as determined for magnetic fields in the plane perpendicular to the c direction, where not resolved. These "in-plane invariant"[42] effective masses were approximated from the model bandstructure for comparison. As with the longitudinal and transverse masses relative to M-Γ, it is desirable to bring these masses in closer agreement with experiment using the nonlocal correction. As in 3C, this altered the conduction bands in Fig. 2.8 only slightly, but the curvature of the bands is altered quite significantly along the M-Γ line in Fig. 2.11. Also, the degeneracy of the first two conduction bands at L is lifted. The nonlocal results were able to attain good agreement with the M-Γ and M-L results, but didn't improve the M-K effective mass much. Better agreement for $m_\perp$ and $m_\parallel$ are also attained. To retain the correct bandgap, the local parameter A_{C2} was readjusted slightly in the nonlocal potential.

For 6H, the band gap was fit without varying A_{C2} appreciably from the C value. The conduction band minimum, found at the L point, was fit to the experimental value of 3.0eV.[2] In DFT bandstructures[72, 74] and other studies,[3] the minimum

is usually found closer to the M point along M-L, but as found in this work, the lowest conduction band is extremely flat along M-L as seen in Fig. 2.12, varying by less than 0.1eV. The minimum has been found to be along M-L in experiment, but since its exact position is still uncertain,[75] our results are consistent. As in the DFT studies, we find the minimum to be essentially doubly degenerate with the splitting of the first and second conduction bands to be less than 0.01eV, while the third conduction band at L is found to be approximately 1.5eV higher than the minimum. The effective masses at the conduction band minimum parallel and transverse to the L-A direction are consistent with the DFT work. When compared to experiment though, $m_{\perp}$ is fitted well, whereas $m_{\parallel}$ is found to be much lower than experiment. This may result from band filling complications in the experiments due to the flat bandstructure along M-L. The longitudinal and transverse components of the effective mass have still not been determined experimentally for 6H, but since the results of the local model potential are consistent with DFT results and what is known experimentally, we see no need for including a nonlocal correction for 6H at this time.

Since bandstructures accurate close to the bandgap are desired, it is useful to examine the density of states in this region. As found experimentally[77] and theoretically,[78] the major differences between the density of states of the individual SiC polytypes calculated with the model bandstructure is in the conduction bands. The results are compared with results from density functional theory (DFT) in Fig. 2.13, with the bandgaps of the latter adjusted to match experimental results. Both results show not only an increasing bandgap, but an increase in the steepness

of the rise in the density of states at the conduction band edge with increasing hexagonality. This is also found in experimentally,[77] as shown in Fig. 2.14, where we have combined the Si $L_{2,3}$ and C K soft x-ray absorption density of states. As in other work[78] and experiment,[77] the valence band density of states was found to be very similar for the different polytypes. In Tables 2.5 and 2.5, the EPM form factors corresponding to the model potential for 4H and 6H are given. To our knowledge these represent the first published form factors for these materials. They can be used within the EPM to reproduce the local model bandstructure of these polytypes. If it is desired to include the nonlocal correction for 4H, the set of appropriate form factors for the local potential are to be used.

2.5 Chapter Summary

We found that by including the appropriate screening and charge transfer, and then refitting, the HA potential could be effectively modified for use as a semi-empirical pseudopotential for semiconductors. A SiC local model potential was developed using Si and C potentials that were each successfully fitted to the homopolar experimental band energies around the band gap region. This potential could then be fitted with one local and one nonlocal parameter to obtain the bandstructure for 3C and 4H SiC. The nonlocal parameter is included as a means to fit the effective masses. For 6H, only the local parameter was needed since the local potential was found to be consistent with experiment. Agreement with experimental band energies and most effective masses is found to be good. The large number of EPM form

factors needed for 4H and 6H are obtained from the local potential and can be used to reproduce the local bandstructures, while the nonlocal term can be included to obtain the fitted effective masses. This represents an enormous reduction in the empirical fitting parameters needed since roughly 30 EPM form factors are needed for 4H and 6H-SiC.

It is likely that the local approach could be applied to SiC polytypes with even larger unit cells than 6H using the variation in bandgap with hexagonality[2, 3] in cases where experimental band gaps are undetermined. When effective mass data is available, then the nonlocal correction may be included. It is also expected that a similar approach could be applied to other materials for which the HA model potential represents a reasonable approximation to the atomic core potentials in the solid. Another possible application is the use for defects which retain the bulk bonding characteristics such as low energy stacking faults.

	A_{Si0}	A_{Si2}	R_{Si}	A_{C1}	A_{C1}^{NL}	A_{C2}	R_C	ΔZ	E_g	α
Si	2.08	2.40*	2.00					0	4.8	4.44
C				4.48	0	3.94*	1.44	0	13.6	5.75
SiC parameters that differ from the Si and C parameters above.										
3C	-	-	-	-	.3*	4.06*	-	1	9.1	-
4H	-	-	-	-	.4*	3.97^{a}*/3.90^{b}*	-	1	9.1	-
6H	-	-	-	-	0	3.93*	-	1	9.1	-

Table 2.1: SiC Model parameters. (Atomic units are used here and the fitting parameters are indicated with (*). Here a is for the local potential and b is for the nonlocal potential.)

Energy	**Model**	**EPM**[b]	**Exp.**[a]
E_{gap}	1.10	0.87	1.12
Γ_{1v}-$\Gamma_{25'v}$	-12.52	-12.60	-12.56
Γ_{15c}-$\Gamma_{25'v}$	3.56	3.34	3.35
Γ_{2c}-$\Gamma_{25'v}$	4.04	4.37	4.16
L_{1c}-$\Gamma_{25'v}$	2.09	2.09	2.05
L_{3c}-$\Gamma_{25'v}$	4.16	3.88	3.91
L_{1v}-$\Gamma_{25'v}$	-7.24	-7.33	-6.82
L_{3v}-$\Gamma_{25'v}$	-1.22	-1.26	-1.22
L_{2v}-$\Gamma_{25'v}$	-10.17	-10.18	-9.34
X_{4v}-$\Gamma_{25'v}$	-2.94	-3.02	-2.90

Table 2.2: Energy levels of Si. (Energies here are in eV. Here a is from reference [62] and b is from [60].)

Energy	**Model**	**EPM**[a]	**Exp.**
E_{gap}	5.50	5.46	5.51^{b}
Γ_{1v}-$\Gamma_{25'v}$	-28.47	-29	-21.00^{c}
Γ_{15c}-$\Gamma_{25'v}$	7.12	6.96	$6^{c}/7^{d}$
Γ_{2c}-$\Gamma_{25'v}$	10.66	19	15.35^{c}
L_{1v}-$\Gamma_{25'v}$	-15.85	-16	-12.83^{c}

Table 2.3: Energy gaps of diamond. (Energies here are in eV, while a is from reference [61], b is from [63], c is from [64], and d is from [65].)

	Model(local)	**Model(nonlocal)**	**EPM**	**Expt.**
X_{1c}-Γ_{15v}	2.30	2.30	$2.35^{c}, 2.42^{d}, 2.39^{e}$	2.39^{a}
X_{3c}-X_{1c}	2.90	2.74	$3.03^{c}, 2.5^{d}$	3.10^{b}
Γ_{1c}-Γ_{15v}	5.73	5.73	$5.92^{c}, 6.0^{d}, 6.0^{e}$	6.0^{a}
L_{1c}-Γ_{15v}	4.26	3.95	$4.38^{c}, 4.26^{d}, 4.20^{e}$	4.20^{a}
X_{1c}-L_{3v}	4.00	4.33	$3.99^{c}, 4.18^{d}$	3.55^{a}
m_1*	.22 ± .02(XW)	.24 ± .02	-	$.247^{f}$
m_2*	.22 ± .02(XW)	.24 ± .02	-	$.247^{f}$
m_3*	1.2 ± .02(XΓ)	.7 ± .1	-	$.667^{f}$

Table 2.4: Band energies and effective masses of 3C-SiC. (Energies are in eV and effective masses are in units of the electron mass. Here a is from reference [48], b is from [49], c is from [45], d is from [46], e is from [47], and f is from [71].)

	Model(local)	Model(nonlocal)	DFT	Expt.
		4H-SiC		
M_{1c}	3.21	3.20	3.2^b	3.26^a
m_1*	$1.50 \pm .05$(MΓ)	$.60 \pm .05$	$.58^c$	$.58^c$
m_2*	$.19 \pm .02$(MK)	$.20 \pm .02$	$.29^c$	$.29^c$
m_3*	$.39 \pm .02$(ML)	$.36 \pm .02$	$.31^c$	$.33^c$
$m_\perp*$	$.53 \pm .03$	$.35 \pm .02$	$.42^c$	$.42^d$
$m_\parallel*$	$.19 \pm .04$	$.31 \pm .05$	$.29^c$	$.29^d$
		6H-SiC		
ML_{1c}^{min}	2.99(L)	-	3.0^b	3.02^a
m_1*	$.90 \pm .03$(LA)	-	$.77^c$	
m_2*	$.22 \pm .02$(LH)	-	$.24^c$	
m_3*	$1.43 \pm .02$(LM)	-	1.42^c	
$m_\perp*$	$.44 \pm .02$	-	$.42^c$	$.42^d$
$m_\parallel*$	$1.14 \pm .14$	-	$1.1 - 2.0^c$	$2.0 \pm .2^d$

Table 2.5: Band energies and effective masses of 4H and 6H SiC. (Energies are in eV and effective masses are in units of the electron mass. Here a is from reference [2], b is from [72], c is from [42], and d is from [73].)

	4H(local)		**4H(nonlocal)**		**6H(local)**	
G^2	V^S	V^A	V^S	V^A	V^S	V^A
$2\frac{2}{3}$	-.463		-.462			
$2\frac{3}{4}$					-.443	-.027
$2\frac{5}{6}$	-.426	-.016	-.425	-.018		
3	-.392	.002	-.390	.000	-.391	.001
$3\frac{5}{12}$	-.314	.040	-.312	.038	-.313	.038
4						.075
$4\frac{1}{3}$	-.180	.090	-.177	.088		
$4\frac{3}{4}$					-.130	.101
$5\frac{2}{3}$	-.046	.117	-.043	.113	-.044	.114
$6\frac{3}{4}$					.030	.113
$7\frac{1}{3}$	.058	.110	.062	.106		

Table 2.6: Model potential EPM form factors of 4H, and 6H-SiC when G^2<8. (Form factors are in Rydbergs. The form factors which exist for G^2, in units of 3C-SiC reciprocal vectors, but whose structure factor vanishes are not shown.)

	4H(local)		**4H(nonlocal)**		**6H(local)**	
G^2	V^S	V^A	V^S	V^A	V^S	V^A
8	.088		.092		.091	
$9\frac{5}{12}$	.135	.078	.140	.073	.138	.075
$10\frac{2}{3}$	.152		.157			
$10\frac{3}{4}$					.156	.055
$10\frac{5}{6}$	.153	.057	.158	.052	.156	.054
11	.153	.055	.159	.049	.157	.051
$11\frac{5}{12}$	.155	.048	.161	.043	.159	.045
$11\frac{5}{6}$	.156	.042	.161	.037		
12		.040		.034		.036
$12\frac{1}{3}$	.154	.035	.159	.030		
$12\frac{3}{4}$					.152	.027
$13\frac{2}{3}$	.126	.020	.130	.016		
$14\frac{2}{3}$		.014		.011		
$14\frac{3}{4}$					.093	.012

Table 2.7: Model potential EPM form factors of 4H, and 6H-SiC when $G^2 \geq 8$. (Form factors are in Rydbergs. The form factors which exist for G^2, in units of 3C-SiC reciprocal vectors, but whose structure factor vanishes are not shown.)

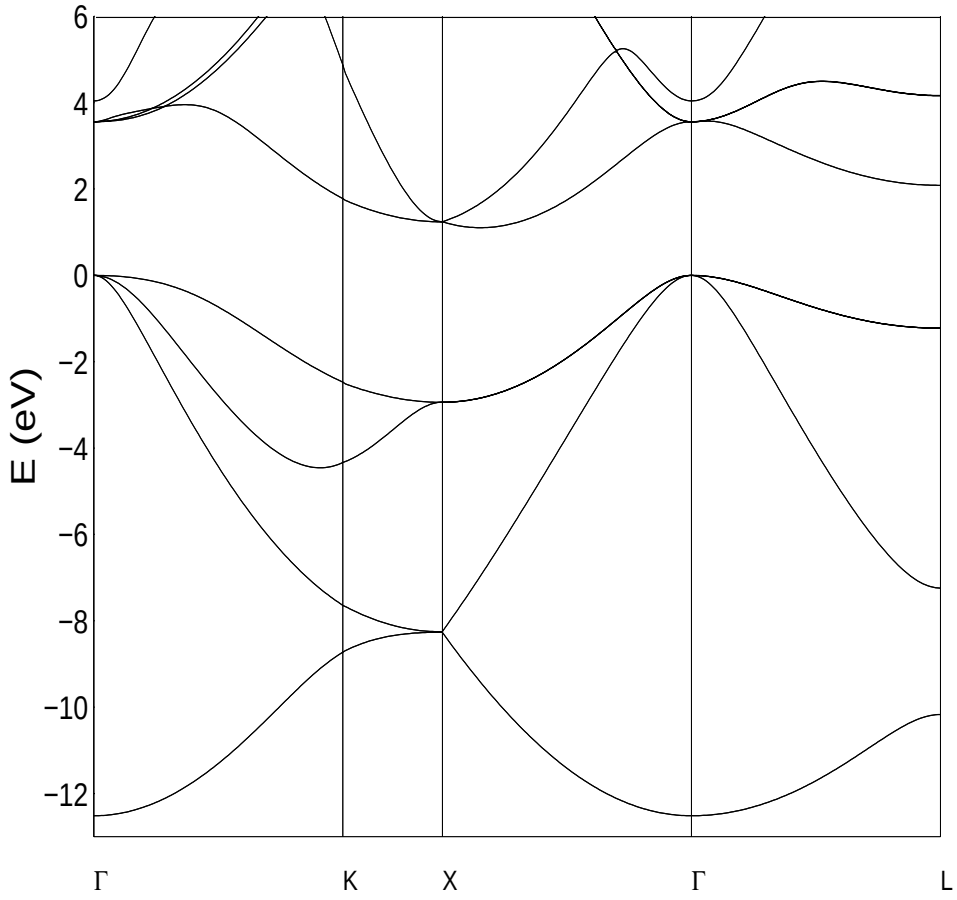

Figure 2.1: Si local-model potential bandstructure.

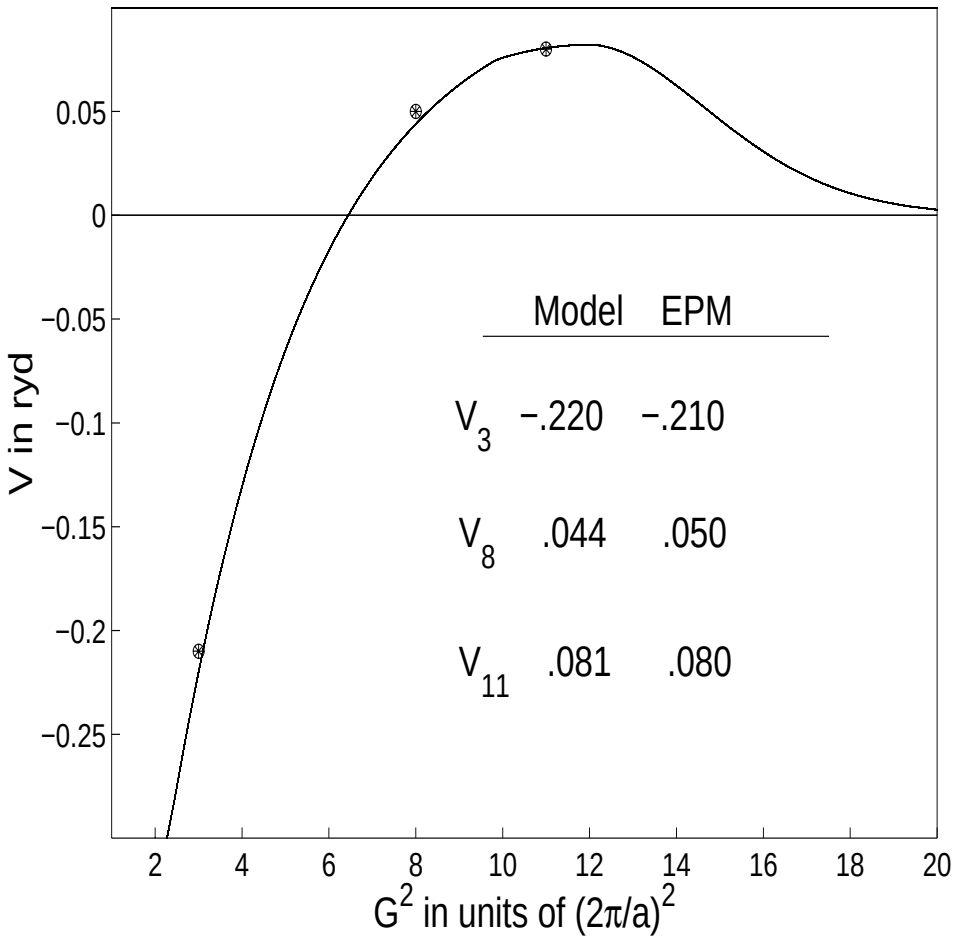

Figure 2.2: Model potential of Si. (EPM form factors of [60] (•) are included.)

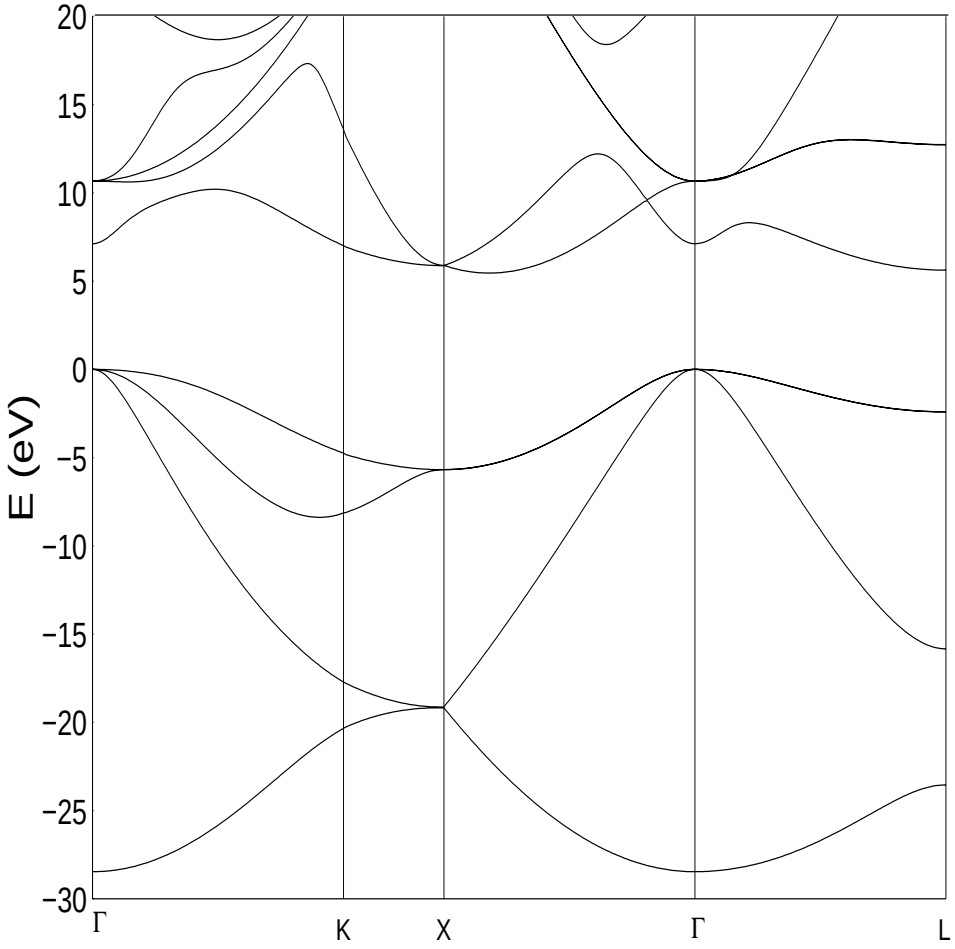

Figure 2.3: Diamond local-model potential bandstructure.

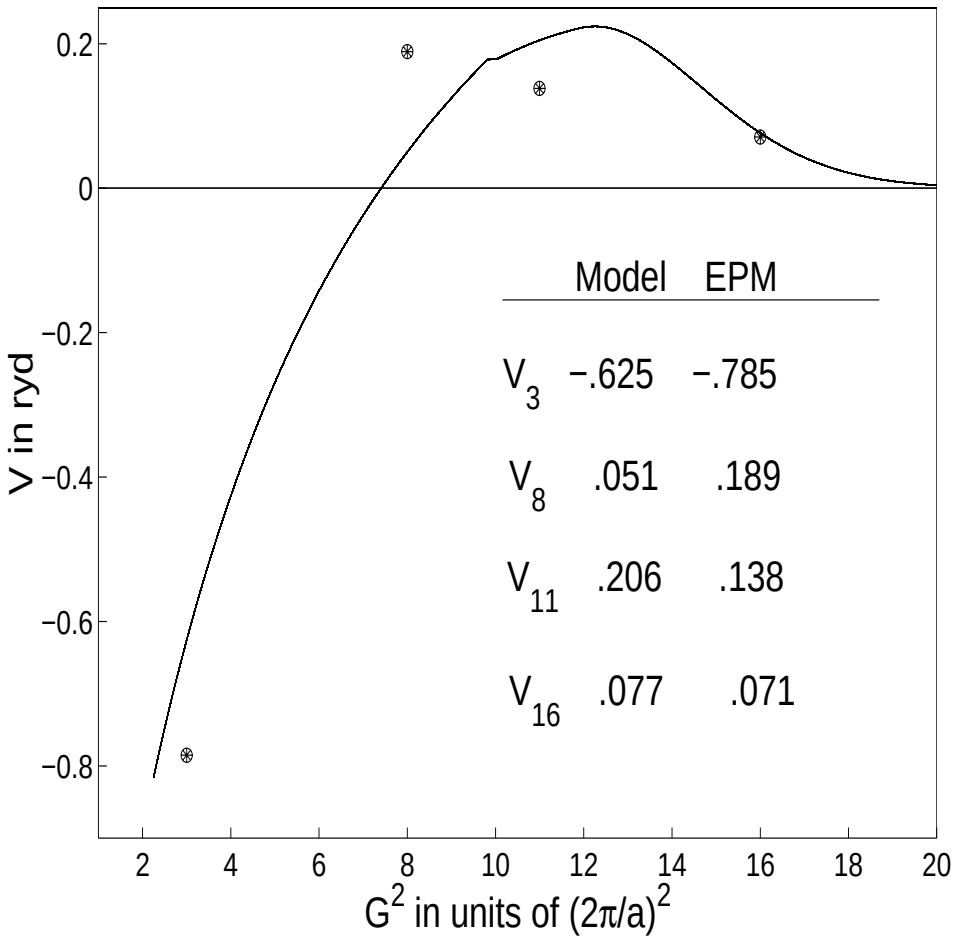

Figure 2.4: Model potential of C. (The EPM form factors of [61] (•) are included).

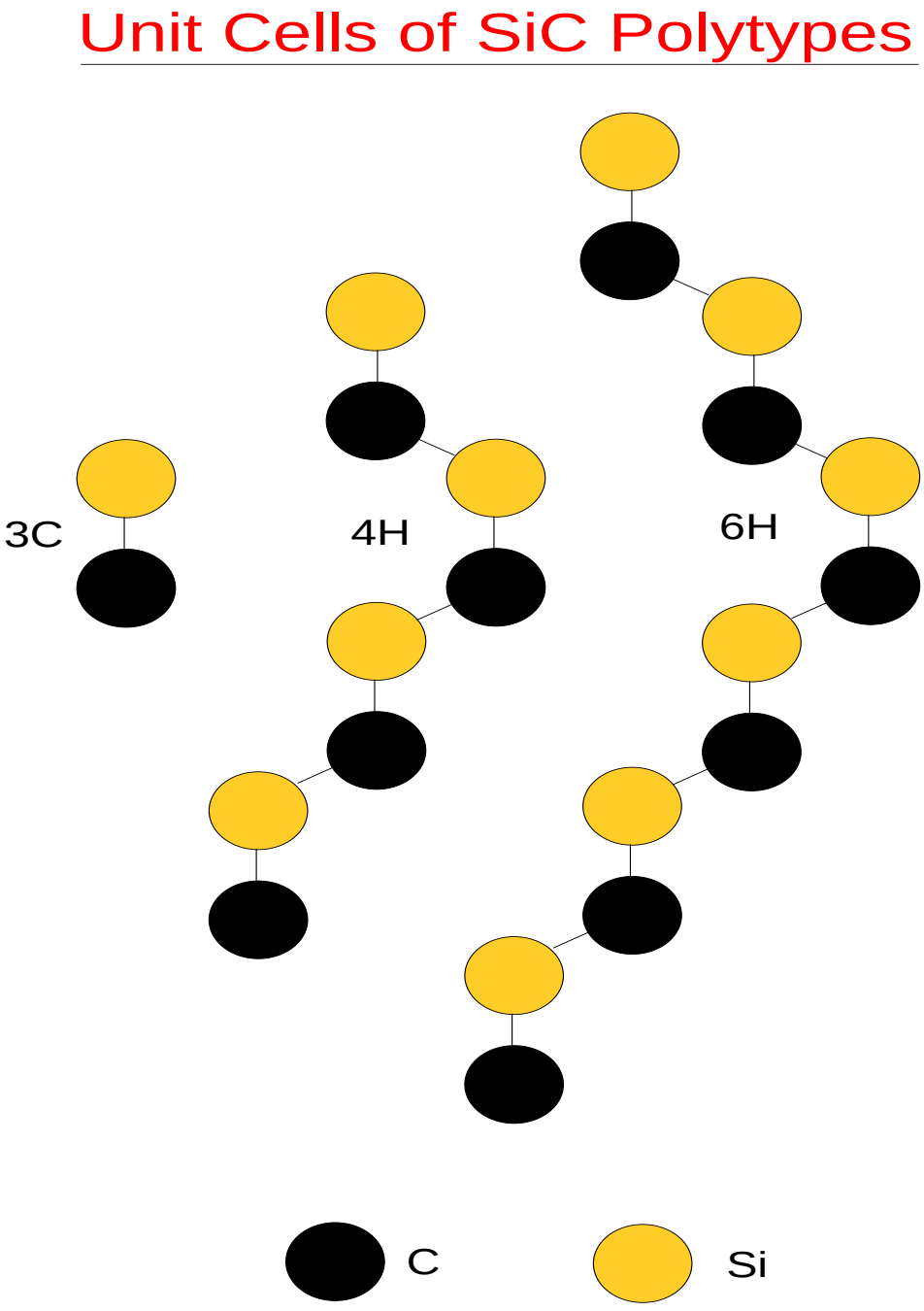

Figure 2.5: Unit cells for the SiC polytypes.

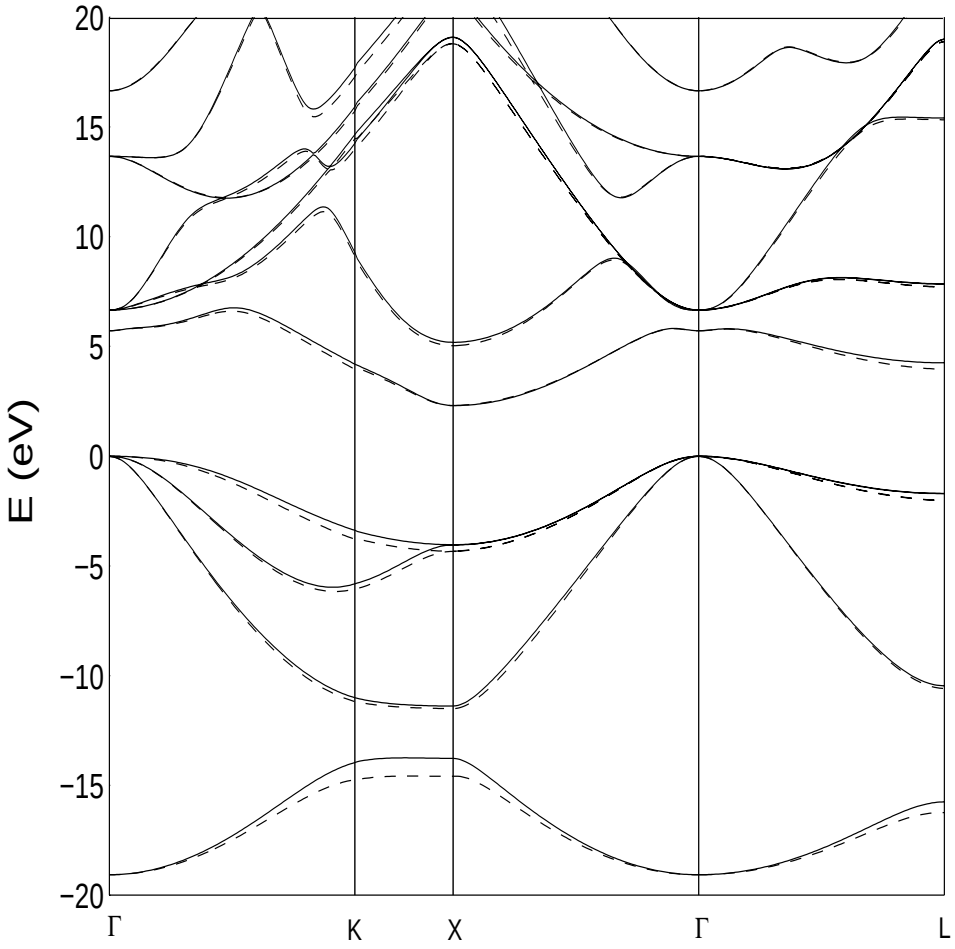

Figure 2.6: 3C-SiC Local(-) and nonlocal(- -) model bandstructure.

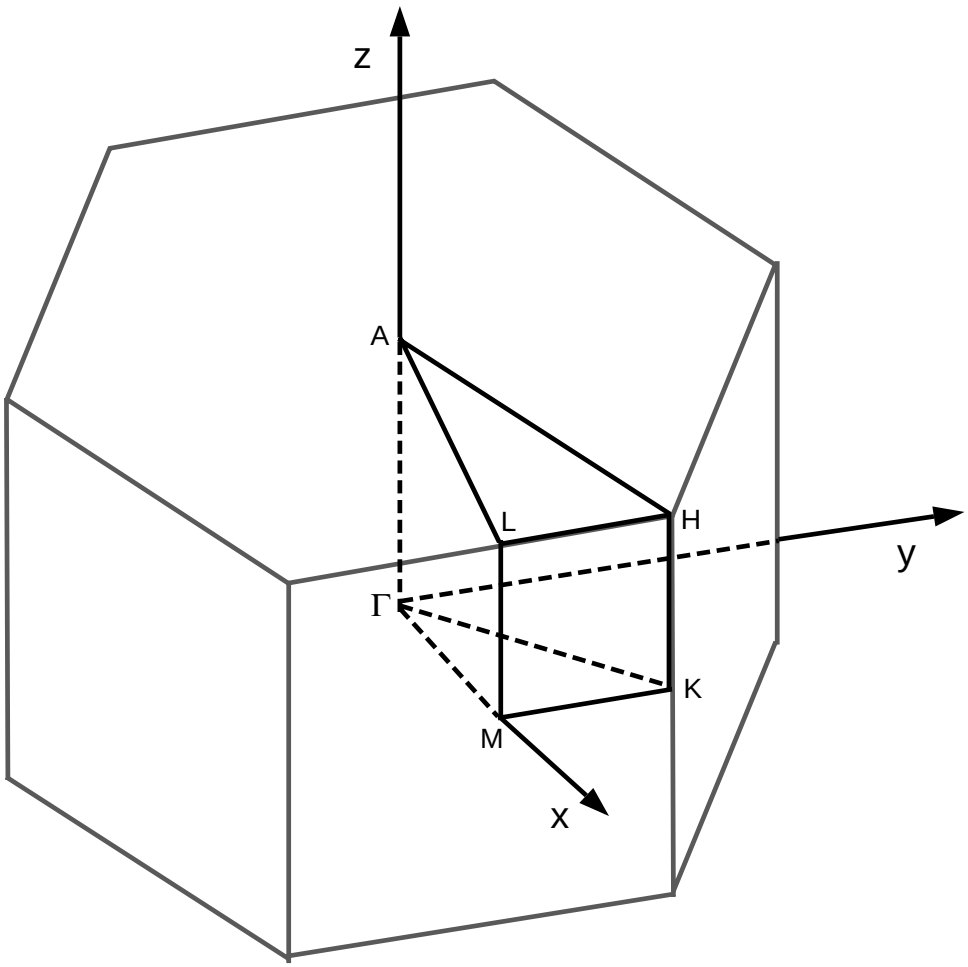

Figure 2.7: Hexagonal Brillouin zone and irreducible wedge.

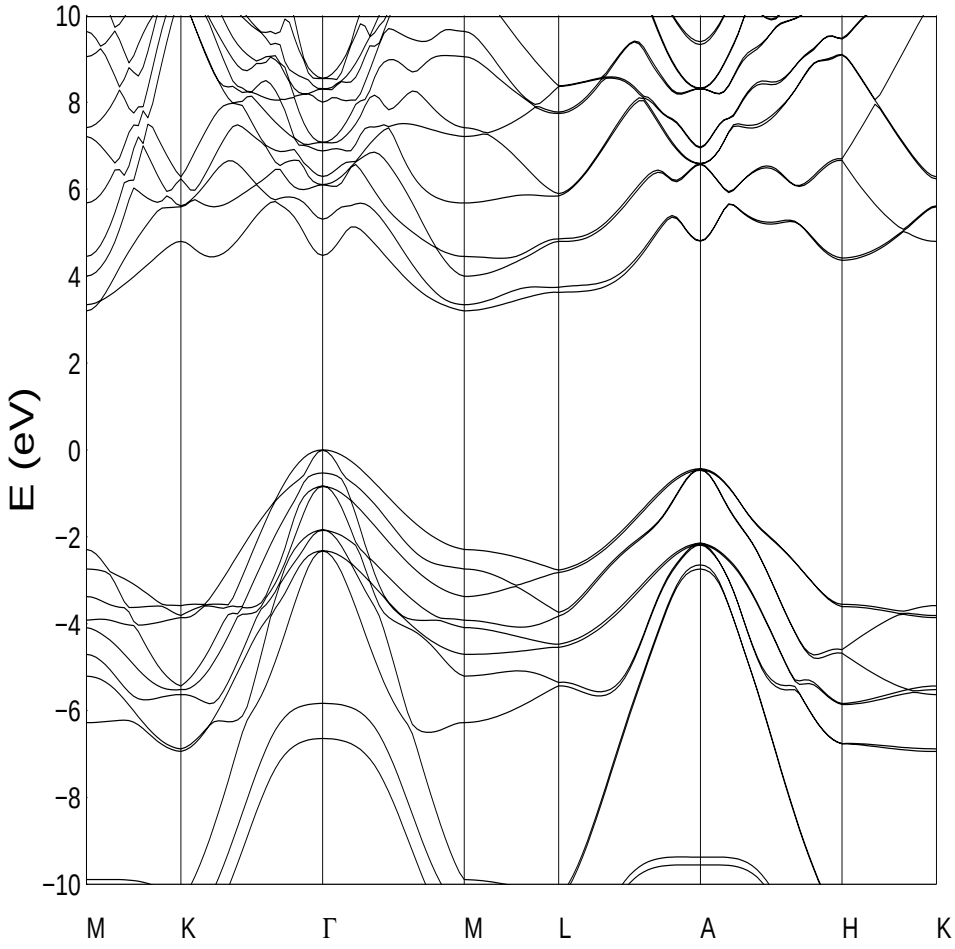

Figure 2.8: 4H-SiC nonlocal model bandstructure.

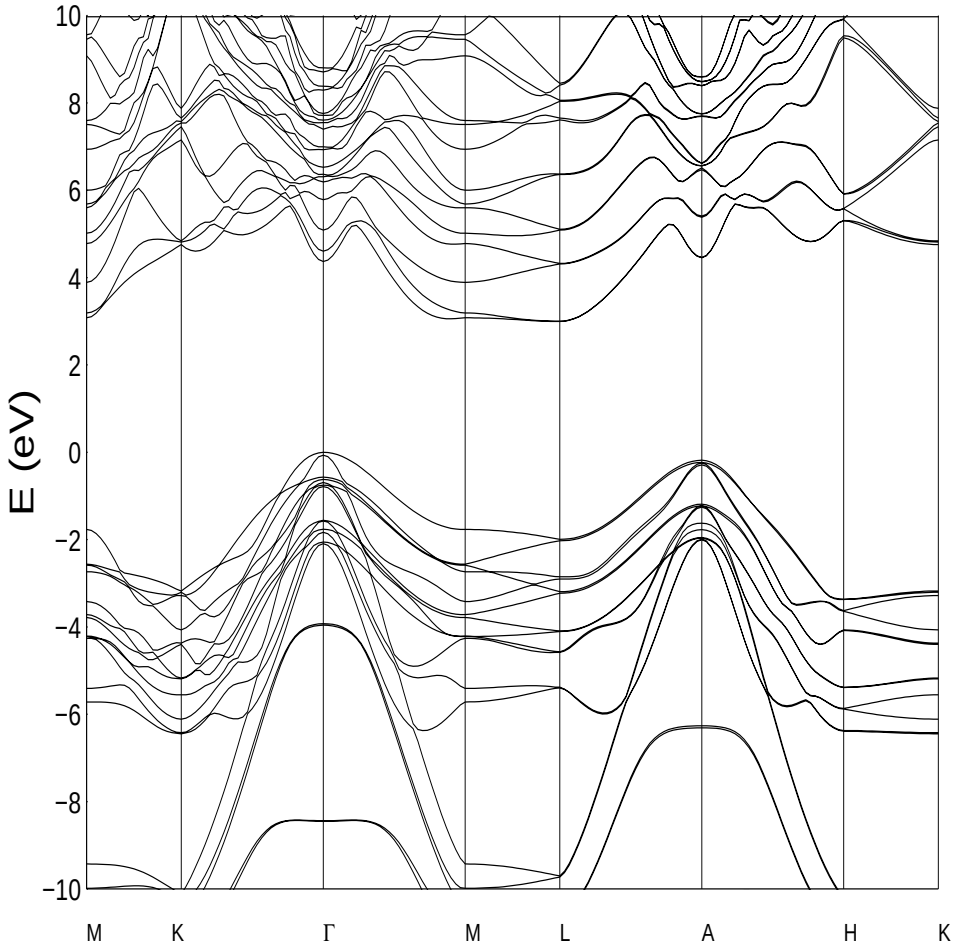

Figure 2.9: 6H-SiC local-model potential bandstructure.

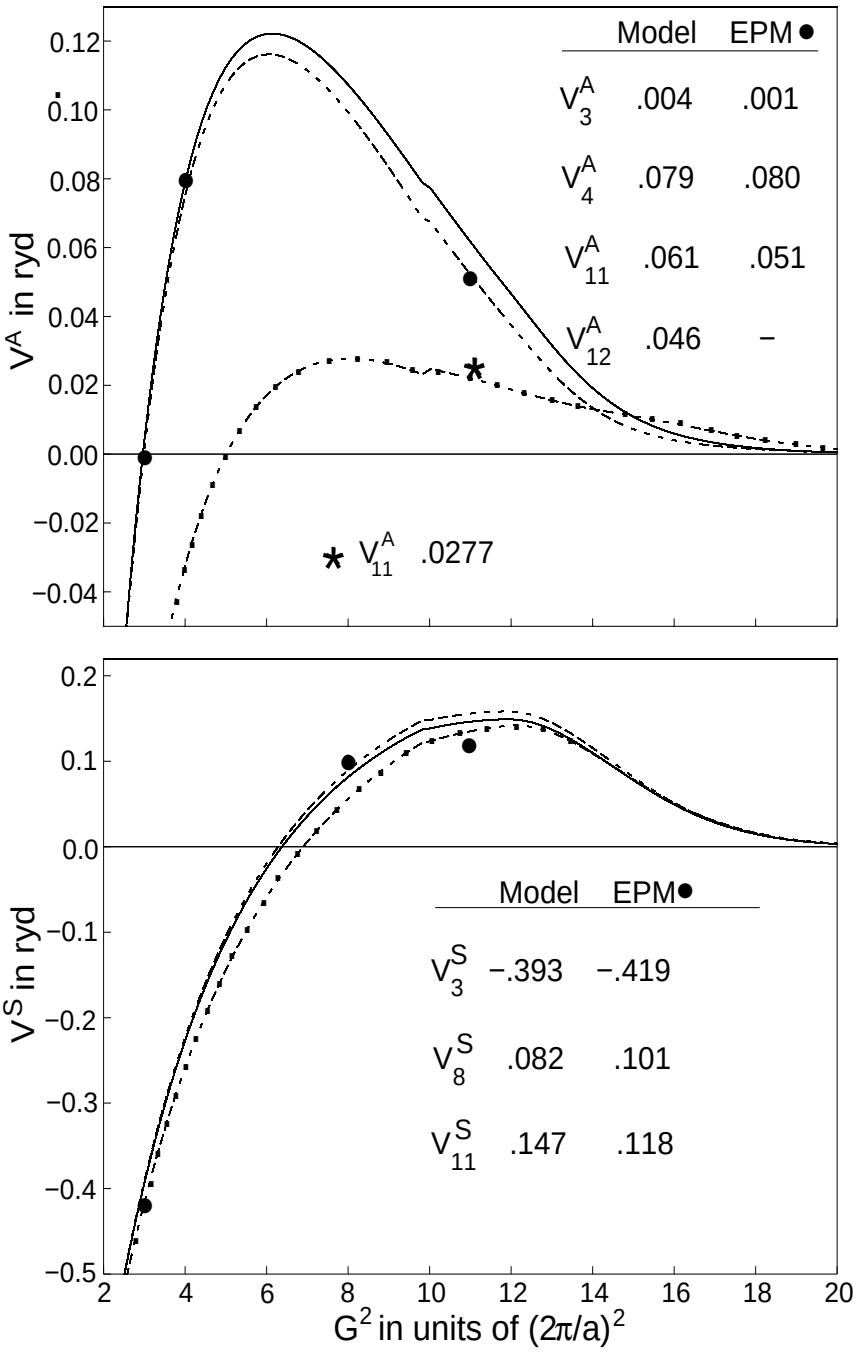

Figure 2.10: Asymmetric(V^A) and symmetric(V^S) model potentials. (The EPM form factors of [45] (•). The form factor for V_{11}^A of both [46] and [47] ($*$) varies significantly and is also shown. The model potentials without charge transfer(-··-), with charge transfer(- -), and fitted to 3C-SiC band energies(—) are shown.)

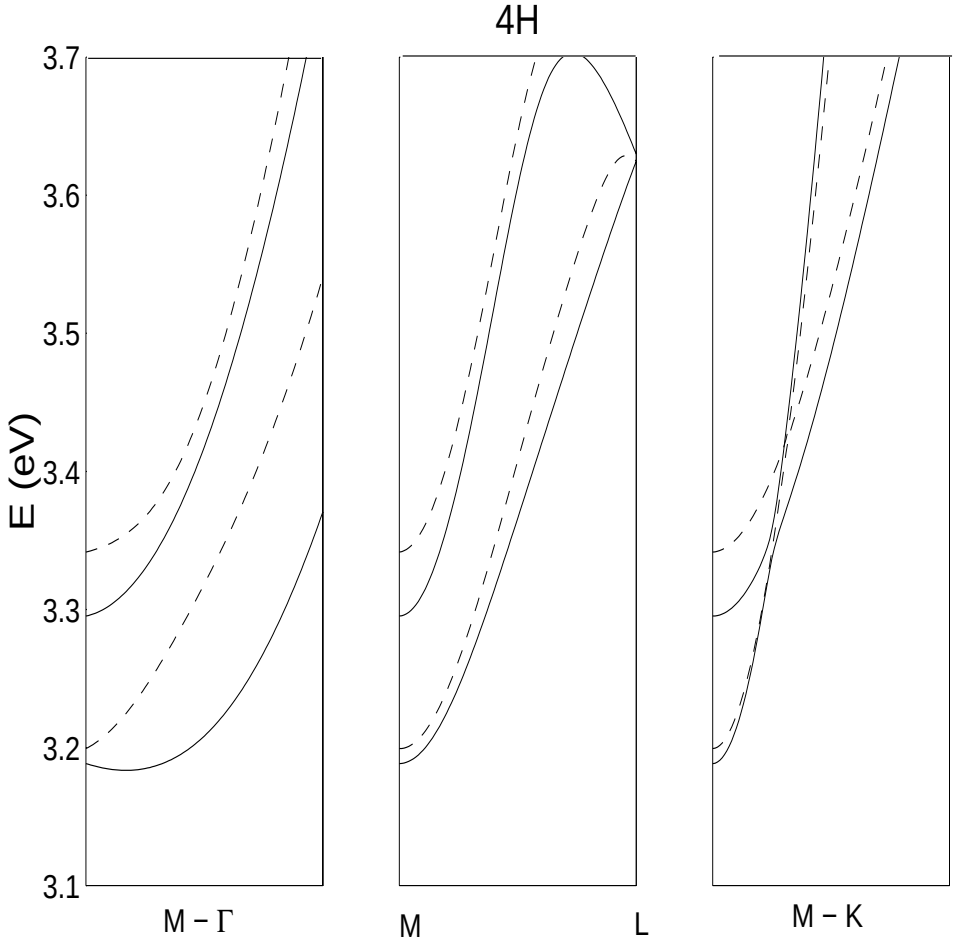

Figure 2.11: Model potential conduction band edge of 4H-SiC. (Here we show the results with(- -) and without(–) the nonlocal correction. The $\mathbf{M-\Gamma}$ and **M-K** distances shown are equal to the **M-L** distance).

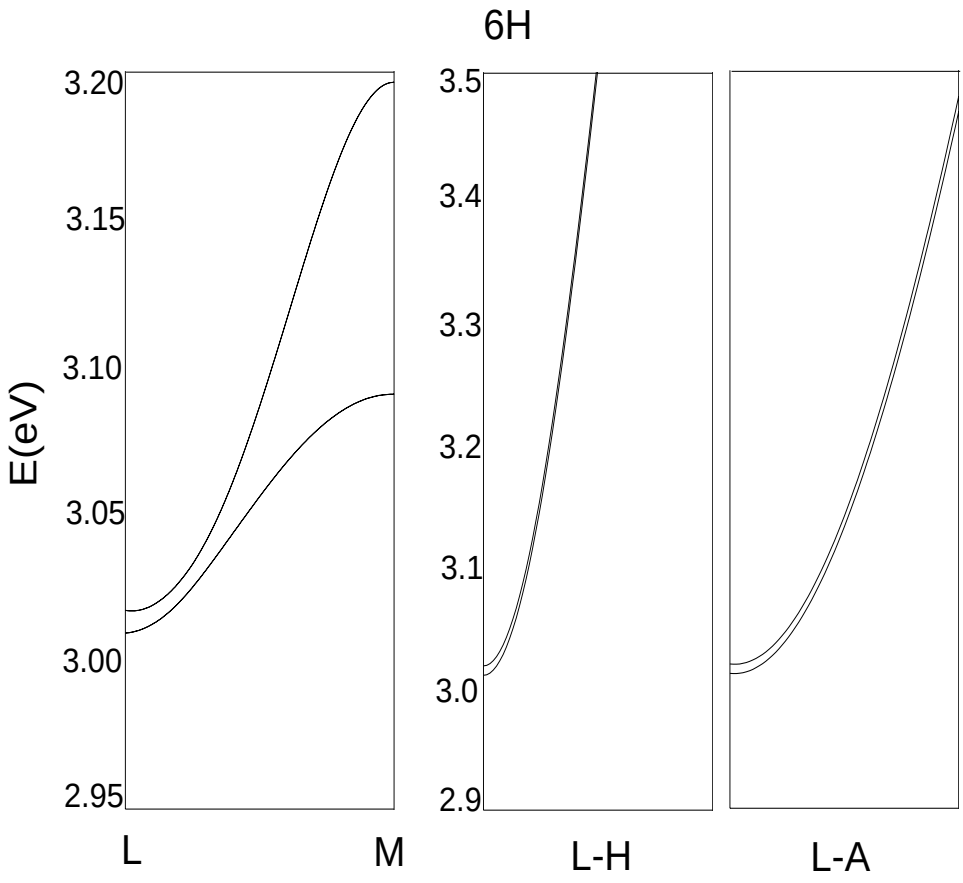

Figure 2.12: Model potential conduction band edge of 6H-SiC. (The **L-A** and **L-H** distances shown are equal to half the total **L-H** distance).

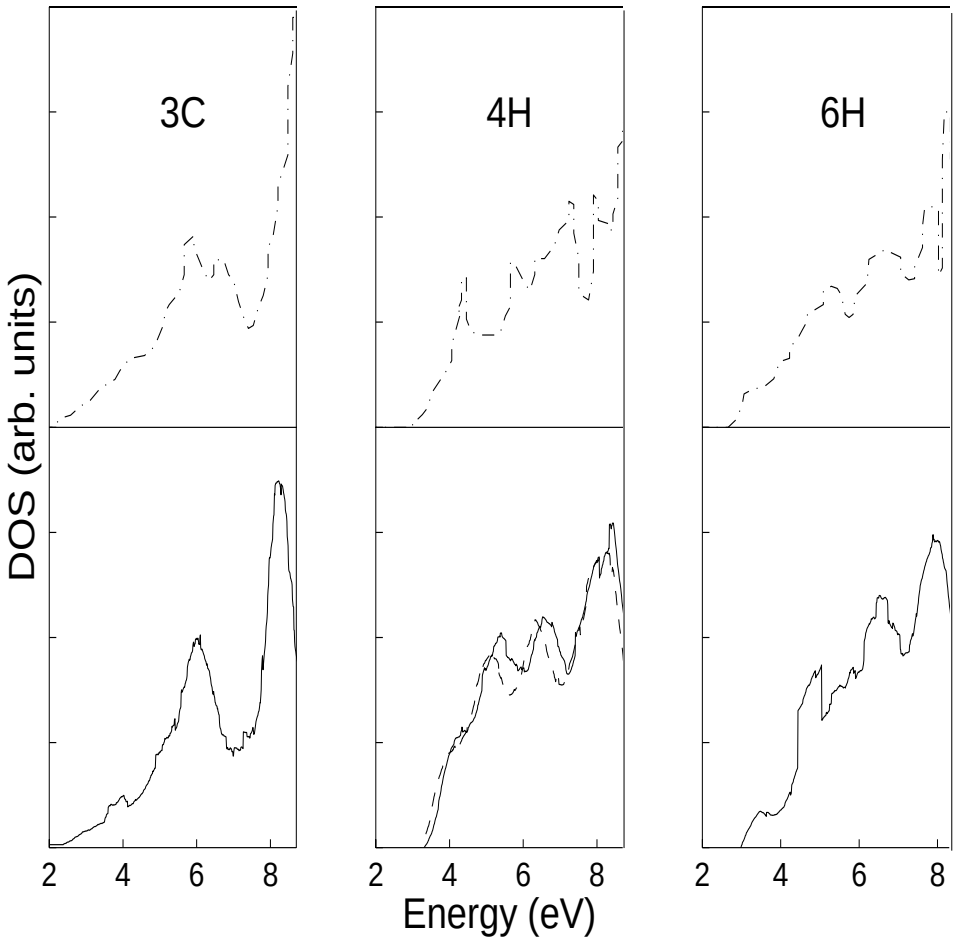

Figure 2.13: Conduction band density of states for the model potential(–) and that calculated from density functional theory of [78] (-··-). (For 4H, the nonlocal(–) and local(- -) results are shown).

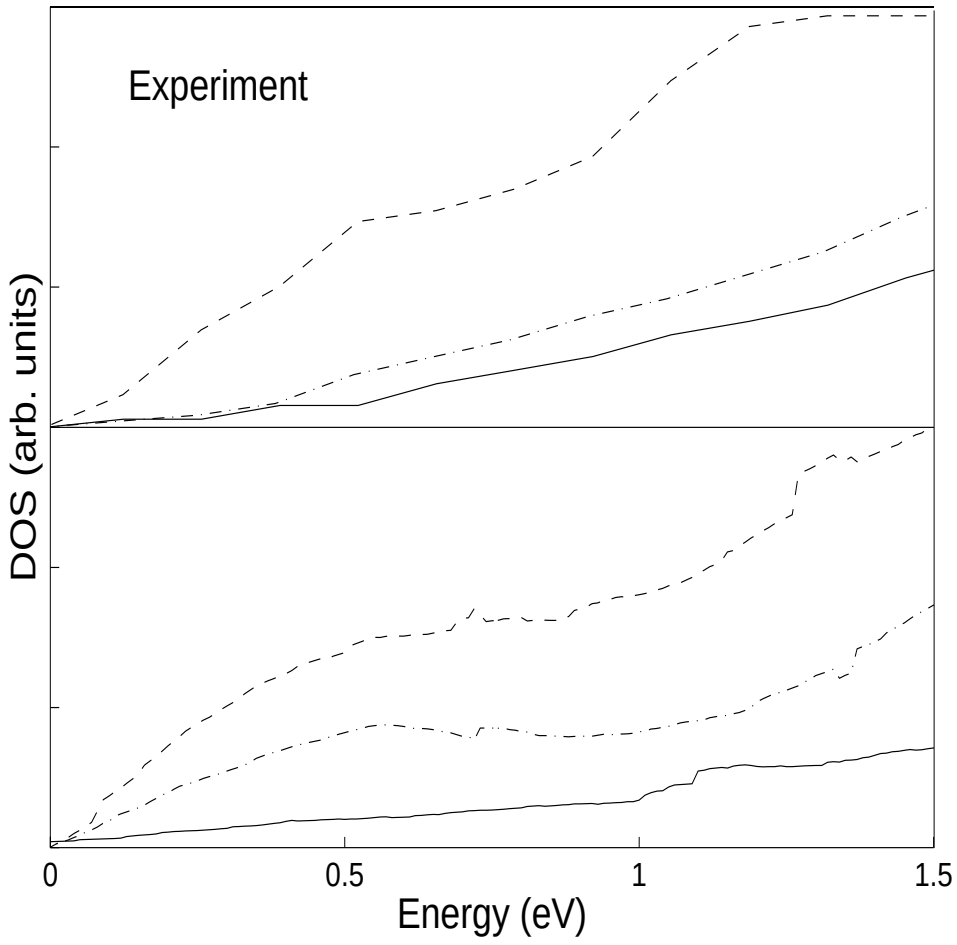

Figure 2.14: Experimental[76] and local model density of states at conduction edge for 3C(–), 4H(- -), and 6H(-·-). (For comparison the conduction band minimum is set to zero for each method. Nonlocal results for 3C and 4H do not vary noticeably).

Chapter 3

Simulation of Bulk Electron Transport in Hexagonal SiC

In this Chapter a study of high-field temperature-dependent electron transport in 6H-SiC is presented. This investigation is carried out using a full-band Monte Carlo simulator which is developed specifically for modeling SiC. The motivation for exploring the transport properties of SiC stems from its high saturation velocity, high thermal conductivity and large breakdown voltage, which lead to a wealth of potential applications in electronic devices operating at high temperature and high power.

3.1 Scattering Rates

The scattering mechanisms considered in our simulations are acoustic phonon, intervalley optical phonon, polar optical phonon, ionized impurity, and impact ionization scattering. The rates are all based on the "Golden Rule" in Eq. (1.2). For an electron with energy ε, the scattering rates Γ are given by

$$\Gamma(\varepsilon) = \Lambda(\varepsilon) DOS(\varepsilon \pm E_q). \tag{3.1}$$

Here DOS is the EPM band structure density of states which is stored in a look-up table before the Monte Carlo simulation begins. The term Λ is the proportionality factor between the rate and the density of states and depends on the type of scatterer involved. The energy transfer E_q also depends on the scattering mechanism in question.

The factor Λ is approximated as the proportionality constant between the scattering rate and the density of states when the electron occupies the nonparabolic minmia of the lowest conduction band. This minima is described by an effective mass of m_d=0.66m_e and a nonparabolic factor of α=0.323. The form for Λ is thus more reliable when the electron energy ε is smaller and electrons stay in the minima of the lowest subband. The rate at higher energies is determined by scaling Λ, which is based on a model band structure, by the realistic empirical pseudopotential density of states DOS. The material parameters for the scattering rates are given in Tables 3.1 and 3.2.

In the case of acoustic phonon scattering, the deformation potential approximation is considered[82]. The rate is determined for the elastic case where the

energy transfer is set to zero. The rate in Eq. (3.1) is determined by

$$\Lambda^{ac}(\varepsilon) = \frac{\pi \left(K_B T\right)^3 D_{ac}^2 DOS(\varepsilon)}{4 m_d \hbar u^4 \rho \sqrt{\gamma}} \left(\left[F_2^{\pm}(X_2) - F_2^{\pm}(X_1) \right] (\pm) \left[F_3^{\pm}(X_2) - F_3^{\pm}(X_1) \right] \right), \tag{3.2}$$

where

$$\gamma(\varepsilon) = \varepsilon \left(1 + \alpha\varepsilon\right), \tag{3.3}$$

and the +(-) sign is for absorption(emission) of an acoustic phonon[38]. The F factors are given by

$$F_n^{\pm}(X) = \int_0^X \left[N_q(x') + \frac{1}{2}(\mp)\frac{1}{2} \right] x'^n dx', \tag{3.4}$$

where N_q is the Bose-Einstein equilibrium distribution function. The values of the limits of integration X are given in Table 3.3.

For scattering with intervalley phonons, a zeroth order and a first order interaction are considered. The zeroth order rate is determined by[38]

$$\Lambda^{iv0}(\varepsilon) = \frac{\pi \hbar D_{iv0}^2}{\rho E_{iv0}} \left[N(E_{iv0}) + \frac{1}{2}(\mp)\frac{1}{2} \right], \tag{3.5}$$

where the upper(lower) sign is for absorption(emission) of an optical phonon with characteristic energy E_{iv0}. The energy transfer in Eq. (3.1) is $\pm E_{iv0}$. This phonon energy is given in Table 3.2. Here D_{iv0} is the deformation potential which is fitted to experiments. The phonon occupation number at fixed energy E_{iv0} is given by

$$N(E_{iv0}) = \left(\exp\left(E_{iv0}/K_B T\right) - 1 \right)^{-1}. \tag{3.6}$$

The first order interaction is given by [83, 84]

$$\Lambda^{iv1}(\varepsilon) = \frac{2\pi m_d D_{iv1}^2}{\rho \hbar E_{iv1}} \left[\gamma(\varepsilon) + \gamma(\varepsilon \pm E_{iv1}) \right] \left[N(E_{iv1}) + \frac{1}{2}(\mp)\frac{1}{2} \right]. \tag{3.7}$$

The deformation potential D_{iv1} will be used as an adjustable fitting parameter.

The scattering rate between a conduction electron and a polar optical phonon is formulated in terms of the Froelich interaction and the effective field strength induced by the phonon. This is the polar field E_o, which is taken as a fitting parameter here. Slight adjustments are made to the theoretically expected result[37, 38, 85]

$$E_o = \frac{m_d e E_{po}}{4\pi^2\hbar^2}\left(\frac{1}{\epsilon_\infty} - \frac{1}{\epsilon_s}\right). \tag{3.8}$$

Here E_{po} is the energy of the polar optical phonon and the dielectric constant at both high-frequencies, ϵ_∞, and at low-frequencies(static), ϵ_s, is included.

The electron energy after scattering is $\varepsilon'=\varepsilon \pm E_{po}$, where the upper sign is for phonon absorption and the lower sign is for phonon emission. In terms of the polar field, the proportionality factor from Eq. (3.1) is then

$$\Lambda^{po}(\varepsilon) = \frac{4\pi^2\hbar^3 E_o}{m_d^2\sqrt{\gamma(\varepsilon)\gamma(\varepsilon')}}\left[A\ln\left|\frac{\sqrt{\gamma(\varepsilon)}+\sqrt{\gamma(\varepsilon')}}{\sqrt{\gamma(\varepsilon)}-\sqrt{\gamma(\varepsilon')}}\right| + B\right] C^{-1}. \tag{3.9}$$

Here we have

$$A = \left[2\left(1+2\alpha\varepsilon\right)\left(1+\alpha\varepsilon'\right) + \alpha\left(\gamma(\varepsilon)+\gamma(\varepsilon')\right)\right]^2, \tag{3.10}$$

$$B = -2\alpha\sqrt{\gamma(\varepsilon)\gamma(\varepsilon')}\left[4\left(1+\alpha\varepsilon\right)\left(1+\alpha\varepsilon'\right) + \alpha\left(\gamma(\varepsilon)+\gamma(\varepsilon')\right)\right], \tag{3.11}$$

and

$$C = 4\left(1+\alpha\varepsilon\right)\left(1+\alpha\varepsilon'\right)\left(1+2\alpha\varepsilon\right)\left(1+2\alpha\varepsilon'\right). \tag{3.12}$$

For the scattering of electrons with ionized impurities, Ridely's method is used[79]. The rate is

$$\Gamma^{imp}(\varepsilon) = \frac{\vartheta_g}{d}\left[1-\exp\left(-d/\vartheta_g\Gamma^{BH}(\varepsilon)\right)\right], \tag{3.13}$$

where ϑ_g is the electron group velocity, and d is the average distance between the ions. A value of $25\pi d{=}N^{1/3}$ is used here, where N is the density of ionized impurities. For this we use $N{=}n + 2N_A$, where n is the mobile charge density and N_A is the density of acceptors. The donor state energies involved in the determination of n are 0.08, 0.12, and 0.45eV. The term Γ^{BH} is the Brooks-Herring scattering rate [86] given by

$$\Gamma^{BH}(\varepsilon) = \frac{Ne^4}{16\sqrt{2m_d}\pi\epsilon_s^2}\left[\log\left(1+\gamma^2(\varepsilon)\right) - \frac{\gamma^2(\varepsilon)}{1+\gamma^2(\varepsilon)}\right]\gamma^{-3/2}(\varepsilon), \tag{3.14}$$

where collisions are taken to be elastic.

For the impact ionization scattering rate the Keldysh expression is used[41]. The rate is given by

$$\Gamma^{ii}(\varepsilon) = \Gamma^T(\varepsilon)P\left(\frac{\varepsilon - E_{th}}{E_{th}}\right)^2. \tag{3.15}$$

Here P, the hardness factor, and E_{th}, the threshold energy, are adjustable parameters. The total rate, including all of the other scattering mechanisms except Γ^{ii}, is given by Γ^T. A threshold of 1.07[87] times the band gap and a hardness factor of 10[87] were used for the impact ionization scattering rate.

3.2 Monte Carlo Simulator

To simulate the electron transport properties we adapt the full-band MC method (FBMCM)[41, 79, 80], to hexagonal SiC. Here we will focus of steady-state simulations of electron transport in 6H-SiC. The electronic band structure is calculated using the method in Chapter 2. We include the six lowest conduction bands shown

in Fig. 3.1. The electronic energy spectrum for each of these bands is implemented on a mesh in electron wavevector space using the scheme of Rauberheimer and Gilat[81].

In this method the irreducible wedge in the hexagonal unit cell is broken up into tiny cells, cubes and triangular prisms, which completely fill the irreducible wedge. This is shown in Fig. 3.2. For the FBMCM, we broke the wedge into 5,610 cells. The band structure energy in the center of each cube and on the center of the ΓKHA plane of each prism, is stored in a look-up table. The gradient of the band structure energy, $dE/d\vec{k}$, is also stored at each of these points. Within each cell, the electronic structure is considered to be constant in a plane perpendicular to the gradient. Each cell volume then contains many k surfaces of constant energy E. These surfaces can be calculated from the values of the stored band structure energy and gradient at the cell midpoint. The maximum and minimum energy, E_{max} and E_{min}, contained in each cell are also calculated and stored.

The look-up table can be accessed during the simulation to give the k-space surface for a constant electron energy ε=E. Given ε, the surface is found by first searching the band structure look-up table for all cells containing ε. Then the surface corresponding to ε can be calculated for each cell using the Rauberheimer and Gilat method[81]. Adding the contributions of all cells gives the k-space surface corresponding to the electron energy ε.

As for the scattering mechanisms in our simulations, we considered acoustic, intervalley optical, polar optical, ionized impurity, and impact ionization scattering. The rates were given in the previous section. The method of Shichijo et al.[41] is

used to determine the final electron state after scattering with an acoustic phonon.

As for the scattering mechanisms in our simulations, we considered acoustic, intervalley optical, polar optical, ionized impurity, and impact ionization scattering. The rates were given in the previous section. The acoustic and intervalley deformation potentials, along with the polar field were treated as adjustable parameters, which were varied from the results of analytical band Monte Carlo transport simulations of SiC[85, 87, 88].

A flowchart of the FBMCM is shown in Fig. 3.3. Once the physical parameters for 6H-SiC are defined and the band structure look-up table is produced, a look-up table, $S(\varepsilon)$, for the total scattering rate is produced. This allows the simulations to proceed faster. The electron then drifts for a time $T_d(\varepsilon)$, which is always sufficiently smaller than the inverse of the total rate in the look-up table $S(\varepsilon)$. Since the band structure of the entire Brillouin zone is contained in the irreducible wedge, the electron energy after the drift can be obtained from the band structure look-up table for the wedge. Before accessing the look-up table, the electron wavevector $\vec{k}$ is first rotated into the equivalent wavevector $\vec{k_w}$ inside the wedge. The electron energy $\varepsilon(\vec{k_w})=\varepsilon(\vec{k})$ is then found by determining the particular cell and the particular constant energy surface within the cell that contains $\vec{k_w}$.

Using the methods of Chapter 1, a random number can then be used to determine if a scattering event occurs. This is facilitated by access to the scattering rate using the look-up table $S(\varepsilon)$. If no scattering occurs then the process repeats with another drift. If a scattering event occurs then a random number is used to pick the particular mechanism according to the procedure in Chapter 1. Now the

electron energy, ε', after the scattering event is determined. If a phonon scattering event is chosen, then the final electron energy is determined by adding (subtracting) the phonon energy for phonon absorption (emission). In the case of acoustic phonon scattering, the average phonon energy is calculated and used to find ε'[41]. Ionized impurity scattering is treated as elastic, while the electron is placed at the conduction band minimum after an impact ionization event occurs.

Once the final energy is determined, the final electron wavevector is found from the band structure look-up table. First the k-space surface A_n for energy ε' is determined in each cell n by the methods mentioned previously. Then a random number r is chosen. If there are N cells which contain ε', the final state cell $n1$ is found from the condition

$$S_{n1-1} \leq r \leq S_{n1}, \tag{3.16}$$

where the partial sum S is defined as

$$S_{n1} = \frac{\sum_{n=1}^{n1} A_n}{\sum_{n=1}^{N} A_n}. \tag{3.17}$$

So the final electron wavevector $\vec{k'}$ is selected to be in the $n1$ cell. If the scattering mechanism is acoustic phonon scattering, there must be a check to make sure the phonon wavevector is not too large[41]. If this check fails then a new final state is determined. If an appropriate final state cannot be found a new scattering mechanism or a new drift is implemented. In the case of polar optical or ionized impurity, where scattering is anisotropic, the area A_n in the sum of equation (3.17) is weighted by the scattering rate $|\Gamma(\theta')|$. Here θ' is the angle between the initial wavevector and the midpoint wavevector of the particular cell. Once the final cell $n1$ is found

the final electron wavevector $\vec{k'}$ is found on the cell constant energy surface A_{n1} using 2 random numbers. Now the final electron state is found and the electron will undergo another drift. This process continues until convergence of the drift velocity.

3.3 Results for Bulk 6H-SiC

The main focus of our FBMCM simulations is to gain insight into the temperature-dependent electron transport properties of 6H-SiC. We aim to determine how much of the electronic band structure is needed in order to simulate high-field electron transport. We also find a set of electron-phonon coupling constants that agree with experimental data. These constants are the acoustic and intervalley deformation potentials and the polar field created by a longitudinally-polarized polar optical phonon. Since the effective mass is very large along the c-axis, as seen in Table 1.5, 6H-SiC devices are typically designed so that current flows perpendicular to the c-axis. Our simulations will therefore focus on transport along this direction.

To find a set of electron-phonon coupling constants that agree with experimental results, we compare to experimental results in both the low and high field regions over a range of temperatures. In each case the doping concentration used in the simulations is adjusted to match that of the experiments. The results of this process can be found in Table 3.2. The acoustic and the first order intervalley deformation potentials where adjusted from the results of analytical band Monte Carlo simulations[85, 87].

In Fig. 3.4 we show the comparison of our FBMCM, with fitted electron-

phonon coupling constants, to experiments at low fields[89]. The low-field mobility over a wide range of temperatures is shown. This mobility shows a characteristic T^{-2} dependence indicative of mobility degradation due to phonon scattering processes. Our simulation results fit these trends well. In 3.5, further comparisons with experiments are shown. Here the full-band Monte Carlo results are compared with experimental measurements of the electron drift velocity at temperatures of 296K, 408K, and 593K. Again the drift velocity decreases with increasing temperature due to an increase in the number of phonon scatterers.

Our FBMCM simulations indicate that a driving field of $1MeV/cm$ leads to the saturation of the drift velocity for temperatures below 1000K. Since SiC is a potential material for high-temperature electronics, it is interesting to determine how the magnitude of the drift velocity at saturation, ϑ_{sat}, will vary with temperature. We find that ϑ_{sat} decreases linearly with temperature, at a rate of $1\text{x}10^4 cm/s$ per one Kelvin increase in the temperature. We show these results in Fig. 3.6.

As can be seen in Fig. 3.1, the band structure for 6H-SiC is quite complicated. It is often convenient to use a model analytical band structure within a Monte Carlo simulation to avoid the complexity of using a large look-up table to obtain the electronic energy spectrum. To precede with such a model, one must first determine how many bands are needed and how many band structure valleys are needed. The answers to these questions will depend on the magnitude of the driving field and the lattice temperature. We have therefore used our full-band Monte Carlo simulations to investigate the portion of the band structure that is occupied by conduction electrons at various fields and temperatures. An occupancy greater than one tenth of

the total electron concentration is defined as significant. The significantly occupied band structure will contribute to the important transport properties of 6H-SiC such as the electron drift velocity and the mobility.

The fraction of time that the simulated electron spends in each of the six conduction bands is shown in Figs. 3.7 and 3.8 for temperatures of 296K, and 598K respectively. This time is proportional to the occupancy of each band by the total concentration of conduction electrons. We see that at low fields there are many more electrons in the second band as the temperature increases. This is the expected result near equilibrium. The onset of significant occupancy of bands 3-6 although occurs at larger fields as the temperature increases. This phenomena occurs since the electron drift to higher energies is inhibited by a larger phonon scattering rate. This does not occur in the case of the second band since it is very close in energy to the first band. The threshold for significant occupancy of the third band occurs at roughly $350kV/cm$ at room temperature and at 450 kV/cm for 598 K. The threshold for the fourth band is found at 750 kV/cm and 1000 kV/cm for these temperatures. At 1000 kV/cm the fifth band is just reaching significant occupancy at room temperature. We conclude that a 3-4 band model should be sufficient for electron transport simulations at room temperature and above.

The conduction band minimum, as seen in Fig. 3.1, occurs in the $L - M$ valley of the Brillouin zone. The Γ valley although is less than $1.5eV$ above. It is therefore interesting to investigate the occupancy of the Γ valley with varying field and temperature and to determine when it is appropriate to include it in an analytical band structure. This is shown in Fig. 3.9 for temperatures of 296 and

598 K. We find that the Γ valley does not become occupied until after 400 kV/cm at these temperatures. The occupancy is greater at lower temperatures as a result of a larger average electron energy. The number of electrons occupying the valley becomes significant for fields above 750 kV/cm. Our results indicate that this valley should be included in a high-field Monte Carlo simulation.

3.4 Chapter Summary

We have presented the methodology for a full-band Monte Carlo method for the simulation of electron transport in hexagonal SiC. The empirical pseudopotential band structure within the irreducible wedge is include on a mesh. A method is presented for determining the constant energy surfaces $\varepsilon(\vec{k})$ using the discretization scheme of Rauberheimer and Gilat[81]. These surfaces are used to determine the electronic states after a scattering event, and to find the electron energy after each incremental drift in the applied field.

Once the electron-phonon coupling constants are adjusted in accordance with experiments, the temperature and applied field dependence of electron transport is studied in 6H-SiC. We find that the saturation velocity decreases linearly from 1.71x10$^7 cm/s$ to 1.05x10$^7 cm/s$ as the lattice temperature increases from 300K to 1000K. We also find the in the high-field regime, the four lowest conduction bands of the $M - L$ valley, along with the lowest band of the Γ valley are significantly occupied with conduction electrons.

The results of the Monte Carlo simulations presented here can be used to

model the mobility of 6H-SiC devices. Theses models could readily be used in other electron transport simulation tools such as drift-diffusion simulators. In Figs. 3.10, 3.11, and 3.12 we show the resulting mobility from the full-band simulations.

Band Structure Parameters:		
m_d=0.66m_e	$\alpha = 0.323$	
Density:		
3.166 $g/cm^3(\rho)$		
Dielectric constant:		
9.66(ϵ_s static)	6.5(ϵ_∞ frequency-dependent)	
Sound velocity:		
1.37x10^{6}cm/s(ϑ_l Longitudinal)	1.0x10^{6}cm/s(ϑ_t Transverse))	
Doping:		
10.5x10$^{16}cm^{-3}$(N_D donors)	0.4x10$^{16}cm^{-3}$ (N_A acceptors)	
Donor levels:		
0.08eV	0.12eV	0.45eV

Table 3.1: Material parameters of 6H-SiC used in Monte Carlo simulations.

Acoustic deformation potential:	
23.0eV(D_{ac})	
Polar optical scattering:	
Polar field(E_o)	1.08x10^5V/cm
Phonon energy(E_{po})	120 meV
Optical intervalley scattering:	
Zero order	
Deformation potential(D_{iv0})	14.0x10^8eV/cm
Phonon energy(E_{iv0})	85.4meV
First order	
Deformation potential(D_{iv1})	2.0eV
Phonon energy(E_{iv1})	33.2meV
Impact ionization scattering	
Hardness(P)	10
Threshold(E_{th})	3.2eV

Table 3.2: Scattering parameters of 6H-SiC used in Monte Carlo simulations.

Absorption	Emission	
$X_1 = C\left(\sqrt{\varepsilon_u} - \sqrt{\varepsilon}\right)$ $X_2 = C\left(\sqrt{\varepsilon_u} + \sqrt{\varepsilon}\right)$	none(rate is zero)	$\varepsilon < \varepsilon_u$
$X_1 = 0$ $X_2 = C\left(\sqrt{\varepsilon} + \sqrt{\varepsilon_u}\right)$	$X_1 = 0$ $X_2 = C\left(\sqrt{\varepsilon} - \sqrt{\varepsilon_u}\right)$	$\varepsilon > \varepsilon_u$

Table 3.3: Acoutic phonon scattering limits of integration. (Here ε is the electron energy, and ε_u=$m_d\vartheta_l^2/2$, where m_d is the effective mass and ϑ_l is the longitudinal sound velocity. Also C=$4\sqrt{\varepsilon_u}/K_BT$.)

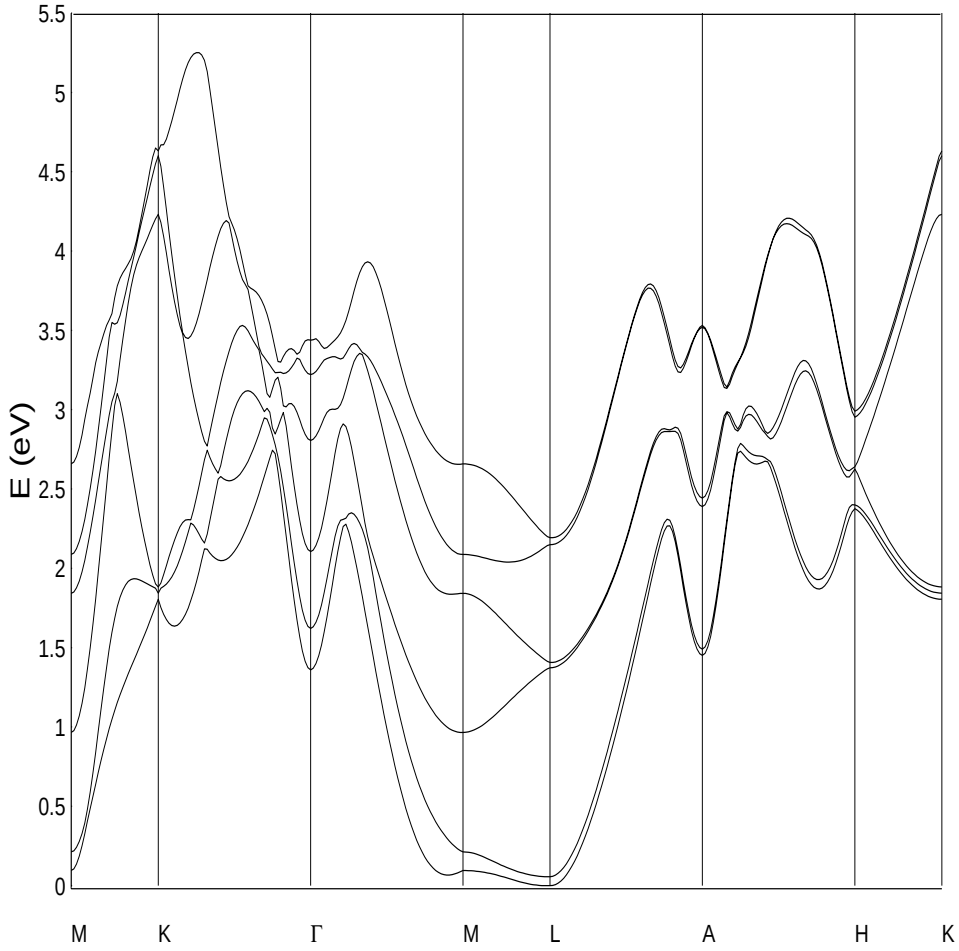

Figure 3.1: Lowest Six Bands of Bulk 6H-SiC Band Structure.

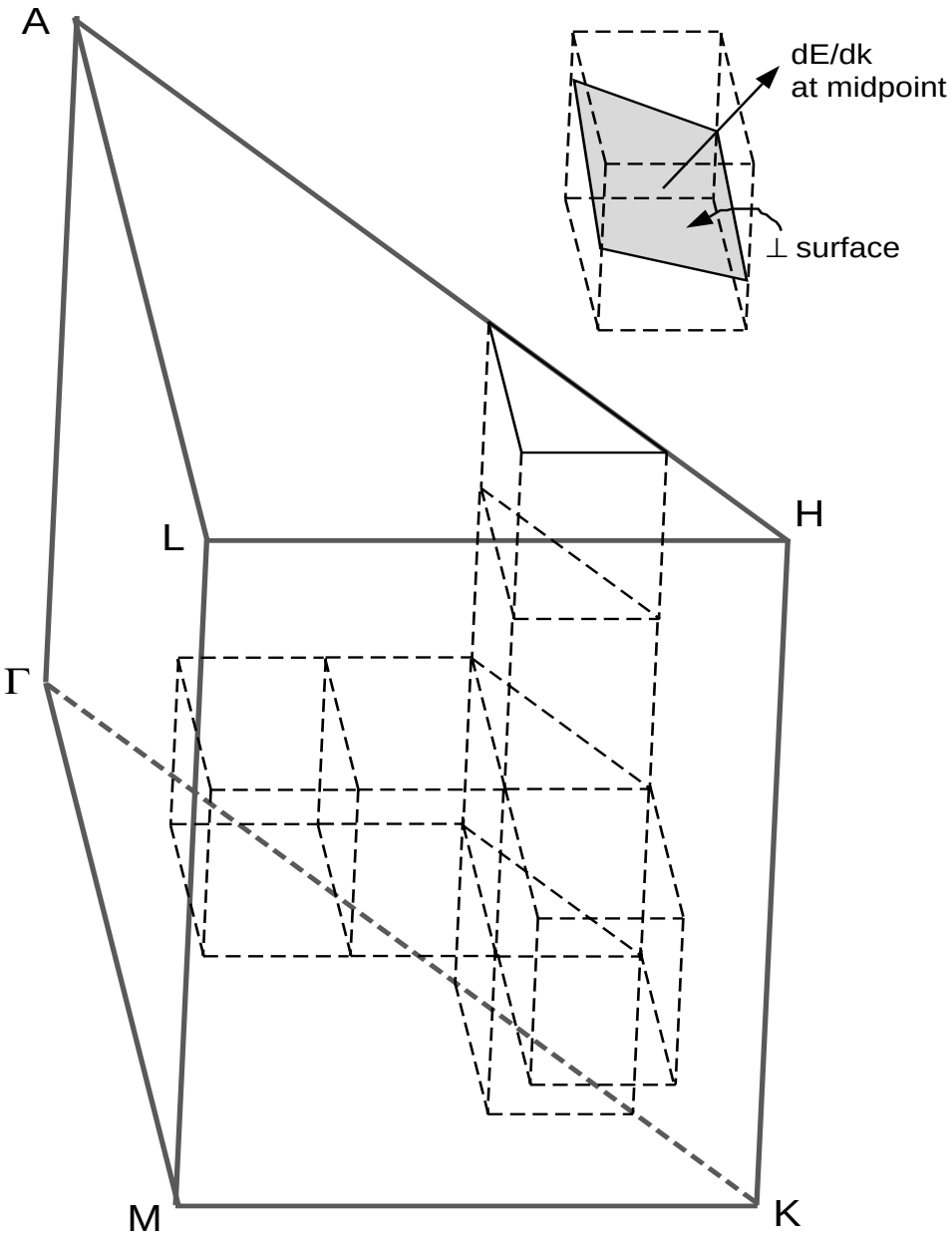

Figure 3.2: Partition of the irreducible wedge of hexagonal SiC

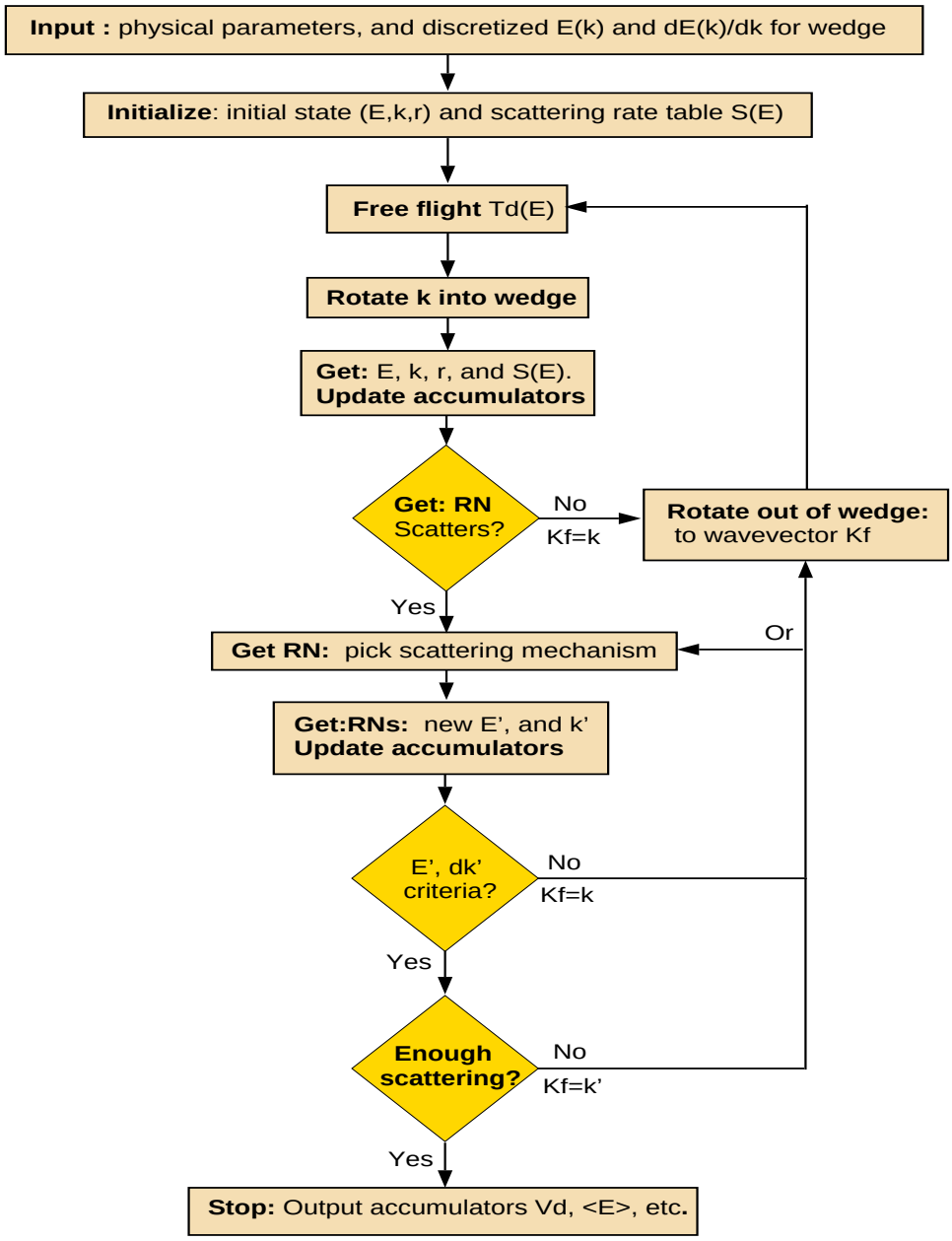

Figure 3.3: Flowchart for the full-band Monte Carlo program. (Here E is the electronic band structure energy, k is the electron wavevector, $S(E)$ is the scattering rate look-up table, $T_d(E)$ is the drift time, and V_d is the drift velocity. Also r is the position of the electron, and RN is a random number.)

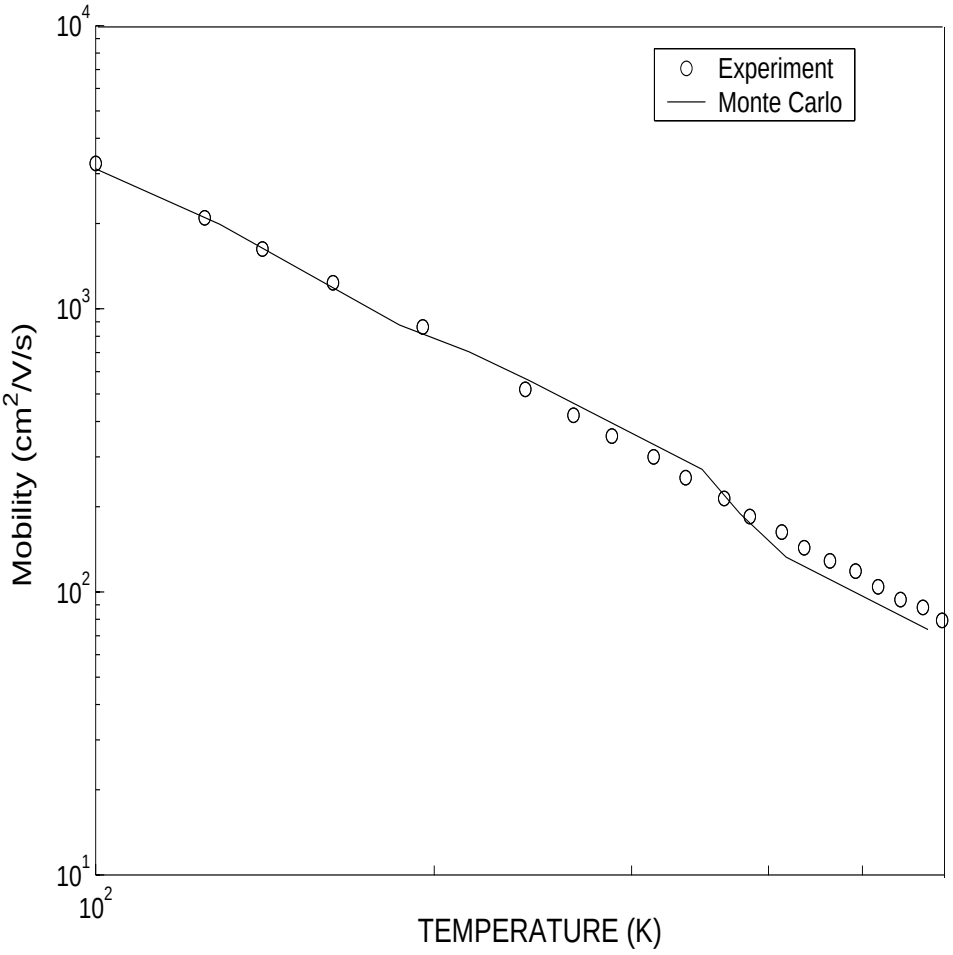

Figure 3.4: Monte Carlo and experimental[89] results for the low-field mobility of 6H-SiC over a wide temperature range.

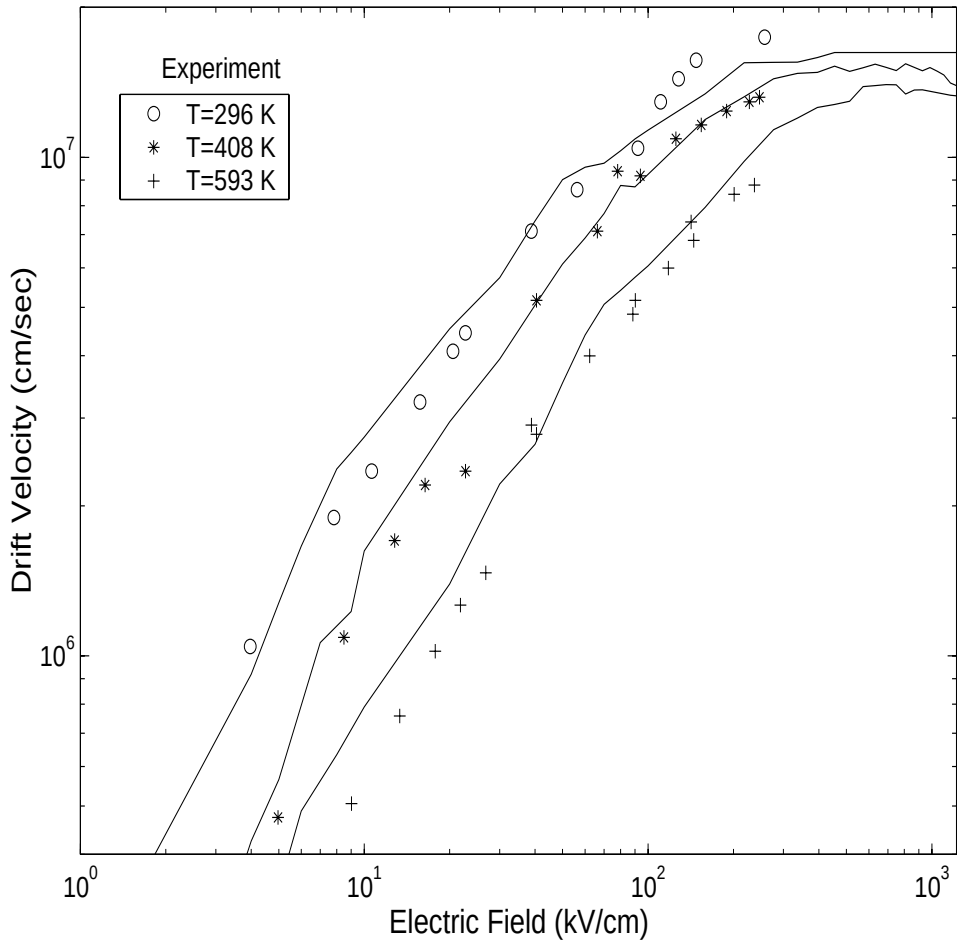

Figure 3.5: Monte Carlo and experimental[90] results for the drift velocity $\perp$ to the c-axis in 6H-SiC.

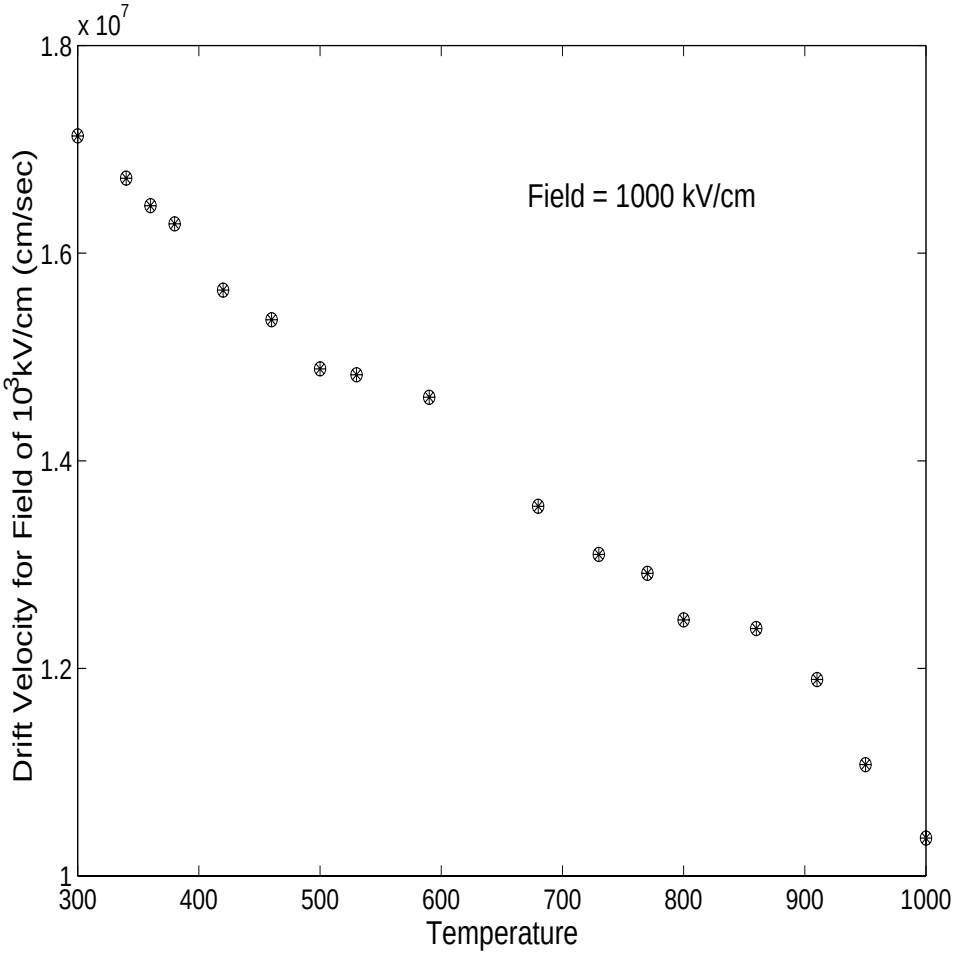

Figure 3.6: Saturation velocity $\perp$ to the c-axis.

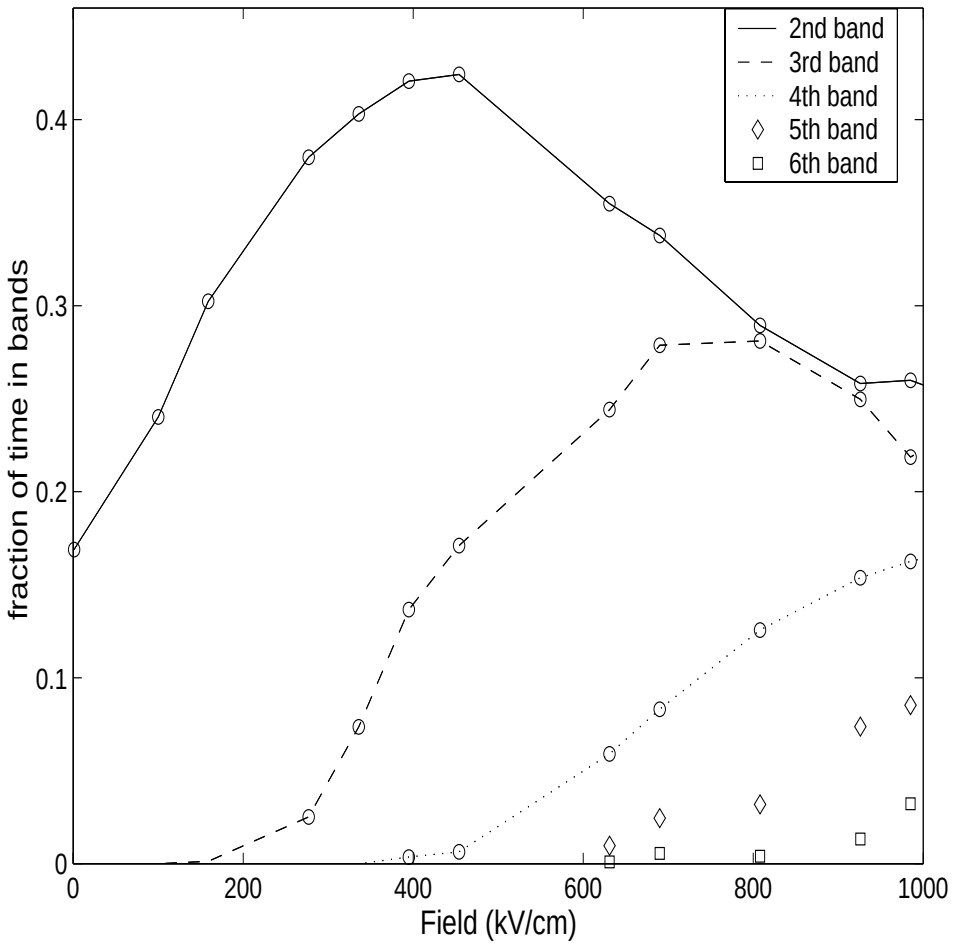

Figure 3.7: Band occupancy at T=296K. (Band 1 is not shown.)

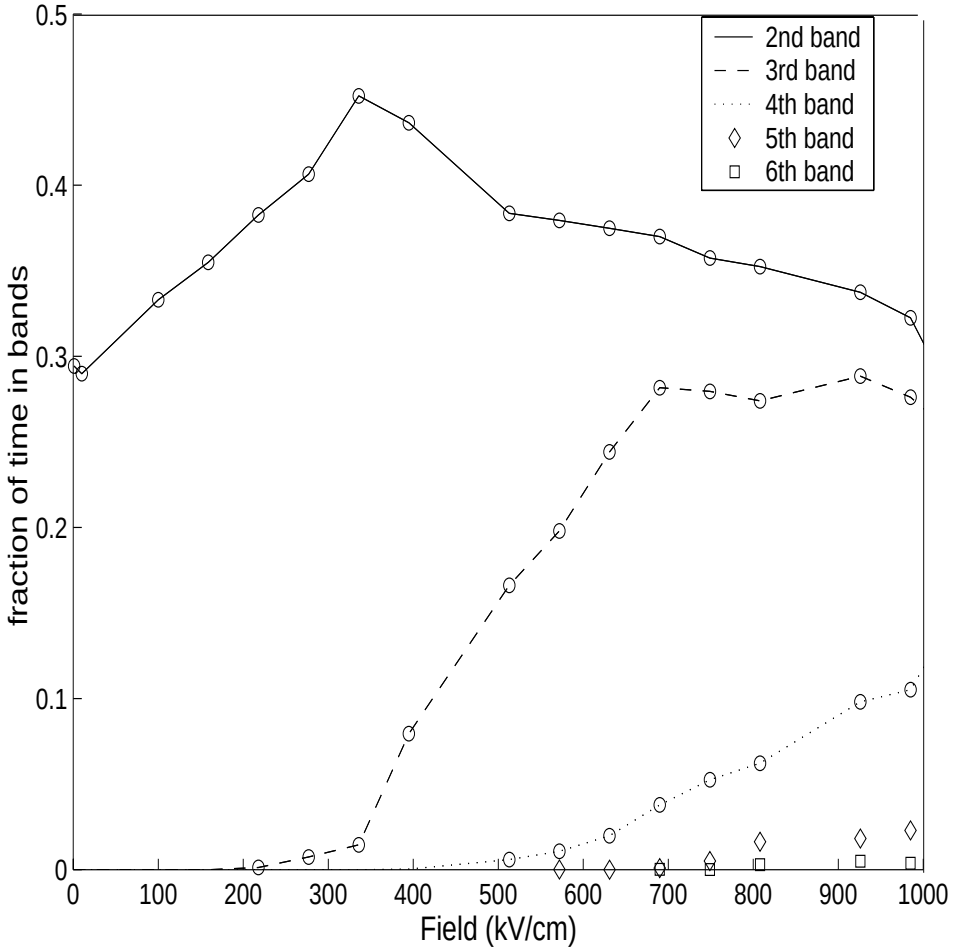

Figure 3.8: Band occupancy at T=598K. (Band 1 is not shown.)

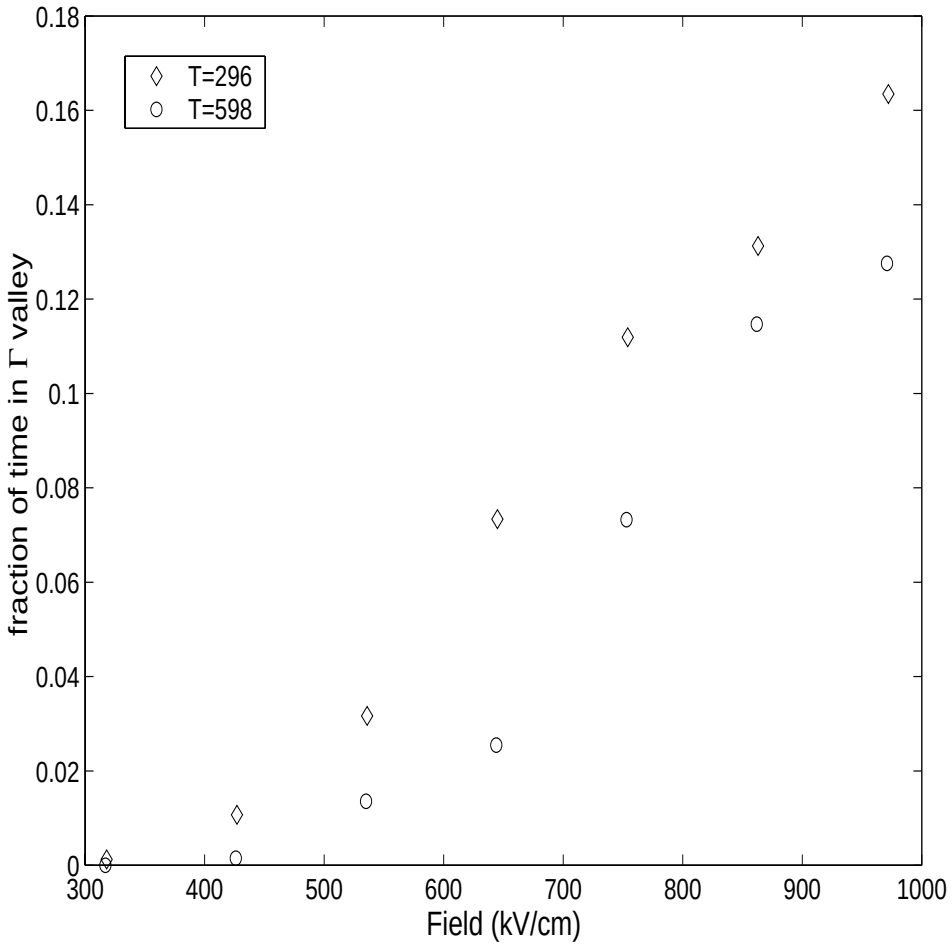

Figure 3.9: Occupancy of the Γ valley.

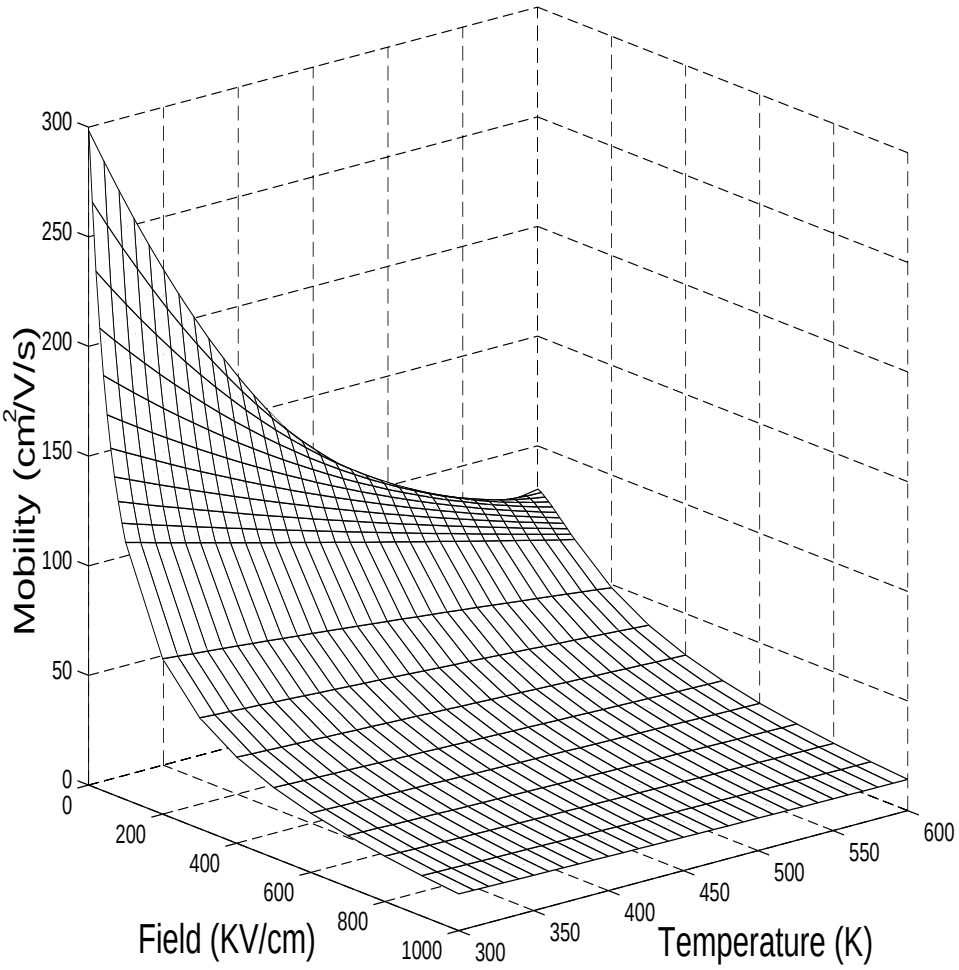

Figure 3.10: Monte Carlo mobility $\perp$ to the c-axis.

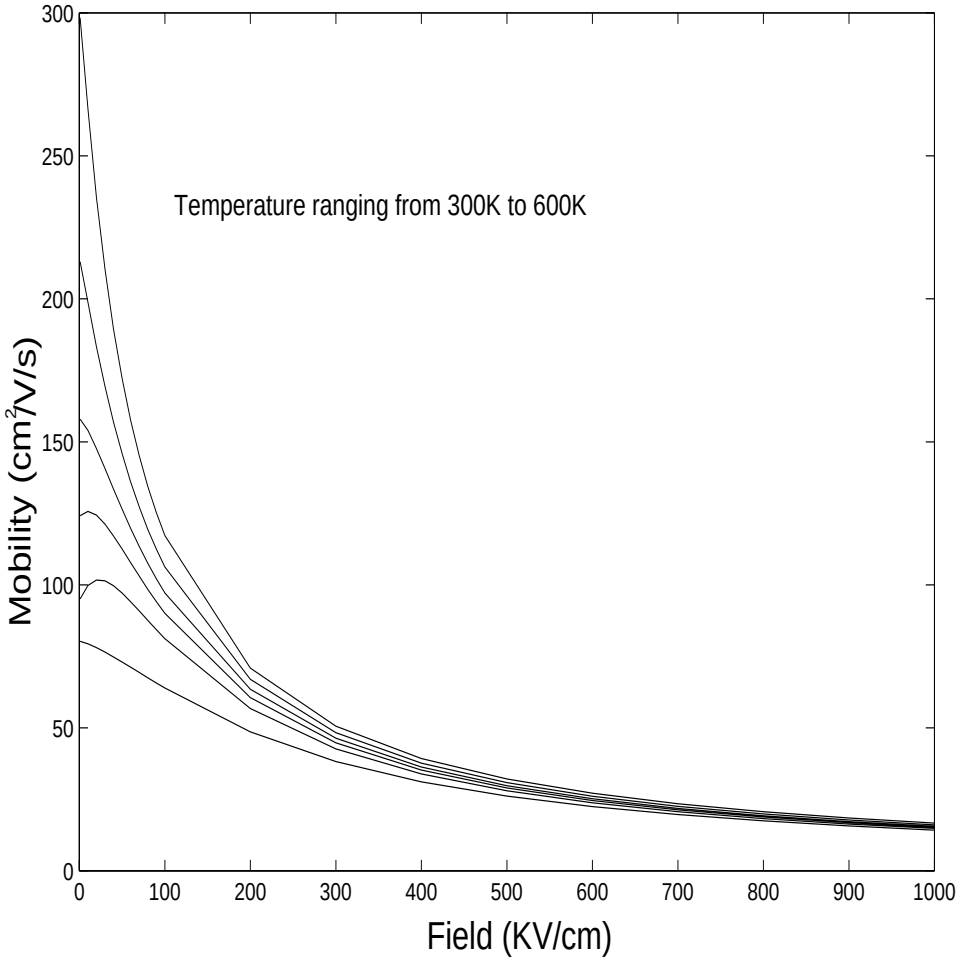

Figure 3.11: Monte Carlo mobility ($\perp c$) for temperatures between 300K and 600K.

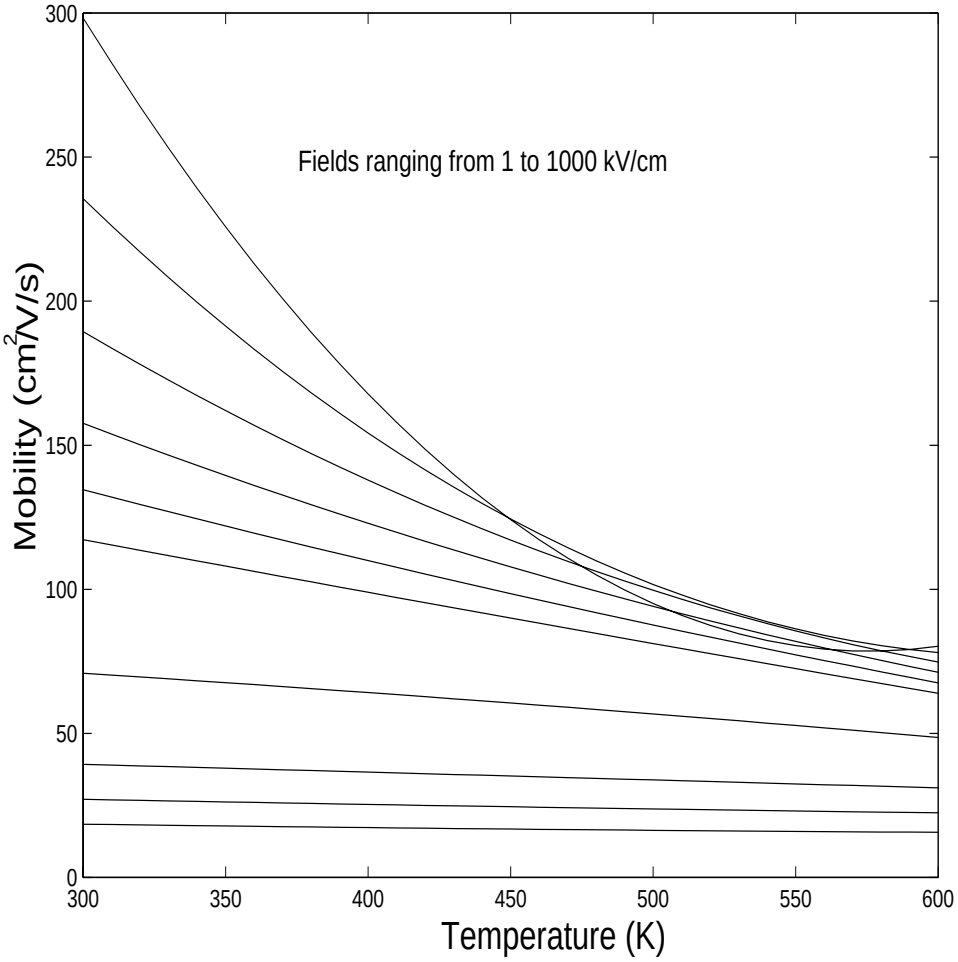

Figure 3.12: Monte Carlo mobility ($\perp c$) for fields between 1 and 1000KV/cm.

Chapter 4

Surface Band Structure Calculations for Hexagonal SiC.

Since it is advantages to be able to use different crystalline orientations at the oxide interface, a study of the surface band structure of SiC is important. Among other things it can be used to predict how different interface planes will impact the transport properties when incorporated in a MOSFET. In this work we investigate the conduction band edge electronic structure at the oxide-SiC interface. The $(01\overline{1}0)$, $(11\overline{2}0)$, $(03\overline{3}8)$, and (0001) orientations of 4H-SiC and 6H-SiC are considered. As in a typical Si MOSFET, band-bending at the interface leads to confinement of electrons perpendicular to the oxide-SiC surface and a departure from the band structure of the bulk.[91] The transverse bands are split into a number of subbands,

and the interface electrons exist as a quasi 2-dimensional gas. Here we determine the electronic structure parallel to the oxide-SiC plane, and determine the perpendicular subband structure self-consistently with the perpendicular electrostatic potential. Comparisons are made between different orientations in both 4H-SiC and 6H-SiC. The results show both interesting similarities and interesting differences among the surfaces and among the two polytypes.

4.1 Surface Band Structure

The method we use to determine the band structure of an n-type inversion layer of 4H and 6H-SiC is based on work that has been done for Si[92, 93, 84] and 3C-SiC[94]. The electric field parallel to the oxide interface is considered small and the bands are therefore accurately treated using the parabolic approximation. Here the constant energy ellipse of the conduction band edge parallel to the surface is determined from the bulk constant energy ellipsoid. For a given surface orientation, the bulk ellipsoid is rotated accordingly and the energy dispersion parallel to the interface is obtained. For the perpendicular direction the confinement of electrons splits the energy spectrum into a number of subbands which as we will see in the next section, can be obtained by solving Shrödinger's equation.

The crystal structure of Si and 3C-SiC are diamond and zincblende respectively, with the conduction band minimum near the X symmetry point in the Brillouin zone. For the case of 4H and 6H-SiC however we have a hexagonal lattice, with the conduction band edge along the M-L symmetry line. In Figs. 2.8 and 2.9 we

show the bulk band structure of 4H-SiC and 6H-SiC calculated using the empirical pseudopotential method.[32] The minimum for 4H-SiC occurs at the high symmetry point M so there will be a valley degeneracy of 3 instead of 6 as in Si. In 6H-SiC the exact location of the conduction band minimum is still uncertain. Experiments do indicate that it is somewhere along the M-L symmetry line.[95, 96] Band structure calculations show varying results with the minimum at L, M, or between M and L.[32, 97, 98, 99] The results in this work will be sensitive to the exact location only if the valley degeneracy is affected. Since the conduction band is so flat along M-L, varying by less than 0.1eV, we therefore consider the minimum of 6H-SiC to occur at the L symmetry point, as seen in Fig. 2.9, and use a valley degeneracy of 3 for 6H as well.

A number of different surface orientations are investigated. In terms of the Miller-Bravais Index notation, the (0001), $(01\overline{1}0)$, and $(11\overline{2}0)$ planes are shown in Fig. 4.1. The $(10\overline{1}0)$ and $(1\overline{1}00)$ planes are also studied since they are equivalent to the $(01\overline{1}0)$ plane. We will also consider the $(03\overline{3}8)$ plane. To find the vector normal to this plane, the normal of the $(03\overline{3}0)$ plane in Fig. 4.1 is rotated $\approx 54.7^o$ towards the c-axis.

Using the effective-mass approximation, Shrödinger's equation for an inversion layer electron in subband s is

$$\left[\frac{-\hbar^2}{2}\sum_{i,j}\omega_{ij}\frac{\partial}{\partial x_i}\frac{\partial}{\partial x_j} - e\phi(z) - \varepsilon_s\right]\psi_s = 0. \tag{4.1}$$

Here the first term is the kinetic-energy operator, ε_s is the electron energy, ψ_s is the electron wavefunction, and $\phi(z)$ is the potential perpendicular to the interface

along z. The elements of the reciprocal effective-mass tensor for a given surface orientation are ω_{ij}. They are obtained from the bulk principle axes elements, ω_{nn}, using the transformation

$$\omega_{ij} = \sum_n A_{in} A_{jn} \omega_{nn}. \tag{4.2}$$

The rotation matrix A is composed of the direction cosines for the rotation. Following the work of Stern and Howard[92], the wavefunction for an inversion layer electrons is expressed as

$$\psi_s(x, y, z) = \left[\zeta_s(z) e^{-iz(\omega_{13}k_1 + \omega_{23}k_2)/\omega_{33}}\right] e^{ik_1 x + ik_2 y}. \tag{4.3}$$

The first term in brackets is the envelope of the wavefunction in the potential well $\phi(z)$, while the wavefunction parallel to the interface is in terms of momentum eigenstates with wavevectors k_1 and k_2. Now substituting the wavefunction into in Eq. (4.1), a Schrödinger equation for $\zeta_s(z)$ is obtained

$$\left[\frac{-\hbar^2}{2m_3}\frac{d^2}{d^2 z} - e\phi(z) - E_s\right]\zeta_s(z) = 0, \tag{4.4}$$

where m_3, the principle axes effective mass perpendicular to the interface, is identified as $m_3{=}\omega_{33}^{-1}$. This equation is used to obtain both the subband energies E_s and the electron charge density, $e|\zeta_s(z)|^2$, along the inversion well. The procedure for this calculation is detailed in the next section. The total electron energy considering motion along x, y and z is

$$\varepsilon_s = E_s + \frac{\hbar^2 k_1^2}{2m_1} + \frac{\hbar^2 k_2^2}{2m_2} + \frac{\hbar^2 k_1 k_2}{2m_{12}}. \tag{4.5}$$

Here m_1 and m_2 are principle axes effective masses of the constant energy ellipse

parallel to the interface when $1/m_{12}$ vanishes. The values of these masses are:

$$\begin{aligned} 1/m_1 &= (\omega_{11} - \omega_{13}^2/\omega_{33}) \\ 1/m_2 &= (\omega_{22} - \omega_{23}^2/\omega_{33}) \\ 1/m_{12} &= (\omega_{12} - \omega_{13}\omega_{23}/\omega_{33})\,. \end{aligned} \tag{4.6}$$

To obtain the principle axes the constant energy ellipse must be rotated in the interface plane so that $1/m_{12}$=0. The new axes are then the principle axes for the ellipse.

So using the rotated inverse effective mass tensor ω_{ij}, the principle axes effective masses are readily obtained. In Fig. 4.2 the constant energy ellipses and Brillouin zones for the various surface orientations are displayed. Here only the ellipses for the lowest conduction band are shown. As discussed previously, the conduction band minimum for 6H-SiC is shown at the L point. If a location closer to the M point is chosen then the minimum would move closer to the 4H-SiC minimum.

In Table 4.1 we show analytical equations for the principle axes effective masses of the surfaces in terms of those of the bulk. These results are general and can be used if the surfaces of other materials with hexagonal symmetry are considered. Here the longitudinal principle axes masses for the rotated surface are m_1 and m_2 in Fig. 4.2. The larger the variation between these two masses, the more anisotropic the transport properties will usually be along the oxide-semiconductor surface. The principle axis mass for the transverse direction, m_3, is also given in Table 4.1. For all except the (0001) orientation, the projection of the bulk constant energy ellipsoids onto the surface creates 2 sets of non-equivalent minima. When these bands are split into subbands in the inversion layer, a subband ladder will result from each of the 2

non-equivalent conduction band minima. The ladder with the lowest energy state is labeled as the "lowest ladder" or the "1st ladder " in Table 4.1 and is characterized by the largest transverse effective mass m_3. The results for m_1 and m_2 in Table 4.1 are accurate for both bands in the $(01\overline{1}0)$, $(11\overline{2}0)$, and (0001) orientations. For the $(03\overline{3}8)$ surface although these results are accurate when the principle axes of the ellipses align closely with the Brillouin zone axes shown in Fig. 4.2. For the case of $(03\overline{3}8)$ 6H-SiC and the second conduction band of $(03\overline{3}8)$ 4H-SiC, the principle axes are only rotated about 11-12 degrees off the Brillouin zone axes. The equations in Table 4.1 are therefore very close approximations. For the first conduction band of $(03\overline{3}8)$ 4H-SiC although the angle is about 40^o. The longitudinal effective mass formulas in Table 4.1 are off by about 15% in this one particular case. For all orientations and all bands, the product $m_1 m_2$ in Table 4.1 is accurate. In Tables 4.2 and 4.3 the values of the effective masses used in this work are given using the accepted bulk values. [32, 99] The results here for m_1 and m_2 of the first conduction band of $(03\overline{3}8)$ 4H-SiC are accurate and do not correspond to the formulas in Table 4.1.

Since the bulk bands are used to determine the nature of the conduction band minimum, two important approximations are made. First of all, no account is made of the effects of surface states on the band structure and second of all the effective mass approximation is used. In Si the first approximation is reasonable since the density of interface states is as low as $10^{10} eV^{-1} cm^{-2}$. Also the effective mass approximation has been found to be justified in Si when the average distance of the electron from the interface is larger than 2nm.[93] For SiC although the interface

state densities are currently found to be as large as $10^{11} - 10^{12} eV^{-1} cm^{-2}$ in 6H and $10^{12} - 10^{13} eV^{-1} cm^{-2}$ in 4H.[15, 16, 17] Such large densities, especially, in 4H-SiC make the use of bulk-like conduction bands at the interface less reliable than in Si.

To determine the utility of the effective mass approximation in the inversion layer of hexagonal SiC, the length scale of lattice periodicity perpendicular to the interface must be considered. This distance, $L_\perp$, will be large when a large component of the c-axis is oriented perpendicular to the interface, making the effective mass approximation questionable. In Fig. 4.3 we display the 4H-SiC lattice in the $ABCA'B'C'$ notation. The periodicity of the lattice for the various orientations is shown. In Table 4.1II we see that $L_\perp$ for the (0001) and $(03\overline{3}8)$ orientations is about twice as large as in Si for 4H-SiC and is about 3 times as large for 6H-SiC. Based on the results for Si, the use of the effective mass theory for these orientations is best applied when the average distance of the electrons from the interface is greater than 4nm in 4H-SiC and greater than 6nm in 6H-SiC. The results of this work will show that these conditions are well met under conditions of very weak inversion. For the $(01\overline{1}0)$, and $(11\overline{2}0)$ orientations the effective mass approximation may be used when electrons in the inversion layer are even closer than the minimum distance found for Si. This occurs because the lattice constant is smaller in SiC($3.08A$) than in Si($5.43A$). For the $(11\overline{2}0)$ surfaces this approximation may be valid down to 1nm.

Although the method we use is of a more limited validity in the larger polytypes of SiC than in Si, there are a number of reasons why this approach can lead to useful knowledge of the electronic structure. Currently a lot of research is focused at reducing the interface state density in 4H and 6H-SiC MOSFET inversion layers.

If these states can be reduced to densities common in Si, then the method we use would certainly be applicable as it is in Si. Also it is not know how significant the effect of the large density of interface states will be. Experimental deviations from the results here could be used to access the effects of the surface states on the band structure. The effective mass approximation should not be a problem for orientations of 4H and 6H-SiC for which the c-axis is parallel to the oxide interface. We will also include the analysis of the (0001) and $(03\overline{3}8)$ orientations since the results likely will help give a qualitative understanding of the band structure along these directions. We also note that the effective mass approximation is routinely used in modeling MOSFETs and agreement with experiment is obtained, even though calculations show the inversion electrons are on the average less than 2nm from the oxide surface. A very important application of this work is its usefulness in transport simulations, such as the Monte Carlo method, which often rely on the use of an electronic energy spectrum in analytic form.

4.2 Subband Calculation

To determine the subband energies and the mobile charge density perpendicular to the interface, Schrödinger's equation, in the form of Eq. (4.4), must be solved. This is complicated however since the confining electrostatic potential at the interface itself depends on the mobile charge that builds up in the inversion layer. A self-consistent $\phi(z)$ must therefore be used in Eq. (4.4) since it depends on each E_s and $\zeta_s(z)$ itself. The method used for this is similar to that used by Stern.[93]

Self-consistency is obtained by requiring that Possion's equation

$$\frac{d^2\phi(z)}{d^2z} = -\left(\rho_{depl}(z) - e\sum_s N_s|\zeta_s(z)|^2\right)\Big/\epsilon, \tag{4.7}$$

be simultaneously satisfied along with Schrödinger's equation. Here N_s are the electron concentrations in each subband, ρ_{depl} is the depletion charge density and ϵ=9.72ϵ_o is the dielectric constant for SiC. So in order to calculate $\phi(z)$, N_s and z_d must be known.

For the electrostatic potential $\phi(z)$ the Hartree approximation is used. We therefore neglect the effects of many-body interactions and of the image charge potential at the surface. This approximation is better than might be expected since these two effects tend to cancel each other to some degree. Exchange and correlation tend to lower the surface energy levels while the image force tends to raise them. [94, 100] The Hartree approximation has been found to be a useful first approximation for the electrostatic potential in Si inversion layers, so we feel confident using it here.[93] As mentioned in the previous section, the electrostatic field parallel to the oxide-semiconductor interface is considered to be small enough so that a parabolic band structure dispersion can be used. This field should also be small so that equilibrium Fermi-Dirac statistics can be employed perpendicular to the interface.

In this work the response of the inversion layer to variations in the total concentration of free electrons at the surface, N_{inv} and the temperature, T, is studied. For fixed N_{inv}, the level in each subband is found according to

$$N_{inv} = \sum_s N_s = \frac{g\sqrt{m_1 m_2}K_BT}{\pi\hbar^2}\sum_s ln\left[1 + exp\left(\left[E_F - E_s\right]/K_BT\right)\right], \tag{4.8}$$

where E_F is the Fermi energy at the interface and the logarithmic term is the solution of the zero index Fermi-Dirac integral. The valley degeneracy, g, and the density of states effective mass, $\sqrt{m_1 m_2}$, are given in Tables 4.2 and 4.3. For all the orientations other than the (0001), more than one band structure ladder is involved. In these cases the subbands from each ladder enter the s sum. In order to determine N_s and thus $\phi(z)$ we need to know more than just the subband energy levels and wavefunctions, the Fermi energy must also be found. Once the Schrödinger equation is solved, Eq. (4.8) is in fact used to find E_F and thus each N_s is subsequently determined.

Considering a p-doped SiC MOSFET, with a uniform acceptor density N_A and a smaller uniform donor density N_D, the ionized impurity charge density at the interface is

$$\rho_{depl}(z) = \begin{cases} -e\,(N_A - N_D) & 0 < z < z_d \\ 0 & \text{else.} \end{cases} \tag{4.9}$$

Here the semiconductor is depleted of holes up to a distance of z_d from the oxide interface. It is assumed that all of the impurities are ionized in this depletion layer. Also the transition region from the depletion region to the bulk occurs abruptly at z_d. Using these approximations, the depletion depth is calculated using

$$z_d = \sqrt{2\epsilon\phi_B / e\,(N_A - N_D)}, \tag{4.10}$$

where the effective band bending from the bulk to the oxide surface is given by[91]

$$e\phi_B = E_g/2 + E_F - K_B T - eN_{inv} Z_{av}/\epsilon. \tag{4.11}$$

Here E_g is the bulk energy gap and the average penetration of the mobile inversion

layer electrons into the semiconductor is

$$Z_{av} = \sum_s N_s \int z|\zeta_s(z)|^2 dz \Big/ N_{inv}. \tag{4.12}$$

The first term in Eq. (4.11) accounts for the band bending of the substrate conduction band to the Fermi Level. The second term, E_F, accounts for an adjustment of the surface band edge relative to the Fermi level, while the third term, $-K_BT$, accounts for the potential falloff at the edge of the depletion region at z_d. The final term then includes the band bending due to the mobile charge at the interface. So once the Fermi energy is obtained using Eq. (4.8), the charge densities entering Poisson's equation can be readily determined.

The self-consistent numerical calculations involve the discretization of Eqs. (4.4) and (4.7) in the z direction. These equations are then solved iteratively along with the calculated Fermi energy that is itself consistent with Eqs. (4.9) and (4.10). The oxide-semiconductor boundary potential barrier is assumed large enough so that the wavefunction does not penetrate into the oxide. This is a good approximation for Si. It would fail only when the surface is inverted well beyond the limits of the effective-mass approximation along z. [93] The larger bandgap makes this approximation less reliable in 4H and 6H-SiC. Here we do assume that the oxide-semiconductor barrier is large enough so that we may allow the wave function to vanish at the oxide ($\zeta_s(0)$=0). The discretization of z goes up to a maximum value of z_{max} which is determined when $\zeta_s(z_{max})$=0 for all the low lying subbands that are significantly occupied. In this work we consider 10 such subbands for each of the two bands considered. The set of wavefunctions for these subbands are the same

for each of the two bands, but the two sets of 10 subband energies are offset by the energy spacing of the bands. The subbands are also divided amongst the different ladders. In the case of the (0001) orientation there is only one subband ladder with 10 subbands, whereas for the other orientations two ladders with 5 subbands each are considered.

The boundary condition used for the potential at the interface is $\phi(0)$=0. We therefore will consider all energies relative to the surface potential. The electric field at the boundary is set equal to F_o where

$$-\frac{d\phi(z)}{dz}\bigg|_{z=0} = F_o = e\left[N_{inv} + (N_A - N_D)\, z_d\right] \Big/ \epsilon. \tag{4.13}$$

Using these boundary conditions, Eq. (4.7) can be solved giving

$$\phi(z) = -F_o z + e\left((N_A - N_D)\, z^2/2 + \sum_s N_s \int_0^z dz' \int_0^{z'} dz'' |\zeta_s(z'')|^2\right) \Big/ \epsilon, \tag{4.14}$$

in the region of interest where $z < z_d$. This equation is used to set the boundary condition $\phi(z_{max})$, where at z_{max} the sum in Eq. (4.14) is zero. Using this boundary condition means that we only discretize z in the region where the wavefunctions are non-zero $0 < z < z_{max}$. Instead of using Poisson's equation, Eq. (4.14) could in effect be used to determine the self-consistent potential but this is not computationally practical unless the double integral can be solved analytically.

Now we will describe the iterative procedure. For the first iteration (1), the initial subband wavefunctions and energies are taken as the analytical solutions for a triangular well. These are the Airy functions (A_i)

$$\zeta_s^{(1)}(z) = A_i\left(\left(2m_{3s}eF_o/\hbar^2\right)^{1/3}\left[z - \left(E_s^{(1)}/eF_o\right)\right]\right) = A_i\left(\left[z - z_1\right]/z_2\right), \tag{4.15}$$

with energies

$$E_s^{(1)} = \left[\frac{3}{2}\pi\left(s+\frac{3}{4}\right)\right]^{2/3} eF_o z_2. \tag{4.16}$$

Here the notation m_{3s} is for the transverse mass of the ladder subband s belongs to. The initial value $E_F^{(1)}$ is calculated from Eq. (4.8), then the initial value of the electrostatic potential, $\phi^{(1)}(z)$, is determined using Eqs. (4.10) and (4.14). In this case Eq. (4.14) is solved analytically since

$$\int_0^z dz' \int_0^{z'} dz'' |\zeta_s^{(1)}(z'')|^2 = z + \frac{z_2}{3}\left[\chi^2 Ai^2(\chi) - \chi Ai'^2(\chi) - 2Ai(\chi)Ai'(\chi)\right]\Big|_{\chi=-z_1/z_2}^{\chi=[z-z_1]/z_2}. \tag{4.17}$$

For weak inversion, when $N_{inv}<\sim N_A z_d$, $\phi^{(1)}(z)$ could be used as a next approximation to the triangular well potential transverse to the interface.

The iterative procedure then begins with the discretization in z and subsequent diagonalization of the Eq. (4.4). This gives the values $E_s^{(2)}$ and $\zeta_s^{(2)}(z)$. Then $E_F^{(2)}$, is obtained and the boundary value $\phi^{(2)}(z_{max})$ is found from Eq. (4.14). Next Eq. (4.7), also discretized in z, is solved giving $\phi^{(2)}(z)$. The iterative procedure is then continued until $\phi^{(n)}(z)=\phi^{(n-1)}(z)$. To aid convergence, after a few iterations we update the new potential by using the average of the newly calculated function with that of the previous iteration.

In Fig. 4.4, we show the self-consistent results for the $(01\overline{1}0)$, and $(11\overline{2}0)$ orientations in 6H-SiC. The lowest 3 or 4 subbands are given for each surface. Also the the potential $\phi(z)$ and the charge density are given as functions of z the penetration depth into the semiconductor. The charge density for electrons in the lowest state of the lower subband ladder E_o is also shown. In the particular example given the

surface is relatively strongly inverted and most of the mobile electrons occupy the lower subbands of the two ladders E_o and E'_o.

4.3 Results

4.3.1 $(01\overline{1}0)$ and $(11\overline{2}0)$ Orientations

The $(01\overline{1}0)$, and $(11\overline{2}0)$ arrangements both have small transverse periodic lengths $L_\perp$, therefore the effective mass approximation used in the band structure calculation is very reliable. From Tables 4.2 and 4.3, it can also be seen that these surfaces have identical principle axes effective masses for the second(higher) subband ladder. This ladder is characterized by a small transverse mass m'_3, and a large anisotropy between the longitudinal masses m'_1 and m'_2 for the first conduction band. The second conduction band has a large m'_3 in 4H-SiC, but since the interband energy gap is large we focus on the first conduction band. The $(01\overline{1}0)$, and $(11\overline{2}0)$ directions are fundamentally different in the first(lower) subband ladder. In the former case the perpendicular mass is significantly larger than that of the second ladder. It is about 1.7 times as large in 4H-SiC and about 2.5 times as large in 6H-SiC. There is a large difference in the nature of the longitudinal masses between the two $(01\overline{1}0)$ polytypes. These masses are very similar in 4H-SiC but there is tremendous anisotropy in 6H-SiC. For the $(11\overline{2}0)$, orientation the lower ladder has effective masses which are very similar to that of the higher subband ladder. The first ladder is therefore characterized by a small transverse mass and anisotropy in the parallel direction.

The fundamental difference between the $(01\overline{1}0)$, and $(11\overline{2}0)$ surface ordering is the relation of the 1st subband ladder to the 2nd. For $(01\overline{1}0)$ surfaces these ladders are distinctly different whereas for the $(11\overline{2}0)$ surfaces they are very similar. In the latter case the subbands almost behave as just one ladder in some situations.

The results for the lowest subband energies are shown in Fig. 4.5. Since the gap between the lowest two conduction bands is $0.1eV$ in 4H-SiC, fewer subbands from the 2nd conduction band are shown for this polytype. The lowest subband from this band is distinctive since it crosses the higher subbands of the 1st conduction band in Fig. 4.5. For 6H-SiC the two conduction bands are closer in energy than the subband spacing. In general these two bands will be simply treated as one band when their energy gap, $0.01eV$, is less than the thermal energy. A noticeable trend in Figs. 4.4 and 4.5 is that the lowest subbands for each of the ladders, E_o and E'_o, are further apart for the $(01\overline{1}0)$ orientation. This occurs because of differences in the transverse mass between the ladders. Since these trends occur at low values of N_{inv}, the results of the triangular-well approximation can be used. We see from Eq. (4.16) that the subband energy ratios of the two ladders are given by

$$E'_i \Big/ E_j = \left(\frac{m_3}{m'_3} \left[\frac{i + 3/4}{j + 3/4} \right]^2 \right)^{1/3}, \tag{4.18}$$

where i and j are subband numbers. Since m_3 is significantly larger than m'_3 in the $(01\overline{1}0)$ arrangement, the subband ladder spacing is quite large. When Eq. (4.18) is applied to the $(11\overline{2}0)$ surface, we see that the similarity between the transverse masses of the two ladders indicates a close interladder energy spacing. We see this in Figs. 4.4 and 4.5.

In Fig. 4.6, results for the distribution of electrons among the subbands are shown as the mobile inversion charge or temperature is varied. For convenience, no distinction is made between the two conduction bands here. This means that for instance the lower ladder in Fig. 4.6 is the addition of the lower ladder for the two conduction bands. In the limit of high temperature or the limit of very weak inversion, the relative population of each ladder falls onto the ratio of valley degeneracies 2/3:1/3 in Tables 4.2 and 4.3. In these limits many subbands are occupied and a 3-D continuum of states exists. The opposite extreme is the ideal 2-D limit of the inversion layer when only one subband is occupied. This is the situation typically for small temperatures or when the inversion is very strong. In the results of Fig. 4.6, the surfaces exist somewhere between these two limits. In the following discussion, when we refer to a ladder as being " *3-D like*" or "*2-D like*", this is relative to the other ladders being considered and does not necessarily mean the surface is at these limits. The inversion layers will only attain these limits under conditions of extremely low or extremely high temperatures or inversion.

The results in Fig. 4.6 are best explained by determining the factors that influence the percent occupation of a particular ladder. Using Eqs. (4.8) and (4.16), the electron distribution depends on the energy difference E_o-$E_F(m_3)$ and the density of states effective mass m_d=$\sqrt{m_1 m_2}$ parallel to the interface. The energy difference between the first subband and the Fermi level, E_o-E_F, depends on the transverse mass. It affects each subband since in the triangular-well approximation each N_{inv} in Eq (8) can be represented as a function of E_o-E_F by using Eq. (4.16). Quantization in the inversion layer tends to push the subband energies above the conduction

band edge of the unquantized surface. In Eq. (4.16), we see that this process is weaker for larger transverse effective masses since $E \propto m_3^{-1/3}$. For a fixed total charge density N_{inv}, the relative occupation of the 1st ladder relative to the 2nd increases when m_3 is larger than m_3' since the subbands of the first ladder are lower in energy. Under these circumstances E_o-E_F would tend to be larger in ladder 1, since the subband energy levels are closer, and more of the higher subbands would be occupied in this ladder. The first ladder would therefore be more "3-D like" than the second.

This is the situation which occurs for the $(01\overline{1}0)$ surface where $m_3 > m_3'$. This can be observed in Fig. 4.6(a), where a larger percentage of the higher subbands are occupied in the first ladder. This occurs for both weak and strong inversion. The same effect can be seen with varying temperature in Fig. 4.6(c). The 1st ladder is more "3-D like" at high temperatures when compared to the 2nd ladder. As the temperature is decreased, the occupation of the higher subbands decreases in both ladders as expected. When the $(01\overline{1}0)$ surface temperature is decreased to very small values(50K) in Fig. 4.6(c), the surface tends towards a perfect 2-D system with only E_o occupied. For temperatures below $100K$(4H) and $200K$(6H) in Fig. 4.6(c), the system is essentially two dimensional. This would typically occur at higher temperatures, but the process is limited by the 1st ladder which progresses to the 2-D state slower as the temperature is lowered. Since m_3 is larger and m_3' smaller in the 6H-SiC polytype, the difference in the two ladders is more pronounced than in 4H-SiC. Also the occupation ratio of the two ladders is significantly larger than the the 3-D limit result of 2. This occurs again because the subbands are lower

in energy in the first ladder due to the larger transverse mass. This effect would be even larger if ratio m_d/m'_d was not smaller than one in the $(01\overline{1}0)$ orientation. So since the two ladders are different the system as a whole is further from a 3-D system. The 3-D limit would therefore only occur at much larger temperatures or at much weaker levels of inversion than those simulated in Figs. 4.6(a) and 4.6(c).

For the $(11\overline{2}0)$ surface, both subband ladders are similar to the 2nd ladder of the $(01\overline{1}0)$ orientation and therefore are more "2-D like" when compared to the $(01\overline{1}0)$ 1st ladder. Also because the subband ladders are equivalent, the fractional occupancy of the two ladders falls very close to the valley degeneracy ratios. In 4H-SiC this persists even when the mobile charge is increased to $1X10^{13}cm^{-2}$. Since m_3/m'_3 is about 8% larger in 6H-SiC, the 1st ladder is occupied slightly more than twice as much as the 2nd at room temperature, especially when the level of inversion is large. In Fig. 4.6(d) it is seen that temperatures need to go below approximately $100K$ in 6H-SiC for the system to be essentially 2-dimensional. For 4H-SiC the situation is different. For this polytype, both subbands are significantly occupied even down to $50K$. In Fig. 4.7, it can be seen that the electrons begin to exist at the interface in a 2-D gas when the temperature is decreased so that the Fermi energy crosses the lowest subband. In $(11\overline{2}0)$ oriented 4H-SiC, the Fermi level crosses the the lowest subband of the second ladder around $120K$. This means that this surface does not tend towards a perfect 2-D system at very low temperatures. Here two subbands, E_o and E'_o, are expected to be filled, even as $T \rightarrow 0$. This is similar to the case of (100) oriented 3C-SiC.[94]

Another interesting result related to the surface band structure calculation

is the determination of the average penetration of the mobile electrons into the semiconductor in Eq. (4.12). Calculations of Z_{av}, shown as a function of mobile charge in Fig. 10a, show that the penetration depth is less in the $(01\overline{1}0)$ orientation. As we saw for the subband energy spacing, this is a trend which occurs for not only strong but also weak inversion. It is therefore useful to consider the triangular-well approximation results again. Using Eqs. (4.12), (4.15) and (4.16), the penetration depth is[93]

$$Z_{av} = \sum_s 2N_s \left[\frac{3}{2}\pi\left(s+\frac{3}{4}\right)\right]^{2/3} \left(\hbar^2/2m_3 eF_o\right)^{1/3} \Big/ 3N_{inv}. \tag{4.19}$$

So $Z_{av} \propto (1/m_3)^{1/3}$ and is therefore smaller for the $(01\overline{1}0)$ orientation, which has a larger ladder 1 transverse mass. These results can also be seen in Fig. 4.4 where the charge density verses distance is shown for 6H-SiC. Since m_3 is quite small for $(11\overline{2}0)$ 6H-SiC and large for $(01\overline{1}0)$ 6H-SiC, the differences are prominent. The charge density is significantly shifted away from the surface in the former case. Since this would tend to lower the MOSFET capacitance, $(01\overline{1}0)$ 6H-SiC MOSFETS should have a larger drive current when compared to 6H-SiC MOSFET using the $(11\overline{2}0)$ orientation.

4.3.2 (0001) and $(03\overline{3}8)$ Orientations

The (0001) and $(03\overline{3}8)$ surfaces of 4H-SiC and 6H-SiC have large transverse periodic lengths due to the large size of the direct lattice primitive cell along the c-axis. As mentioned, the results here are based on the use of an effective mass transverse to the interface. This approximation is questionable for these orientations since

$L_\perp$ is large, but it is still likely that this method will lead to a useful qualitative understanding of these surfaces. This is especially true for 4H-SiC for which $L_\perp$ is only approximately twice that of Si. The results of the method will also be more reliable when the temperature is larger or the surface inversion is weaker.

In 4H-SiC the (0001) subband ladder is very similar to the 1st ladder of the $(11\overline{2}0)$ orientation, with the same transverse mass in fact. Since both ladders are very similar for the $(11\overline{2}0)$ surface, these two surfaces are therefore very similar. The only significant difference is that only one subband ladder occurs in the (0001) orientation. The (0001) surface in 6H-SiC is however different as a result of the huge transverse mass. Indeed, this property makes (0001) 6H-SiC unique among all the other surfaces we consider.

So unlike all the other surface orientations, the (0001) surface is very different in 4H-SiC and 6H-SiC. In Fig. 4.9 we see that the the 2-D limit occurs at a much lower temperature in 6H-SiC. For higher temperatures the distribution of electrons in the higher subbands is much larger in 6H-SiC. Continuing the comparison of the various surfaces in terms of how relatively close they are to the 2-D or 3-D limits, the (0001) 4H-SiC surface turns out to be more "2-D like" while in the case of 6H-SiC, the surface is the most "3-D like" of all the surfaces. Since m_3 is large in 6H-SiC, the subband energies in Fig. 4.10(a) are low in energy and very closely spaced. Here E_o-E_F is typically large and many of the higher subbands are significantly occupied when the surface is weak to moderately inverted. Comparing the average penetration depth of electrons into the semiconductor in Fig. 4.8(b), Z_{av} is much larger in 4H-SiC. This is expected in a more '2-D like" surface since m_3 is small.

In 6H-SiC Z_{av} is the by far the smallest of any orientation considered. Even at moderate inversion strengths, N_{inv}=$5X10^{12}cm^{-2}$, this distance is only $2nm$ or less. This is at the limit of the effective mass approximation in Si. Since $L_{\perp}$ is three times as large, the 6H-SiC (0001) surface appears to far exceed the limits of this approximation. Such a small penetration depth is likely to translate in a larger MOSFET drive current though. For the (0001) surface of 4H-SiC the situation is different. When the inversion is weak, the effective mass approximation should likely be reliable.

We find that the $(03\overline{3}8)$ orientation is very similar to the $(01\overline{1}0)$ orientation. As seen in Tables 4.2 and 4.3, the transverse mass is large in the 1st ladder and small in the 2nd. The results for the distribution of electrons among the subbands is shown in Fig. 4.11. These results are similar to the $(01\overline{1}0)$ surface since the ratio m_3/m_3' is very similar. Most of the discussion of the $(01\overline{1}0)$ surface in the last section can therefore be applied to the $(03\overline{3}8)$ arrangement. One difference although warrants mentioning. The transverse mass for 6H-SiC is larger for the $(03\overline{3}8)$ surface allowing more of the higher subbands to become occupied in Fig. 4.11. This also results in a lower Z_{av} in Fig. 10.

4.4 Chapter Summary

Here we have determined the band structure of an n-type inversion layer in 4H-SiC and 6H-SiC. The subband levels have been self-consistently calculated using the Hartree and effective masses approximations. The latter approximation is believed

to be reliable for the $(01\overline{1}0)$ and $(11\overline{2}0)$ surface orientations but is more questionable for the $(03\overline{3}8)$ and (0001) orientations where the lattice periodicity perpendicular to the interface occurs over a relatively large length scale. In these cases though we do believe that the results lead to a potentially useful qualitative understanding of the trends in the subband structure of these surfaces.

Results show that the conduction band edge for the $(01\overline{1}0)$ and $(03\overline{3}8)$ orientations is split into 2 distinct subband ladders. Electrons in the ladder of lowest energy are found to in general occupy the higher subbands, and are generally further from the interface when compared to the 2nd ladder. The 1st ladder is relatively more "3-D like" than the second. For the electronic structure parallel to the interface there are differences among the two polytypes. In 6H-SiC the two longitudinal masses are very different and the material properties of these surfaces, such as the electron mobility, are likely to exhibit anisotropy. For 4H-SiC the situation is different, here m_1 and m_2 are similar in the 1st subband ladder. This should lead to anisotropy in the electron transport properties of these surface only when the higher energy subband becomes occupied with electrons.

The $(11\overline{2}0)$ and (0001) surfaces and very similar in 4H-SiC. Here the 2 subband ladders in the $(11\overline{2}0)$ orientation are both similar to the one ladder for the (0001) surface. The properties of these orientations turn out to be relatively more "2-D like" when compared to the other surfaces. The 6H-SiC $(11\overline{2}0)$ orientation is similar to that in 4H-SiC, but the 6H-SiC (0001) orientation is unique. Due to the huge transverse mass, this orientation is extremely "3-D like" when compared to all the other surfaces consider. Here the electrons are therefore generally found to exist in

a number of closely spaced subband levels, very close to the oxide interface. In each ladder of both polytypes, there is significant anisotropy in the $(11\overline{2}0)$ and (0001) surface band structure parallel to the interface.

Surface	m_1	m_2	m_3
$(01\overline{1}0)$			
lower(1)	$(3m_1' + m_2')/4$	m_3'	$4m_1'm_2'/(3m_1' + m_2')$
higher(2)	m_2'	m_3'	m_1'
$(11\overline{2}0)$			
lower(1)	$(m_1' + 3m_2')/4$	m_3'	$4m_1'm_2'/(m_1' + 3m_2')$
higher(2)	m_2'	m_3'	m_1'
$(03\overline{3}8)$			
lower(1) *	$(3m_1' + m_2')/4$	$M/(9m_1' + 3m_2')$	$12m_1'm_2'm_3'/M$
higher(2)	m_2'	$(m_1' + 2m_3')/3$	$3m_1'm_3'/(m_1' + 3m_3')$
(0001)			
all	m_1'	m_2'	m_3'

Table 4.1: Effective mass transformations. (Here m are the principle axes effective masses and m' are the bulk values. The 4H-SiC bulk values used in this work are $(0.29, 0.58, 0.33)$ and $(0.90, 0.58, 0.33)$ for the first(lower) and second(higher) conduction bands respectively.[32, 99] The bulk values for 6H-SiC are $(0.22, 0.90, 1.43)$.[32, 99] Also $M = (4m_1'm_2' + 6m_1'm_3' + 2m_2'm_3')$. * Results for $(03\overline{3}8)$ m_1 and m_2 are when the principle axes lie close to the the Brillouin zone axes shown Fig. 4.2(b). This is not the case for the 1st conduction band of 4H-SiC where this formula is off by 15% from the values used in this work. The product m_1m_2 is valid in all cases.)

Surface	$(01\bar{1}0)$		$(11\bar{2}0)$		$(03\bar{3}8)$		(0001)
	(1)	**(2)**	**(1)**	**(2)**	**(1)**	**(2)**	**all**
Degen.	2	1	2	1	2	1	3
***(Band 1)**	**4H**						
Transverse mass							
m_3	.46	.29	.33	.29	.41	.30	.33
Longitudinal masses							
m_1	.36	.58	.51	.58	.36	.58	.29
m_2	.33	.33	.33	.33	.37	.32	.58
Density of states mass							
	.35	.44	.41	.44	.37	.43	.41
***(Band 2)**	**4H**						
Transverse mass							
m_3	.64	.90	.79	.90	.49	.57	.33
Longitudinal masses							
m_1	.82	.58	.66	.58	.82	.58	.90
m_2	.33	.33	.33	.33	.43	.52	.58
Density of states mass							
	.52	.44	.47	.44	.60	.55	.72

Table 4.2: Effective masses for 4H-SiC surface orientations. (Ladder 1(2) is the lower(higher) ladder.)

Surface	$(01\bar{1}0)$		$(11\bar{2}0)$		$(03\bar{3}8)$		(0001)
	(1)	**(2)**	**(1)**	**(2)**	**(1)**	**(2)**	**all**
Degen.	2	1	2	1	2	1	3
***(Band 1)**	**6H**						
Transverse mass							
m_3	.51	.22	.27	.22	.65	.31	1.43
Longitudinal masses							
m_1	.39	.90	.73	.90	.39	.90	.22
m_2	1.43	1.43	1.43	1.43	1.12	1.03	.9
Density of states mass							
	.75	1.13	1.02	1.13	.66	.96	.45

Table 4.3: Effective masses for 6H-SiC surface orientations. (Masses of band 2, not shown, are the same as those of band 1. Ladder 1(2) is the lower(higher) ladder.)

Surface	$(01\overline{1}0)$	$(11\overline{2}0)$	$(03\overline{3}8)$	(0001)
$L_\perp$(nH-SiC)	$\sqrt{3}a$	a	$\sqrt{3a^2+c^2}$	c
$L_\perp$(nH-SiC)/$L_\perp$(Si)	1	$1/\sqrt{3}$	$\sqrt{1+2n^2/9}$	$\sqrt{2}n/3$
$L_\perp$(4H-SiC)/$L_\perp$(Si)	1	$1/\sqrt{3}$	2.1	1.9
$L_\perp$(6H-SiC)/$L_\perp$(Si)	1	$1/\sqrt{3}$	3.0	2.8

Table 4.4: Periodicity perpendicular to the interface. ($L_\perp$ is the length of lattice periodicity perpendicular to the interface. For SiC, a=3.08A and c=$\sqrt{2/3}an$.

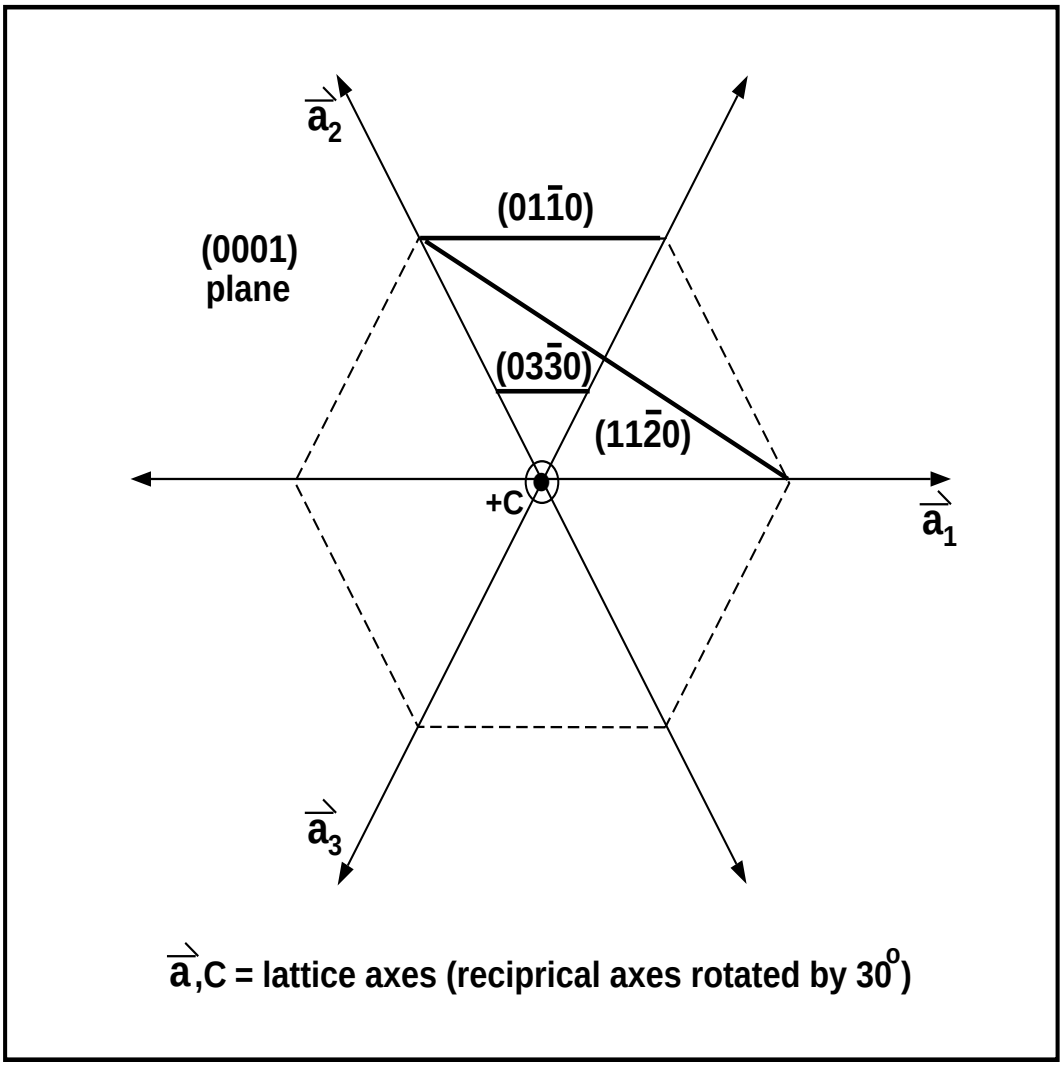

Figure 4.1: SiC Lattice shown in the (0001) plane.

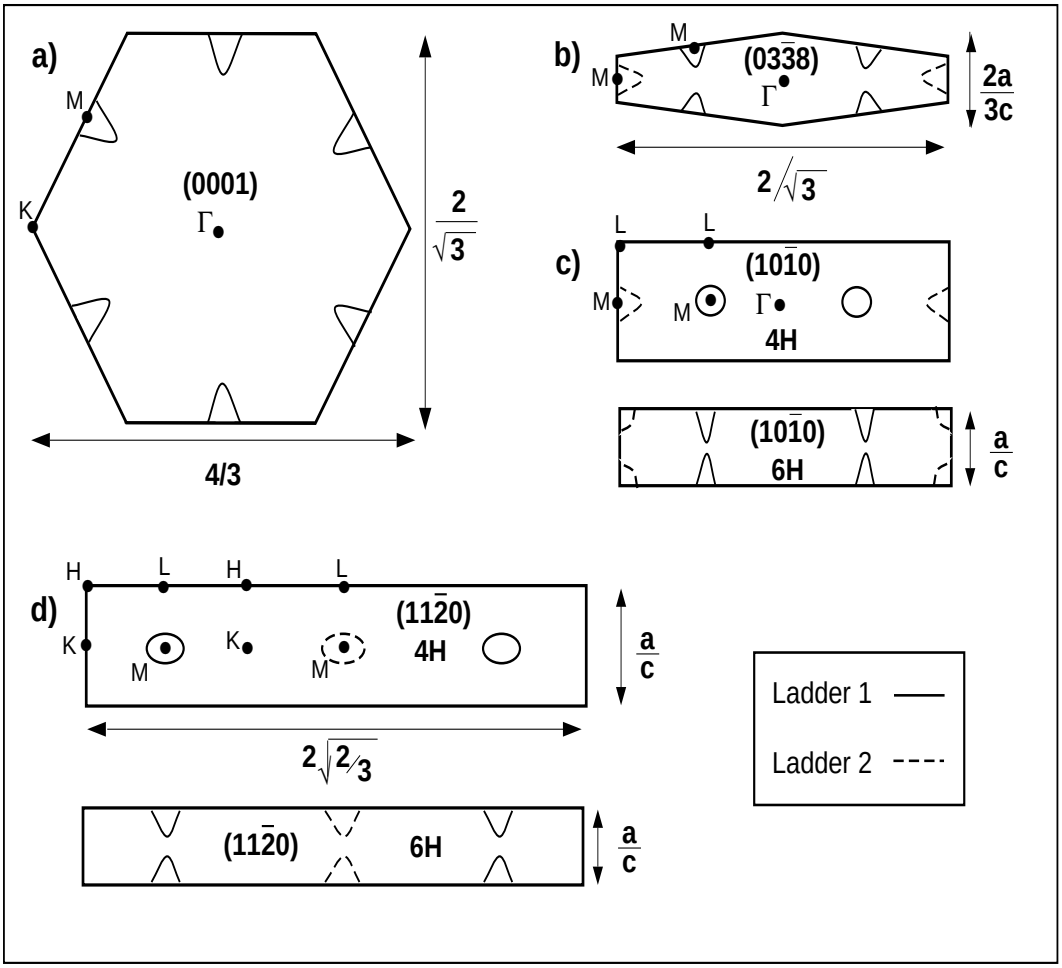

Figure 4.2: Brillouin zones and conduction-edge band structure for 4H and 6H-SiC. Only the lowest conduction band is shown. Since the results are similar for both polytypes, only the 4H results are shown in a) and b). Note if the 2nd conduction band is considered for 4H-SiC, the ladders are switched.

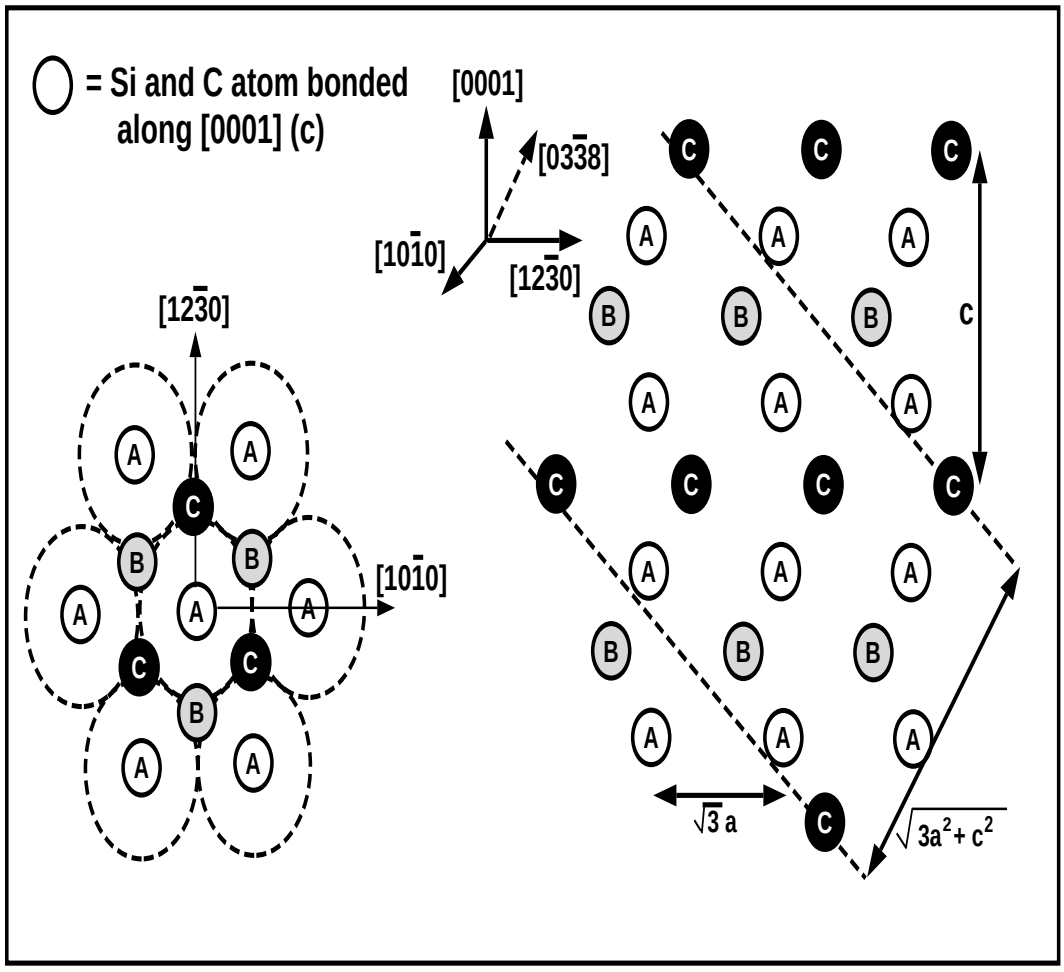

Figure 4.3: Lattice structure of 4H-SiC.

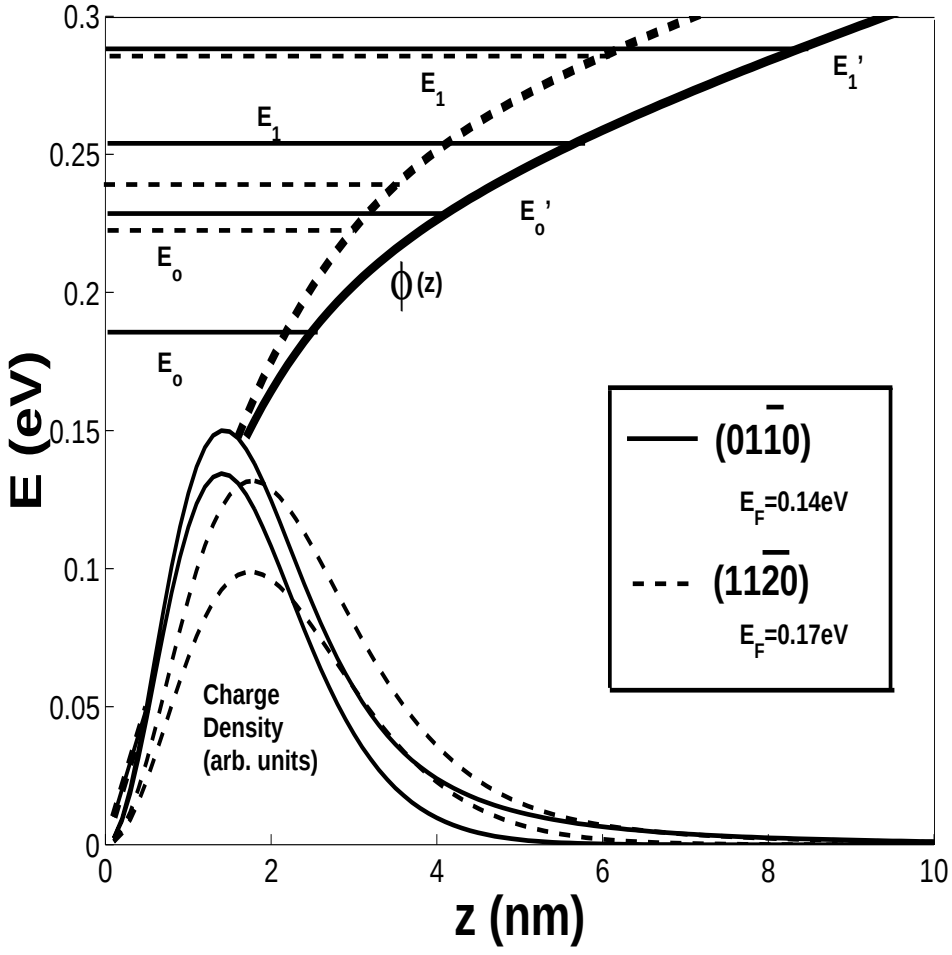

Figure 4.4: Self-consistent results for the $(01\bar{1}0)$ and $(11\bar{2}0)$ orientations of 6H-SiC. The subband ladders are labeled as unprimed(lower) and primed(higher) identically for both surfaces. The total charge density and charge density in the subband E_o are shown. The results are for a temperature of $300K$, mobile charge of $N_{inv} = 5X10^{12}cm^{-2}$ and doping of $N_A - N_D = 1X10^{16}cm^{-3}$.

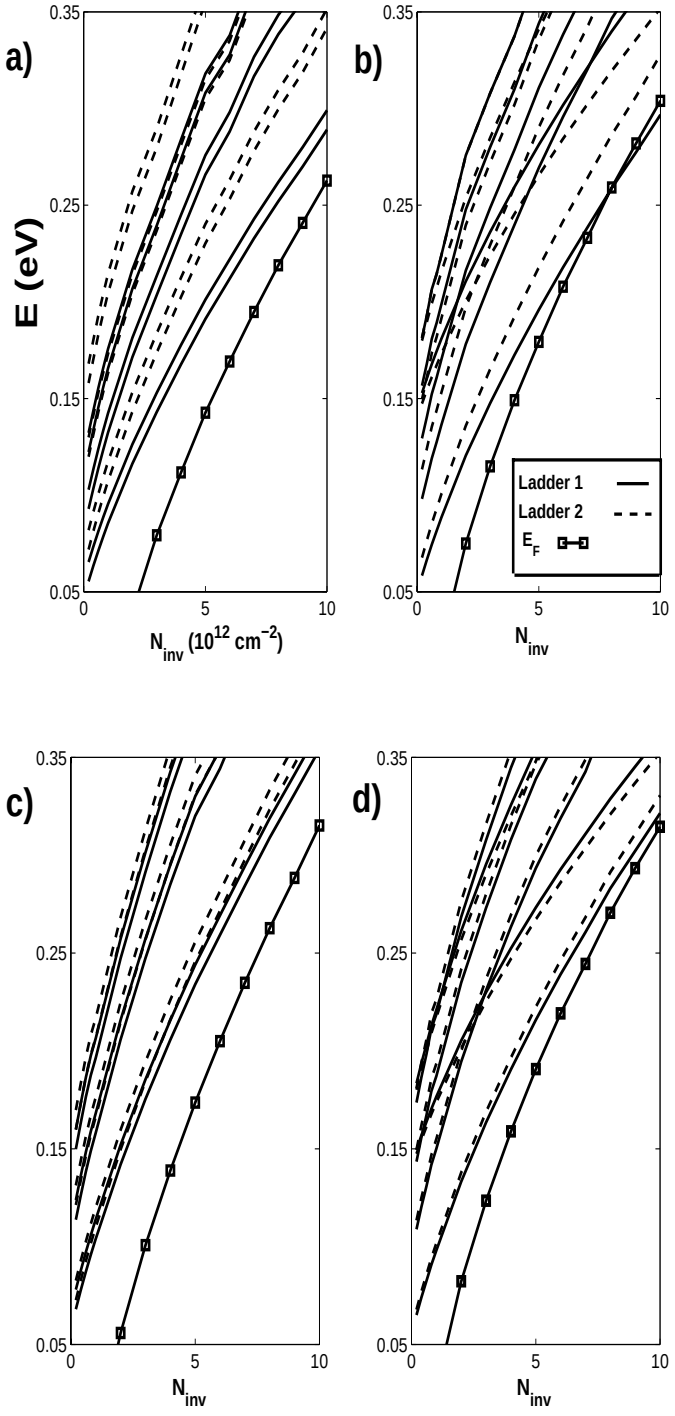

Figure 4.5: Subband energies for a) $(01\overline{1}0)$ 6H-SiC, b) $(01\overline{1}0)$ 4H-SiC, c) $(11\overline{2}0)$ 6H-SiC, and d) $(11\overline{2}0)$ 4H-SiC. The lowest 10 subbands are shown. The results are for a temperature of T=300K and a doping density of $N_A - N_D = 1X10^{16}cm^{-3}$.

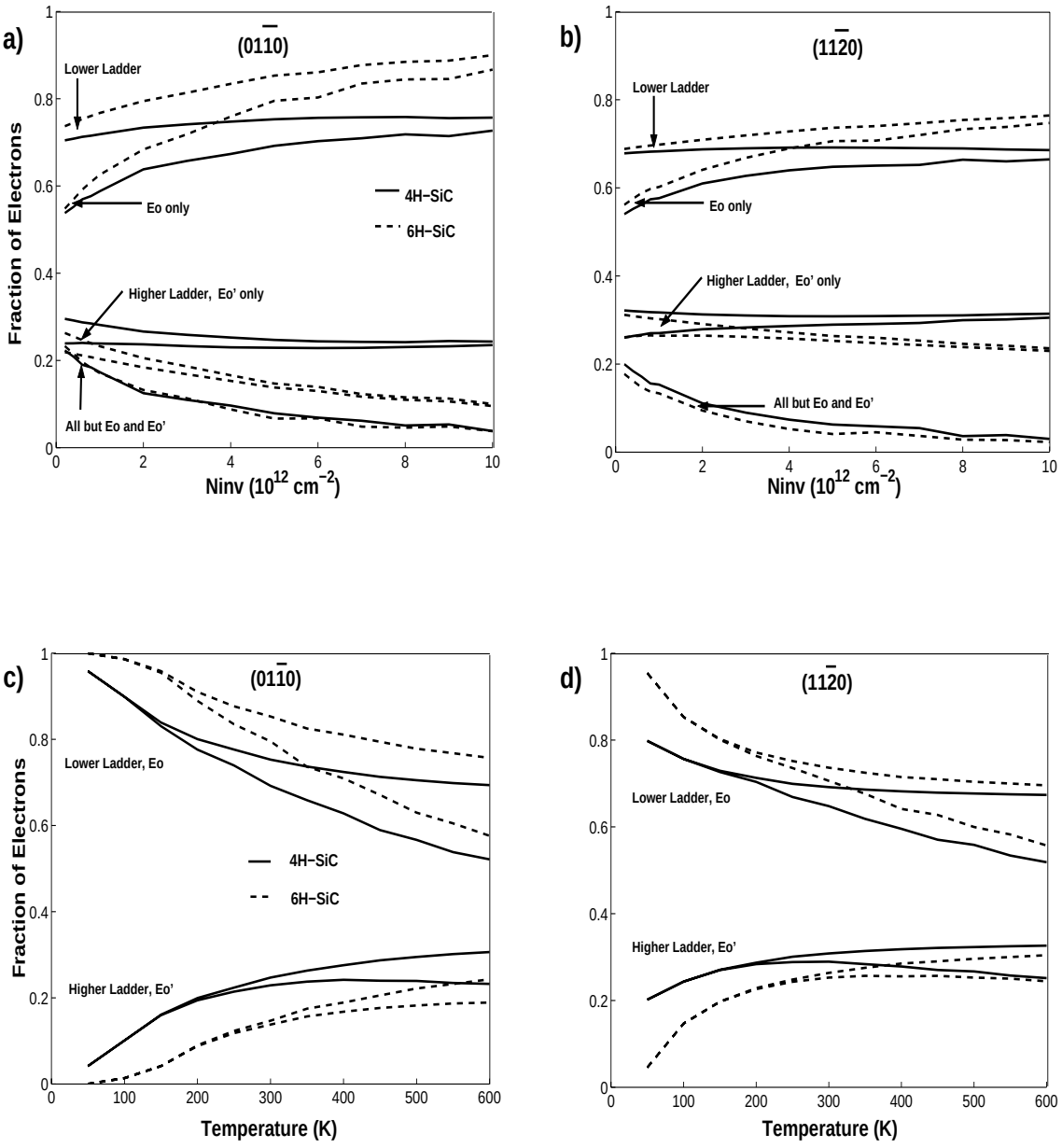

Figure 4.6: Fraction of electrons vs. mobile inversion layer charge at T=300K for the a) (01$\bar{1}$0) and b) (11$\bar{2}$0) directions. Fraction of electrons vs. temperature for the c) (01$\bar{1}$0) and d) (11$\bar{2}$0) directions where $N_{inv} = 5X10^{12}cm^{-2}$. The results are for a doping density of $N_A - N_D = 1X10^{16}cm^{-3}$.

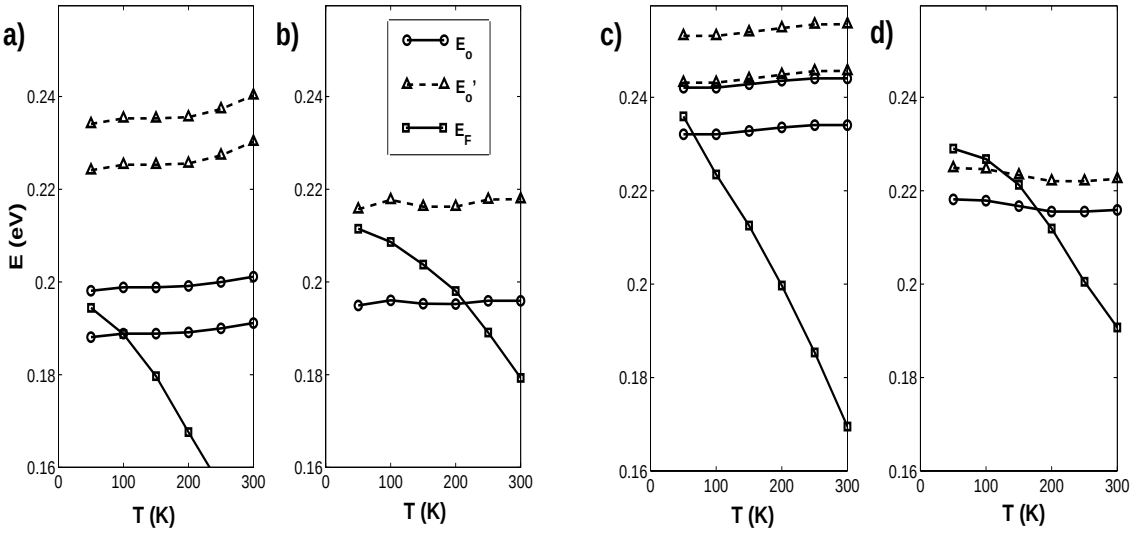

Figure 4.7: Low-lying energy bands vs. temperature(T) for a) $(01\overline{1}0)$ 6H-SiC, b) $(01\overline{1}0)$ 4H-SiC, c) $(11\overline{2}0)$ 6H-SiC, and d) $(11\overline{2}0)$ 4H-SiC. The electron and doping densities here are $N_{inv} = 5X10^{12}cm^{-2}$ and $N_A - N_D = 1X10^{16}cm^{-3}$ respectively.

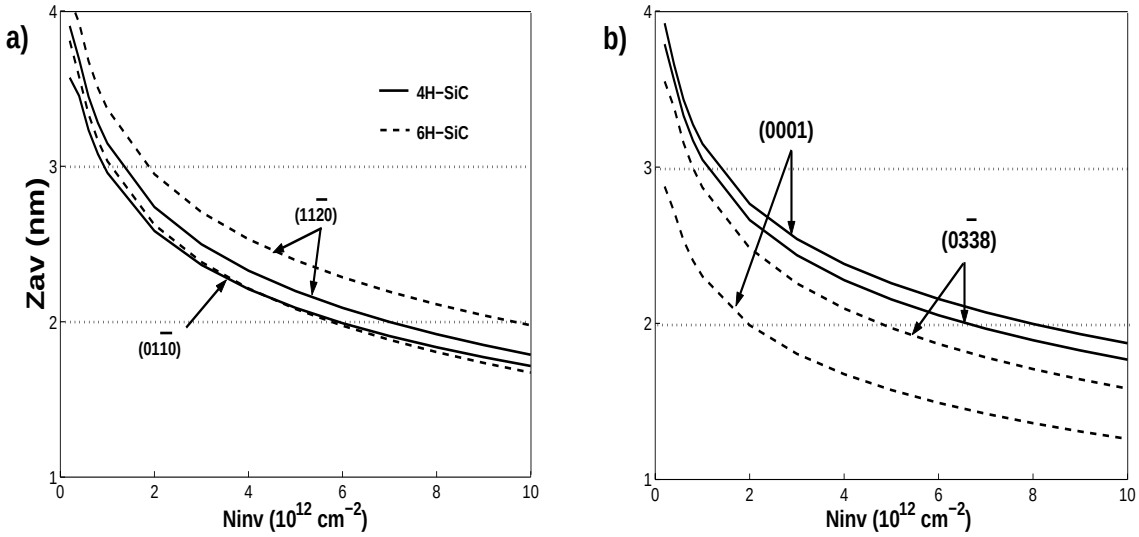

Figure 4.8: Average penetration depth for electrons at the interface when T=300K and $N_A - N_D = 1X10^{16}cm^{-3}$. In a) have the $(01\overline{1}0)$ and $(11\overline{2}0)$ orientations, while in b) have the $(03\overline{3}8)$ and (0010) orientations.

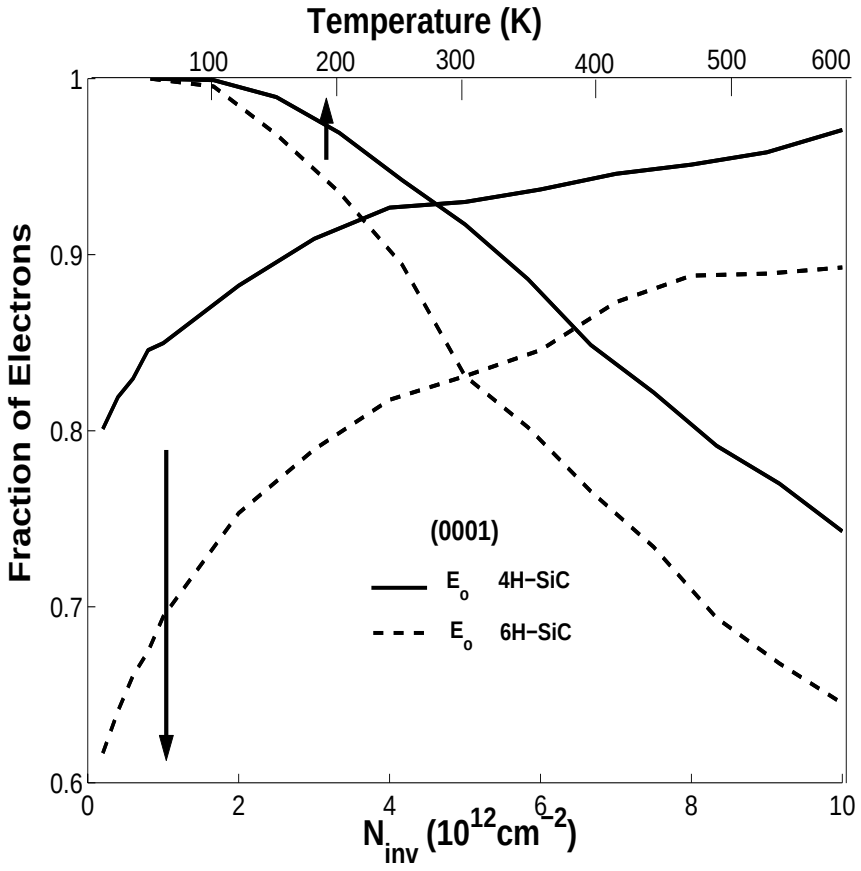

Figure 4.9: Fraction of electrons in lowest subband, with energy E_o, vs. mobile inversion layer charge. When the mobile charge density is varied T=300K, while N_{inv} is fixed at $5X10^{12}cm^{-2}$ when the temperature is varied. The doping density is $N_A - N_D = 1X10^{16}cm^{-3}$.

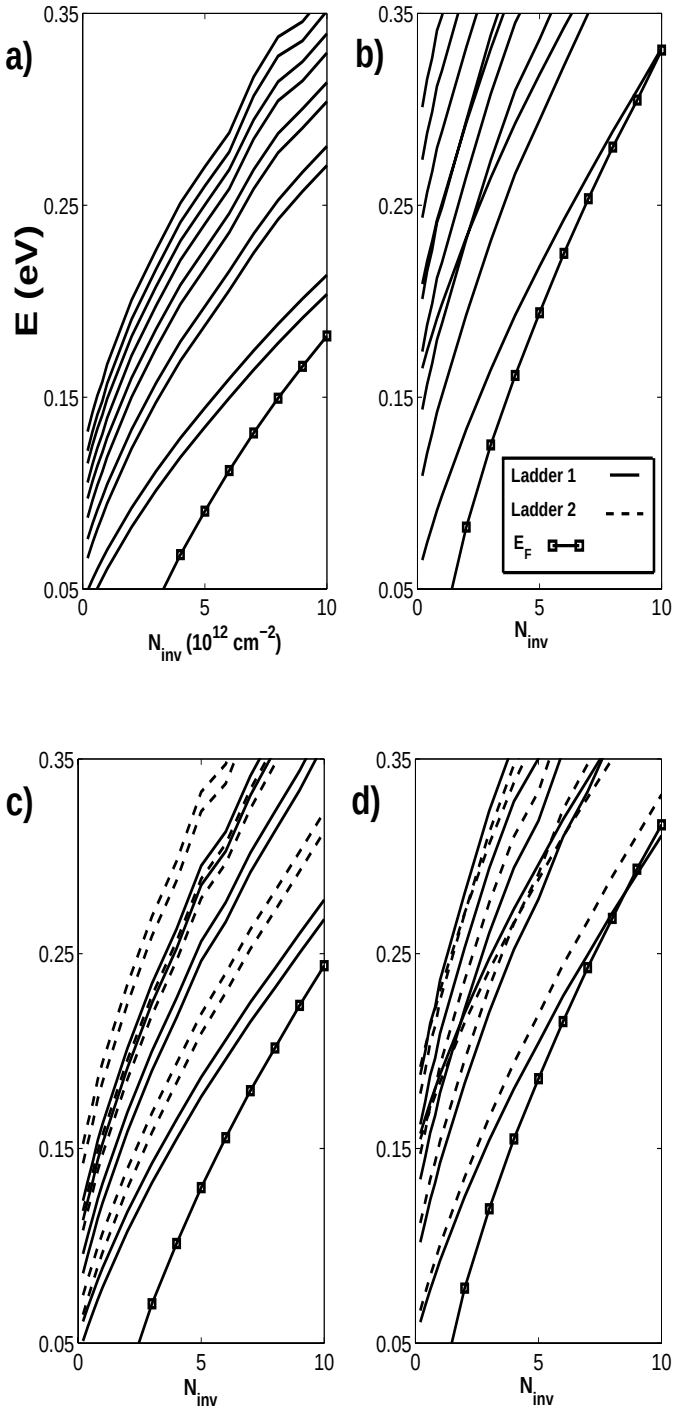

Figure 4.10: Subband energies for a) (0001) 6H-SiC, b) (0001) 4H-SiC, c) (03$\overline{3}$8) 6H-SiC, and d) (03$\overline{3}$8) 4H-SiC. The lowest 10 subbands are shown. The results are for a temperature of T=300K and a doping density of $N_A - N_D = 1X10^{16}cm^{-3}$.

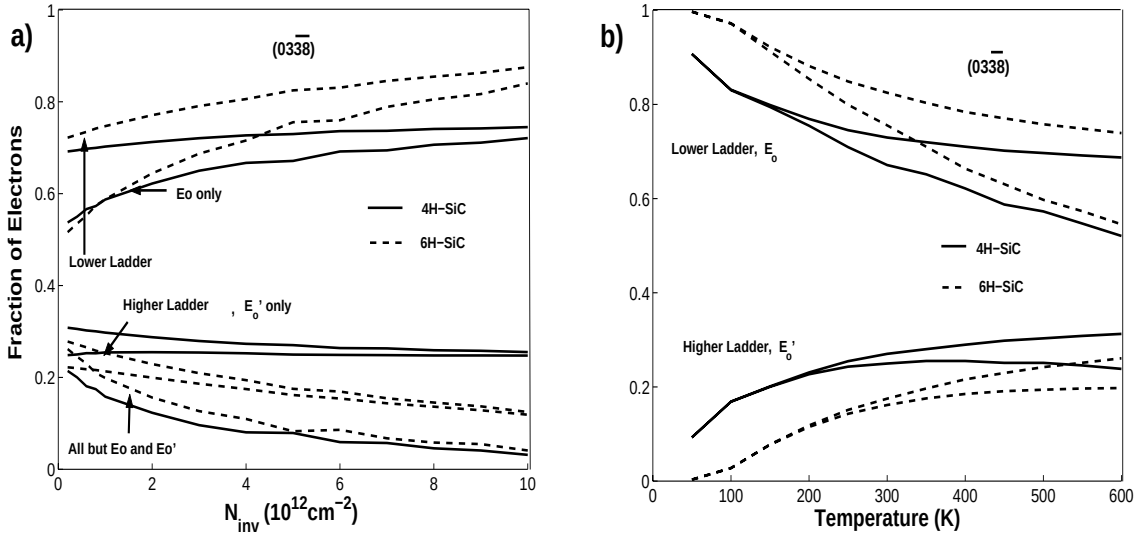

Figure 4.11: In a) have the fraction of electrons vs. mobile inversion layer charge at T=300K for the (03$\overline{3}$8) surface. In b) have the fraction of electrons vs. temperature for the (03$\overline{3}$8) surface when $N_{inv} = 5X10^{12}cm^{-2}$. The results are for a doping density of $N_A - N_D = 1X10^{16}cm^{-3}$.

Chapter 5

Simulation of Surface Electron Transport in Hexagonal SiC.

The applications of SiC MOSFETs in high-power electronic devices are severly limited by small inversion layer electron mobilities[12, 13, 14], that likely result from the presence of a larger interface trap density[15, 16, 17, 18]. It is believed that these traps exist in a sub-oxide layer between the true oxide and the 4H-SiC inversion layer[101]. Since these near interface traps (NIT) become very large near the conduction band edge, it has been postulated that they may be the result of suboxide Si-Si antibonding states.

Of all the SiC polytypes, 4H-SiC has the largest bulk drift velocity ($2\text{x}10^7 cm/s$), and therefore is expected to have the best performance in electronic applications.

The channel mobility for (0001) oriented 4H-SiC although is extremely low (typically $10cm^2/Vs$ or less)[13, 102, 103, 104, 11]. It has recently been discovered that the trap density in 4H-SiC MOSFETs is significantly less when the $(11\overline{2}0)$ crystalline orientation is used as opposed to the typical (0001) orientation[16]. Furthermore, the surface low-field mobility has been observed to increase ten-fold when the $(11\overline{2}0)$ surface is used[105]. These results suggest that the choice of a $(11\overline{2}0)$ orientation may well improve the problematic small mobilities in 4H-SiC MOSFETs.

In this Chapter we present the results of a Monte Carlo simulation of electron transport along the inversion layer channel of a 4H-SiC/SiO_2 interface. We simulate both the (0001) and $(11\overline{2}0)$ orientations, and compare the results to experiments.

5.1 Surface Electronic Band Structure

Electron transport in the inversion layer of 4H-SiC/SiO_2 MOSFET, shown in Fig. 5.1, will depend on the quasi 2-dimensional band structure at the interface. This is composed of two parts, a subband structure perpendicular to the interface along the z direction, and a 2-dimensional band structure parallel to the interface. The subband structure along z is determined by the methods in Chapter 4. As for the surface parallel to the interface, the electron energy, $\varepsilon(k)$, is considered as a continuous function of the electron wavevector k. Since we will simulate low-field transport, we consider only energies near the subband minima. To model the electron energy a spherical band structure is used within the effective mass approximation. The effective mass for an electron in subband s is given by m_s=$\sqrt{m_1 m_2}$. Here, in the no-

tation of Chapter 4, m_1 and m_2 are the principle axes effective masses parallel to the interface. Here m_s depends on the occupied subband perpendicular to the interface since it depends on the particular subband ladder that the electron occupies.

The electron energy dispersion, $\varepsilon(k)$, parallel to the interface is then determined by:

$$\frac{\hbar^2 k^2}{2m_s} = (\varepsilon(k) - E_s)\left(1 + \alpha_s(\varepsilon(k) - E_s)\right), \tag{5.1}$$

where the nonparabolicity factor for each subband is given by $\alpha = 0.323$ for 4H-SiC. To occupy the subband s, the energy $\varepsilon(k)$ must be larger than the subband minimum energy E_s. Since we deal with conduction band electrons, the zero level for the electron energy is set equal to E_0, the energy of the lowest subband.

Usually the scattering rates are proportional to the density of final electron states DOS. Here in 2-dimensions, parallel to the interface, we have

$$DOS_s(\varepsilon) = \frac{2\pi m_s(1 + \alpha\,(\varepsilon - E_s))}{\hbar^2}\Theta(\varepsilon - E_s), \tag{5.2}$$

where the heavy side step function Θ insures that DOS_s is zero if the electron energy is less than the subband minimum energy E_s.

5.2 Scattering

In this section we develop the quasi-2D scattering rate for a free conduction electron at the 4H-SiC/SiO_2 interface. The mechanisms considered are scattering by acoustic phonons, optical phonons, trapped interface charge, ionized impurities, and surface roughness. We assume that the effect of these scatterers on the electronic structure

is weak, and can be treated using first order perturbation theory[106]. The rate is then described by the well known "Fermi's Golden Rule". Using the method of Price [107], the scattering rate for an electron with wavevector $\vec{k}$ in subband s is expressed as a sum over possible final states in each subband s' with wavevector $\vec{k'}$. This can be represented as

$$\Gamma_s(\varepsilon(k)) = \frac{2\pi}{\hbar} \sum_{s'} \int_0^{2\pi} d\theta' \int k' dk' |M_{ss'}(Q)|^2 \delta(\varepsilon(k') - \varepsilon(k) \ \pm \ E_p(Q)), \tag{5.3}$$

where $M_{ss'}(Q)$ are the matrix elements for the electron-scatterer interaction energy, and $E_p(Q)$ is the energy lost upon scattering. Here $\vec{Q} = \vec{k'} - \vec{k}$, is the 2D wavevector involved in the transfer or electron momentum parallel to the interface. The momentum transfer in the perpendicular direction, along z, is defined as q_z. Integrations over k' and q_z will occur over the limits of 0 to infinity, though this will not be shown explicitly.

The quasi-2D interaction, $M_{ss'}$, is found by the integration of the 3-dimensional interaction , $H_{ss'}$, over q_z. This is represented by the expression:

$$|M_{ss'}(Q)|^2 = (2\pi)^2 \int |H_{ss'}(Q, q_z)|^2 |I_{ss'}(q_z)|^2 dq_z, \tag{5.4}$$

where $I_{ss'}(q_z)$ is the overlap integral. Using the self-consistent wavefunctions in Eq. (4.4), the square of the overlap integral is

$$|I_{ss'}(q_z)|^2 = \int |\zeta_s(z)|^2 |\zeta_{s'}(z')|^2 \exp(iq_z(z - z')) dz dz', \tag{5.5}$$

and upon integration over the perpendicular momentum transfer,

$$\int |I_{ss'}(q_z)|^2 dq_z = 2\pi \int |\zeta_s(z)|^2 |\zeta_{s'}(z)|^2 dz \equiv \frac{\pi}{b_{ss'}}. \tag{5.6}$$

Here $b_{ss'}$ is a characteristic length scale for the overlap integral, where $1/b_{ss'}$ identifies how fast $|I_{ss'}(q_z)|^2$ falls off with increasing q_z.

When many different types of scatterers are present, the total rate is the sum of the rates of the individual unique scatterers. Here we consider acoustic phonon (ac), optical phonon (po), ionized impurity (ii), trapped inversion charge (it) , and surface roughness scattering (sr). The total scattering rate, Γ_s, is then given by the sum

$$\Gamma_s = \Gamma_s^{ac} + \Gamma_s^{po} + \Gamma_s^{ii} + \Gamma_s^{it} + \Gamma_s^{sr}. \tag{5.7}$$

In the next subsections each individual rate will be discussed.

5.2.1 Acoustic Phonon Scattering

The interaction between a free mobile conduction electron and an acoustic phonon is treated within the deformation potential theory[108]. Here long wavelength phonons are considered, and the shift in the electronic energy upon scattering is considered to be analogous to the effect of an equivalent locally homogeneous strain. The scattering rate then depends on the deformation potential parameter D_{ac}, which is the proportionality constant between the band structure energy shift and the strain.

For acoustic phonon scattering, the 3-D matrix element is then

$$|H_{ss'}^{ac}|^2 = \frac{\hbar D_{ac}^2 K_B T}{2(2\pi)^3 \rho u_l^2}, \tag{5.8}$$

were the limit of small phonon energies, relative to $K_b T$, is assumed and the Bose-Einstein phonon occupation number, N, is approximated as

$$N(q) \approx= \frac{K_B T}{\hbar q u_l}. \tag{5.9}$$

Here only longitudinal phonon modes are considered and u_l is the longitudinal velocity of sound in the material. For 4H-SiC we use u_l=1x10$^6 cm/s$. Also ρ here is the 3-dimensional mass density. Using the results of the bulk transport simulations in Chapter 3, an acoustic deformation potential of D_{ac}=17eV is used for the surface simulations.

Now since $|H_{ss'}|^2$ is independent of q_z and Q, the acoustic rate from equation 5.3 becomes

$$\Gamma_s^{ac}(\varepsilon(k)) = \sum_{s'} \frac{2\pi^2 |H_{ss'}^{ac}|^2}{\hbar b_{ss'}} \int_0^{2\pi} d\theta' \int k' dk' \delta(\varepsilon(k') - \varepsilon(k) \mp \hbar u_l Q \delta_{ss'}), \qquad (5.10)$$

where the $-(+)$ sign is for phonon absorption(emission). The phonon energy is $E_p = \hbar u_l Q$ for intra-subband transitions and zero for inter-subband transitions when $s \neq s'$. In the later case the resulting integration of $\vec{k'}$ is difficult to solve if inelastic scattering is considered. Here the scattering is therefore approximated as elastic. For intra-subband transitions however, the inelastic rate is used because the $\vec{k'}$ integration can be solved analytically. Using the method of Basu [109], the rate becomes

$$\Gamma_s^{ac}(\varepsilon(k)) = \frac{D_{ac}^2 K_B T}{8\pi\rho u_l^2} \sum_{s'} \frac{1}{b_{ss'}} DOS_{s'}(\varepsilon) \left(1 \pm \frac{2}{\pi} arcsin(m_{s'} u_l / \hbar k) \delta_{ss'}\right). \qquad (5.11)$$

When k and thus the electron energy is zero, the intra-subband scattering rate is also elastic and the $arcsin$ term vanishes.

5.2.2 Polar Optical Phonon Scattering

Since SiC is a polar material, with the C atoms being more electronegative than the Si atoms, a longitudinal optical phonon will produce a polarization field in the

lattice. This field leads to a significant perturbation of the electronic band structure and conduction band electrons are in effect scattered by the phonon. In the case of polar optical scattering, the interaction energy is given by[107, 111, 112]

$$|H^{po}_{ss'}(Q, q_z)|^2 = \frac{e^3 E_o a_o}{4\pi(2\pi)^3\hbar\,(Q^2 + q_z^2 + q_{sc}^2)}, \tag{5.12}$$

where E_o is the polar field and a_o is the Bohr radius. The polar field is taken as E_o=1.08x10$^5 V/cm$ from the bulk simulations in Chapter 3. The screening wavevector, q_{sc}, is taken as the inverse of the Debye length

$$q_{sc} = \sqrt{\frac{e^2 N_{inv}}{\epsilon Z_{av} K_B T}}, \tag{5.13}$$

where ϵ=9.72ϵ_o is the static dielectric constant of 4H-SiC. The term N_{inv} is the 2-dimensional number density of mobile electrons in the inversion layer and Z_{av} is their average distance from the 4H-SiC/oxide interface. This is the screening wavevector expected in 3D for the screening of slowing varying potentials in space and time.

The 2D interaction for polar optical phonon scattering is given by performing a contour integration of $|H^{po}_{ss'}(Q, q_z)|^2$ in the complex q_z plane according to equation (5.4). The result is

$$|M^{po}_{ss'}(Q)|^2 = \frac{e^3 E_o a_o}{4\pi(2\pi)^3\hbar\sqrt{Q^2 + q_{sc}^2}} F_{ss'}, \tag{5.14}$$

where the form factor is

$$F_{ss'}(Q) = \pi \int\int |\zeta_s(z)|^2 |\zeta_{s'}(z')|^2 \exp(-\sqrt{Q^2 + q_{sc}^2}|z - z'|) dz dz'. \tag{5.15}$$

This form factor will also appear in the scattering rate for the interface charge. Now

for polar optical scattering, the scattering rate from equation 5.3 is

$$\Gamma_s^{po}(\varepsilon(k)) = \frac{e^3 E_o a_o}{2(2\pi)^3\hbar} \sum_{s'} \left(N\ DOS_{s'}(\varepsilon + E_{po}) P_{s'}^{-}(k) + (N+1)\ DOS_{s'}(\varepsilon - E_{po}) P_{s'}^{+}(k) \right). \tag{5.16}$$

where the (-) sign is for optical phonon absorption and the (+) sign is for optical phonon emission. The phonon occupation probability is

$$N = \left(\exp\left(E_{po}/k_B T\right) - 1\right)^{-1}, \tag{5.17}$$

with the phonon energy, E_{po}=120meV, taken from the bulk simulations in Chapter 3. The P terms are integrals over θ', the angle between the initial and final electron wavevectors. They are equal to

$$P_{s'}^{\mp} = \frac{1}{2\pi} \int \frac{F_{ss'}(Q^{\mp})}{\sqrt{(Q^{\mp})^2 + q_{sc}^2}} d\theta', \tag{5.18}$$

where $Q^{\mp}$ is

$$Q^{\mp} = \sqrt{(K_{s'}^{\mp})^2 + k^2 - 2K_{s'}^{\mp} k cos(\theta')}. \tag{5.19}$$

The term $K_{s'}^{\mp}$ in the equation for $Q^{\mp}$ is the magnitude of the final electron wavevector. It is fixed by the k' integration to the value

$$K_{s'}^{\mp} = \sqrt{2m_{s'}(\varepsilon\ \pm\ E_{po})(1 + \alpha_{s'}(\varepsilon\ \pm\ E_{po}))}/\hbar. \tag{5.20}$$

Here the integrand of $P_{s'}^{\mp}$ is related to probability of scattering into a final state at an angle of θ' from the initial wavevector $\vec{k}$. A look-up table is produced for these values at the beginning of the Monte Carlo program in order to easily select the final scattering states as the program runs. This look-up table stores the rate for any selection of k and θ'. The $P_{s'}^{\mp}$ integrals are also solved numerically to determine

a second look-up table for the total polar optical rate for any k or energy ε. This is used to determine how often electrons scatter from the polar field as they are transported across the inversion layer by the applied field.

5.2.3 Ionized Impurity Scattering

In the case of a uniform distribution of charge scatterers in the inversion layer, we can continue to find the quasi 2-dimensional scattering rates from the 3-dimensional interaction potential. Here we will assume a uniform density of dopants $N_A - N_D$, using the notation of previous Chapters. Beginning with the 3-D interaction between a free conduction electron and an ionized impurity of charge e, we have

$$|H_s^{ii}(Q, q_z)|^2 = \frac{e^4}{(2\pi)^3 \epsilon^2 \left(Q^2 + q_z^2 + q_{sc}^2\right)^2}. \tag{5.21}$$

We include only intra-subband scattering events since inter-subband scattering will be weak as long as the subband energy minima are not very close in energy. Proceeding to determine the 2-D interaction using equation (5.4) and performing a contour integral we obtain

$$|M_s^{ii}(Q)|^2 == \frac{e^4}{(2\pi)^3 \epsilon^2 \left(Q^2 + q_{sc}^2\right)^{3/2}} \left(F_{ss}(Q) + \sqrt{Q^2 + q_{sc}^2}\; F_{ss}^*(Q)\right). \tag{5.22}$$

Here a second form factor is introduced and is given by

$$F_{ss'}^*(Q) = \pi \int\int |\zeta_s(z)|^2 |\zeta_{s'}(z')|^2 |z - z'| \exp(-\sqrt{Q^2 + q_{sc}^2}|z - z'|) dz dz', \tag{5.23}$$

shown here for the general case when inter-subband transitions are included.

Since the rate decreases sharply with 2-D wavevector Q, scattering can be

treated as elastic to a good approximation. In this case the wavevector becomes

$$Q = 2ksin(\theta'). \tag{5.24}$$

Now the rate is

$$\Gamma_s^{ii}(\varepsilon(k)) = \frac{(N_A - N_D)e^4 DOS_s(\varepsilon)}{(2\pi)^2\hbar\epsilon^2} P(k), \tag{5.25}$$

where the integral of θ' is

$$P(k) = \frac{1}{2\pi}\int_0^{2\pi} d\theta' \frac{F_{ss}(Q) + \sqrt{Q^2 + q_{sc}^2}\, F_{ss}^*(Q)}{(Q^2 + q_{sc}^2)^{3/2}} \left(1 - \frac{2C_{ii}J_1(QR_{ii})}{QR_{ii}}\right), \tag{5.26}$$

and the wavevector Q is given by equation 5.24. The last term in the equation above takes into account the correlation of the charged impurities. The term J_1 is the 1st order spherical Bessel function. If C_{ii} is set to zero then these charges are uncorrelated in a random distribution and may even overlap. Here we use, C_{ii}=1, in which case the charged impurities are no closer than a distance R_{ii} where

$$R_{ii} = \left(\frac{3C_{ii}}{4\pi(N_A - N_D)}\right)^{1/3}. \tag{5.27}$$

Here again the integrand of P will be used to select the angle θ' between the initial and final electron wavevectors. Look-up tables are produced at the beginning of the Monte Carlo algorithm for the rate at each k and the rate at each (k, θ').

5.2.4 Interface Trap Scattering

Interface traps are interface states that readily trap conduction electrons and then subsequently serve as charged scatterers for other mobile conduction electrons. They are presently believed to be the cause of the low mobilities typically observed in

the inversion layers of SiC MOSFETs. The interface traps in SiC MOSFETs are believed to reside close to the semiconductor-oxide interface. These may be carbon complexes that seem to penetrate the semiconductor to some degree, or NITs located very close to the interface, maybe in the sub-oxide layer between the SiC and SiO_2 layers[101]. The states which act as NITs are likely Si-Si bonds in this sub-oxide which produce antibonding bands very close to the conduction band of SiC. Since at the present it seems that the NITs are the major source of mobility degradation in SiC MOSFETs, we will here assume that all the interface trap charge is located right at the semiconductor-oxide interface. The rate although will be presented in a format which can handle changes in the location of the trap density.

In the case of interface traps, the charge density is not uniform throughout the inversion layer. As a result we cannot develop the rate based on the 3-D interaction energy as in the cases of acoustic phonon, polar optical phonon, and ionized impurity scattering. Here we begin with the 2-D interaction energy term [112, 113, 91]

$$|M_s^{it}(Q)|^2 = \frac{e^4}{4\pi(2\pi)^3\epsilon^2\left(Q+q_{sc}\right)^2}\sum_t N_{it}(z_t)F_{ss}(Q,z_t)\left(1-\frac{2C_tJ_1(QR_t)}{QR_t}\right). \quad (5.28)$$

The sum here is over a specified number of layers t along the z direction into the semiconductor. A small distance is chosen for the interlayer distance. Here we used 1 angstrom. The contribution of each 2-dimensional layer of trapped charge $N_{it}(z_t)$ is then added to attain the total rate due to all of the trapped charge. The form factor here is the integrand of $F_{ss}(Q)$ in equation (5.15), but for the bare potential case without q_{sc}. It takes the form

$$F_{ss}(Q,z_t) = \pi\int_0^{z_{max}} |\zeta_s(z')|^2|\exp(-Q|z_t-z'|)dz'. \quad (5.29)$$

Since the rate is not developed directly from the 3D rate in the case of interface trap scattering, a screening wavevector appropriate for a quasi-2D system should be used. Other forms for q_{sc} where investigated, such as the result of the random-phase approximation in quasi-2D[91] and a perturbation solution for the screened coulomb potential in quasi-2D, but these did not agree with experiments as well as equation (5.13) did. So in this work the potential of a trapped interface charge is also screened using the inverse of the Debye length for q_{sc}.

The correlation factor for the charges is also included here for each layer, but in this case

$$R_t = \sqrt{\frac{C_t}{\pi N_{it}(z_t)}}. \tag{5.30}$$

Here C_t is set equal to 1 for each layer of charge corresponding to a uniform distribution of charges. We will also consider just one layer of interface traps right at the interface at z=0. The model could easily be extented to include a distribution of charges away from the interface. This was not found to alter the mobility significantly although. The rate for a nonuniform distribution of ionized impurities could also be easily developed with the method of this section.

The rate for scattering between a free conduction electron and a layer of trapped charge of density N_{it} directly at the semiconductor-oxide interface is

$$\Gamma_s^{it}(\varepsilon(k)) = \frac{e^4 N_{it} DOS_s(\varepsilon)}{4\pi(2\pi)^3\epsilon^2} P(k), \tag{5.31}$$

where again we assume elastic collisions. In this case the integral $P(k)$ is

$$P(k) = \frac{1}{2\pi}\int_0^{2\pi} d\theta \frac{F_{ss}(Q,0)\left(1-\frac{2C_0 J_1(QR_0)}{QR_0}\right)}{(Q+q_{sc})^2}. \tag{5.32}$$

Again as in the previous cases we collect look-up tables for $\Gamma_s^{it}(\varepsilon(k),\theta)$ and $\Gamma_s^{it}(\varepsilon(k)$ before the Monte Carlo simulations of electron transport proceed.

5.2.5 Surface Roughness Scattering

Another scattering mechanism that must be included is surface roughness scattering. Surface roughness encompasses the wide range of chemical disorder in the fabrication of surfaces between two dissimilar materials. Here we will use a simple but commonly used model to describe these surface effects [91, 114, 115]. At the MOS interface, the point of transition from $Si0_2$ to SiC along the z direction is described as a random fluctuation about the average surface position. This average is specified as the z=0 position in this work. The surface fluctuation, $\Delta z(\vec{\rho})$, depends on $\vec{\rho}$, the position vector along the interface, perpendicular to the z direction in Fig. 5.1. The potential $\phi(z)$ in the inversion layer is assumed to vary due to these fluctuations by an amount

$$\Delta\phi^{sr}(\vec{\rho},z) = \frac{d\phi(z)}{dz}\Delta z(\vec{\rho}). \tag{5.33}$$

The potential $\phi(z)$ here is the inversion layer potential determined self-consistently by the methods in Chapter 4. Since the effects of surface roughness are not uniform throughout the inversion layer volume, we will again develop the 2-dimensional interaction directly. The square of these matrix elements takes the form

$$|M_{ss'}^{sr}(Q)|^2 = \left|\int d\vec{\rho}\Delta z(\vec{\rho})\exp\left(-i\vec{Q}\cdot\vec{\rho}\right)\right|^2 \left|\int dz\zeta_{s'}^*(z)\frac{d\phi(z)}{dz}\zeta_s(z)\right|^2. \tag{5.34}$$

We use the self-consistent wavefunctions and inversion layer potential to determine the square of the effective field defined as

$$e^2 E_{eff}^2 = \left| \int dz \zeta_{s'}^*(z) \frac{d\phi(z)}{dz} \zeta_s(z) \right|^2, \tag{5.35}$$

where $\phi(z)$ is in eV.

The best fit to experiments is often obtained by taking $\Delta z(\vec{\rho})$ to be exponential in form according to [114]

$$\Delta z(\vec{\rho}) = \overline{\Delta z} \exp\left(-\rho/\Lambda\right), \tag{5.36}$$

where $\overline{\Delta z}$ is the average displacement of the surface and Λ is the average range of its spatial variation along $\vec{\rho}$. The square of the matrix element then becomes

$$|M_{ss'}^{sr}(Q)|^2 = \left(\frac{\pi e^2 E_{eff}^2 \left(\overline{\Delta z}\Lambda\right)^2}{1 + \left(\Lambda Q\right)^2 / 2} \right). \tag{5.37}$$

The terms $\overline{\Delta z}$ and Λ are parameters usually obtained by the fitting of transport simulations to experiment in cases where surface roughness scattering dominates, for example in cases when the inversion charge is large. In silicon MOSFETs, typical values are found to be $\overline{\Delta z}$=0.2nm and Λ=2.2nm. These length scales are related to the size of 2D islands of Si protruding from the surface prior to the deposition of SiO_2. As a rough approximation we will assume that such islands in SiC will have the same number of unit cells as for Si. In this case we will approximate the dimensions of these islands in SiC by simply scaling the corresponding value for Si to account for the unit cell of SiC. To illustrate this scaling we use the case of the (0001) orientation in 4H-SiC. Referring to Chapter 4, here the lattice periodicity along z is 1.9 times that of Si, while the lattice periodicity is $1/\sqrt{3}$ times that of Si

along the interface surface. We therefore use values of $\overline{\Delta z}$=0.38nm and Λ=1.2nm for (0001) oriented 4H-SiC.

Assuming that surface roughness causes only elastic intra-subband transitions, the rate is

$$\Gamma_s^{sr}(\varepsilon(k)) = \frac{e^2 E_{eff}^2 \left(\overline{\Delta z}\Lambda\right)^2 DOS_s(\varepsilon)}{2\hbar} P(k). \tag{5.38}$$

The integral over θ' here is

$$P(k) = \frac{1}{2\pi}\int_0^{2\pi} d\theta' \frac{Q}{(Q+q_{sc})\left(1+(\Lambda Q)^2/2\right)}, \tag{5.39}$$

where Q is given by equation (5.24) for elastic collisions. As in the case of polar optical phonon and interface charge scattering, the screening wavevector, q_{sc}, is given by equation (5.13). As in the previous cases, look-up tables are made for the rate at each value of (k, θ') , and also at each value of k by solving $P(k)$ numerically.

5.3 Monte Carlo Method

For the surface Monte Carlo simulations the general method of Chapter 1 is employed, but without a look-up table for the electronic band structure as in Chapter 3. Here we will discuss a few unique aspects of the surface Monte Carlo simulations. These are the inclusion of the self-consistent surface calculations of Chapter 4, the method for determining scattering events using look-up tables, and the determination of the mobility through a simulation of the diffusion constant.

5.3.1 Self-Consistent Calculations

Before starting the Monte Carlo simulations, the self-consistent properties of the inversion layer are determined perpendicular to the interface. The 2-dimensional mobile charge density N_{inv} and trapped interface charge density N_{it} are fixed at specified values. The subband energy structure E_s, the subband wavefunctions $\zeta(z)$, the inversion layer potential $\phi(z)$, and the average penetration of the electrons into the SiC inversion layer Z_{av}, are all determined using the self-consistent method of Chapter 4 with one exception. Due to the presence of trapped charge at the semiconductor/oxide interface, the surface field in equation (4.13) must now include N_{it}. This field now becomes

$$F_o = e\left[N_{inv} + (N_A - N_D)\, z_d + N_{it}\right]/\epsilon. \tag{5.40}$$

Since N_{it} is quite large in 4H-SiC, the effect on the subband structure is significant, raising the subband energies and increasing the subband energy spacing compared to the results of Chapter 4 when N_{it} was not present.

The results of the self-consistent calculations are then used to determine the various look-up tables for the scattering rates. These tables specify $\Gamma(k)$ and also $\Gamma(k, \theta')$ for each scattering mechanism. For the tables we use a mesh size of 50 for the magnitude of the electron wavevector k, which ranges from k=0 to k=$\pi/2a$. The mesh size for the scattering angle θ' is again 50, where θ' ranges from 0 to 2π.

5.3.2 Determination of Scattering Events

In the surface Monte Carlo simulations, an electron is allowed to drift freely in the applied field for a drift time (T_d). This time must be shorter than the relaxation time due to the scattering $T_r(\varepsilon(k))$, which is the inverse of the scattering rate. This time depends on the electron energy $\varepsilon(k)$ before the drift. For the simulations we used T_d=1x10^{-16} seconds when $10T_d<T_r$. In the case of low gate voltages and low temperatures Γ^{it} may be very large when the electron energy is very small. In these cases the drift time is shortened so that the condition $10T_d<T_r$ is still met.

After an electron drifts for a time T_d, the rates for every scattering mechanism for every allowed subband transition are calculated using the look-up table for the electron wavevector k. The determination of the rate from the look-up table can be explained with the following example for an arbitrary scattering mechanism n. If k lies between two mesh points $k1$ and $k2$ in the look-up table, the rate at k is then determined by

$$\Gamma^n(k) = \Gamma^n(k1)\frac{|k1-k|}{|k2-k1|} + \Gamma^n(k2)\frac{|k2-k|}{|k2-k1|}. \tag{5.41}$$

The rates are all summed up to attain the total rate $\Gamma_T(k)$. A random number with a flat distribution between 0 and 1 is then assigned. If this random number is less than $T_d\Gamma_T(k)$ a scattering event occurs and another flat random number $r2$ between 0 and 1 is then produced to pick the particular scattering event. The event n' which overlaps this second random number in the sum

$$\sum_{n=1}^{n'-1}\frac{\Gamma^n(k)}{\Gamma_T(k)} < r2 < \sum_{n=1}^{n'}\frac{\Gamma^n(k)}{\Gamma_T(k)}, \tag{5.42}$$

is then the stochastically selected event which scatters the electron.

The final energy after the scattering event is unchanged if an elastic event such as a Γ^{it} or Γ^{sr} mechanism is chosen. If polar optical scattering is chosen then the energy of the optical phonon involved, 120meV from Chapter 3, must be added (absorption) or subtracted (emission) from the initial electron energy. For acoustic phonon scattering the final energy is determined by the method of Basu[109]. In this method the magnitude of the phonon wavevector, q, is found from a flat random number r between 0 and 1 according to:

$$q = 2k\left(sin\left[\frac{r\pi}{2} \pm (r-1)sin\left(\frac{m_s u_l}{\hbar k}\right)\right] \pm \frac{m_s u_l}{\hbar k}\right). \tag{5.43}$$

Here, as defined previously, m_s is the effective mass parallel to the interface, u_l is the longitudinal velocity of sound in 4H-SiC, and the +(-) indicates absorption(emission). Once q is determined, the final electron energy is found from the relation

$$\varepsilon(k') = \varepsilon(k) + \hbar u_l q, \tag{5.44}$$

where we continue the notation of labeling ε as the electron energy, and k' as the magnitude of the electron wavevector after the scattering occurs.

As for the determination of the angle between the initial electron wavevector $\vec{k}$ and the final wavevector $\vec{k'}$, a uniform probability between 0 and 2π is used for acoustic phonon scattering. The angle can then be chosen with a random number r according to θ'=θ+ $2\pi r$. In the case of the other scattering mechanisms the look-up table in (k, θ') is used to find θ'. To illustrate the procedure we take the case of interface trap scattering. Here the (k, θ') look-up table contains the integrand values in equation (5.32), which we will label as $P(k, \theta')$. The angle θ' is divided up into

increments $d\theta'$ in the look-up table. We Label the partial sum S_{n1} as

$$S_{n1} = \sum_{n=1}^{n=n1} |P(k, nd\theta')|/S_T. \tag{5.45}$$

where S_T is the sum of $|P(k, nd\theta')|$ over all of the 50 mesh points. The index $n1$ can be identified as bounding the final angle θ' if the criteria

$$S_{n1-1} < r < S_{n1}, \tag{5.46}$$

is met. Here again r is a flat random number between 0 and 1. Once $n1$ is found, the final angle θ' can be found according to the expression:

$$\theta' = n1d\theta \frac{|S_{n1} - r|}{|S_{n1} - S_{n1-1}|} + (n1 - 1)d\theta \frac{|S_{n1-1} - r|}{|S_{n1} - S_{n1-1}|}. \tag{5.47}$$

This procedure is followed for scattering by polar optical phonons, interface traps, and surface roughness. The final electron wavevector $\vec{k'}$ is then assigned at an angle of $\theta + \theta'$, where θ is the angle before the scattering event. Angles are defined so that an angle of 0 lies along the direction of the driving field.

5.3.3 Determination of the Mobility

Monte Carlo simulations at low-fields often take a long time to converge, especially in the case where the primary scattering mechanism is elastic. This is the case here where scattering from charged interface traps dominates the total scattering rate. Here we determine the low-field mobility (μ) from a simulation of the diffusion constant (D). Once the diffusion constant is obtained, the mobility is found using the Einstein relation

$$\mu = \frac{eD}{k_B T}. \tag{5.48}$$

The method we use requires the calculation of the velocity autocorrelation function C[38]. The diffusion constant is found through the relation

$$D = \int C(t)dt = \int \langle \delta\vartheta(t')\delta\vartheta(t'+t)\rangle \, dt, \tag{5.49}$$

where the angle brackets indicate an ensemble average over time t' and $\vartheta(t')$ is the velocity at time t'. The fluctuation of the velocity from the average velocity at time t' is given by $\delta\vartheta(t')$. The average velocity is the drift velocity ϑ_d. The autocorrelation function can readily be reduced according to

$$C(t) = \langle [\vartheta(t') - \vartheta_d]\,[\vartheta(t'+t) - \vartheta_d]\rangle = \langle \vartheta(t')\vartheta(t'+t)\rangle - \vartheta_d^2. \tag{5.50}$$

To determine $C(t)$ a correlation time T_c is chosen and broken into N_c intervals. Each interval lasts for a time ΔT_c=T_c/N_c. As the transport simulation proceeds, the velocity is stored at each time interval $i\Delta T_c$ where $i = 1, ..., N_c$. Once $i = N_c$, or equivalently $i\Delta T_c$=T_c, the product $\vartheta(i\Delta T_c)\vartheta((i-j)\Delta T_c)$ is stored for each $j = 1, ..., N_c$. The simulation then repeats for a fresh time T_c. This process continues N_T times for a total time of $N_T T_c$. Afterwards the total product $\vartheta(i\Delta T_c)\vartheta((i-j)\Delta T_c)$ is averaged over i and the autocorrelation function is found as

$$C(j\Delta T_c) = \overline{\vartheta(i\Delta T_c)\vartheta((i-j)\Delta T_c)} - \vartheta_d^2, \tag{5.51}$$

The drift velocity, ϑ_d, is determined using the methods in Chapter 3. The diffusion constant is then found by summing $C(j\Delta T_c)$ over all times $j\Delta T_c$.

The method requires that T_c be long enough so that $C(t)$=0, for all times longer than T_c. Here we broke the correlation time into steps of duration ΔT_c=1x10^{-14}s.

Taking $50,000$ correlation steps, T_c is 5x$10^{-9}s$. We then found convergence by proceeding through N_T=2000 steps of time T_c.

5.4 Results for (0001) 4H-SiC

5.4.1 Analysis of Data

In order to simulate electron transport at the MOS interface in 4H-SiC, we use the experimental data of Saks and Agarwal (SA)[11]. Here the Hall mobility was determined for a MOS Hall bar. Capacitance and gate voltage measurements can typically be used to obtain the total charge density in the MOS channel under inversion conditions, but cannot distinguish between the free and trapped charge densities present. The advantage of using Hall measurements is the ability to accurately determine the mobile free charge density N_{inv} from measurements of the Hall voltage. The density of trapped charge can then be found by subtracting N_{inv}, from the total inversion layer charge.

The experiments of SA were performed on polysilicon gated MOS hall bars. A 10 micron epitaxial later of lightly p-doped (1x$10^{16}cm^{-3}$) 4H-SiC was laid onto a heavily p-doped (P^+) 4H-SiC substrate. Then heavily doped n-type (N^+) regions for the source and drain contacts were produced by ion implantation of nitrogen. The wafers were then annealed at relatively low temperatures to reduce step bunching of 4H-SiC. Following this a $31nm$ oxide was deposited and then reoxided to reduce the interface trap density. A layer of phosphorus-doped poly-silicon was laid down

onto the oxide for the gate, and nickel contacts were made to the source and drain N^+ regions. The MOS hall bar is shown in Fig. 5.2.

By measuring the Hall voltage (V_H) and the drain current (I_d) as a function of the gate voltage (V_G), Saks and Agarwal (SA) were able to determine the V_G-dependent mobile change density in the inversion layer (N_{inv}). These results were reported in terms of the variation of N_{inv} per one volt change in the gate voltage, a quantity we will label as $\Delta N_{inv}(V_G)$. These results are reproduced in Fig. 5.3 for temperatures of $200K$, $297K$, and $440K$. For a fixed gate voltage, ΔN_{inv} is found to increase with temperature. We also show in Fig. 5.3 our analytical fits used in the Monte Carlo simulations:

$$\Delta N_{inv} = \begin{cases} \left[\chi_1(T)\left(\frac{V_G}{12V}\right)^2 + \chi_2(T)\left(\frac{V_G}{12V}\right) + \chi_3(T)\right] \ 10^{10} cm^{-2} & V_G < 12\text{V} \\ \left[\chi_1(T) + \chi_2(T) + \chi_3(T)\right] \ 10^{10} cm^{-2} & \text{else} \end{cases} \tag{5.52}$$

The values for the coefficients $\chi_1 - \chi_3$ are given in Table 5.1.

To determine the charge concentration $N_{inv}(V_G)$, we use standard theoretical methods for the onset of inversion in MOSFETs [116]. Here the total charge density in the channel (N_T) is found from the oxide capacitance per unit area (C_{ox}) and the threshold voltage for the onset of inversion (V_T) according to:

$$N_T(V_G) = \frac{C_{ox}}{e}\left(V_G - V_T\right), \tag{5.53}$$

where

$$\Delta N_T = C_{ox}/e = \Delta N_{inv} + \Delta N_{it}. \tag{5.54}$$

The term ΔN_{it} is the change in trapped charge per one volt change in gate voltage. In Fig. 5.4a we show the experimental results for the drain vs. gate voltage. It

is clear that there is a dramatic increase in the threshold voltage as the temperature decreases. The threshold voltage appears to vary as T^{-2}. In Si MOS surfaces, where there is significantly less trapped charge, the threshold voltage tends to increase much slower as the temperature decreases, with an approximate dependence of T^{-1}[117]. It is therefore very likely that the behavior of V_T in 4H-SiC is due to the large number of charges that are trapped in the inversion layer. The procedure we use to determine V_T from the SA experiments is to weight each drain current curve so that the saturation values are the same, then the threshold voltage is determined as the gate voltage when the drain current is about 1/400th of its saturation value. This is shown in Fig. 5.4b. We find that the extracted gate voltages agree very well with the formula:

$$V_T(T) = 1.5 + \left(\frac{424}{T}\right)^2 V. \tag{5.55}$$

This form, essentially a $1/T^2$ dependence with an offset, agrees very well with the experiments of Harada et al.[118], though they observed an offset in the range of $2-3$ instead of 1.5.

Once obtaining V_T we can then reasonably approximate the free charge density as

$$N_{inv}(V_G, T) = \Delta N_{inv}\left(V_G - V_T(T)\right), \tag{5.56}$$

were the charge density is zero below the threshold and then increases linearly with V_G above the threshold. If we assume that the uncharacteristicly large increase in the threshold voltage with decreasing temperature is a result of the interface traps only, we can identify the threshold voltage at large temperatures as the threshold

voltage for a trap-free surface. For gate voltages in the range of $1.5<V_G<V_T(T)$ in this model, there will be a build-up of trapped charge of density $dN_{it}(T) = (V_T(T) - 1.5)\, C_{ox}/e$. We therefore model the occupied trap density as

$$N_{it}(V_G, T) = (C_{ox}/e - \Delta N_{inv})\,(V_G - V_T(T)) + dN_{it}(T). \tag{5.57}$$

In Fig. 5.5 we plot the free charge density and the trapped charge density using the results above. These densities are used in the Monte Carlo simulation of electron transport at the 4H-SiC/oxide interface. The density of surface traps increases with decreasing temperature while the density of free electrons decreases. This can be explained by the observation of a large density of surface trap states near the conduction band edge[16]. As the temperature drops, the occupation of states near the Fermi level increases relative to those further above. For a fixed total charge in the channel, the Fermi energy moves up towards the band edge with decreasing temperature, increasing the trapped charge density and decreasing the free charge density.

5.4.2 Simulation Results

Using our analytical formulas for N_{inv} and N_{it} in equations (5.56) and (5.57), we perform a Monte Carlo simulation of electron transport along the (0001) SiC-SiO_2 interface. Electron mobilities are determined for a low field of $5kV/cm$ parallel to this interface (in the (0001) plane), as the gate voltage V_G is increased. In Fig. 5.6, the results for temperatures of $200K$, 297K, and $440K$, are shown. The results agree with the average Hall mobilities observed by SA, which are roughly $\approx$ 15,

25, and 40 cm^2/Vs at temperatures of $200K$, 297K, and $440K$ respectively. In Fig. 5.6 we see that the mobility actually increases with temperature for all the simulated gate voltages. For a Si/SiO_2 interface with a relatively low density of interface traps, the low-field mobility characteristically decreases with temperature above 300K. This decrease is due to an increase in acoustic phonon scattering and approximately depends on the inverse square of the lattice temperature (T^{-2})[117]. In the case of (0001) oriented SiC, the temperature dependence of the rate indicates that the scattering of electrons from trapped interface charges, not from acoustic phonons, is the dominant scattering mechanism for both high and low temperatures. This can be readily seen from the plots of the scattering rate for electrons in the 1st subband in Fig. 5.7.

The rates for scattering from interface traps (Γ^{it}), surface roughness (Γ^{sr}), acoustic phonons (Γ^{ac}), and polar optical phonons (Γ^{po}), are all shown in Fig. 5.7. The rate for ionized impurity scattering is included in Γ^{it}, but since it is small compared to the scattering from trapped electrons, we still label the combined rate as Γ^{it}. We see that Γ^{it} is very large and essentially dominates the other scattering mechanisms within the range of gate voltages and temperatures simulated in Fig 5.7. It is larger at lower temperatures where the number of trapped electrons is larger and the number of free electrons is lower. Both trends, seen in Fig. 5.5, increase the rate. The smaller the number of free electrons N_{inv} the weaker the screening of the electric field from the trapped electrons. This corresponds to a larger scattering rate. Furthermore, as the gate field increases, there is a decrease in Γ^{it}. This occurs since the increase of the screening charge with increasing V_G dominants the increase

in the trapped charge N_{it}.

As for the other rates, the phonon scattering rates increase with increasing temperature. We see that Γ^{sr}, decreases with increasing temperature due to more effective screening, and increases with increasing gate potential since the effective field increases. At reasonably low temperatures, it is likely that Γ^{sr} will eventually rise with increasing V_G to become the dominant rate. Here a mobility peak should occur, at a particular value of V_G. This gate voltage could possibly be used to determine the surface roughness parameters $\overline{\Delta z}$ and Λ. It is most likely that this critical point in the mobility could have been identified if the experimental results of SA were extended to higher gate voltages. Such peaks at large gate voltages have been observed in the experiments of Harada et al. [118].

To simulate the low-field mobility as a function of temperature T, we need to determine $N_{inv}(T)$ and $N_{it}(T)$ at a number of temperatures. By fitting to the SA results at temperatures of $200K$, $297K$, and $440K$, we find the following analytical formulas for gate voltages of V_G=$8V$ and V_G=$12V$:

$$N_{it}(T, V_G) = \left[\chi_4(V_G) + \left(\frac{T - 200K}{200K}\right)\right] \ 10^{12} cm^{-2}, \tag{5.58}$$

and

$$N_{inv}(T, V_G) = \left[\chi_5(V_G) + \chi_6(V_G)\left(\frac{T - 200K}{200K}\right)^{3/2}\right] \ 10^{10} cm^{-2}. \tag{5.59}$$

The fitting parameters $\chi_4 - \chi_6$ are given in Table 5.1. These fits are shown in Fig. 5.8. The SA experiments do not extend beyond T=440K, but we want to simulate higher temperatures. We have therefore extrapolated the fits of $N_{inv}(T)$ and $N_{it}(T)$

to higher temperatures assuming the same trends as found in the SA data range below T=440K.

The Monte Carlo simulations over a wide temperature range are shown in Fig. 5.9, for gate fields of $8V$ and $12V$. We find that the mobility increases linearly ($\propto T$) with temperature. This agrees with the results of Saks and Agarwal (SA), also shown in Fig. 5.9. Experiments by Matsunami et al. [105] although have indicated a temperature rise $\propto T^{2.6}$. In this work a very large threshold voltage of $7.78V$ was measured at 300K. Since the value extracted from the SA experiments, $3.5V$, was much smaller, the sample of Matsunami et al. likely contained a much larger density of interface traps. This would indicate that the exponent n for the temperature dependence of the mobility (T^n), may very likely increase in samples were there tends to be a larger number of trapped charges at the interface.

It is important to note that no adjustable parameters are used in the Monte Carlo simulations. Electron-phonon coupling constants and the polar field are fixed according to the results of Chapter 3 by fitting to experimental data in the bulk. There are no adjustable parameters within the interface charge scattering rates. The parameters for surface roughness scattering were obtained by scaling the results from Si. Since we find that this is not a dominant scattering mechanism in the case here, where a large number of charges are trapped at the interface, we feel this is justified. As mentioned, it might be possible to determine these roughness parameters from the mobility peaks at high gate voltages.

5.5 Results for $(11\overline{2}0)$ 4H-SiC

It has been determined experimentally by Yano, Hirao, Kimoto and Matsunami (YHKM) that if the $(11\overline{2}0)$ instead of the (0001) surface of 4H-SiC is used for the interface with SiO_2, the interface trap density is significantly reduced[16]. This can be seen in Fig. 5.10, were we plot the experimental results of YHKM. Now to compare the simulated Monte Carlo mobility along the (0001) surface of 4H-SiC with that along the $(11\overline{2}0)$ surface, we need to determine how the density of trapped states changes. We accomplish this by using the SA results for the (0001) surface as in the last section, but we now scale the density of trapped states according to

$$N_{it}^{(11\overline{2}0)}\Big|_{SA} = \left(\frac{N_{it}^{(11\overline{2}0)}}{N_{it}^{(0001)}}\right)\Big|_{YHKM} N_{it}^{(0001)}\Big|_{SA}. \tag{5.60}$$

This can be used to obtain $N_{it}^{(11\overline{2}0)}\Big|_{SA}$ for comparision with the experiments of Saks and Agarwal (SA). This method enables us to estimate this density in a way which is as independent of sample processing differences as possible. The differences in the processing of the two orientations in the work of Yano et al. (YHKM) is assumed to be at a minimum. To determine the trapped interface charge densities from the YHKM experiments, we use the experimental density of traps $DOS_{it}(E)\Big|_{YHKM}$ in Fig. 5.10. The result for each surface (X), where (X) is (0001) or $(11\overline{2}0)$, is

$$N_{it}^{(X)}\Big|_{YHKM} = \int_0^{E_s+E_g} f(E) DOS_{it}^{(X)}(E)\Big|_{YHKM} dE. \tag{5.61}$$

Here the energy integrals run from the valence band edge at $E = 0$, to the relative energy of the first subband. With a bulk gap energy of E_g=3.2eV for 4H-SiC, the energy of the first subband, relative to the valence band edge, is $E_s + E_g$. The term

$f(E)$ is the Fermi-Dirac equilibrium distribution function

$$f(E) = \left(1 + .5 \exp\left(\frac{E - (E_f + E_g)}{K_b T}\right)\right)^{-1}, \tag{5.62}$$

where E_f is the Fermi energy calculated self-consistently with the adjusted densities N_{inv} and N_{it} for the $(11\overline{2}0)$ orientation. Contary to the case for the (0001) orientation, N_{it} will not be fixed during the self-consistent calculations in the inversion layer , since it depends on E_f. As in Chapter 4, E_f is defined relative to the bulk conduction band edge at E_g. To evalue equation (5.61), we use the following analytical fits to $DOS_{it}(E)\Big|_{YHKM}$ in Fig. 5.10

$$log_{10}(DOS_{it})\Big|_{YHKM} = \chi_7(E) E^{\chi_8} + \chi_9, \tag{5.63}$$

where the density of states is in units of cm^{-2}. The results for the fitting constants χ, which depend on the surface orientation and energy, are given in Table 5.1.

We also adjust the SA results for the mobile electron density N_{inv}. This occurs through the adjustment of the threshold voltage in equation (5.55). Since the number of trapped charges decreases on going from the (0001) to the $(11\overline{2}0)$ surface, V_T should approximately change according to

$$V_T(T) = 1.5 + \left(\frac{424}{T}\right)^2 \left(\frac{N_{it}^{(11\overline{2}0)}}{N_{it}^{(0001)}}\right)\Bigg|_{YHKM} V. \tag{5.64}$$

The Fermi energy used here in the calculation of the ratio of trapped charge densities is the value that can be used along with $DOS_{it}^{(0001)}\Big|_{YHKM}$ to obtain the build-up of trapped interface charge before inversion in the SA experiments. This requires

$$N_{it}^{(0001)}\Big|_{YHKM} = \left(\frac{424}{T}\right)^2 C_{ox}/e. \tag{5.65}$$

We therefore obtain for the threshold voltage in $(11\overline{2}0)$ 4H-SiC

$$V_T^{(11\overline{2}0)}(T) = 1.5 + \frac{N_{it}^{(11\overline{2}0)}}{C_{ox}/e}\Big|_{YHKM}, \tag{5.66}$$

with $N_{it}^{(11\overline{2}0)}\Big|_{YHKM}$ evaluated at the formentioned Fermi energy. We find that the threshold voltages for the $(11\overline{2}0)$ orientation are significantly less and can be accurately model as

$$V_T^{(11\overline{2}0)}(T) = 3.5 - \frac{T}{440}. \tag{5.67}$$

The mobile charge density in equation (5.59) for the (0001) orientation is then adjusted according to

$$N_{inv}^{(11\overline{2}0)}(T, V_G) = N_{inv}^{(0001)}(T, V_G)\left[\frac{V_G - V_T^{(11\overline{2}0)}(T)}{V_G - V_T^{(0001)}(T)}\right], \tag{5.68}$$

where $N_{inv}^{(0001)}$ and $V_T^{(0001)}$ are given by equations (5.59) and (5.55) respectively.

In Fig. 5.11 we show the result of our Monte Carlo simulations of low-field electron mobility for a large temperature range. We find that the mobility for the $(11\overline{2}0)$ orientation, using the adjusted charge densities, is much larger than that of the (0001) orientation. Mobilities as large as $90cm^2/Vs$ at room temperature are found. This agrees very well with the experimental results for this orientation where a value of $95.9cm^2/Vs$ for current along the <0001> crystalline direction and $81.7cm^2/Vs$ along the $<1\overline{1}00>$ direction where obtained for $(11\overline{2}0)$ oriented surfaces[105]. In our simulations we assumed a spherical conduction band since not current direction was specified in the SA experiments. This approximation is still reasonable for comparison with the $(11\overline{2}0)$ experiments since the effective masses along <0001> and $<1\overline{1}00>$ are very similar. Our results are close to the average

of the two experimental results. We find that the temperature falls of as $T^{-.5}$. The experiments of Matsunami et al. found a fall off proportional to $T^{-2.2}$ however[105].

We also determine the mobility for electron transport in the (0001) plane, but fix N_{it} and N_{inv} equal to those used in the simulations of the $(11\overline{2}0)$ surface. As seen in Fig. 5.11, the results are very similar to the simulations for the $(11\overline{2}0)$ orientation. This occurs since the surface band structure of the two orientations is very similar, even though the $(11\overline{2}0)$ orientation has two subband ladders while the (0001) orientation has but one. There are two main reasons for this similarity. The first is a result of the principle-axes effective masses, m_1 and m_2 and m_3 in the notation of Chapter 4, which vary little between the two orientations. The second reason is the very small spacing between the two subband ladders in the $(11\overline{2}0)$ orientation. We see this in Fig. 5.12, where the low-lying subband electronic structure of the two orientations is very similar. Here in Fig. 5.12 there is no density of trapped charge at the interface, but if we did included trapped charge, the subband structure would still be similar for the two orientations. In Fig. 5.13 we also see that the relative occupancy of each $(11\overline{2}0)$ ladder falls very closely to their degeneracy contributions 2/3 and 1/3, even when inversion is weak. This occurs since the energy spacing between the ladders is very small. One material property, directly related to the subband structure, is the average distance, Z_{av}, that the inversion layer mobile electrons penetrate into the semiconductor. The larger this distance the larger the mobility since scattering from both the occupied traps and the surface roughness will be weakened. Since the fraction of occupied higher energy subbands is very similar in each orientation, we see in Fig. 5.14 that Z_{av} is also very

similar for the two orientations of 4H-SiC. So based on a comparison of the self-consistent electronic structure calculation at the interface, it is clear to see why the mobility for both (0001) and $(11\overline{2}0)$ 4H-SiC would be similar if the same density of trapped charge where present at the surface.

5.6 Chapter Summary

Using the results of experimental data[11] for free and trapped charge densities in the (0001) orientation, low-field mobilities were simulated. The simulation results were found to agree qualitatively very well with experiments. The mobility was found to rise linearly with increasing temperature, in agreement with experiments[11].

We also simulated transport along the inversion layer of a $(11\overline{2}0)$ oriented 4H-SiC/SiO_2 interface. We found that the reduction in electron traps near the interface lead to a dramatic improvement in the mobility. The mobility increased from $\approx$ 0-40cm^2/Vs in the (0001) orientation to $\approx 90cm^2/Vs$ in the $(11\overline{2}0)$ orientation. We also found that the mobility decreased with increasing temperature. These results agreed well with experiments on $(11\overline{2}0)$ oriented 4H-SiC[105].

We also found that a commensurate reduction in the density of interface traps for the (0001) orientation lead to mobilities that were essentially equivalent to those simulated for the $(11\overline{2}0)$ orientation. An analysis of the electronic subband structure revealed a strong similarity amongst the two orientations. This similarity means that if the density of interface traps could be reduced in the (0001) orientation, the transport properties should be very similar to those of the $(11\overline{2}0)$ orientation.

T=200K	T=297K	T=440K
χ_1=17	χ_1=17	χ_1=0
χ_2=0	χ_2=0	χ_2=32
χ_3=-4.0	χ_3=-0.72	χ_3=-5.5
V_G=8V	V_G=12V	(0001)
χ_4=4.4	χ_4=6.5	χ_7=2.63x10^{-5}
χ_5=7.2	χ_5=78	χ_8=10
χ_6=62	χ_6=70	χ_9=10.64
$(11\overline{2}0)(E > 3eV)$	$(11\overline{2}0)(2.6eV \leq E \leq 3eV)$	$(11\overline{2}0)(E < 2.6eV)$
χ_7=4.69	χ_7=2.20	χ_7=1.07
χ_8=1	χ_8=1	χ_8=1
χ_9=-2	χ_9=6.1	χ_9=9

Table 5.1: Fitting parameters χ

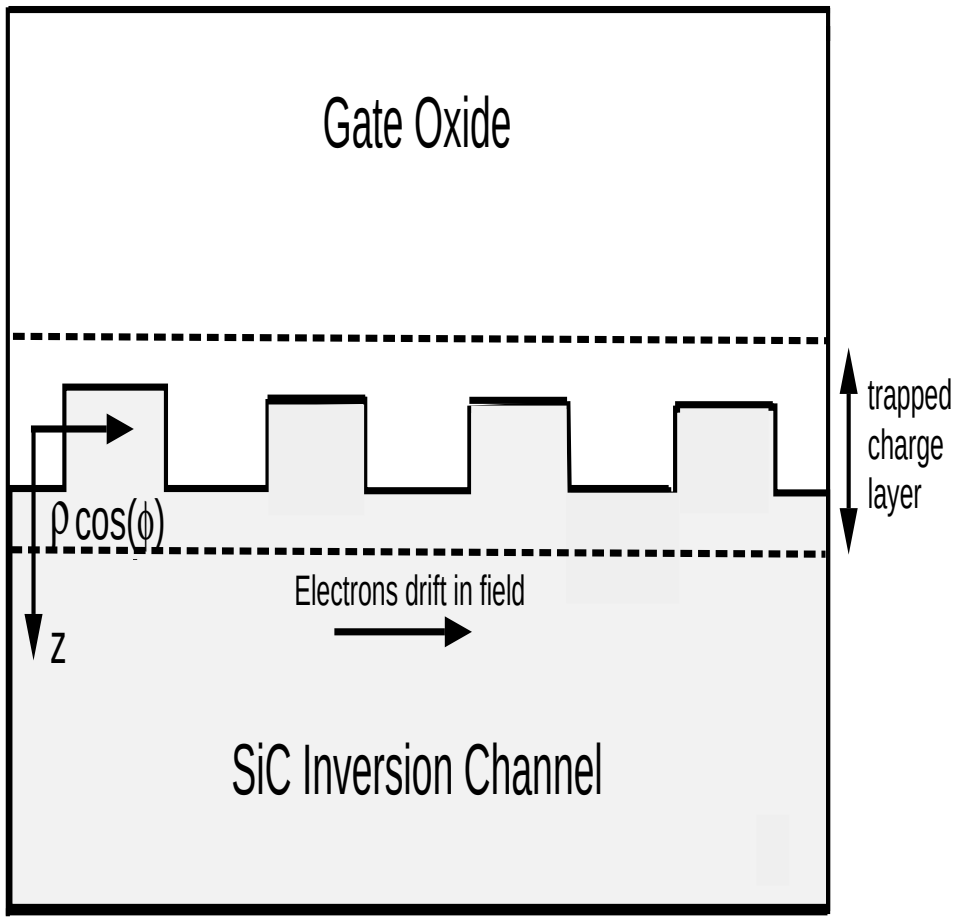

Figure 5.1: SiC/oxide interface

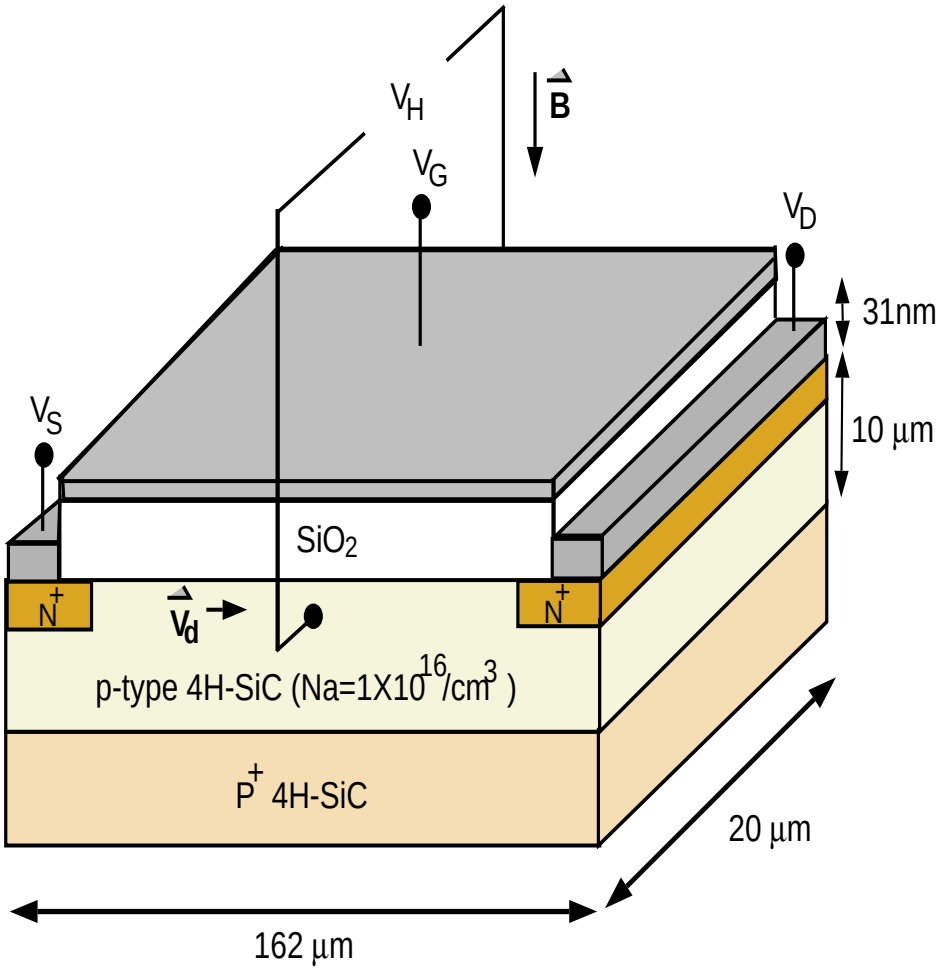

Figure 5.2: 4H-SiC MOS Hall bar

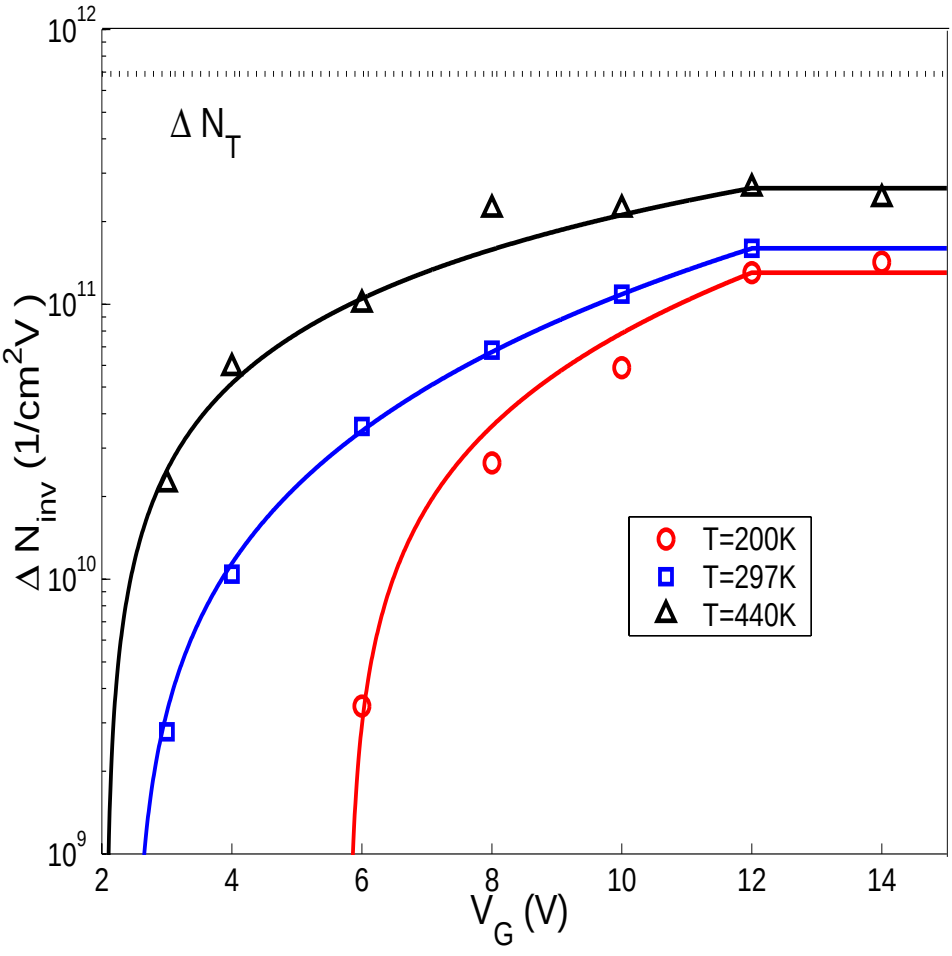

Figure 5.3: Change in inversion layer mobile electron concentration N_{inv} per one volt change in the gate voltage V_G for the Hall experiments of Saks and Agarwal (SA)[11]. Temperatures of $200K$, $297K$, and $440K$ are shown. The solid lines are the analytical fits used in our Monte Carlo calculations. Here ΔN_T is the oxide capacitance C_{ox}/e, the expected result for ΔN_{inv} in the absence of trapped charge.

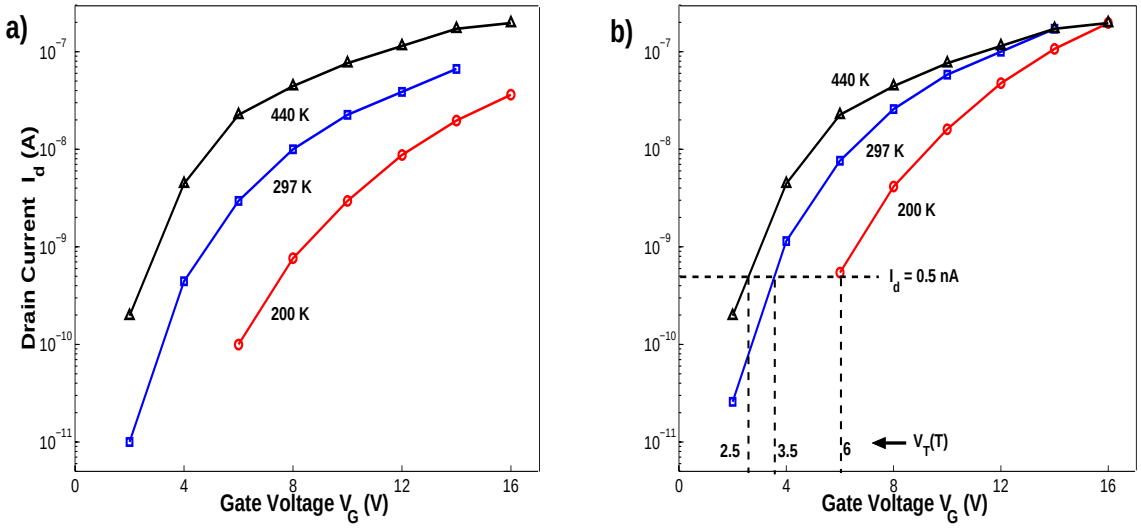

Figure 5.4: In a) have experimental drain current vs. gate voltage in a 4H-SiC MOS Hall bar at temperatures of $200K$, $297K$, and $440K$ [11]. In b) the currents are scaled for a determination of the threshold voltage V_T which is consistent amongst the three temperatures.

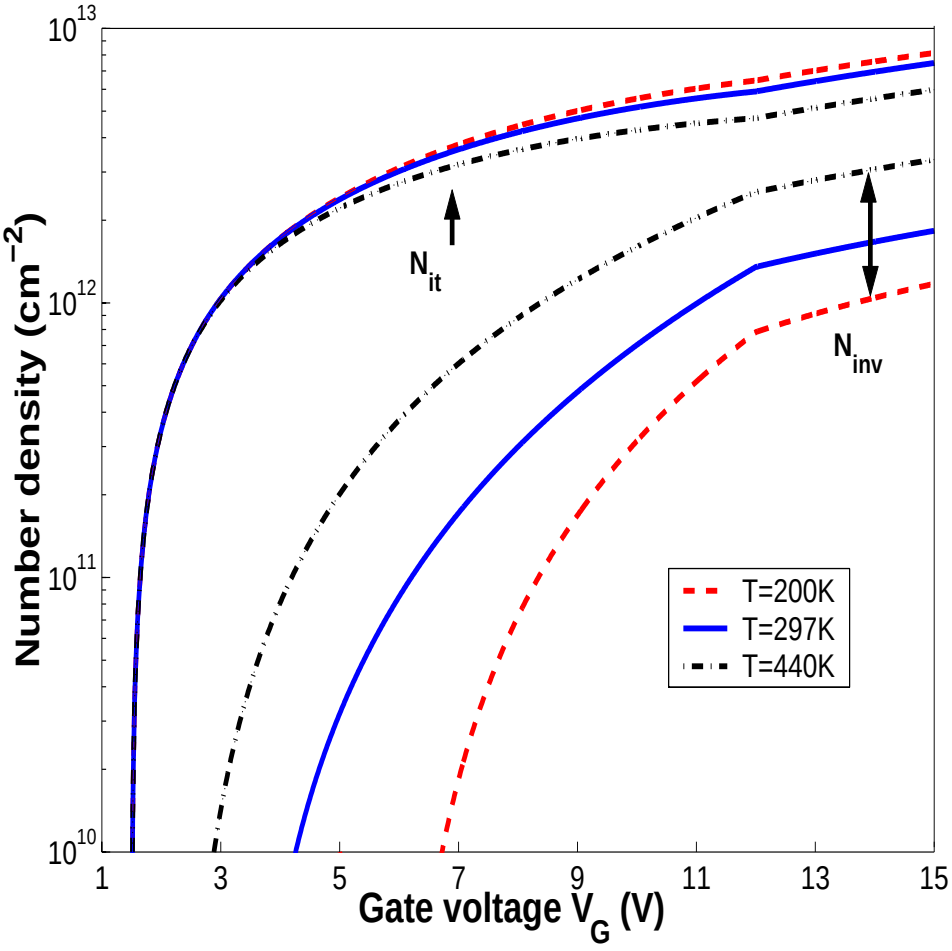

Figure 5.5: Model for mobile interface charge density and trapped interface charge density vs. gate voltage for temperatures of $200K$, $297K$, and $440K$. .

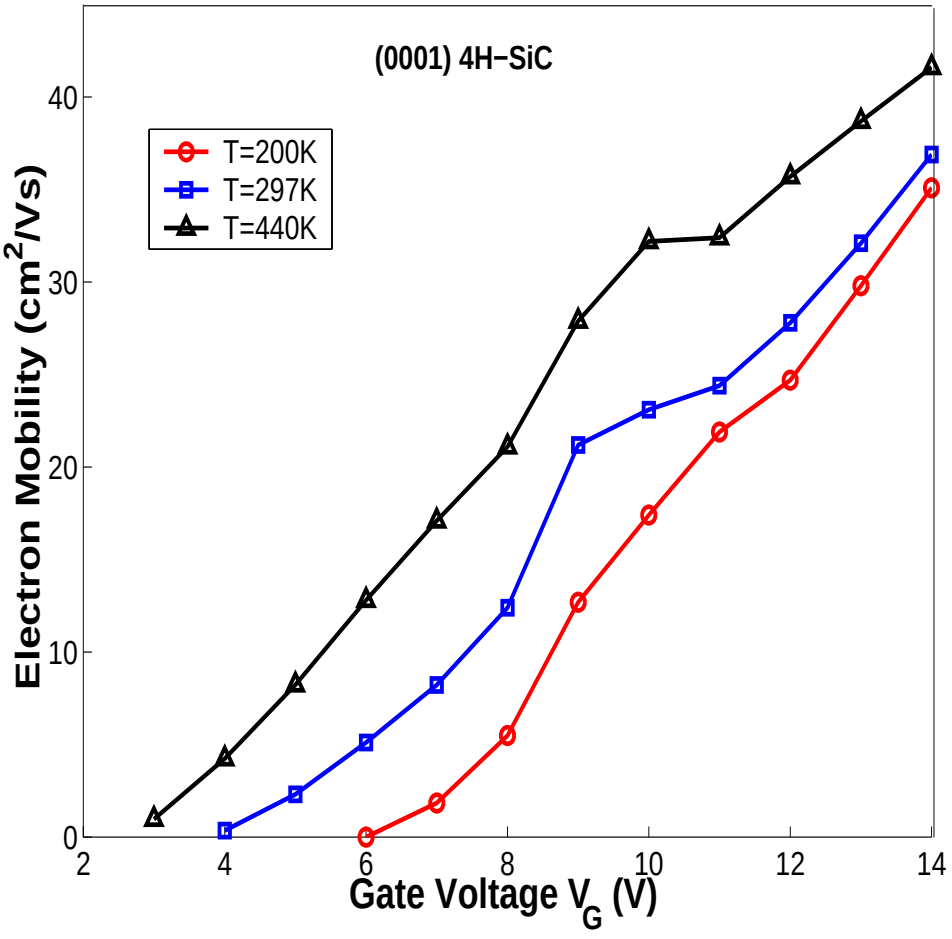

Figure 5.6: Results of Monte Carlo simulations of the low-field electron mobility in (0001) 4H-SiC for temperatures of $200K$, $297K$, and $440K$. Gate voltages correspond to the experiments of SA[11].

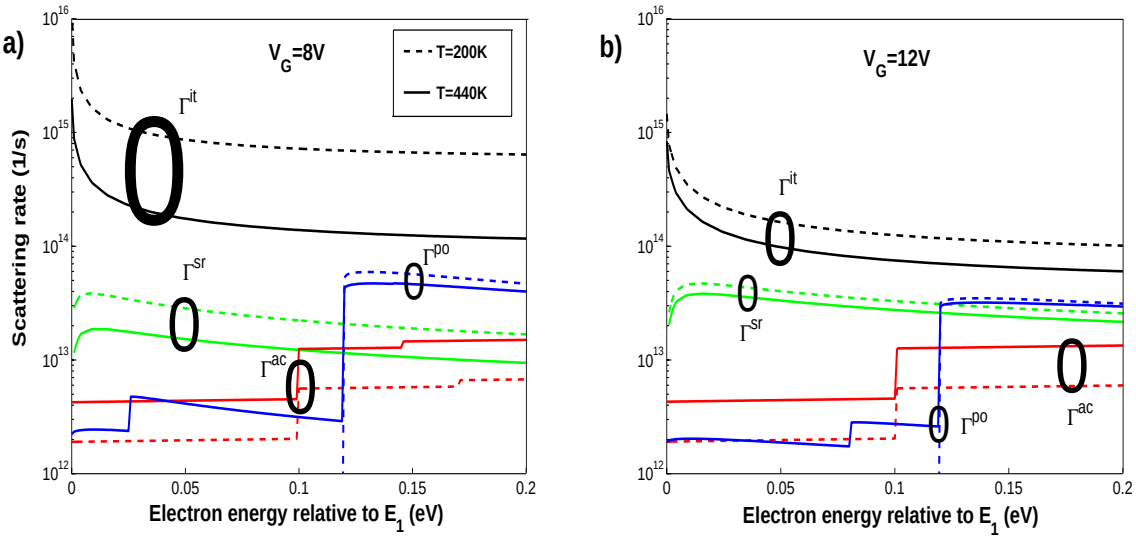

Figure 5.7: Scattering rate for an electron in the 1st subband of (0001) 4H-SiC. In a) the rates are for a gate voltage of $8V$ and temperatures of $200K$, and $440K$. In b) the rates are for a gate voltage of $12V$ and temperatures of $200K$, and $440K$.

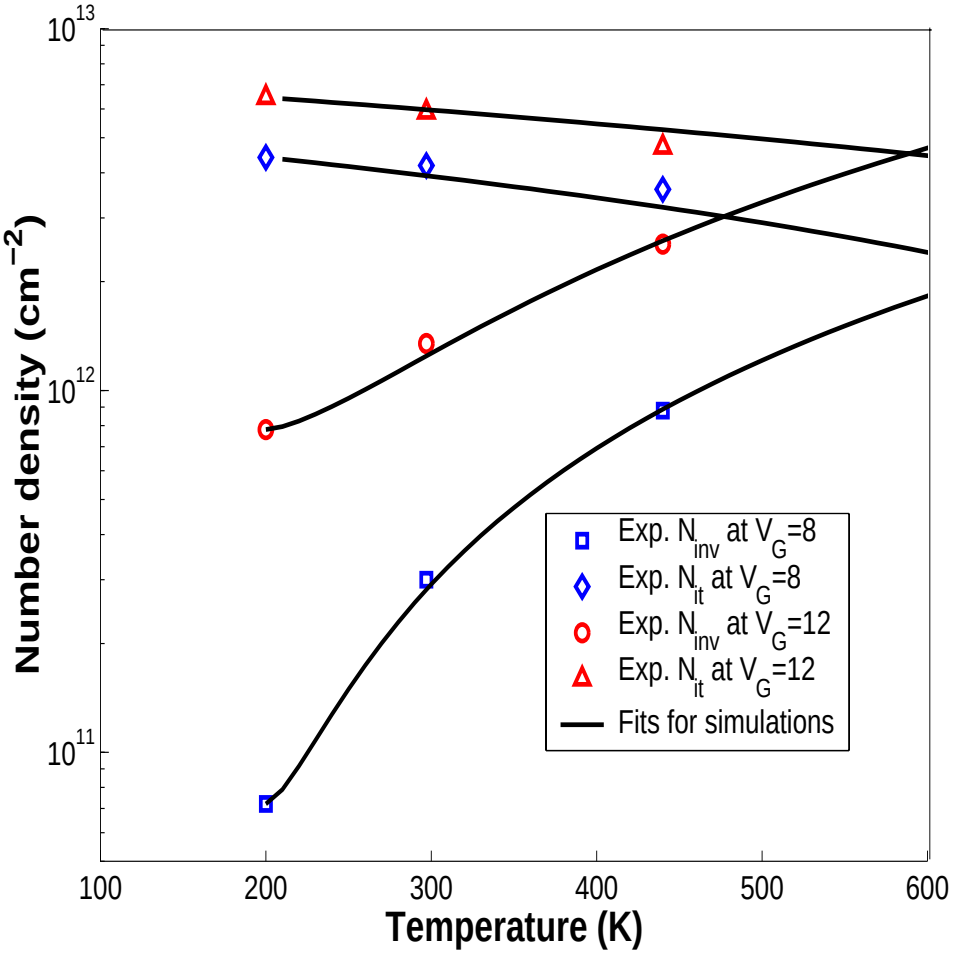

Figure 5.8: Fits for the free carrier density (N_{inv}) and trapped carrier density (N_{it}) to SA experiments[11] as a function of temperature.

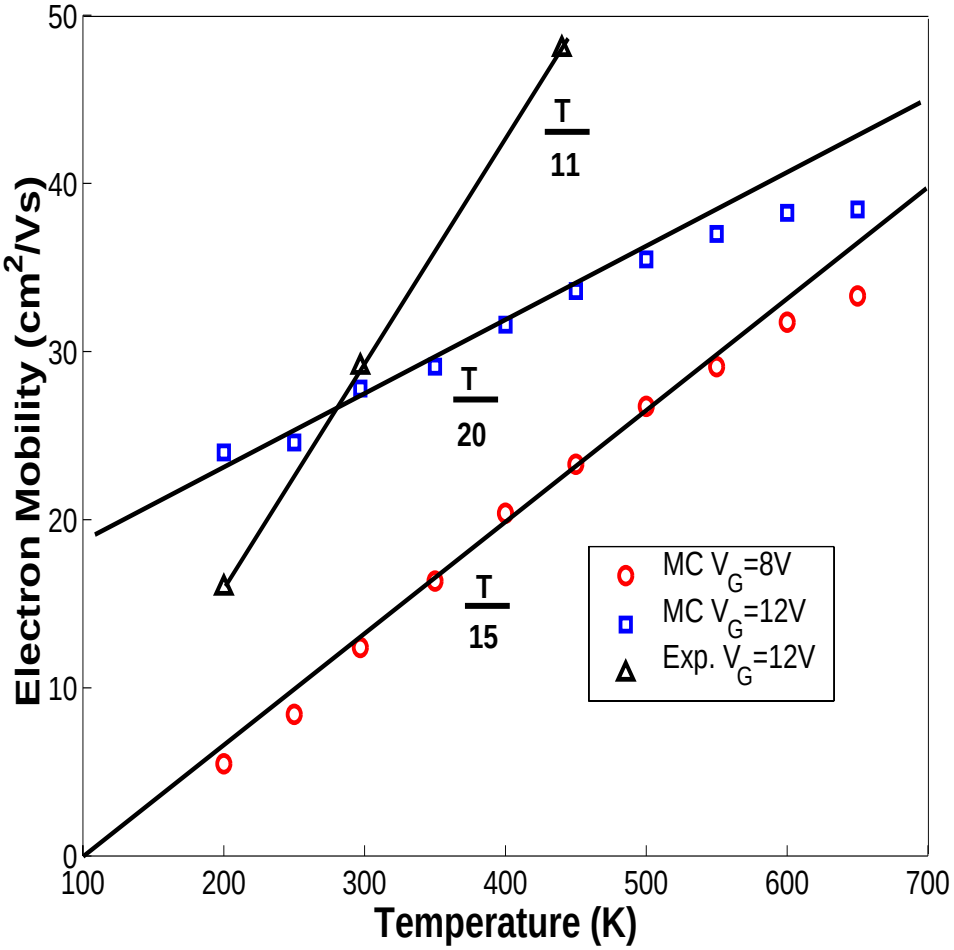

Figure 5.9: Experimental and Monte Carlo mobility vs. temperature for gate voltages of 8V, and 12V.

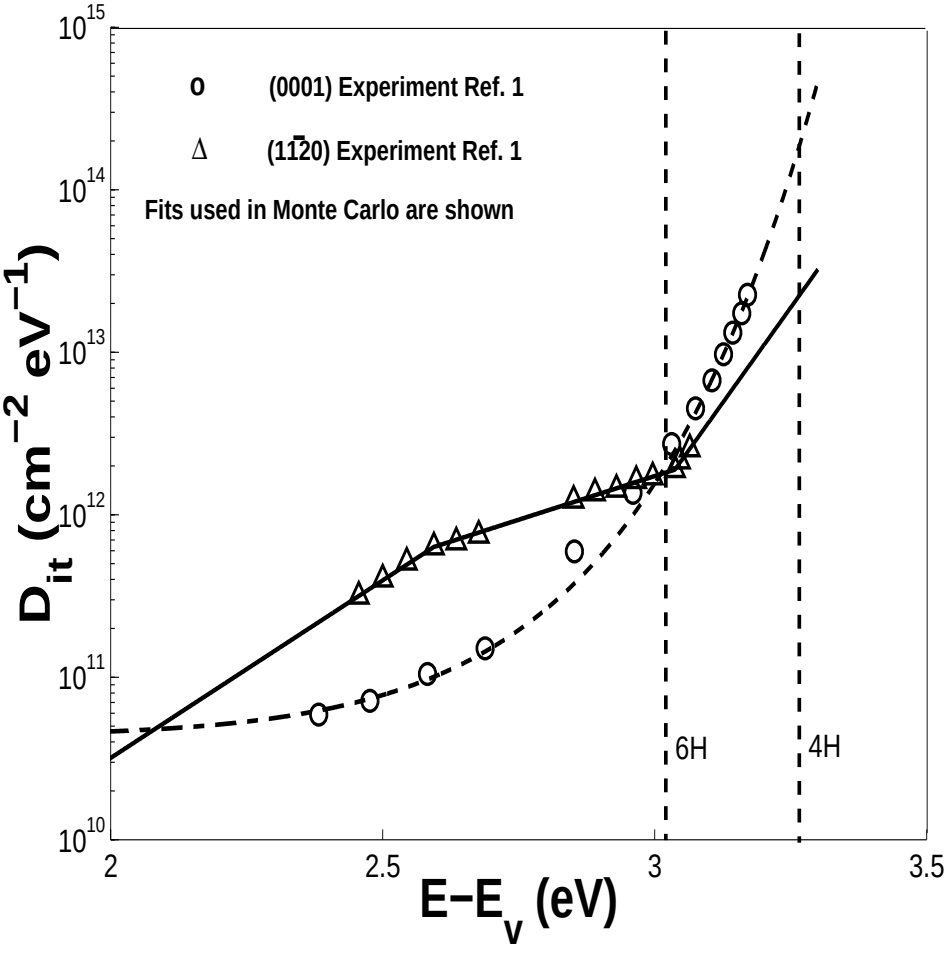

Figure 5.10: Experimental interface trap density of states [16].

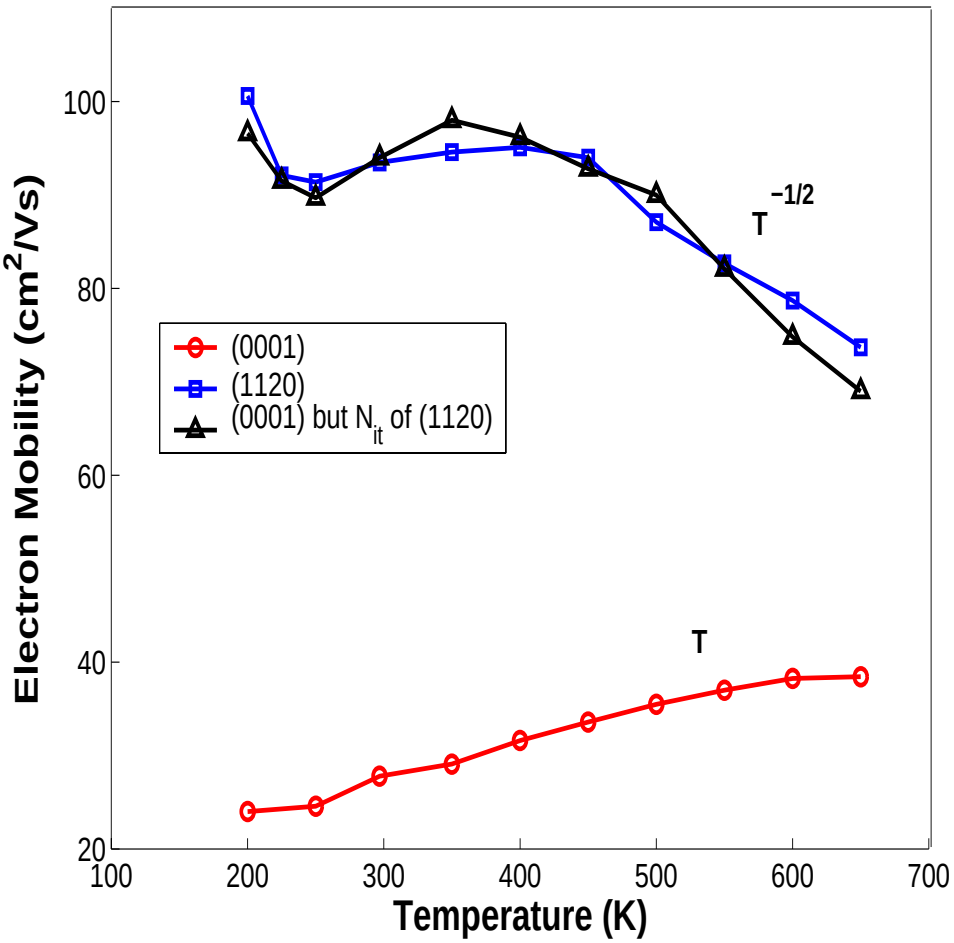

Figure 5.11: Monte Carlo simulation of electron mobility for (0001) and $(11\bar{2}0)$ oriented 4H-SiC inversion layers vs. temperature.

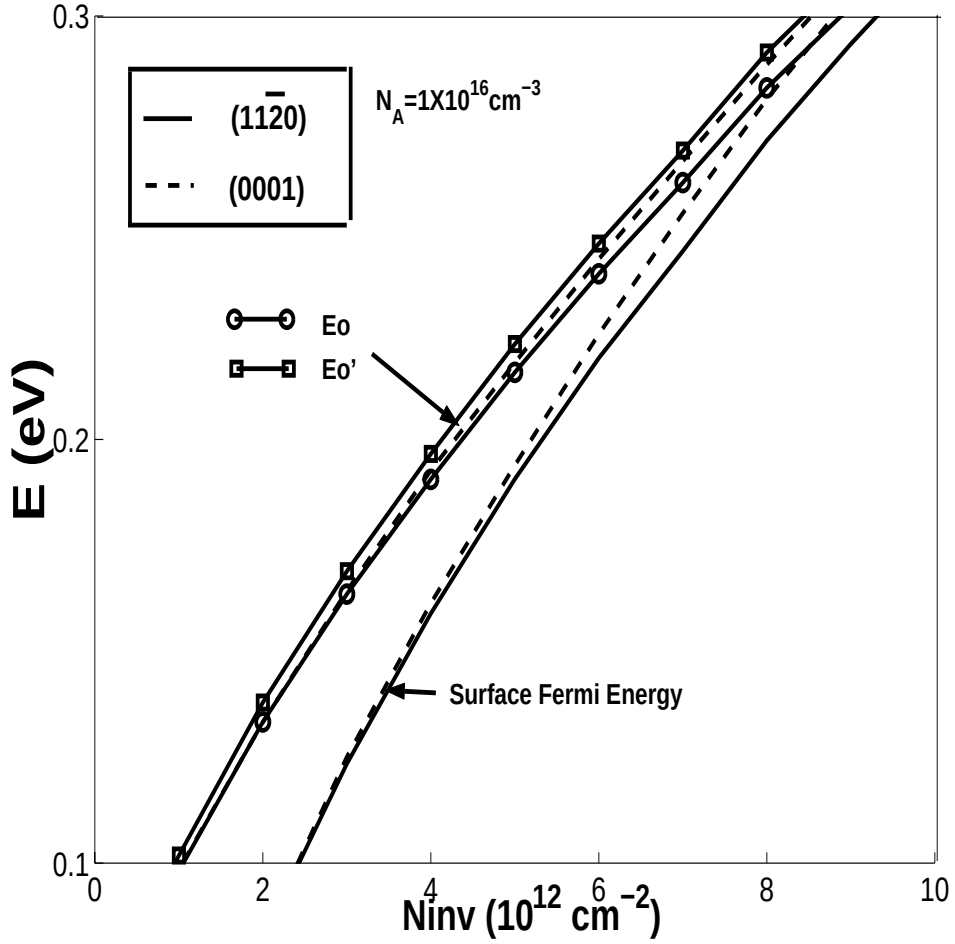

Figure 5.12: Low-lying subband structure for (0001) and (11$\bar{2}$0) oriented 4H-SiC surfaces. Here E_o and E_o' are the lowest subbands of ladder 1 and 2 respectively.

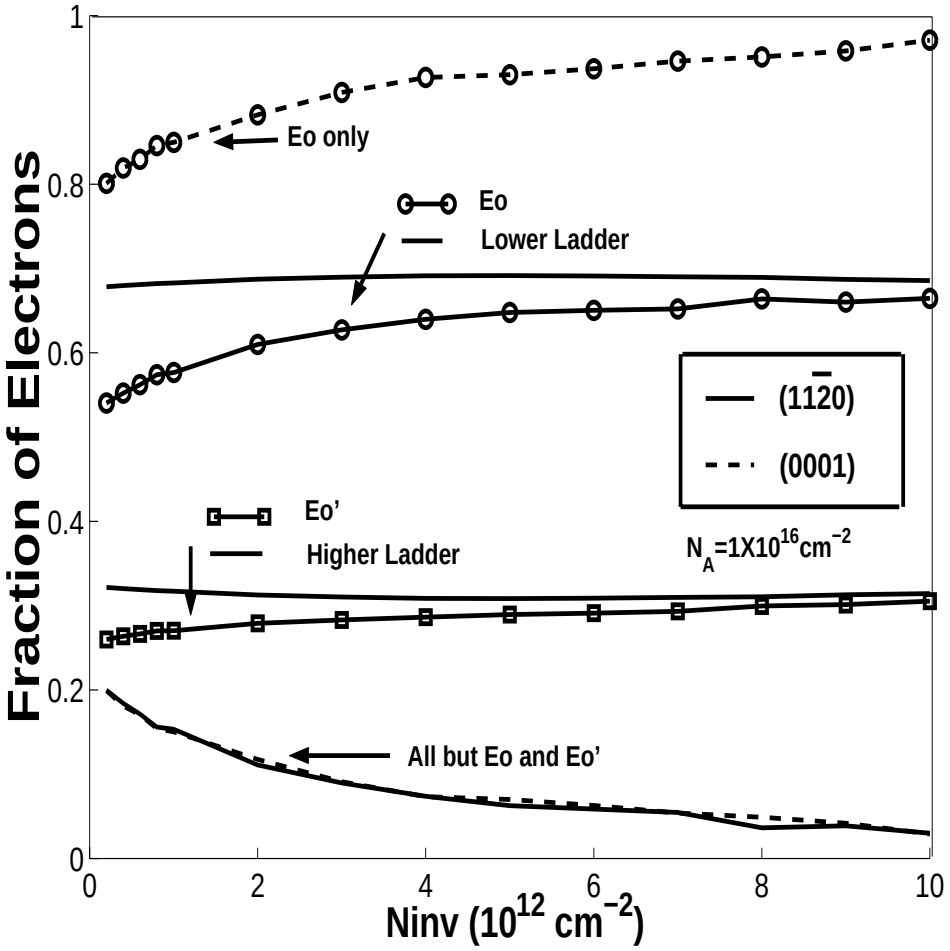

Figure 5.13: Occupancy of electrons in (0001) and (11$\bar{2}$0) oriented 4H-SiC surfaces. Here E_o and E_o' are the lowest subbands of ladder 1 and 2 respectively.

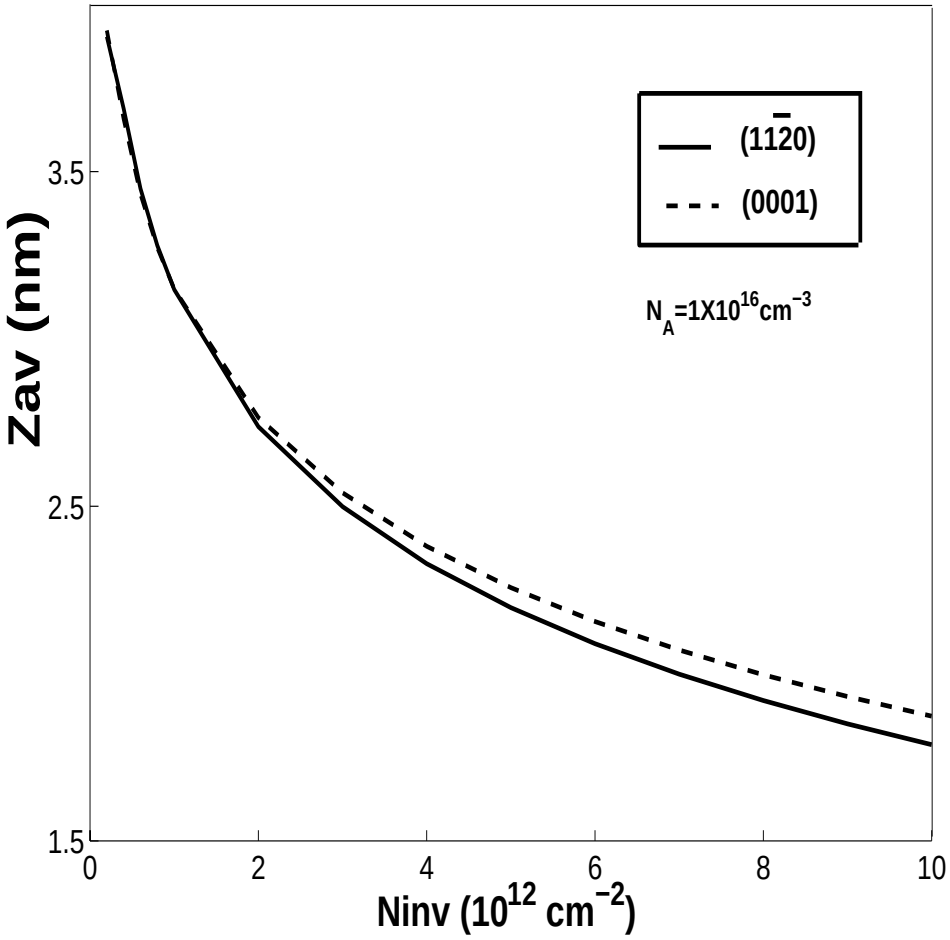

Figure 5.14: Average distance of electrons from the surface in (0001) and (11$\bar{2}$0) oriented 4H-SiC

Chapter 6

Semiclassical Electron Transport in Carbon Nanotubes

As with conventional electronic devices, theoretical modeling should play a key role in the development of CNT-based electronics by predicting performance at both the device and circuit level. Industrial device modeling is typically performed using *"semiclassical approximations"*, and solving transport equations based on either the drift-diffusion approximation or by solving the Boltzmann's equation. For the latter approach it is common to either solve Boltzmann's equation directly, using an analytical approximation for the distribution function,[128] or indirectly with the Monte Carlo method[38, 129]. An intriguing question is in what form can these techniques be used in the modeling of nanoscale devices based on materials such as CNTs.

With the advent of the miniaturization of feature lengths in conventional devices to submicron distances, this question is being addressed. It has been found that MOSFETs with inversion layer widths of only a few nanometers, can be simulated using full quantum mechanical treatment along the nanoscale inversion layer potential well only, while maintaining semiclassical transport elsewhere[130, 131]. For a CNT, there is nanometer scale confinement along the circumference, but along the tube there are indications that delocalization of π-electrons can occur[132]. For long tubes under these conditions, a *"semiclassical treatment"* of electron transport along the tube axis may well be an apt treatment. This is supported by electrical measurements on nanotube transistors and diodes which indicate that semiclassical band-bending models can describe operation at room temperature[120, 127].

Often, the basic properties of the electronic structure and the phonon spectrum of CNTs can be well approximated by the zone-folding method (ZFM)[22]. In this method the wrapping of graphene into a CNT imposes restrictions on the available wavevector space, but for allowed wavevectors, the electron and phonon energy spectrum are not altered from that of graphene. The effect of the ZFM on the material properties can be quite significant. For example two-thirds of all CNTs are predicted to be semiconductors, whereas graphene itself is a semimetal. These trends as well as the ZFM results for electronic bandgaps and the density of states in CNTs, have been verified experimentally[133, 134, 135]. Since calculations[22, 136, 137] which go beyond the ZFM, considering the curvature of the CNT, don't significantly improve the portions of the electron and phonon energy spectrum that is relevant in this work, only the ZFM is considered.

The material properties of carbon nanotube depend on the tube diameter and the orientation of bonds between the carbon atoms that make up the tube. These properties can be described uniquely by the fundamental tube indices n and m. These indices relate the lattice vector of graphene to the nanotube lattice vectors. The bonding orientation in any carbon nanotube lies between the two extreme cases of the zig-zag(m=0) and the armchair(n=m) tubes. These are the highly symmetrical achiral tubes. They are characterized by a small lattice vector along the tube axis and thus a small unit cell.

In this Chapter we focus on a semiclassical charge transport model in semiconducting CNTs based on the ZFM. Since such a model is expected to be more accurate as the length of the unit cell along the tube axis decreases, we will consider the highly symmetrical zig-zag nanotubes. The internal forces on the electrons are described via quantum mechanics whereas external fields act by altering the electronic crystal momentum via Newtonian mechanics. We consider long and "perfectly intrinsic" tubes without deformities, defects, and impurities. Since the bandgap decreases with increasing diameter, we focus on small diameter semiconducting CNTs were the bandgap at room temperature is significantly larger than the thermal energy. A diagram of a n=10 single-walled CNT is shown in Fig. 6.1. Along the tube axis, wavevectors are continuous and restricted from the case of graphene due only to the larger length of the CNT unit cell in this direction. Perpendicular to the tube axis although, significant confinement of the electron and phonon eigenvectors allows only discrete wavevector values. The electron is therefore treated as a wavepacket of Bloch states along the tube axis but around the tube circumference it is typically

delocalized in the small CNT diameters considered here. An analogous treatment for phonons is also used. Electron transport occurs through the action of a uniform electric field directed solely along the tube axis.

Using this semiclassical model, we employ a 1-D steady-state Monte Carlo simulation of electron transport along the tube axis of single-walled semiconducting CNTs. Zig-zag tubes, where $m = 0$, are considered with wrapping indices of $n = 10$ to 59. Since the diameter is proportional to n whereas the the bandgap is inversely proportional to n, this corresponds to a diameter range of $\approx$ .8 to 4.6nm and a bandgap range of $\approx$ 1.1 to 0.1eV. Transport occurs within electronic subbands obtained from the zone-folded graphene antibonding π-orbital band. Two of the six graphene K point band structure valleys are contained within these subbands. Upon scattering with phonons, electrons may make intrasubband, intersubband-intravalley, or intersubband-intervalley transitions. The particular phonon involved depends on selection rules that conserve the total energy and crystal momentum of the electron-phonon system. The crystal momentum is conserved around the circumference as a result of the periodic boundary conditions for both the electrons and phonons. We observe field controlled negative differential mobility (NDM) caused by the electron transfer between the 2 lowest energy subbands in the Monte Carlo simulations.

6.1 Electron and Phonon Energy Spectra

As mentioned, both the CNT band structure and phonon spectrum are calculated from graphene by the zone-folding method. The CNT Brillouin zone that results is a collection of N 1-D slices through the k-space of graphene, each with a length of $\frac{2\pi}{T}$, where T is the length of the CNT unit cell and N is the number of graphene unit cells within a single CNT unit cell. For a zig-zag tube of index n, $N = 2n$ and $T \approx .43$nm. The Brillouin zone for a n=10 zig-zag tube is shown in Fig. 6.2. It is well know that a metallic CNT is obtained by tube wrappings for which $n - m$ is a multiple of 3[22]. The semiconducting tubes which do not meet this criteria can further be separated into two types, those for which $n-m+1$ is a multiple of 3 and thus a metal and those for which $n-m-1$ would be a metal. These two tube types are distinguished by different trends in the zone-folded electronic energy states near the Fermi level as n and m vary[138]. As shown in Fig. 6.2, the difference depends on whether the lowest conduction band is obtained right before or right after the zone slices reach the graphene conduction band minimum at the K point.

Zone-folding allows just one discrete value for the wavevector perpendicular to the tube axis for each of the $2n$ graphene unit cells within the zig-zag CNT unit cell. The result is that each band of graphene is broken into $2n$ subbands in the nanotube. For a zig-zag tube of diameter d, the electron wavevector is:

$$\vec{k} = (k_z, \eta) = k_z\hat{z} + \frac{2\eta}{d}\hat{\theta}, \qquad (\eta = -n, ...n), \tag{6.1}$$

where confinement along $\hat{\theta}$ is described by the electronic quantum number η. The wavevectors at $\eta = \pm n$ are treated as one shared zone boundary wavevector. Since

we are dealing with long tubes, the z-component along the tube axis, k_z, is treated as continuous. This is equivalent to previous representations of the CNT Brillouin zone where the slices proceed from 0 to $2n-1$,[22] except now symmetry in $\pm\eta$ can be utilized. This is important since, except for the zone boundary value, the electronic subbands are degenerate for $\pm\eta$. There are thus $n+1$ distinct states, $n-1$ of which are doubly degenerate. As seen in Fig. 6.2, this degeneracy in η corresponds to two equivalent valleys in the subband structure each centered near a graphene K point. It is found that electrons may scatter between and occupy both of these valleys.

As mentioned previously, we consider electron conduction within delocalized π-orbitals along the nanotube axis. We therefore are interested in the subbands produced from the π-antibonding band of graphene. This band structure is obtained from the π-orbital nearest-neighbor tight-binding band structure of a graphene sheet, calculated using a nearest-neighbor π-hopping integral of $\gamma \cong 3$ eV[22]. We do not include the wavefunction overlap integral. The energy dispersion for a zig-zag tube is:

$$E(\vec{k}) = E(k_z,\eta) = \pm\gamma\sqrt{1+4\cos\left(\frac{Tk_z}{2}\right)\cos\left(\frac{\pi\eta}{n}\right)+4\cos^2\left(\frac{\pi\eta}{n}\right)} \quad (-\frac{\pi}{T} < k_z < \frac{\pi}{T}). \tag{6.2}$$

Results agree with experimentally measured band gap energies and density of states in CNTs[133, 134]. The conduction electron wavefunction, consistent with the zone-folding method, is

$$\psi_{\vec{k}} = \sum_{\vec{k}} < \vec{r}|\vec{k} >= \frac{1}{\sqrt{2\pi L}}\sum_{k_z\eta} e^{i(k_z z+\eta\theta)}u_{k_z\eta}(z,\theta), \tag{6.3}$$

where L is the CNT length, and u are the graphene π-antibonding orbitals that are normalized over the graphene unit cell. Since we are interested electron transport at relatively low applied fields, we focus on the electron band structure of the first few subbands. The energy $E_b(k_z)$ of the first three of these subbands, labeled by the subband index b, is modeled using the following analytical expression:

$$\frac{\hbar^2 k_z^2}{2m_b^*(n)} = (E_b - E_b^m(n))\left[1 + \alpha_b(n)(E_b - E_b^m(n))\right], \qquad (b = 1, 2, 3). \tag{6.4}$$

The density of states for subband b is:

$$DOS_b(E_b) = \frac{\sqrt{m_b^*}(1 + 2\alpha_b E_b)}{\hbar\sqrt{2E_b(1 + \alpha_b E_b)}}. \tag{6.5}$$

Here $E_b^m(n)$, $m_b^*(n)$, and $\alpha_b(n)$ are the energy minimum, effective mass, and non-parabolicity factor of subband b respectively. In Table 6.1, each is given as a function of the fundamental tube index n or equivalently, since $d \propto n$, as a function of diameter d. The subband quantum numbers, $\eta_b(n)$ in Table 6.1, are also n-dependent. For low-field transport in the first few subbands, it is desirable that this energy model be accurate for electron energies up to $5E_1^m$ above the Fermi level, where the Fermi level is located halfway between the conduction and valence subbands. In this range, the subband energy model reproduces the tight-binding band structure with percent error of less than 2%. Considering just the band structure near the Fermi level is a good approximation since at equilibrium a conduction electron is over 10 million more times likely to occupy the first subband minimum than an energy as high as $5E_1^m$. The band structure of zig-zag semiconductors with $n = 10$ and $n = 59$ are shown in Fig. 6.3, representing the n index range of the simulations. This range is chosen since the energy separation between the first two subbands is much larger

than the thermal energy, allowing the relative population of these subbands to be controlled by the external field.

The phonon wavevector, $\vec{q} = (q_z, \eta_p)$, also takes the form of Eq. (6.1). Similarly to the electron, the axial component, q_z, is continuous and the phonon is localized as a wavepacket along this direction. In the high-symmetry achiral zig-zag tubes that we focus on, the presence of mirror planes allows the phonon eigenvectors to generally fall into longitudinal and transverse polarizations[139]. A torsional polarization is also possible in a CNT. For the phonon energy spectrum of graphene we use a fourth-nearest-neighbor force constant model. Force parameters are used which have been successfully fitted to experiments[22]. Similarly to the electronic energy bands, zone-folding splits up each of the 6 phonon branches of graphene into $2n$ subbranches in the nanotube, each specified by a subbranch quantum number η_p.

In this work the CNT subbranches of the graphene acoustic and optical modes are considered. First we discuss the acoustic modes. Of these phonons, there are four for which the phonon energy, E_p, vanishes as the wavevector, q_z, vanishes. These include a longitudinal, torsional, and a doubly degenerate transverse mode. Once the electron-phonon scattering selection rules are determined in the next section, its found that these four phonons are involved in only intraband-intravalley electron transitions. This results since each of these modes has a subbranch quantum number of zero, and thus has no wavevector component perpendicular to the tube axis. Due to the quantization of the wavevector along the circumference, most of the CNT acoustic modes have a dispersion relation in which the phonon energy is

nonzero as $q_z \rightarrow 0$. These subbranches all have a nonzero η_p and turn out to be involved in intersubband electron scattering. Those with a large η_p mediate intervalley scattering.

Since theory predicts that the change in the π-electronic energy under longitudinal strain is larger than under torsional[140, 141] or transverse[142] strain, electron scattering by longitudinal polarizations is treated as the most dominant of the acoustic modes. The importance of these longitudinal modes has been observed in thermal relaxation studies of nanotubes[143]. We therefore consider just the longitudinal acoustic modes. For scattering of electrons within the first three conduction bands, the spectra of the acoustic phonons considered is shown in Fig. 6.4. The particular phonon subbranches that maybe involved in the scattering of electrons between the first three electronic subbands is limited by selection rules. These selection requirements will be derived later in this chapter. The energy dispersion relation is

$$E_p(q_z, \eta_p) = E_p^o(\eta_p) + \hbar \upsilon_s \Theta(q_z, \eta_p) \left(|q_z| - |\frac{\eta_p}{d}| \right), \tag{6.6}$$

were $\upsilon_s = 20km/s$ and the phonon energies at $q_z = 0$, $E_p^o(\eta_p)$, are given in Table 6.2. For the $LAIV$ phonon $\Theta = 0$, whereas for the other acoustic modes

$$\Theta(q_z, \eta_p) = \begin{cases} 1 & |q_z| > |\frac{\eta_p}{d}| \\ 0 & \text{else.} \end{cases} \tag{6.7}$$

As the tube diameter increases the intravalley acoustic phonons all converge to the graphene longitudinal acoustic phonon. The intervalley subbranches, grouped together as $LAIV$ in Fig. 6.4, are to a good approximation dispersionless with

an energy of $\cong 158\ meV$. An exception though is the intervalley acoustic phonon that scatters electrons between the 3rd subband of different valleys. This phonon has less energy, but as the tube diameter increases, its energy also approachs 158 meV. As the tube diameter increases the intervalley acoustic phonons all become dispersionless with a phonon energy of 158 meV.

For the optical modes we also consider only the longitudinally polarized phonon of graphene. There are three dispersionless subbranches ($LO, LOIV$-1, $LOIV$-2). The other intervalley phonons are grouped together as one phonon subbranch ($LOIV$) with significant dispersion. The dispersion relation for the optical modes is

$$E_p(q_z, \eta_p) = E_p^o(\eta_p) + \hbar \upsilon_s \Theta_{op}(q_z, \eta_p)|q_z|, \tag{6.8}$$

where Θ_{op}, which is nonzero only for the $LOIV$ phonon, is given by

$$\Theta_{op}(q_z, \eta_p) = \begin{cases} \frac{2.5}{n} & \text{LOIV} \\ \\ 0 & \text{else.} \end{cases} \tag{6.9}$$

As the tube diameter increases the intervalley optical phonons all become dispersionless with a phonon energy of 158 meV, the common phonon energy for longitudinally polarized acoustic and optical phonons at the K-point in graphene.

6.2 Electron-Phonon Scattering

Electron-phonon scattering in CNTs is treated using the standard methods of lattice scattering[106]. The effect of ion vibrations on the periodic crystal potential is

considered small enough to treat using first-order perturbation theory. Considering the duration of a scattering event to be short, the rate of electron-phonon scattering is represented by the familiar "Golden Rule"

$$\Gamma = \frac{2\pi}{\hbar} | < f|H^{ep}|i > |^2 \delta(E_f - E_i), \tag{6.10}$$

where i and f are the initial and final states of the system, E is the energy, and H^{ep} is the space-dependent electron-phonon interaction. Assuming short-range interactions we will use the deformation theory[108] to approximate H^{ep}. Using longitudinally polarized phonon eigenvectors in a form consistent with confinement in the ZFM, the displacement of the lattice at a tube position of $\vec{r} = z\hat{z} + \frac{\theta d}{2}\hat{\theta}$ is

$$U(\vec{r}) = \sum_{\vec{q}} \sqrt{\frac{\hbar}{2M\omega_{\vec{q}}}} \left[a_{\vec{q}}\ e^{i(\vec{q}\cdot\vec{r})} \hat{q} + c.c \right]. \tag{6.11}$$

The sum is over phonon wavevectors $\vec{q} = q_z\hat{z} + \frac{2\eta_p}{d}\hat{\theta}$, where z and θ are the coordinates along the tube axis and around the tube circumference respectively. As mentioned the component of the wavevector along the tube, q_z, is treated as continuous since the tube length is large, whereas the component along θ is quantized. So the sum includes all subbranches η_p. The amplitude of each eigenvector depends on the lattice mass M, the subbranch wavevector-dependent frequency $\omega_{\vec{q}}$, and the phonon creation and anniliation operators $a^\dagger$ and a. The electron-phonon interaction, H^{ep}, is found from the shift in electronic energy due to a phonon. Within the deformation potential theory, this shift is given by the perturbation of the electronic energy when an electron interacts with a long wavelength phonon and is set equivalent to

the effect of a locally homogeneous strain. This electronic energy change is then

$$\begin{aligned} < \vec{k'}|\Delta E|\vec{k} > &=< \vec{k'}|D\sum_{\vec{q}}\sqrt{\hbar/2M\omega_{\vec{q}}}\left[iqa_{\vec{q}}\ e^{i(\vec{q}\cdot\vec{r})} + c.c\right]|\vec{k} > \\ &= D\sum_{q_z\eta_p}\sqrt{\hbar Q^2/2M\omega_{q_z\eta_p}} < \vec{k'}|ia_{q_z\eta_p}\ e^{i(q_z z+\eta_p\theta)} + c.c.|\vec{k} >, \end{aligned} \tag{6.12}$$

for an electron transtion from state $\vec{k}$ to state $\vec{k'}$. The acoustic deformation potential D is the proportionality constant between the electronic energy shift and the lattice strain. For zig-zag tubes, D has been calculated to be approximately 3γ[140, 142].

The electron-phonon coupling constant for optical phonons depends on the acoustic deformation potential D in this work. It is approximated as $\frac{1}{2}DQ$, where Q is the wavevector when the two atoms in the graphene unit cell vibrate in opposite directions. Similar approximations are found to work well in traditional bulk semiconductors [38, 106]. For both acoustic and optical phonons Q is:

$$Q(q_z,\eta_p) = \begin{cases} \sqrt{|q_z|^2 + |\frac{2\eta_p}{d}|^2} & \text{acoustic} \\ \\ \frac{2\sqrt{(3)}\pi}{T} & \text{optical.} \end{cases} \tag{6.13}$$

Now we concentrate on the matrix elements that determine the electron-phonon selection rules. Using the electron wavefunction in Eq. (6.3) and the lattice symmetry along the tube axis the following matrix element becomes

$$< \vec{k'}|e^{i(q_z z+\eta_p\theta)}|\vec{k} >= \frac{N_T\delta_{k_z-k'_z,q_z}}{2\pi L}\int_0^T dz\int_0^{2\pi} d\theta e^{i\delta\eta\theta}u^*_{\vec{k'}}(z,\theta)u_{\vec{k}}(z,\theta), \tag{6.14}$$

where $\delta\eta$=$\eta-\eta'+\eta_p$. Here the integral along the entire tube is replaced by the integral along just the CNT unit cell by using the axial-symmetry relations

$$\sum_{j=1}^{j=N_T} e^{i(k_z-k'_z+q_z)jT} = N_T\delta_{k_z-k'_z,q_z}, \tag{6.15}$$

and

$$u_{\vec{k}}(z + jT, \theta) = u_{\vec{k}}(z, \theta), \tag{6.16}$$

where jT are the lattice vectors along z and N_T is the total number of CNT unit cells in the tube.

Now using the CNT symmetry vector[22] for a zig-zag tube, $\vec{R}$, the positions of each graphene unit cell can be found according to

$$\alpha\vec{R} = \alpha\left[\frac{T}{2}\hat{z} + \frac{\pi d}{N}\hat{\theta}\right], \qquad \alpha = integers(1.....N). \tag{6.17}$$

The z-component of $\alpha\vec{R}$ wraps back around so that it always stays within the unit cell, which has a of length T along the z direction. This is shown in Fig. 6.5(a). The unit cell can be redrawn as in Fig. 6.5(b), so that the integration along z is now continuous. Then Eq. (6.12) may be written as

$$< \vec{k'}|e^{i(q_z z + \eta_p \theta)}|\vec{k} >= \frac{N_T \delta_{k_z - k'_z, q_z}}{2\pi L} \sum_{\alpha=1}^{\alpha=N} \int_{\frac{T(\alpha-1)}{2}}^{\frac{T\alpha}{2}} dz \int_{\frac{2\pi(2z-T)}{TN}}^{\frac{2\pi(2z+T)}{TN}} d\theta e^{i\delta\eta\theta} u^*_{\vec{k'}}(z,\theta) u_{\vec{k}}(z,\theta). \tag{6.18}$$

Now using the $\vec{R}$ symmetry of the graphene unit cells, which are contained within the CNT unit cell,

$$u_{\vec{k}}(\vec{r} + \alpha\vec{R}) = u_{\vec{k}}(\vec{r}), \tag{6.19}$$

Eq. (6.18) may be reduced to a integration over a single graphene unit cell

$$< \vec{k'}|e^{i(qz + \eta_p \theta)}|\vec{k} >= \frac{N_T \delta_{k_z - k'_z, q_z}}{2\pi L} \int_0^{\frac{T}{2}} dz \int_{\frac{4\pi(z-T)}{TN}}^{\frac{4\pi z}{TN}} d\theta e^{i\delta\eta\theta} u^*_{\vec{k'}}(z,\theta) u_{\vec{k}}(z,\theta) \sum_{\alpha=1}^{\alpha=N} e^{i\delta\eta\frac{2\pi\alpha}{N}}. \tag{6.20}$$

Since there is periodicity around the circumference, the sum may be equivalently redrawn by starting the sum at an arbitrary graphene unit cell $\beta + 1$, where β is an

integer

$$\sum_{\alpha=1}^{\alpha=N} e^{i\delta\eta\frac{2\pi\alpha}{N}} = \sum_{\alpha=\beta+1}^{\alpha=\beta+N} e^{i\delta\eta\frac{2\pi\alpha}{N}} = e^{i\delta\eta\frac{2\pi\beta}{N}} \sum_{\alpha=1}^{\alpha=N} e^{i\delta\eta\frac{2\pi\alpha}{N}}. \tag{6.21}$$

To satisfy this condition for arbitrary β, $\delta\eta$ must be zero and thus

$$\sum_{\alpha=1}^{\alpha=N} e^{i\delta\eta\frac{2\pi\alpha}{N}} = N\delta_{\delta\eta,0} = N\delta_{\eta'-\eta,\eta_p}. \tag{6.22}$$

This gives

$$< \vec{k'}|e^{i(qz+\eta_p\theta)}|\vec{k} >= \frac{NN_T\delta_{k_z-k'_z,q_z}\delta_{\eta'-\eta,\eta_p}}{2\pi L}\int_0^{\frac{T}{2}} dz \int_{\frac{4\pi(z-T)}{TN}}^{\frac{4\pi z}{TN}} d\theta u^*_{\vec{k'}}(z,\theta)u_{\vec{k}}(z,\theta) = \delta_{k_z-k'_z,q_z}\delta_{\eta'-\eta,\eta_p}, \tag{6.23}$$

since the graphene π-antibonding orbitals are normalized over the graphene unit cell.

These are the selection rules for phonons involved in a given transition from an initial $\vec{k} = (k_z, \eta)$ to a final $\vec{k'} = (k'_z, \eta')$ electron state. Electron-phonon scattering must not only conserve momentum along the tube axis but also conserve the quantum number η. The periodic boundary conditions for the electrons and phonons along the circumference retain the conservation of the 2-D crystal momentum in the CNTs. The electron-phonon interaction is

$$\begin{aligned} | < f|H^{ep}|i > |^2 &= | < \vec{k'}; N(\pm)1|\Delta E|\vec{k}; N > |^2 \\ &= \textstyle\sum_{q^*_z\eta^*_p} \hbar^2 D^2 \left(Q(q^*_z,\eta^*_p)\right)^2 \left(N(q^*_z,\eta^*_p) + \frac{1}{2}(\pm)\frac{1}{2}\right)/2ME_p(q^*_z,\eta^*_p), \end{aligned} \tag{6.24}$$

where the sum includes all phonon wavevectors q^*_z and quantum numbers η^*_p that satisfy the selection rules in Eq. (6.23). N is the phonon occupation number represented using the Bose-Einstein distribution function, while in the bracketed $(\pm)$ sign, the upper sign is for phonon emission and the lower for phonon absorption.

Using Eq. (6.10) the "Golden Rule" and integrating over all final electron states, the scattering rate from an electronic state in subband b with wavevector k_z to to an electronic state in subband b' is

$$\Gamma_{bb'}(k_z) = \sum_{q_z^* \eta_p^*} \frac{\hbar D^2 \left(Q(q_z^*, \eta_p^*)\right)^2 (q_z^*, \eta_p^*)}{2\rho E_p(q_z^*, \eta_p^*)} \left(N(E_p(q_z^*, \eta_p^*)) + \frac{1}{2}(\pm)\frac{1}{2}\right) I_{bb'}(k_z, q_z^*, \eta_p^*), \tag{6.25}$$

where conservation of energy and crystal momentum is also required. Here ρ is the CNT mass density along the tube axis. It is proportional to n according to:

$$\rho(n) = 1.9nX10^{-15} g/cm. \tag{6.26}$$

The term $I_{bb'}$ would typically correspond to a function of the density of final states under the golden rule formalism. Since semiclassically the density of states diverges in 1-D, higher order quantum effects are needed. It has been found in quantum wires that a full quantum mechanical treatment of the 1-D scattering rate can be well approximated by including collisional broadening within the golden rule[144, 145]. Following these results we adjust Eq. (6.25) by broadening the semiclassical $I_{bb'}$ with a Gaussian according to

$$I_{bb'}(k_z, q_z^*, \eta_p^*) = \frac{\sqrt{2/\pi}}{\Delta\left(1 + erf(E/\Delta)\right)} \int_{-E}^{\infty} \frac{e^{-(\frac{E'^2}{2\Delta^2})} DOS_{b'}(E + E')dE'}{1 \ (\pm) \ \frac{q_z^*}{|q_z^*|}\hbar \upsilon_s \Theta(E_p + E') DOS_{b'}(E + E')}, \tag{6.27}$$

where $DOS_{b'}$ is the density of states in band b', erf is the error function and

$$E = E_b(k_z) \ (\mp) \ E_p(q_z^*, \eta_p^*). \tag{6.28}$$

The broadening of final states Δ is determined self-consistently for each member of

the sum in Eq. (21) according to

$$\Delta = \hbar\Gamma_{bb'}(k_z, q_z^*, \eta_p^*). \tag{6.29}$$

When b and b' correspond to different valleys in the electronic subband structure, η_p is large. The intervalley phonons, grouped as $LAIV$ or $LOIV$, have the same phonon energy, but since they cause different subband electron transitions and therefore have different quantum numbers η_p, they will have different scattering rates. As previously mentioned and given in Eq. (6.6) and (6.7), the acoustic phonon energy dispersion is significant for the intravalley subbranches with small η_p. For the LA intrasubband branch when E_p is much less than the thermal energy K_bT_L, only backscattering occurs and we use the small phonon energy limit[106]

$$\frac{q_z^{*2}\left(N(E_p(q_z^*)) + \frac{1}{2}(\pm)\frac{1}{2}\right)}{E_p(q_z^*)} \cong \frac{K_bT_L}{\hbar^2\upsilon_s^2}, \tag{6.30}$$

in Eq. (6.25).

In all, eight different phonon processes may potentially contribute to the $b \rightarrow b'$ scattering rate in Eq. (6.25). These include absorption and emission of both acoustic and optical phonons of the intravalley or intervalley variety. For each process, a maximum of 2 phonon wavevectors, q_z^*, will enter the sum in Eq. (6.25). This gives a maximum of sixteen terms. Fewer terms typically appear in practice though due to the constraints of energy and crystal momentum conservation. For a given phonon process, the two possible phonon wavevectors involved in the scattering rate are:

$$q_z^*(k_z, b, b') = \frac{-B \pm \sqrt{B^2 - 4AC}}{2A}, \tag{6.31}$$

where

$$A = 1 - 2\alpha_{b'} m^*_{b'} \upsilon_s^2 \Theta^2,$$

$$B = 2k_z \ (\mp)\frac{q^*_z}{|q^*_z|}\frac{4m^*_{b'}\upsilon_s\Theta(1+2\alpha'_b E_a)}{\hbar},$$

$$C = k_z^2 - \frac{2m^*_{b'}E_a(1+\alpha_{b'}Ea)}{\hbar^2}, \tag{6.32}$$

and

$$E_a = E_b(k_z) - E^m_{b'} \ (\mp)E'_p.$$

The term E'_p is the phonon energy in Eq. (6.6) and Eq. (6.8) minus the q_z dependent part. It is given by

$$E'_p(\eta^*_p) = E_p(q^*_z, \eta^*_p) - \hbar\Theta(q^*_z, \eta^*_p)|q^*_z|. \tag{6.33}$$

The scattering rates for electrons in the first 2 subbands are shown in Fig. 6.6 when the deformation potential D is set at 9eV. The total optical, intravalley acoustic, and intervalley acoustic are shown. Unlike the acoustic rate, the optical rate is not divided since the intravalley and intervalley rates are very similar. The large peaks occur when electrons are able to scatter into a subband minima where the density of final states is large. The peaks in the acoustic intervalley rate occur at energies close to where the optical peaks occur since the longitudinal acoustic and optical branches of the graphene spectrum are degenerate near the graphene zone-boundary. Double peaks can be seen in both the intravalley acoustic and optical

rates. In the former case these are the result of an absorption peak followed closely with increasing electron energy by an emission peak. For the optical rate, the double peaks occur since the intervalley phonons have less energy than the intravalley. In the case of the optical scattering rate, the double peaks therefore correspond to an intervalley peak followed closely by an intravalley peak.

We show the rate for two different tubes sizes in Fig. 6.6. These are for the smallest diameter, n=10, and largest diameter, n=59, tubes simulated here. First we will concentrate on the scattering rate for the n=10 tube in Fig.s 6.6(a) and 6.6(c). For scattering of electrons in the first band, phonon scattering is dominated by $1 \rightarrow 1$ intravalley acoustic scattering until around $158meV$. Once this threshold energy is reached optical and acoustic intervalley emission mechanisms dominate. When electrons are in the second band the scattering rate can be divided into 3 regions. The first is at very low electron energies near the minimum of the second subband. Here intravalley acoustic scattering dominates. The next region occurs as the electron energy is increased but is below the threshold for $2 \rightarrow 2$ scattering. Here optical and acoustic intervalley $2 \rightarrow 1$ emission scattering dominate but acoustic intravalley scattering also contributes. Once the $2 \rightarrow 2$ threshold energy at $158meV$ is reached, optical and acoustic intervalley emission scattering then dominates strongly for electrons within the second subband.

The phonon scattering rates indicate that the threshold for significant electron-phonon scattering occurs around 158eV. This is due to scattering with both acoustic and optical intervalley, or near zone-boundary, phonons. The threshold occurs when conduction electrons attain the energy of the intervalley phonon, which is 158eV

for both the acoustic and optical modes. High-field experiments on metallic carbon nanotubes are indeed consistent with a dominant phonon energy around this energy[146, 147].

Now comparing with the larger tube in Fig.s 6.6(b) and 6.6(d), we see that the scattering rates markedly decrease as n increases. This occurs since with increasing diameter the density of final scattering states decreases and the CNT mass per unit length increases, both decreasing the scattering rate. From Eq.s 6.5 and 6.25, we find at low energies

$$\Gamma \propto \frac{D^2}{n\sqrt{\gamma}}. \tag{6.34}$$

In large tubes electrons in subband 1 are scattered significantly by intravalley ($1 \rightarrow 2$) phonon emission and absorption processes at low energies. This is not seen in the smaller tubes since before the electron can reach energies to allow these intravalley ($1 \rightarrow 2$) processes, the threshold at 158 meV for the strong ($1 \rightarrow 1$) intervalley process is reached. For electrons in subband 2 of the small tubes, near the energy minimum, strong ($2 \rightarrow 1$) intervalley phonon emission processes occurs. In the larger tubes, the energy gap between the subbands is too small and only the intravalley ($2 \rightarrow 2$) process occurs. For comparison we plot the total rate for a small n=10 tube together with a larger n=58 tube in Fig. 6.7.

6.3 Transport Simulation

Charge transport in zig-zag semiconducting CNTs is studied using standard Monte Carlo techniques[38]. Simulations are homogeneous and of sufficient time duration

to characterize steady-state phenomena of many non-interacting electrons using the single-electron method[38]. CNTs are treated as "ideal", in that they are extremely long, undoped, and without any defects or other imperfections. The basic principles of semiclassical transport[148] are used, in which quantum mechanics is used to determine the electronic energy levels and scattering rates due to the lattice, whereas applied external fields accelerate electrons semiclassically. In this work a homogeneous external electric field directed solely along the CNT axis is considered. This field is not considered strong enough to cause intersubband transitions in the CNTs simulated. The validity of this approximation requires that the subband separation, ΔE, always obey the relation[148]

$$\Delta E > \sqrt{E_F e F T}, \tag{6.35}$$

where E_F is the Fermi energy of graphene, e is the electron charge, F is the external electric field, and T the the magnitude of the translation vector. An obvious exception occurs in the smaller diameter tubes where subband crossing occurs. This can be seen in Fig. 6.3. For simplicity in this work, the consequences of subband crossing are ignored.

As mentioned, the only scattering mechanisms considered involve the subbranches of the graphene longitudinal acoustic and optical modes. Electron-electron scattering is not included here but may contribute to the electron drift velocity by increasing the intersubband-intravalley scattering rate. This would be more likely in the larger tubes we consider, where both the transverse momentum transfer between the subbands and the phonon scattering rate are small. Intrasubband scattering via

electron-electron interactions though should not effect the electron drift velocity since the initial and final interacting electron pair would be indistinguishable in one dimension, leading to no net randomization of the net electron momentum of the system[149].

It is necessary to point out that in one dimension the Monte Carlo simulation is complicated by peaks in the scattering rate, Γ , which can be seen in Fig. 6.6. Between stochastically chosen scattering events during the simulation, electrons drift in the applied electric field. This drift time, τ_d, should be small compared to $\frac{1}{\Gamma(E)}$, so that the scattering rate is properly resolved in the Monte Carlo simulation. This requires that the drift time always be adjusted so that at all times $\tau_d(E) \leq \frac{1}{10\Gamma(E)}$. For convergence in the low-field regime, where the electron mobility is constant, this criteria is adjusted so that $\tau_d(E) \leq \frac{1}{100\Gamma(E)}$.

In Fig. 6.8 we show simulation results when only acoustic phonon scattering is included. The simulated electron drift velocity, υ_d, varies distinctly with applied electric field. Results are shown in Fig. 6.8 for fields where the average electron energy, which increases with increasing field, is below the band structure model limit of $5E_1^m(n)$. Peaks reaching values of υ_d as large as $\cong$ 3 - 5 $X10^7$ cm/s as n increases from 10 to 59 are observed. The critical field, $F_c(n)$, at which the drift velocity maximum occurs is seen to decrease with increasing n from $\cong$ 60 to 2 kV/cm in the range of n that is simulated. The low-field mobility is large, increasing as n, and thus the tube diameter, increases. This mobility increases from 0.4 $X10^4$ to 12 $X10^4$ cm^2/Vs as n increases from 10 to 59. Results for graphite, $\cong$ 1.5 $X10^4$ cm^2/Vs,[150] lie within this range. In the larger tubes, the low-field mobility is likely

overestimated since electron-electron scattering is not considered. This is not the case in the smaller tubes since the phonon scattering rate is large and intersubband transitions at low fields are rare.

Negative differential mobility occurs when the slope of the drift velocity with field becomes negative. The simulated results show that $\frac{dv_d}{dF}$ does indeed become negative once the velocity peak occurs. NDM is caused by the 'transferred-electron effect' [151, 152] involving the first two subbands. This occurs since the conduction velocity, $\frac{1}{\hbar}\frac{dE}{dk}$, is larger in the first subband than in the second. The differential mobility becomes negative as the concentration of electrons in the second subband increases in response to an increasing applied electric field. For field-controlled NDM, the energy gap between the first two subbands should be large compared to the thermal energy of the electrons. This condition is met for the CNTs considered here, but for larger tubes this condition may not be satisfied.

Analysis of the dependence of the peaks in the drift velocity on the tube diameter and the band structure hopping integral γ, indicates a peak height of

$$\upsilon_d^{max}(n,\gamma) = \left(\frac{3n\gamma^2}{8}\right)^{1/3}\left(1-\frac{\beta}{2n}\right)\times 10^7 cm/s. \tag{6.36}$$

occurring at a critical field of

$$F_c(n,D,\gamma) = \left(1-\beta\left(\frac{8}{n}\right)^2\right)\frac{\gamma D^2}{27n^{3/2}}\times 10^6 V/cm. \tag{6.37}$$

The weak increase of υ_d^{max} with n is related to the increase of the conduction velocity of the first subband. Also F_c increases as the phonon scattering increases and is approximately proportional to D^2/n.

Differences based on the tube type are represented by the use of the term β. Here $\beta = [gcd(n+1,3) - 1] = 0$ or 2, where $gcd(n+1,3)$ indicates the greatest common divisor between $(n+1)$ and 3. The origin of the β correction can be seen in Fig. 6.9. For a type 2 tube, the minimum energy lies at k_z=0 along the K-K symmetry line, whereas for a type 1 tube the minima lies along the Γ-K symmetry line. In the smaller tubes the subbands are far enough from the K point so that the there is a significant difference in the electronic structure between the two tube types. This difference is reduced as the tube diameter increases and the fundamental tube index n increases since the minimum subband approaches the K point in both tube types. Furthermore the type 1 and type 2 zig-zag tubes likely represent the extreme cases for the semiconducting tubes and other, chiral tubes, should have a β between 0 and 2. We can see this by considering the electronic structure of graphene[22]. If we sample the electronic structure of graphene at a k point along the Γ-K symmetry line near the K point, and then continue to sample the band structure moving towards a point on the K-K symmetry line while keeping $\sqrt{|k^2 - K^2|}$ constant, we will find no critical points. For fixed $2n + m$, which determines the subband spacing from the K point in both achiral and chiral nanotubes, the maximum band structure difference between $(2n + m) \pm 1$ is that found in the zig-zag tubes. We therefore expect Eq.s (6.36) and (6.37) could be used in the chiral carbon nanotubes once the $2n$ dependence of the zig-zag tubes is replaced with the appropriate $2n + m$ dependence for the general semiconducting tube. The correction factor β would then be expected to have the extreme values of 0 in the type 2 zig-zag tubes and 2 in the type 1 zig-zag tubes, with β for the chiral

tubes lying between. More work is needed to test this hypothesis.

As n approaches 59, the drift velocities of the two tube types become virtually indistinguishable. This is illustrated in Fig. 6.8(b) where the peaks for both tube types are shown together. Since important features of charge transport occur at the critical field, Eq. (6.35) should be satisfied at this field value. We find that it is satisfied for the tubes considered. The band separation between the first and second subband satisfies Eq. (6.35) with at least a factor of 2.5 to spare in the tubes considered in this work. For increasing larger tubes although, the condition would eventually fail to be satisfied and field-mediated intersubband transitions would occur readily.

One thing that determines the characteristics of the drift velocity peak is the decrease in the scattering rate with increasing n, as seen in Eq. (6.34), With less scattering as n increases, electrons gain energy and occupy the second subband more readily as the field increases. This lowers the critical field significantly. The conduction velocity of the first subband, υ_{c1}, also strongly influences the drift velocity. As n increases, this velocity increases weakly with n, allowing the electrons to reach higher drift velocities before the second subband is occupied. Differences in the peaks of υ_d as the tube type varies result largely from alterations in υ_{c1}. As seen in Fig. 6.10, the average velocity and the occupation of the second subband both increase much faster with increasing field when $n = 10$ as opposed to when $n = 11$. This occurs since compared to the type 1 tubes, the effective mass of the type 2 tubes is smaller. Since the conduction velocity is proportional to $\frac{1}{m_1^*(n)}$, it follows from the results in Table 6.1 that $\upsilon_{c1}(\vec{k}, n)$ is larger in the type 2 tubes by a factor

of $\frac{(n+4)}{n}$. For the large tubes considered this is a small increase, but for the smaller tube this factor approaches 1.5. This leads to the β deviations for the different tube types in Eq.s (6.36) and (6.37) when n is small.

The effect of optical phonon scattering on the drift velocity is seen in Fig. 6.11. Here Monte Carlo results are shown along with a model analytical fit. The model will be addressed in the following discussion. The analytical fit is given for the case including optical and acoustic phonon scattering along with the case when only acoustic scattering is considered. We see that optical phonon scattering acts to broaden the drift velocity peaks on the high-field side. There is also a slight reduction in the peak high.

Now we will discuss the analytical model presented in Fig. 6.11. From the results of the Monte Carlo simulations, we obtain a single-walled carbon nanotube (SWCNT) mobility model that depends on tube index (n), deformation potential (D), band structure parameter (γ), and electric field (F). We find that the low-field mobility μ_0 is independent of the field, and increases quadratically with n/D according to

$$\mu_0(n, D, \gamma) = \left(\frac{n\gamma^{3/4}}{4D}\right)^2 \left(1 - \frac{\alpha}{n^{2/3}}\right) \times 10^4 cm^2/Vs. \tag{6.38}$$

This form for low field mobility from is analogous to the familiar expression: $q/\Gamma m^*$. To see this, we note that the effective mass (m^*) in a zig-zag SWCNT is $\propto 1/n\gamma$ in Table 6.1 and the scattering rate (Γ) for small fields, is $\propto D^2/n\sqrt{\gamma}$. Combining these expressions we see that the mobility in the CNT ohmic region near equilibrium is proportional to $q/\Gamma m^*$. The low-field mobility is larger in the larger tubes considered

in this work since both the effective mass and the scattering rate are smaller.

Using the expressions in Eq.s 6.36 and 6.37, the mobility takes on the familiar $\frac{v_d^{max}}{F}$ characteristic of high-field transport. In addition, the model must be further modified to account for the negative differential mobility (NDM) that results from electrons transferring to higher subbands. The NDM effect can be expressed using a Gaussian

$$\mu_1(F,n,D,\gamma) = \frac{v_d^{max}}{F} exp\Big(-\left[log_{10}(F/F_c)\right]^2/S\Big) \times 10^4 cm^2/Vs. \tag{6.39}$$

Here the Gaussian broadening parameter S is

$$S(F,n,D,\gamma) = 1.3 + \Theta(F-F_c)\frac{\sqrt{n}}{2}, \tag{6.40}$$

where Θ is a heavy side step function. The broadening is therefore larger on the high-field side of the velocity peak.

We have presented both low and high field mobilities. The transition point from low-field to high-field mobility occurs at the electric field F_0. At this unique point $\mu_1(F_0,n,D,\gamma) = \mu_0(n,D,\gamma)$; solving for F_0 gives:

$$F_0(n,D,\gamma) = exp\left(log(F_c) - \frac{31}{9} + \sqrt{\left(\frac{31}{9} - log(F_c)\right)^2 + \frac{62}{9}log(v_d^{max}/\mu_0) - log^2(F_c)}\right). \tag{6.41}$$

In Fig. 6.14 we show the resulting mobility model vs. applied field for a number of SWCNTs. The mobility is high in the low-field region, then drops as the electrons begin to significantly populate the second subband. The larger mobilities for wider tubes is attributed to a smaller effective mass and a smaller scattering rate. In Fig. 6.12 and 6.13 we compare electron velocity calculated with the new

analytical mobility model with values that were calculated by Monte Carlo. We see that agreement is excellent for both fixed and variable values of the deformation potential. Results are for three values of the deformation potential D, ranging from $\approx$3-15eV. This wide range allows comparison with theoretical predictions since calculations for zig-zag CNTs indicate a $D\approx 9eV$[140, 142], whereas calculations for graphite have resulted in a deformation potential of $D\approx 16eV$[153]. We see in Fig. 6.13 that the critical field, F_c, at which the drift velocity peak occurs, increases with increasing D. This is expected since the larger the scattering rate the larger the field must be to significantly populate the second subband. There is however little change in the drift velocity peak with D indicating that v_d^{max} is much more sensitive to the conduction velocity of the first subband than the scattering rate. The low field mobility decreases with increasing D as expected from Eq. 6.38.

6.4 Chapter Summary

In summary, semiclassical transport has been applied to electron conduction through long "perfect" semiconducting zig-zag carbon nanotubes with wrapping indexes between 10 and 59. The zone-folding method is used to calculate the electronic energy levels consisting of two valleys, while scattering occurs through the interaction of electrons with the zone-folded longitudinally-polarized acoustic and optical phonons of graphene. Steady-state charge transport simulations considering a homogeneous applied electric field are performed using the Monte Carlo method.

Simulations at low fields show electron mobilities as large as in graphite for

the larger tubes. At higher fields, the drift velocity is found to rise and peak with increasing field, reaching values as high as 5 $X10^7$ cm/s in the larger tubes. It should be noted that the ability to extend the transport model to even larger zig-zag tubes in order to determine how these properties evolve further is limited by the decreasing energy spacing between the first two subbands. In larger tubes, the transport model must be altered if this spacing becomes small enough to allow field-assisted intersubband transitions or if the spacing approaches the thermal energy of the electrons.

The peaks in the electron drift velocity, which vary with n, show negative differential mobility due to electron transfer between the first two electronic sub-bands. This transfer may occur within the same or within different but equivalent band structure valleys. This effect also occurs in other traditional semiconductors with small direct bandgaps such as GaAs, but in these materials electron transfer between unequivalent valleys in the electronic band structure is usually involved. It is likely that some of the electronic properties of these materials may also exist in CNTs. One interesting property of GaAs related to NDM is its ability to support microwave fluctuations in the electron current know as the Gunn-effect[154]. There are many applications of the NDM in these materials. Applications in electronics include use in oscillators, amplifiers, and logic and functional devices[155]. It may be possible that similar applications for CNTs may also exist.

Using our Monte Carlo results, we have developed a mobility model to describe transport in semiconducting SWCNTs. Large low-field mobilities are found to be $\approx 0.4 - 13\text{x}10^4 cm^2/Vs$, which is of the same order of those observed in recent

experiments [30, 31]. The results also indicate negative differential mobility at larger fields, and a very large drift velocity peak of ≈ 3 to $6\text{x}10^7 cm/s$.

The mobility model can be used to easily predict the characteristics of electron transport in these tubes, and should find significant applications in the simulation and understanding of nanotube-based electronic devices. In Fig. 6.14 we show the resulting mobility model vs. applied field for a number of SWCNTs. The mobility is high in the low-field region, then drops as the electrons begin to significantly populate the second subband. The larger mobilities for wider tubes is attributed to a smaller effective mass and a smaller scattering rate.

Subband 1

$E_1^m(n) = \frac{\pi\gamma}{\sqrt{3}n}$ **[0.55eV]**

$m_1^*(n) = \frac{3m_e}{n\gamma}\big(1 - .0044n + \frac{gcd(n+1,3) - gcd(n-1,3)}{n}\big)$ **[0.068**m_e**]**

$\alpha_1(n) = \frac{3}{2\gamma}(.3n - 1)$ **[1.43]**

$\eta_1(n) = \pm\eta_0$ **[±7]**

Subband 2

$E_2^m(n) = 2E_1^m(n)\big(1 + \frac{gcd(n-1,3) - gcd(n+1,3)}{3n}\big)$ **[1.18eV]**

$m_2^*(n) = m_1^*(n)\Big(\frac{E_2^m(n)}{E_1^m(n)} + \frac{5}{n}\big[\frac{E_2^m(n)}{E_1^m(n)}(gcd(n-1,3) - 1) - (gcd(n+1,3) - 1)\big]\Big)$ **[0.327**m_e**]**

$\alpha_2(n) = \frac{3}{2\gamma}(.2n - 1)$ **[0.64]**

$\eta_2(n) = \pm 2(n - \eta_0)$ **[±6]**

Subband 3

$E_3^m(n) = 4E_1^m(n)\big(1 + \frac{1 + 2gcd(n+1,3) - 3gcd(n-1,3)}{4n}\big)$ **[1.90eV]**

$m_3^*(n) = m_1^*(n)\Big(\frac{E_3^m(n)}{E_1^m(n)} + \frac{5}{n}\big[\frac{E_3^m(n)}{E_1^m(n)}(gcd(n+1,3) - 1) - (gcd(n-1,3) - 1)\big]\Big)$ **[0.202**m_e**]**

$\alpha_3(n) = \frac{3n^2}{300\gamma}$ **[0.39]**

$\eta_3(n) = \pm 2(2\eta_0 - n)$ **[±8]**

Table 6.1: CNT Band Structure Properties. (Results for n=10 are shown in brackets []. Here η_0 is $\frac{2n}{3}$ rounded to the nearest integer, and $gcd(x, y)$ is the greatest common divisor of x and y.)

Phonon	**Band Transfer**	$E_p^o(\eta_p)$ **(meV)**	$\eta_p(n)$
LA	intrasubband-intravalley	0	0
$LA-1$	intersubband-intravalley $1 \leftrightarrow (2,3)$	$\frac{3000}{8n}$[**38**]	± 1
$LA-2$	intersubband-intravalley $2 \leftrightarrow 3$	$\frac{3000}{4n}$[**74**]	± 2
$LAIV$	intersubband-intervalley $1 \leftrightarrow 1$	158	$\pm 2(n-\eta_0)$[**6**]
$LAIV$	intersubband-intervalley $2 \leftrightarrow 2$	158	$\pm 2(2\eta_0-n)$[**8**]
$LAIV-1$	intersubband-intervalley $3 \leftrightarrow 3$	$158(1-\frac{12}{n^2})$[**132**]	$\pm 2(3n-4\eta_0)$[**4**]
$LAIV$	intersubband-intervalley $1 \leftrightarrow 2$	158	$\pm\eta_0$[**7**]
$LAIV$	intersubband-intervalley $1 \leftrightarrow 3$	158	$\pm(4n-5\eta_0)$[**5**]
$LAIV$	intersubband-intervalley $2 \leftrightarrow 3$	158	$\pm 2(n-\eta_0)$[**6**]

Table 6.2: CNT acoustic phonon properties. (Results for n=10 are shown in brackets []. Here η_0 is $\frac{2n}{3}$ rounded to the nearest integer and $E_p^o(\eta_p(n))$ is the phonon energy at q_z=0. Intravalley modes show linear dispersion with a characteristic velocity of υ_s=20 km/s.)

Phonon	**Band Transfer**	$E_p^o(\eta_p)$ **(meV)**	$\eta_p(n)$
LO	intrasubband-intravalley	.200	0
LO	intersubband-intravalley $1 \leftrightarrow (2,3)$	200	± 1
LO	intersubband-intravalley $2 \leftrightarrow 3$	200	± 2
$LOIV$	intersubband-intervalley $1 \leftrightarrow 1$	158	$\pm 2(n-\eta_0)$**[6]**
$LOIV$	intersubband-intervalley $2 \leftrightarrow 2$	158	$\pm 2(2\eta_0 - n)$**[8]**
$LOIV-2$	intersubband-intervalley $3 \leftrightarrow 3$	$158(1+\frac{30}{n^2})$**[190]**	$\pm 2(3n-4\eta_0)$**[4]**
$LOIV$	intersubband-intervalley $1 \leftrightarrow 2$	158	$\pm\eta_0$**[7]**
$LOIV-1$	intersubband-intervalley $1 \leftrightarrow 3$	$158(1+\frac{30}{2n^2})$**[180]**	$\pm(4n-5\eta_0)$**[5]**
$LOIV$	intersubband-intervalley $2 \leftrightarrow 3$	158	$\pm 2(n-\eta_0)$**[6]**

Table 6.3: CNT optical phonon properties. (Results for n=10 are shown in brackets []. Here η_0 is $\frac{2n}{3}$ rounded to the nearest integer and $E_p^o(\eta_p(n))$ is the phonon energy at q_z=0. $LOIV$ modes show linear dispersion with a characteristic velocity of υ_s=50/n km/s.)

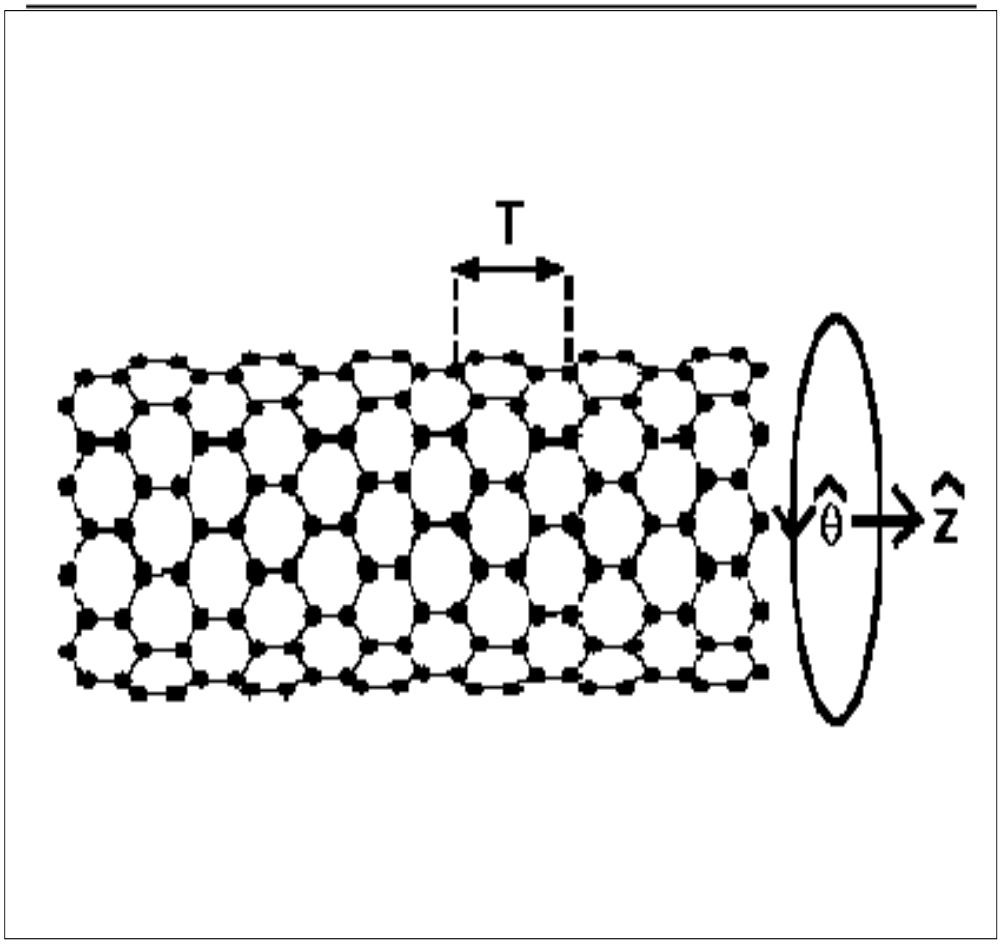

Figure 6.1: Zig-zag n=10 carbon nanotube, where T is the unit cell length.

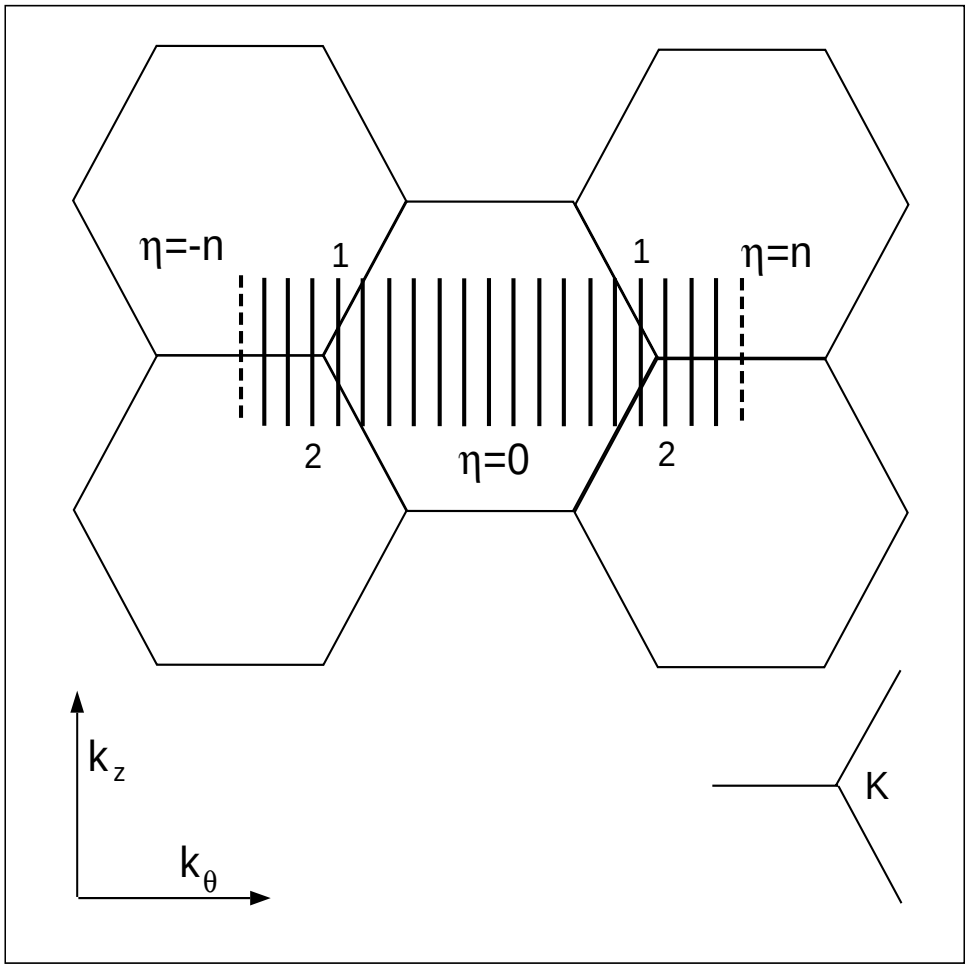

Figure 6.2: Brillouin zone for a zig-zag semiconducting CNT superimposed on graphene k-space. (The example here is for an n=10 tube. The wavevector along the tube axis and perpendicular to it are k_z and k_θ respectively. Two types of semiconductors are possible depending on if slice 1 or slice 2 gives bands closest to the Fermi level. Type 1 is when the greatest common divisor $gcd(n+1,3) = 3$ and type 2 is when $gcd(n-1,3) = 3$. The 2 dashed(- - -) lines for $\eta = \pm 10$ are for the zone boundary and count as just one complete slice. The tube type labeling here is distinct from the subband labeling used.)

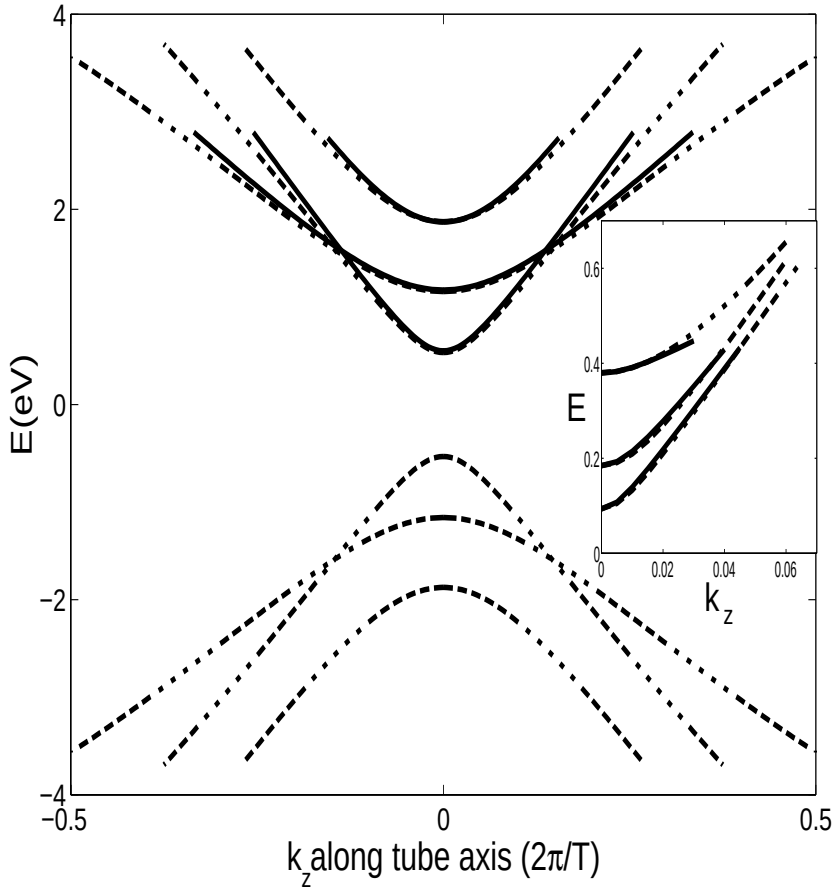

Figure 6.3: Band Structure for a $n = 10$ zig-zag CNT. (Tight-binding band structure (dash line) and the model subands (solid line) of Eq. (6.4) are shown. The inset is for a $n = 59$ tube. These represent the range of CNT sizes simulated in this work.)

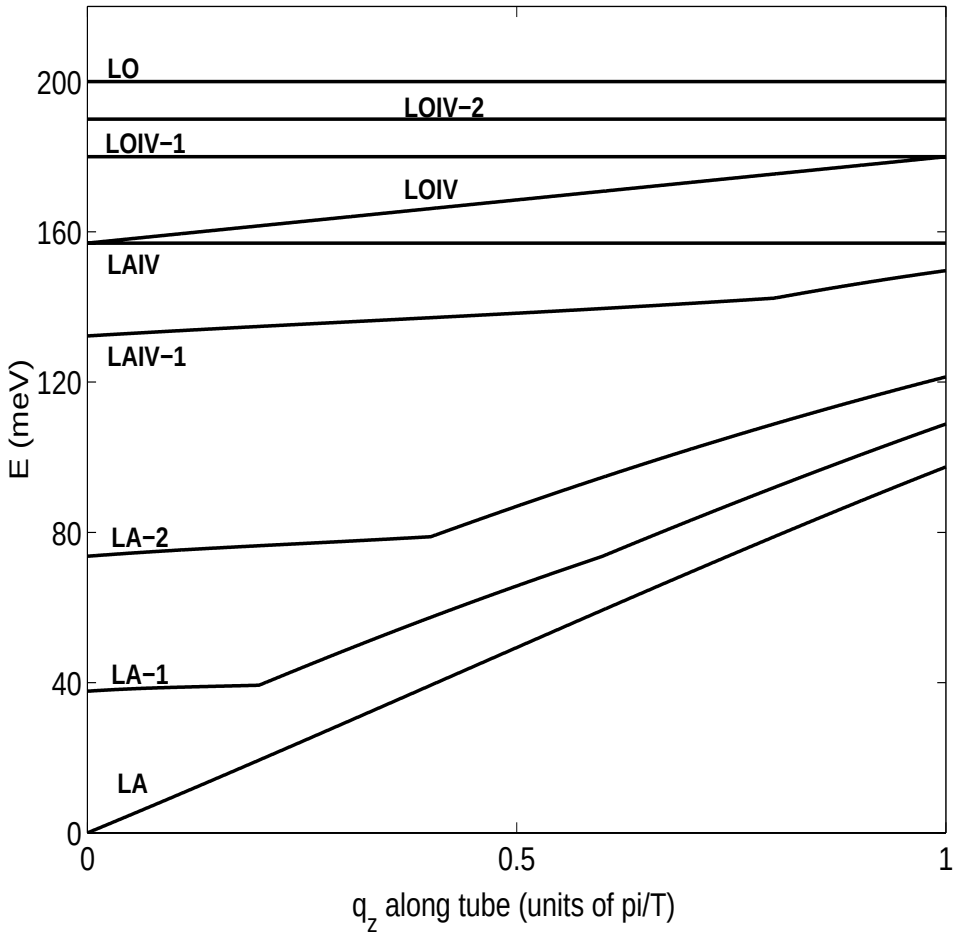

Figure 6.4: Carbon nanotube phonon dispersion for a $n = 10$ zig-zag tube.

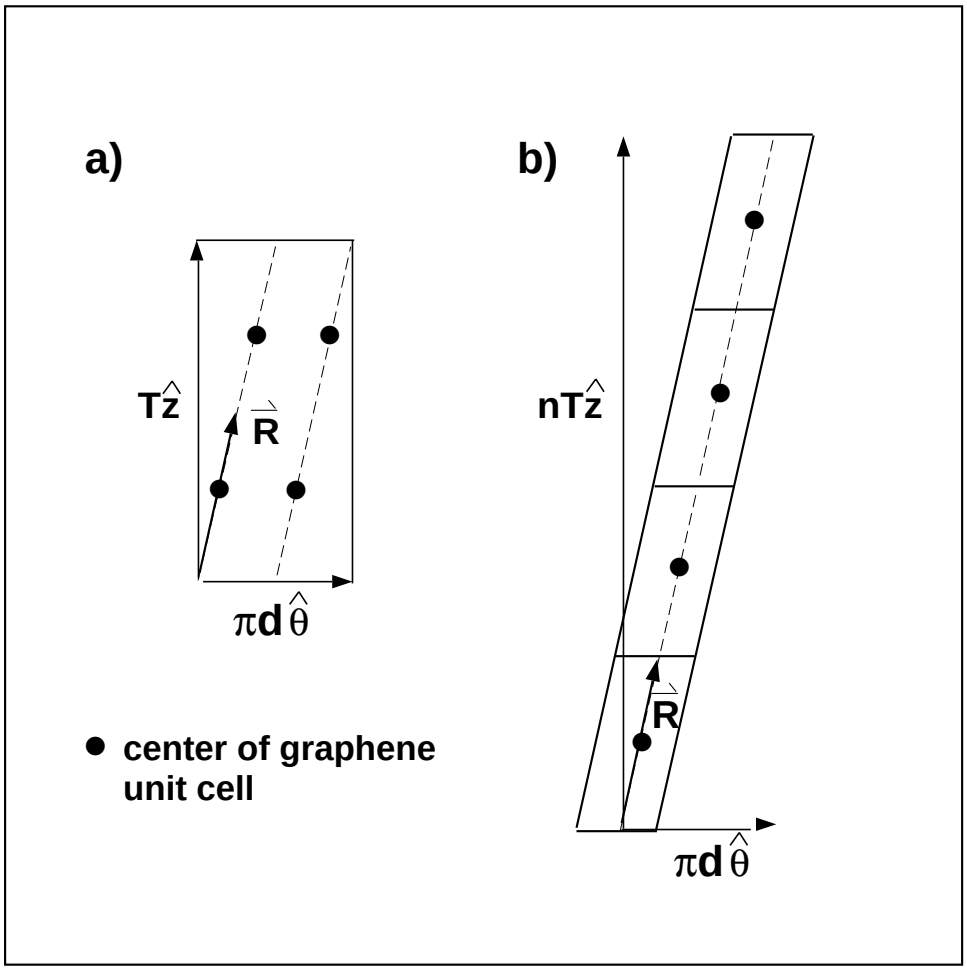

Figure 6.5: a) Unit cell for a (n,m)=(2,0) CNT. (Four graphene unit cells are contained and located at multiples of the wrapped symmetry vector $\vec{R}$.) b) Unwrapped CNT unit cell.

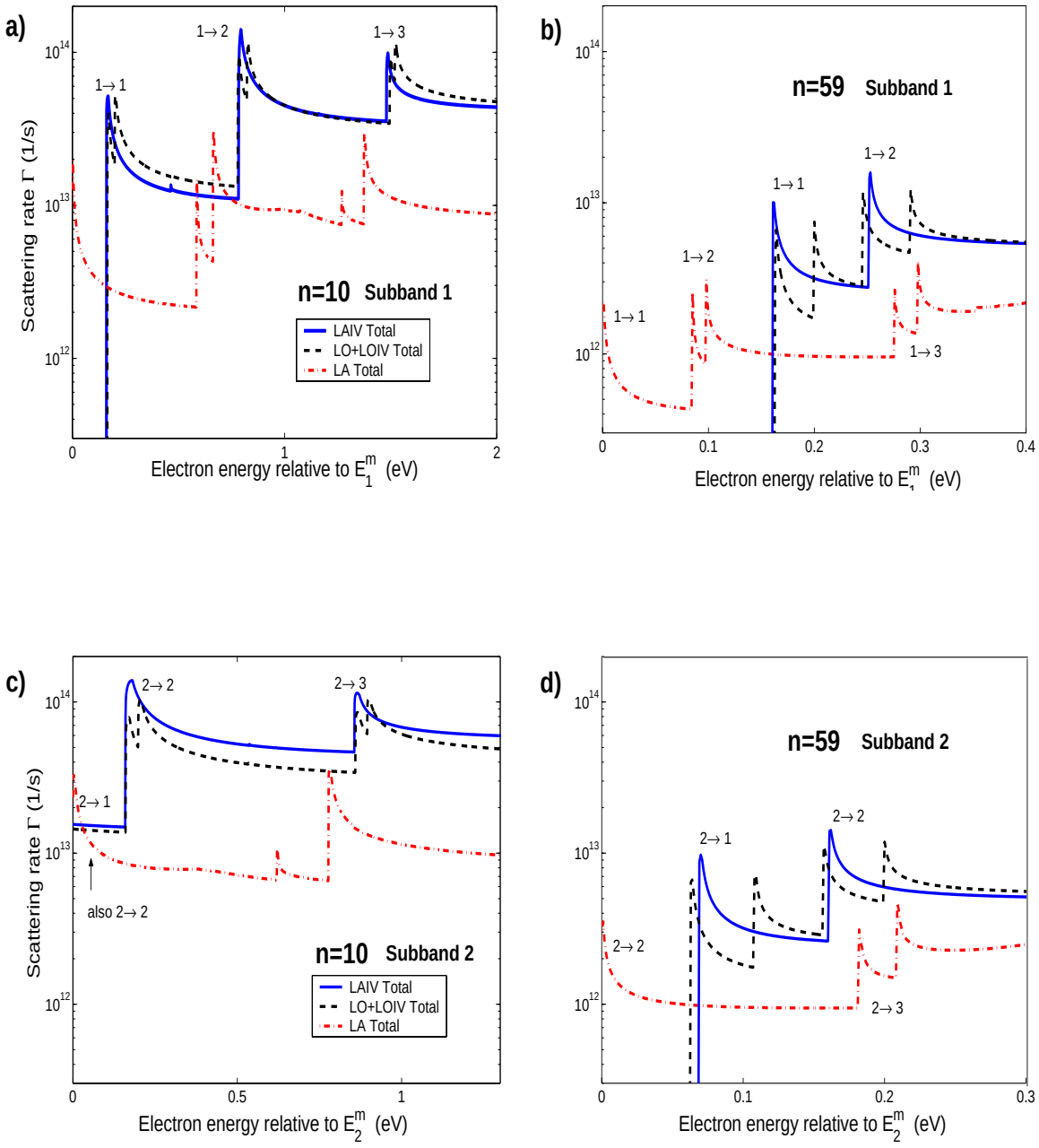

Figure 6.6: Room temperature scattering rate Γ as a function of electron energy for: a) electron in band 1 of an $n = 10$ tube, b) electron in band 1 of an $n = 59$ tube, c) electron in band 2 of an $n = 10$ tube, and d) electron in band 2 of an $n = 59$ tube.

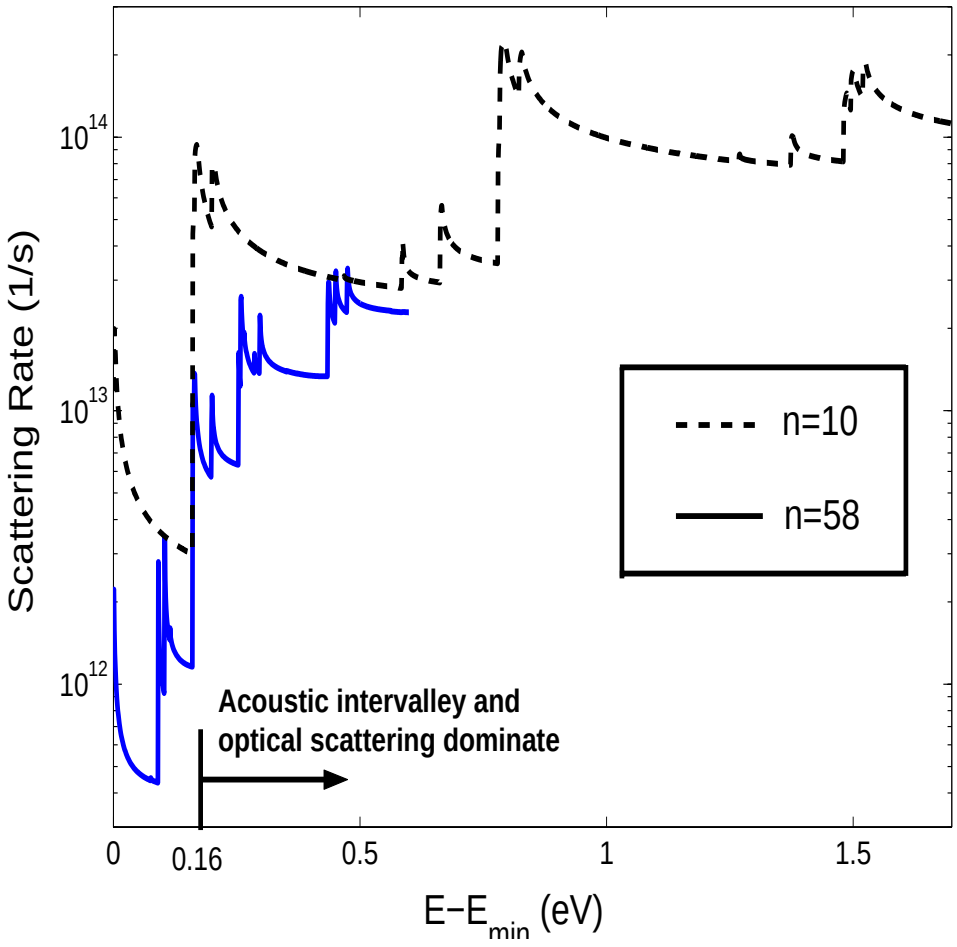

Figure 6.7: Total scattering rate of a subband 1 electron for a n=10 and a n=58 carbon nanotube.

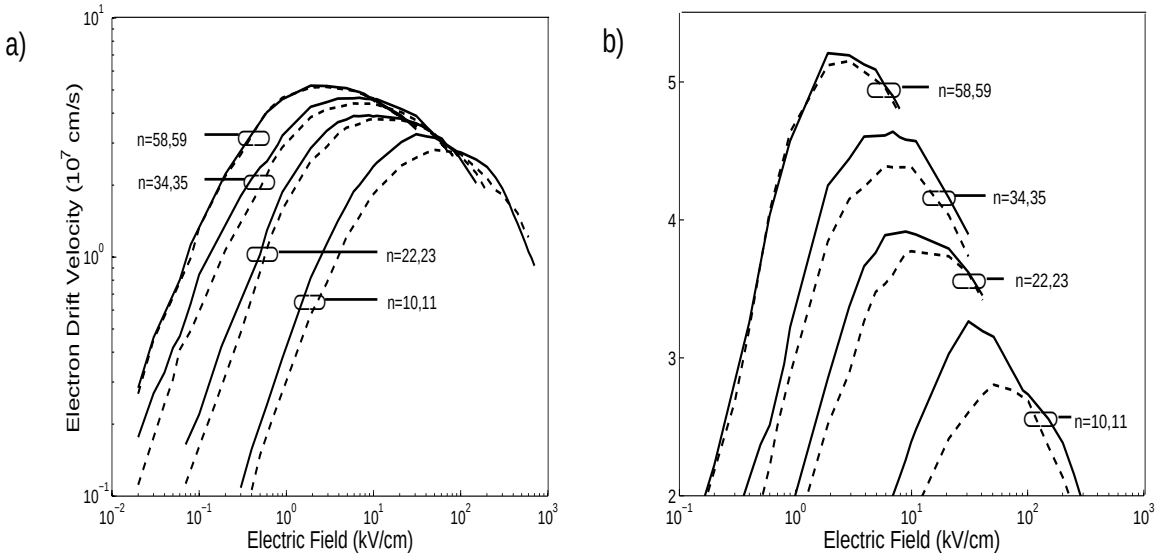

Figure 6.8: Simulated drift velocity vs. homogenous electric field for a number of zig-zag CNTs with indices n. (Only acoustic phonon scattering is included here. Both the high and low field results are shown in *a)*, while *b)* focuses on the peaks in the simulated drift velocity. Monte Carlo results are shown for type 1 tubes (- -), where $n+1$ is a multiple of 3, and for type 2 tubes (—), where $n-1$ is a multiple of 3. The variation in the drift velocity between the two tube types is significant only for the small tubes.)

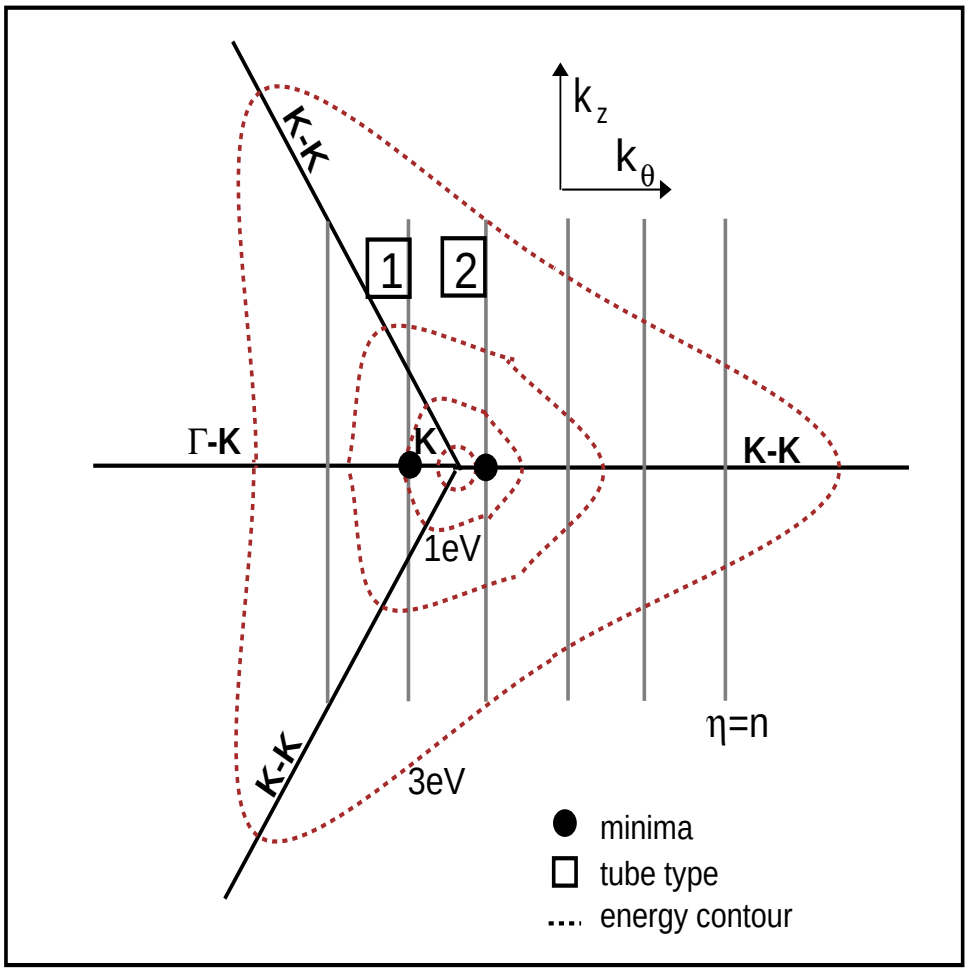

Figure 6.9: Tridiagonal warping of the electronic bandstructure. (Here the Brilliouin zone for a tube-type 2 n=10 tube is shown. For a type 1 tube the lowest subband would be along Γ-K as shown.

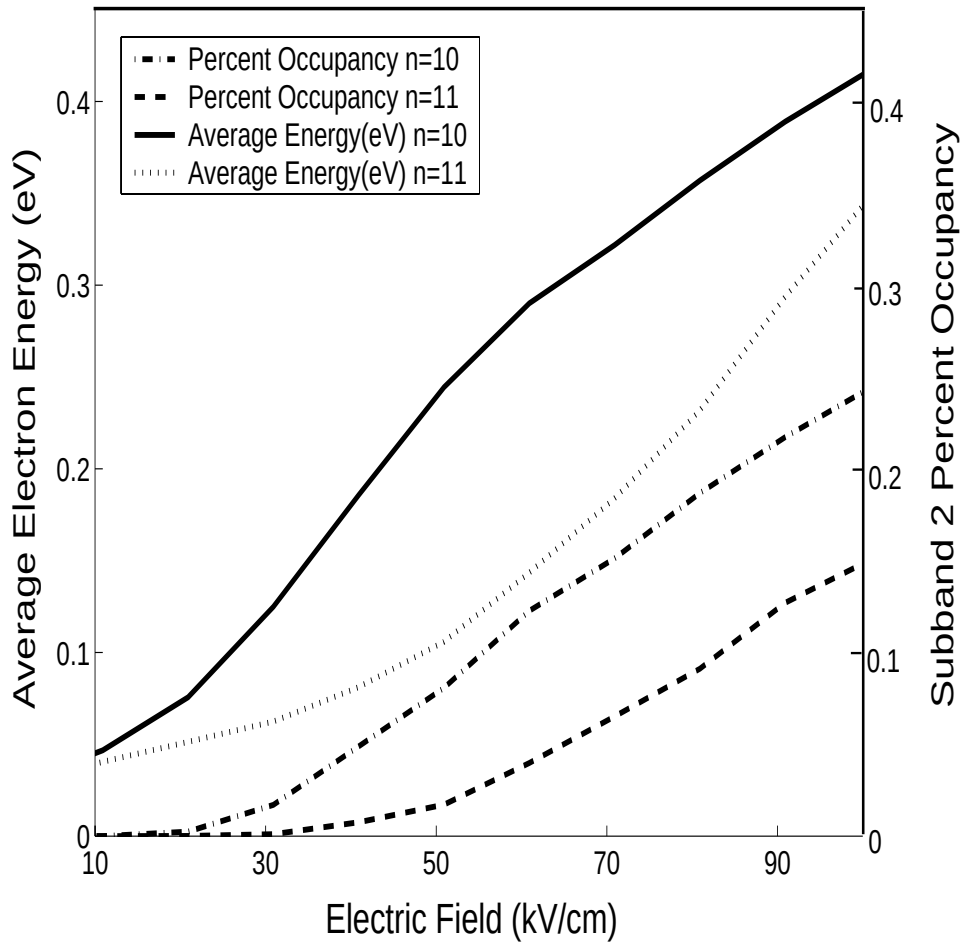

Figure 6.10: Simulated average electron energy and percent occupancy of subband 2 vs. electric field in a $n = 10$ and a $n = 11$ zig-zag CNT.

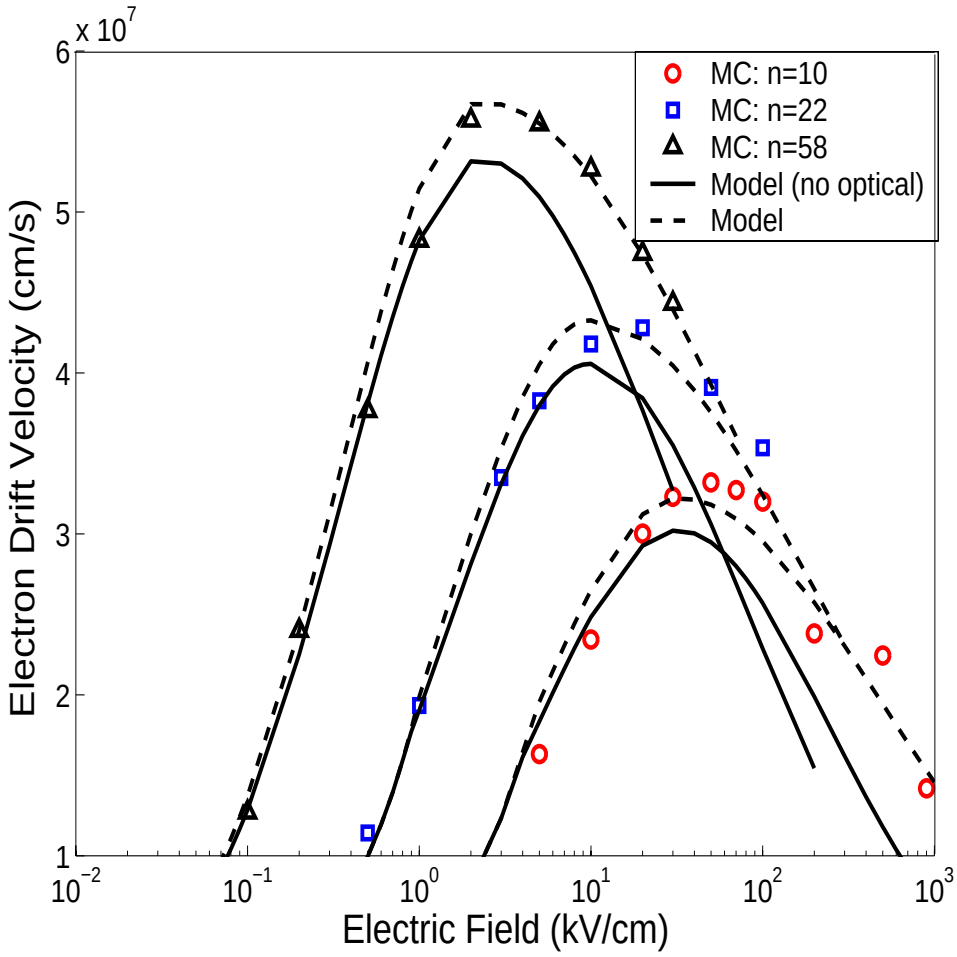

Figure 6.11: Monte Carlo drift velocity peaks for a number of tube diameters. The peaks with and without including optical phonon scattering are shown.

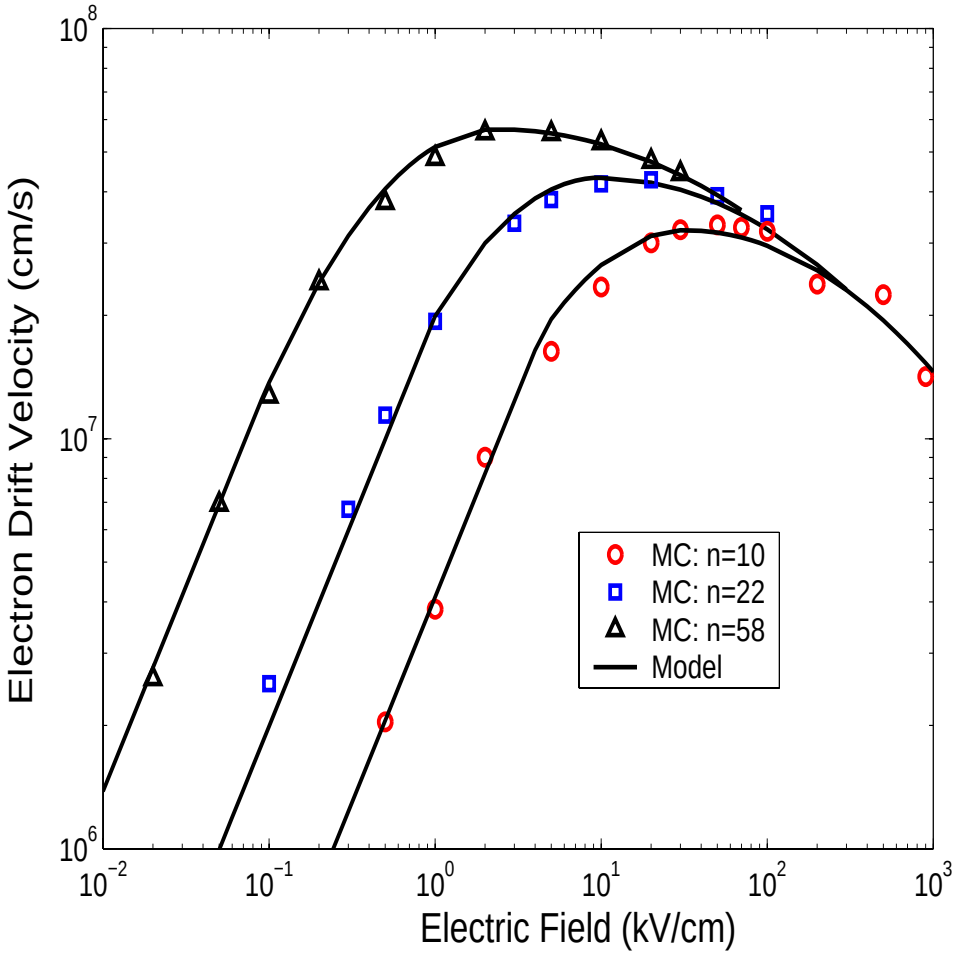

Figure 6.12: Monte Carlo electron drift velocity vs. applied electric field for zig-zag SWCNTs with indices n= 10, 22, and 58 (symbols). The results of the mobility model multiplied by the applied field are also shown (solid lines).

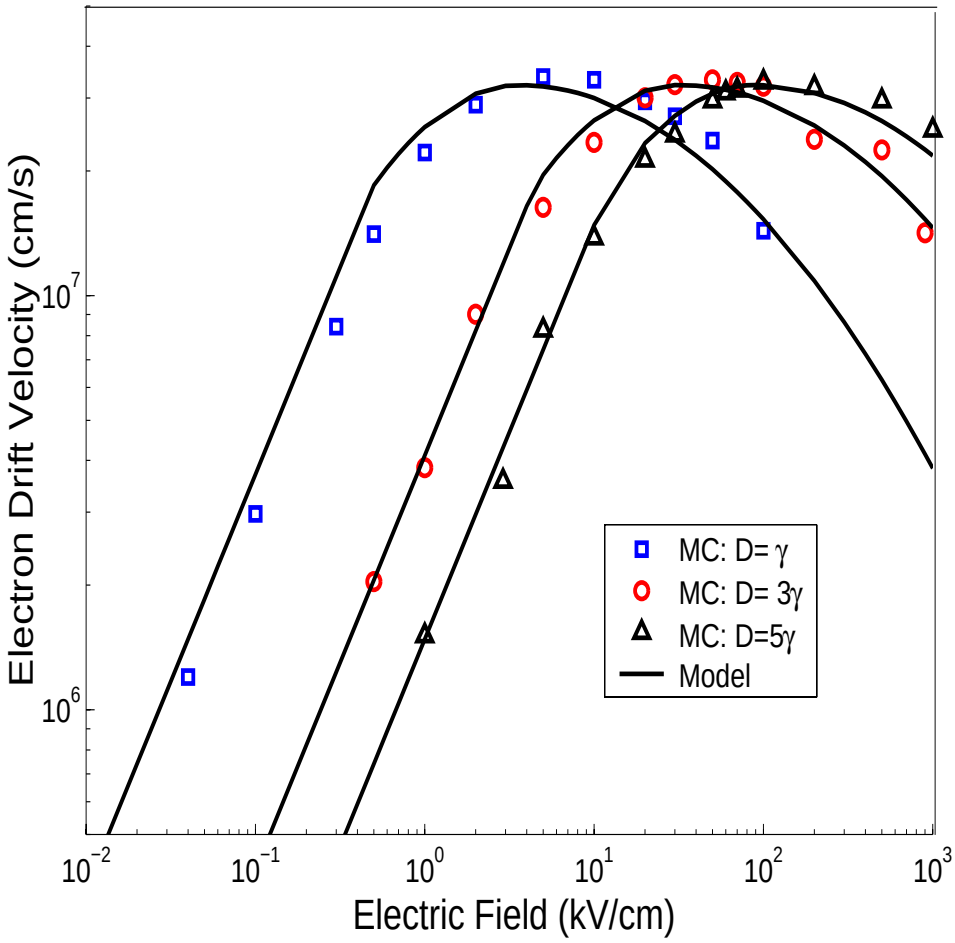

Figure 6.13: Monte Carlo electron drift velocity vs. applied electric field for an n=10 zig-zag SWCNT with varying deformation potentials of D= γ, 3γ, and 5γ (symbols). The results of the mobility model multiplied by the applied field are also shown (solid lines).

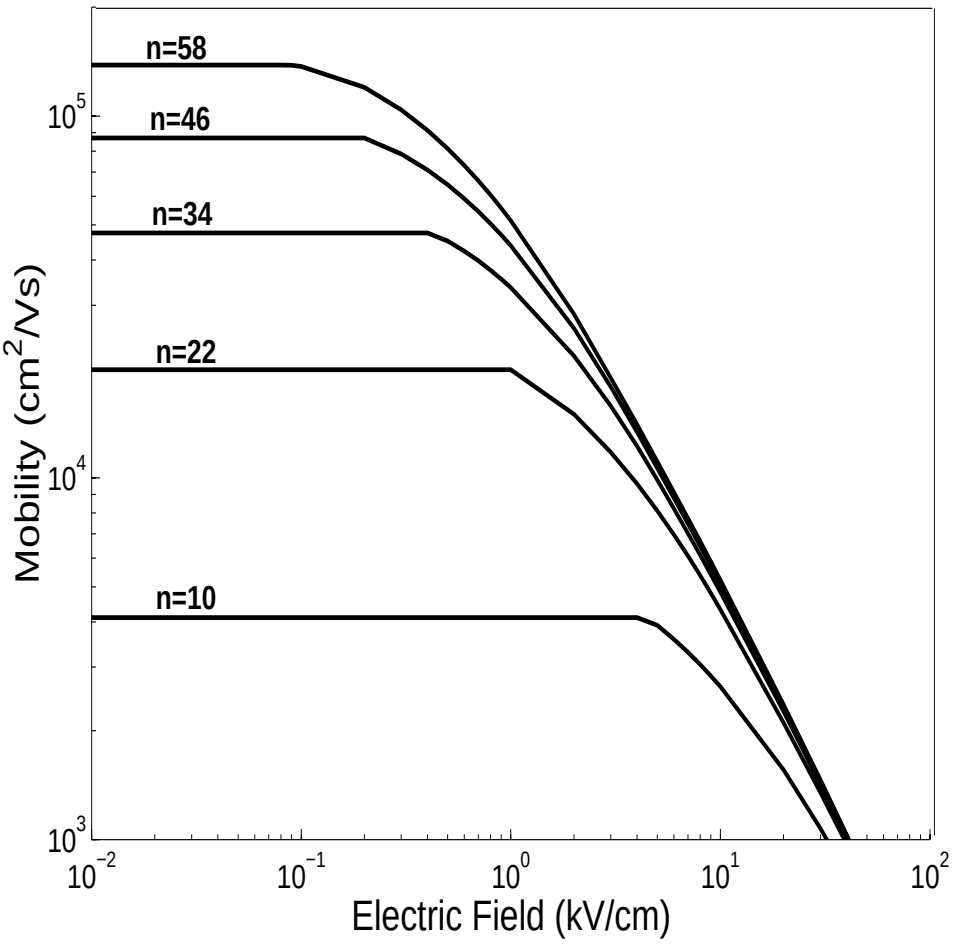

Figure 6.14: Mobility model vs. applied electric field for a number of zig-zag SWCNTs.

Chapter 7

Conclusion

In this dissertation a study of silicon carbide and carbon nanotubes is presented. Both are materials with potentially new applications in electronics. For each we studied the material properties related to the transport electrons. This included calculations of the electronic structure and the Monte Carlo simulation of electron transport.

7.1 Silicon Carbide

The motivation for exploring the transport properties of SiC stems from its high saturation velocity, high thermal conductivity and large breakdown voltage, which leads to a wealth of potential applications in electronic devices operating at high

temperature and high power. A new approach to the empirical pseudopotential method (EPM) calculation of the band structure of SiC is presented which overcomes the need for extensive experimental data. The method reduces the roughly 30 EPM fitting parameters needed to just two for 4H and one for 6H SiC. This allows fitting to the limited amount of experimental data available for these polytypes and the subsequent use of the EPM to calculate their band structure. A means of fitting to experimental effective masses through a nonlocal correction is also introduced. The procedure involves the construction of the empirical pseudopotential of diamond phase Si and C from local-model potentials based on the Heine and Abarenkov potential. These potentials successfully reproduce the experimental band energies around the band gap region using one fitting parameter for each material. Once charge transfer is introduced, the potentials are then transferred to the heteropolar polytypes of SiC and the local potential is fit to the experimental band energies using just one local fitting parameter for each polytype. A nonlocal correction, introducing a second additional fitting parameter, is then included to fit the experimental effective masses of 3C and 4H SiC. Since reasonable agreement with experimental effective mass measurements was obtained in 6H SiC with just the one local parameter, the nonlocal correction was not used.

A study of high-field temperature-dependent electron transport in bulk 6H-SiC is also presented. This investigation is carried out using a full-band Monte Carlo method(FBMCM) simulator which is developed specifically for modeling SiC. Since the effective mass is extremely large along the c-axis[32], transport was simulated in the plane perpendicular to the c-axis. With a large number of highly anisotropic

conduction bands close to the band edge, the transport properties of 6H-SiC is highly dependent on the band structure. Here the full details of the multiband band structure is included, using the model pseudopotential approach of Chapter 2. The resulting band structure, was inputed into the FBMCM code, Using temperature-dependent drift velocity measurements[90] and the FBMCM simulator, results for the acoustic and intervalley optical deformation potentials were determined. The fitted deformation potentials were found to compare well with experiments over a wide temperature range. The number of conduction bands and band structure valleys needed for high field simulations was addressed. The first four conduction bands are found to be significantly occupied in the saturation region at room temperature, while only the first three are occupied at 600 K. The Γ valley is found to be significantly occupied at large fields. The temperature dependence of the saturation velocity and high field mobility was also determined from the Monte Carlo simulations. The simulations showed that the drift velocity in the plane perpendicular to the c-axis saturated at $1.71X10^7$ cm/s at room temperature and at $1.05X10^7$ cm/s at 1000 K.

In Chapter 4 results for the surface band structure calculation of 4H-SiC and 6H-SiC was presented. This was carried out by solving for the electronic subband levels and the electrostatic potential together self-consistently. The Brillouin zones for a number of surface orientations were found and presented for the first time.

It was found that the conduction band edge for the $(01\overline{1}0)$ and $(03\overline{3}8)$ orientations was split into 2 distinct ladders. The effective masses parallel to the interface were found to be similar in 4H-SiC for each orientations. This was not the case in

6H-SiC although where considerable anisotropy was found.

In the case of the $(11\overline{2}0)$ surface, two subband ladders where also found. these two ladders were very similar in 4H-SiC, and were enfact similar to the one (0001) ladder. This was not the case in 6H-SiC were each of the $(11\overline{2}0)$ ladders were found to be very distinct from the single (0001) 6H-SiC ladder. The behavior of $(11\overline{2}0)$ 4H-SiC was unique at very low temperatures. In this orientation the two ladders are so closely spaced, $\approx .01eV$ for the doping in Fig. 4.7(d), that both ladders are occupied at very low temperatures. The (0001) orientation of 6H-SiC was found to be very distinct from every other orientation considered. Here the inversion layer electrons tend to reside very close to the oxide interface.

In Chapter 5 the surface band structure calculations were incorporated into Monte Carlo simulations of electron transport in (0001) and $(11\overline{2}0)$ 4H-SiC. With a careful analysis of experimental data[11] for the (0001) orientation, analytical models for the free carrier and trapped carrier densities along with the threshold voltage were extracted. The threshold voltage decreased with increasing temperature as T^{-2}. The trapped carrier density was very large at the (0001) 4H-SiC/oxide interface. It decreased with increasing temperature. The free carrier density however increased with increasing temperature. These trends are related to the increasing trap density near the conduction band edge of 4H-SiC.

Upon simulation of the low-field mobility for the (0001) orientation, a $1/T$ dependence was found, matching the experimental findings[11]. This was found to be the result of both a decrease in the trapped charge density and an increase in the screening of the trapped charge by the free electrons in the inversion layer.

Procceding to simulate the $(11\overline{2}0)$ surface of 4H-SiC, the simulated mobility far exceeded the results for the (0001) orientation. This was due to a reduced density of trap states. The result agreed well with experiments on the $(11\overline{2}0)$ orientation[118]. Our results support the belief that a $(11\overline{2}0)$ 4H-SiC/SiO_2 should improve the problematic low mobilities of 4H-SiC inversion layers.

7.2 Carbon Nanotubes

Experiments have indicated that gated single-walled carbon nanotubes (SWCNTs) act as tiny field-effect transistors[29]. The mechanism is believed to be the gate potentials manipulation of a Schottky barrier at the nanotube/metal contact junction[156]. It is hoped that arrays of such FETs could be developed into integrated circuits that could be used to perform computer logic[157]. The advantage would be the ability to pack an enormous number of transistors into a small space, due to the small dimensions of the nanotube.

Nanotubes could also however be used to supplement the existing silicon technology. In this case the apparently large mobility[123] of SWCNTs could be used to produce fast electronic devices. One example is to embed a SWCNT into a silicon MOSFET[35]. In such applications long nanotubes could be used, and a semiclassical picture of electron transport developed. The work in Chapter 6 was aimed at developing such a semiclassical transport picture. Models for the electronic energy spectrum and the phonon energy spectrum as a function of tube index were developed. Only semiconducting zig-zag tubes where considered.

Monte Carlo simulations indeed showed large mobilities in the low-field region. Increasing with tube index n for tube with diameters in the range of approximately 0.8-4.6nm .This was the result of a decrease in the effective mass and an increase in the linear mass density as n increased. The simulations showed mobilities on the order of experiments[123, 30]. Also large drift velocity peaks reaching 5x10$^7 cm/s$ were simulated. After the peak, negative differential mobility (NDM) was observed. These effects were found to result from the increase in effective mass as electrons are transferred from subband 1 to subband 2 with increasing field. This is the first prediction of such a transferred electron effect NDM in carbon nanotubes. It is believed that electronic device applications, such as oscillators, may result from such an effect.

7.3 Thesis Journal and Conference Paper Publications

G. Pennington, Akin Akturk, and N. Goldsman, "Electron Mobility of a Semiconducting Carbon Nanotube.", 2003 International Semiconductor Device Research Symposium Proceedings, Washington, D.C.

G. Pennington, N. Goldsman, James M. McGarrity, Aivars Lelis, and Charles J. Scozzie "Mobility of (1120) and (0001) Oriented 4H-SiC Quantized Inversion Layers.", 2003 International Semiconductor Device Research Symposium Proceedings, Washington, D.C.

G. Pennington, A. Akturk, and N. Goldsman, "Drift Velocity and an Electron Mobility Model for Carbon Nanotubes.", Elec. Dev. Lett. "submitted for publication".

G. Pennington and N. Goldsman, "Self-consistent calculations for n-type hexagonal SiC inversion layers.", J. Appl. Phys. "submitted for publication".

A. Akturk, G. Pennington, and N. Goldsman, "Modeling the Enhancement of Nanoscale MOSFETs by Embedding Carbon Nanotubes in the Channel," 3rd IEEE Conf. on Nanotech. (NANO 2003), San Francisco, USA, p24.

G. Pennington and N. Goldsman, "Theory and design of field-effect carbon nanotube transistors.", 2003 International Conference on Simulation of Semiconductor Processes and Devices (SISPAD 2003), Boston, USA, p. 167.

G. Pennington and N. Goldsman, "Semiclassical transport and phonon scattering of electrons in semiconducting carbon nanotubes.", Phys. Rev. B **68**, 45426 (2003).

G. Pennington and N. Goldsman, "Monte Carlo study of electron transport in a carbon nanotube.", IEICE Trans. Electron. **E86-C**, 372 (2003).

G. Pennington and N. Goldsman, "Monte Carlo simulation of electron transport in a carbon nanotube.", 2002 International Conference on Simulation of Semiconductor Processes and Devices (SISPAD 2002), Kobe, Japan, p. 279-82

G. Pennington, N. Goldsman, S. Scozzie, J. M. McGarrity, "Investigation of temperature effects on electron transport in SiC using unique full band Monte Carlo simulation.", 2001 International Semiconductor Device Research Symposium Proceedings, Washington, D.C., p.531-4

G. Pennington, N. Goldsman, "Modeling the effective mass and Y-junction rectifying current of carbon nanotubes.", 2001 International Semiconductor Device Research Symposium Proceedings, Washington, D.C., p.310-13

G. Pennington and N. Goldsman, "Modeling semiconductor carbon nanotube rectifying heterojunctions.", 2001 International Conference on Simulation of Semiconductor Processes and Devices (SISPAD 2001), Athens, Greece, p. 218-21

G. Pennington and N. Goldsman, "Empirical pseudopotential band structure of 3C, 4H, and 6H SiC using transferable semiempirical Si and C model potentials.", Phys. Rev. B **64**, 45104 (2001).

G. Pennington, N. Goldsman, S. Scozzie, J. M. McGarrity, "Investigation of temperature effects on electron transport in SiC using unique full band Monte Carlo simulation.", 2001 International Semiconductor Device Research Symposium Proceedings, Washington, D.C., p.531-4

G. Pennington, N. Goldsman, J. M. McGarrity, and F. Crowne, "A physics-based empirical pseudopotential model for calculation band structures of simple and complex semiconductions.", 2000 International Conference on Simulation of Semiconductor Processes and Devices (SISPAD 2000), Seattle, USA, p. 229-32

G. Pennington, N. Goldsman, J. M. McGarrity, and F. Crowne, "Nonlocal-empirical pseudopotential calculation of 4H-SiC band structure for use in electron transport investigations.", 1999 International Semiconductor Device Research Symposium Proceedings, Charlottesville, USA

7.4 Thesis Talks and Poster Presentations

Electron Mobility of a Semiconducting Carbon Nanotube., 2003 International Semiconductor Device Research Symposium Proceedings, Washington, D.C.

Mobility of (1120) and (001) Oriented 4H-SiC Quantized Inversion Layers., 2003 International Semiconductor Device Research Symposium Proceedings, Washington, D.C.

Comparison of $(11\bar{2}0)$ and (0001) Surface Orientations in 4H-SiC Inversion Layers., 2003 Semiconductor Interface Specialists Conference (SISC 2003), Washington, D.C., USA

Theory and design of field-effect carbon nanotube transistors., 2003 International Conference on Simulation of Semiconductor Processes and Devices (SISPAD 2003), Boston, USA

Degradation of Inversion Layer Mobility in 6H-SiC by Interface Charge. 2002 Semiconductor Interface Specialists Conference (SISC 2002), San Diego, USA (poster only)

Monte Carlo simulation of electron transport in a carbon nanotube., 2002 International Conference on Simulation of Semiconductor Processes and Devices (SISPAD 2002), Kobe, Japan,

Investigation of temperature effects on electron transport in SiC using unique full band Monte Carlo simulation., 2001 International Semiconductor Device Research Symposium Proceedings, Washington, D.C.

Modeling semiconductor carbon nanotube rectifying heterojunctions., 2001 International Conference on Simulation of Semiconductor Processes and Devices (SISPAD 2001), Athens, Greece

A physics-based empirical pseudopotential model for the calculation of band structures of simple and complex semiconductions., 2000 International Conference on Simulation of Semiconductor Processes and Devices (SISPAD 2000), Seattle, USA (poster only)

Nonlocal-empirical pseudopotential calculation of 4H-SiC band structure for use in electron transport investigations., 1999 International Semiconductor Device Research Symposium Proceedings, Charlottesville, USA

Appendix A

Model Pseudopotential

A.1 Theory of the Atomic Pseudopotential

The choice of a successful band structure method to attain the electronic structure of a crystalline solid, depends on how strongly the valence electrons interact with the atomic cores of the crystal. The core consists of the nucleus and the tightly bound electrons. If electrons interact strongly with the cores, then the electronic wavefunctions will be similar to the atomic wavefunctions and a band structure method such as the tight-binding method would be appropriate. In cases where the electrons stay out of the atomic cores, then a plane wave band structure method would typically be more appropriate.

The pseudopotential band structure method (PM)[43] falls into the relm of plane

wave methods where the electron-core interaction is considered to only weakly impact the electronic structure. The electron-core interaction can therefore be simplified. In the PM the atomic core is assumed to be frozen in an atomic-like configuration, and is represented as an ion. To built into the formalism the lack of valence electron density within the core, a fictitious repulsive force V_r is included within the core. This could be interpreted as an overestimation of the repulsive force between the core electrons and the valence electrons. The calculation of the electronic structure is simplified by the addition of this force since it allows the use of a smooth potential and wavefunction in the core region. These are the pseudopotential and the pseudowavefunction, and differ from the real potential and real wavefunction only in the core. The primary concern within the core then becomes the adjustment of the boundary conditions, which influences the valence electron wavefunction outside of the core.

The form of the fictitious repulsive potential can be realized with the use of the orthogonal-plane-wave method. Here the purpose is also to smooth the core potential. The real wavefunction is expected to be smooth outside of the core and rapidly oscillating inside the core where it will assume a form orthogonal to the core states due to c electron-electron interactions. This can be represented as

$$\psi = \phi - \sum_t < \phi_t | \phi > \phi_t, \tag{A.1}$$

where ϕ is a smooth function and ϕ_t are the occupied core states. The expansion coefficients of the ϕ_t states are fixed by requiring the weak increase of υ_d^{max} with n is related to the increase of the conduction velocity of the first subband. Also F_c

increases as the phonon scattering increases and is approximately proportional to D^2/n.

ψ be orthogonal to these core states.

Now assuming $H\psi = E\psi$ and $H\phi_t = E_t\phi_t$, and operating on the wavefunction with the Hamiltonian

$$H = \frac{p^2}{2m} + V_c^a + V_r^a, \tag{A.2}$$

the result is

$$\left[\frac{p^2}{2m} + V^C + V^R\right]\phi(\vec{r}) = E\phi(\vec{r}). \tag{A.3}$$

Here V^C is the crystal potential and V^R is the pseudizing repulsive potential of the atomic core:

$$V^R(\vec{r},\vec{r'}) = \sum_t [E - E_t]\,|\phi_t(\vec{r'}) >< \phi_t(\vec{r})| = \sum_{l=0}^{\infty} V_l^R(r)|lm >< lm'|, \tag{A.4}$$

where in the notation we will use, there is a sum over m and m' from $-l$ to l. Notice that V^R is energy dependent and nonlocal, depending not only on the valence electron's coordinate, but also the spatial distribution of the core states. The sum over core states becomes a sum over their orbital angular momentum components and the nonlocality its determined by the quantum number l. The repulsive potential V^R is made strong enough to nearly cancel V^C within the core allowing ϕ, the pseudowavefunction, to be represented as a sum of low frequency plane waves. This potential also fixes the boundary conditions at the edge of the core so that the real band structure energies E are obtained.

The total potential including the repulsive term is the pseudopotential

$$V(\vec{r},\vec{r'}) = V^C(\vec{r}) + V^R(\vec{r},\vec{r'}) = V^L(\vec{r}) + V^{NL}(\vec{r},\vec{r'}). \tag{A.5}$$

Here the local potential V^L contains the crystal potential V^C plus the local part of V^R. The term V^{NL} is the nonlocal correction. It is usually desirable to use an energy independent and local potential. This is possible when the realm of valence electron energies of interest are much larger than the energy of the core states, so that $E - E_t$ can be assumed constant, and the cancellation at different values of l is the same. In such cases V^R is treated in a local approximation plus a small nonlocal correction V^{NL}.

The full atomic potential[50, 51, 52] consists of interactions with the ions, including the nucleus and core electrons, the valence electrons considered as a uniform density free-electron gas, and the potential due to a 1st order screening correction to the uniform density of the valence electrons. This can be written

$$V = [V_h + \Sigma_x + \Sigma_c]^i + [V_h + \Sigma_x + \Sigma_c]^b + [V_h + \Sigma_x + \Sigma_c]^{screening} + \left[\Sigma_c^{i+b} - \Sigma_c^i - \Sigma_c^b\right] \tag{A.6}$$

The first bracketed term is the ion potential including the average potential(Hartree h) along with the exchange(x) and correlation (c) potentials of the ion. The second term is for the valence(band) electrons while the third term is the screening term which will be included through the dielectric constant and nonlocal screening. The final term is a correction due to the nonadditivity of the correlation potentials.

Due to the translational symmetry of the lattice, the Fourier sum of the pseudopotential involves reciprocal lattice vectors $\vec{G}$ only. For the local potential

we have

$$V^L(\vec{r}) = \sum_{\vec{G}} V^L(\vec{G}) e^{i\vec{G}\cdot\vec{r}} \tag{A.7}$$

Here the Fourier coefficient is

$$V^L(\vec{G}) = \sum_{\alpha} S_\alpha(\vec{G}) V_\alpha^L(\vec{G}), \tag{A.8}$$

with the sum over each atomic species α present. Within this sum, $V_\alpha^L(\vec{G})$ is the Fourier transform of the atomic potential of an atom of type α. The structure factor, S, is

$$S_\alpha(\vec{G}) = \frac{1}{N_\alpha} \sum_{cell_j} \sum_{\vec{\tau}_\alpha} e^{-i\vec{G}\cdot(\vec{R}_j + \vec{\tau}_\alpha)}, \tag{A.9}$$

where the sums are over every unit cell j in the lattice and the basis vectors of species α. N_α is the total number of atoms of species α in the lattice, and $\vec{R}_j$ is the position of the jth unit cell. This can be simplified using the relation

$$\sum_{cell_j} e^{-i\vec{G}\cdot\vec{R}_j} = N_j, \tag{A.10}$$

where N_j is the number of unit cells in the lattice. The structure factor then becomes

$$S_\alpha(\vec{G}) = \frac{1}{n_\alpha} \sum_{\vec{\tau}_\alpha} e^{-i\vec{G}\cdot\vec{\tau}_\alpha}, \tag{A.11}$$

with n_α then total number of atoms of species α in the unit cell. The problem of finding the sum of potentials for each atom in the crystal has now been reduced to finding the potential of the unit cell.

The atomic potentials in Fourier space can be evaluated from the real space atomic pseudopotential according to

$$V_\alpha^L(\vec{G}) = \frac{1}{\Omega_\alpha} \int_{\Omega_\alpha} V_\alpha^L(\vec{r}) e^{-i\vec{G}\cdot\vec{r}} d^3r \tag{A.12}$$

where Ω_α is the atomic volume and $V_\alpha(\vec{r})$ is the atomic pseudopotential of species α.

So far we have been considering only the local potential, but the formalism for the nonlocal potential is the same, except that the nonlocal Fourier transform

$$V_\alpha^{NL}(\vec{k}+\vec{G_1},\vec{k}+\vec{G_2}) = \frac{1}{\Omega_\alpha^2}\int_{\Omega_\alpha} d\vec{r}\int_{\Omega_\alpha} d\vec{r'}V_\alpha^{NL}(\vec{r},\vec{r'})e^{-i\left[(\vec{k}+\vec{G_1})\cdot\vec{r}+(\vec{k}+\vec{G_2})\cdot\vec{r'}\right]}, \quad \text{(A.13)}$$

is used. Here $\vec{G}$=$\vec{G_2}$-$\vec{G_1}$, and the Fourier sum is over $\vec{G}$. Now we will consider the Fourier transform of the total potential, $V(\vec{G})$, which contains both local and nonlocal components.

For diamond(A^N) or zinc-blende($A^N B^{8-N}$) phases, the Fourier transform of the pseudopotential is represented in terms of symmetric, V^S, and antisymmetric, V_A, parts of the A and B atomic potentials

$$V(\vec{G},\vec{k}) = V^S(\vec{G},\vec{k})cos(\vec{G}\cdot\vec{\tau}) + iV^A(\vec{G},\vec{k})sin(\vec{G}\cdot\vec{\tau}) \quad \text{(A.14)}$$

where

$$\begin{aligned} V^S(\vec{G},\vec{k}) &= \frac{V_A(\vec{G},\vec{k}) + V_B(\vec{G},\vec{k})}{2} \\ V^A(\vec{G},\vec{k}) &= \frac{V_A(\vec{G},\vec{k}) - V_B(\vec{G},\vec{k})}{2} \end{aligned} \quad \text{(A.15)}$$

Now the phase space potential can be found by determining the Fourier transform of the atomic potential. This involves a number of components as seen in Eq. (A.6). In the following sections we will discuss in detail the different components of the atomic potential $V_\alpha(\vec{G},\vec{k})$.

A.2 Model for the Atomic Ion Pseudopotential

Here we will concentrate on the ion potential, V^i in Eq. (A.6), which was calculated using the nonlocal model potential of Heine-Abarenkov. In this model the bare core potential is represented as a sum of angular-momentum-dependent square wells extending over a nonlocal core of radius R_l within which valence electrons interact with the core electrons. As a first approximation, the model parameters for each semiconductor atom were taken from the Heine-Animula metallic values. These results were obtained by comparison of the model potential well depths, A_l, with the experimental energy levels of the corresponding free ions. Taking into account their energy dependence, metallic values were then obtained by extrapolating from the free ion energy to the corresponding equivalent energy relative to the Fermi level of the metal. An approximation to the metal values was thus obtained by fitting to atomic spectroscopic data. For simplicity, Heine-Animula considered the metallic square wells to be energy independent with the same radius, R, used for each. Here this restriction is not invoked, so that l-component of the ion potential has a characteristic well radius of R_l. The model potential is:

$$V_\alpha^i = \sum_{l=0}^{l=\infty} V_l^i |lm><lm'|, \tag{A.16}$$

where

$$V_l^i(\vec{r}) = \begin{cases} -A_l & r <= R_l \\ -\frac{Z}{r} & r > R_l \end{cases} \tag{A.17}$$

Here Z is the number of valence electrons of the α atomic species. The relevant members of the sum will only involve the l values of the unexcited valence and

core electrons. As is evident from the Phillips-Kleinman cancellation theorem,[54] these are the angular-momentum components that will be canceled in the core to produce a smooth pseudopotential. HA argued that higher harmonics would produce pseudowavefunction nodes within the core. Such structure in the pseudowavefunction would be incompatible with the concepts of the pseudopotential method. For Si and C, we will therefore not need to include members of the sum for $l > 1$. Based on the cancellation theorem, these unnecessary angular-momentum components of the potential should all be roughly the same size. They can therefore all be removed from the sum by removing the $l = 2$ component as an average. The $l = 2$ well then forms the local potential. The potential will then be

$$V_\alpha^i = V_2^i + \sum_{l=0}^{l=1} [A_l - A_2] \, |lm >< lm'| \tag{A.18}$$

where $V_l^i(r) - V_2^i(r) = (A_l - A_2)\Theta(R_l - r)$, with $\Theta(R_l - r)$ the heavy side step function. Here the second term represents the nonlocal correction in Eq. (A.5). The radii R_l and potential well depths A_l are parameters that can be fit to experimental data by varying these parameters from those obtained by Heine and Abarenkov.

An example for Carbon is shown in Fig. A.1. Here the full flexibility of the model potential is invoked, and each l-component of the ion potential has an independent radii R_l. This can be used to obtain an accurate band structure for carbon using only 125 plane waves, reproducing the results of all-plane-wave methods. In Chapter 2 of this dissertation, we used the same radius for every l-component of

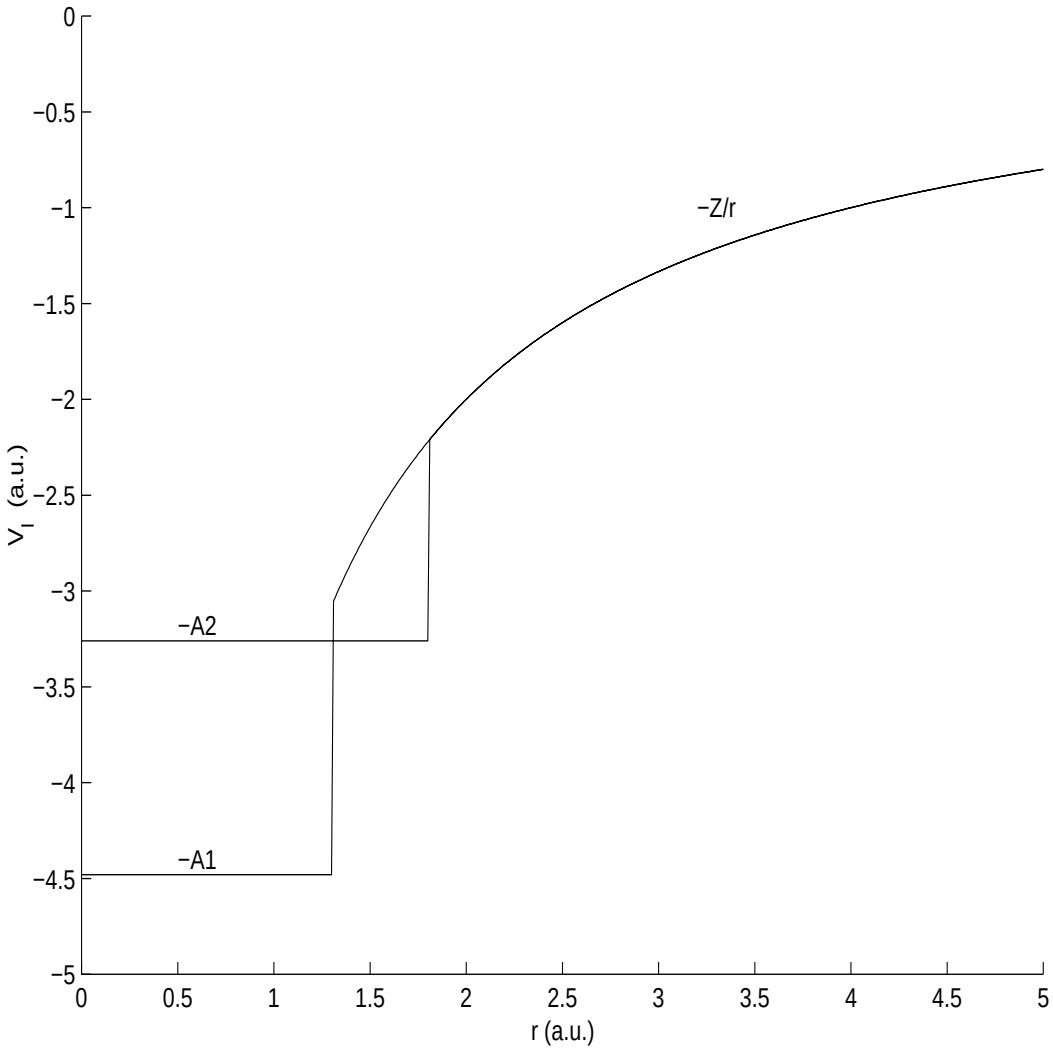

Figure A.1: Ion Pseudopotential for Carbon

the carbon core potential to limit the number of fitting parameters needed to construct the SiC model potential.

As mentioned, the local atomic pseudopotential for the ion of species α is given by the l=2 term in Eq. (A.16). The result is

$$V_\alpha^L(\vec{G}) = \frac{1}{\Omega G}\int V_2(\vec{r})e^{i\vec{G}\cdot\vec{r}}d^3r = \frac{4\pi}{\Omega G}\int V_2(\vec{r})r\sin(Gr)dr$$
$$= \frac{4\pi}{\Omega G}\left[\frac{A_l R_2\cos(GR_2)}{G} - \frac{A_l\sin(GR_2)}{G^2} - Z\cos(GR_2)G\right]$$

$$= \frac{-8\pi Z}{\Omega G^2}\left[\left(1 - \frac{A_l R_2}{Z}\right)\cos\left(GR_2\right) + \frac{A_l}{ZG}\sin\left(GR_2\right)\right] \tag{A.19}$$

The nonlocal correction for the ion potential is

$$V_\alpha^{NL}(\vec{r},\vec{r'}) = \sum_{l=0}^{1}(A_l - A_2)\Theta(R_l - r)\delta(r - r')Y_{lm}(\theta,\phi)Y_{lm'}(\theta',\phi'). \tag{A.20}$$

Here again we do not explicitly include the sums over m and m' from $-l$ to l. Now to determine the Fourier transform of Eq. (A.13), the following spherical harmonics expansion is used:

$$e^{i\vec{K_1}\cdot\vec{r}} = 4\pi\sum_{l_1 m_1}(i^{l_1})j_{l_1}(K_1 r)Y^*_{l_1 m_1}(\theta_{\vec{K_1}},\phi_{\vec{K_1}})Y_{l_1 m_1}(\theta,\phi). \tag{A.21}$$

The Fourier transform of the nonlocal correction to the atomic potential then becomes

$$V_\alpha^{NL}(\vec{K_2},\vec{K_1}) = \sum_l 4\pi(2l+1)P_l(\cos\theta_{\vec{K_1},\vec{K_2}})\Lambda_l(K_1,K_2). \tag{A.22}$$

where

$$\Lambda_l(K_1,K_2) = \frac{1}{\Omega_\alpha}\int_0^{R_l} j_{l_1}(K_1 r)j_{l_2}(K_2 r)V_l(r)r^2 dr. \tag{A.23}$$

Here we have used the addition theorem

$$\sum_{mm'} Y^*_{lm}(\theta_{\vec{K_1}},\phi_{\vec{K_1}})Y_{lm'}(\theta_{\vec{K_2}},\phi_{\vec{K_2}}) = \frac{2l+1}{4\pi}P_l(\cos\theta_{\vec{K_1},\vec{K_2}}) = \begin{cases} 1/4\pi, & l=0 \\ 3/4\pi\cos\theta_{\vec{K_1},\vec{K_2}}, & l=1 \end{cases} \tag{A.24}$$

For l, the cosine of the angle between $\vec{K_1}$ and $\vec{K_1}$ must be included according to equation (35). This becomes

$$\cos\theta_{\vec{K_1},\vec{K_2}} = \begin{cases} \left(1 - \frac{\left(\vec{K_2}-\vec{K_1}\right)^2}{2K_1^2}\right), & K_1 = K_2 \\ \left(\frac{K_2^2+K_1^2-\left(\vec{K_2}-\vec{K_1}\right)^2}{2K_1K_2}\right), & K_1 \neq K_2 \end{cases} \tag{A.25}$$

The term $\Lambda_l(K_1, K_2)$ is solved by integration by parts for the cases $K_2 = K_1$ and $K_2 \neq K_1$ separately.

The result for$K_1 = K_2$ is:

$$\Lambda(K_1, K_2, q) = \begin{cases} \frac{-(A_0 - A_2)R_a^3}{\Omega_a}\left[j_0^2(K_1R_a) - \frac{\cos(K_1R_a)j_1(K_1R_a)}{K_1R_a}\right], & l = 0 \\ \frac{-(A_1 - A_2)R_a^3}{\Omega_a}\left[j_1^2(K_1R_a) - j_0(K_1R_a)j_2(K_1R_a)\right], & l = 1 \end{cases} \tag{A.26}$$

and for $K_1 \neq K_2$ have:

$$\Lambda(K_1, K_2, q) = \begin{cases} \frac{-2(A_0 - A_2)R_a^2}{\Omega_a\left[K_2^2 - K_1^2\right]}\left[K_1 j_1(K_1R_a)j_0(K_2R_a) - K_2 j_1(K_2R_a)j_1(K_1R_a)\right], & l = 0 \\ \frac{-2(A_1 - A_2)R_a^2}{\Omega_a\left[K_2^2 - K_1^2\right]}\left[K_1 j_2(K_1R_a)j_1(K_2R_a) - K_2 j_2(K_2R_a)j_1(K_1R_a)\right], & l = 1 \end{cases} \tag{A.27}$$

where the j's are the spherical Bessel functions.

A.3 Model for the Atomic Orthogonality Hole Correction to the Band Potential

The band or valence electron potential V^b in Eq. (A.6) is considered to be uniform in space and is therefore neglected since it will only scale the electron energies. An orthogonality hole correction is however included onto the uniform Hartree band potential. This occurs due to the overestimation of the density of valence electrons in the core in the pseudopotential method. The real wavefunction will be highly structured in the core reducing the probability-density amplitude as opposed to that of the pseudowavefunction which is smooth in the core. Unlike the uncorrected Hartree band potential, the orthogonality correction is not uniform. In the core it is positive and attractive owing to the overestimation of charge

density there by the pseudopotential method. Outside of the core it is zero.

A correction to the band exchange potential is also included. This potential is also only nonzero in the core but will be negative and repulsive since exchange is attractive. The two orthogonality hole corrections can be combined, approximating the exchange as 1/2 of the Hartree correction as might be expected when dealing with uniform densities. The orthogonality hole charge density in the core is then

$$n(r) = \begin{cases} \frac{2Z\alpha}{\Omega_c} = \frac{Z}{\Omega_c}\left(\frac{R_c}{R_a}\right)^3 & r <= R_c \\ 0 & r > R_c \end{cases} \tag{A.28}$$

Here R_c is the radius of the core for a given atomic species ignoring its weak angular-momentum dependence. Also Ω_c is the core volume corresponding to R_c. The potential due to the orthogonality hole is local and is represented by the expression:

$$\begin{aligned} V_{oh}(G) &= \frac{-4\pi n(G)}{G^2} = \frac{-8\pi Z\alpha}{\Omega_c G^2 \Omega_a} \int r \sin(Gr) dr \\ &= \frac{-24\pi Z\alpha}{\Omega_a G^3 R_c^3} \left[\sin(GR_c) - GR\cos(GR_c)\right] \end{aligned} \tag{A.29}$$

A.4 Model for the Atomic Correlation Correction

In this section the model potential for the correction in Eq. (A.6) due to the nonadditivity of the correlation potentials within the ion and band model potentials is detailed. Since the correlation potential depends on the electron

density, we can write

$$Vcc = \left[\Sigma_c^{i+b} - \Sigma_c^i - \Sigma_c^b\right] = \mu_c(n_i + n_b) - \mu_c(n_i) - \mu_c(n_b). \tag{A.30}$$

The result must be considered within and outside of the core since inside the core $n = n_i + n_b \simeq n_i$ and outside of the core $n = n_b$. Therefore

$$Vcc(r) = \begin{cases} -\mu_c(n_b) = -E_c & r <= R_c \\ 0 & r > R_c \end{cases} \tag{A.31}$$

The correlation correction potential then becomes the Fourier transform of a square well of depth $-E_c$, the correlation strength, and radius R_c

$$Vcc(G) = \frac{4\pi E_c}{\Omega_c G^3}\left[\sin(GR_c) - GR\cos(GR_c)\right] \tag{A.32}$$

A.5 Screening of Ion Potential

The bare local local potential is screened by a dielectric function appropriate for semiconductors. The Penn dielectric function[56]

$$\epsilon(G; E_g) = 1 + \frac{\left[\frac{\hbar\omega_p}{E_g}\right]^2\left[1 - \frac{E_g}{4E_F}\right]}{\left[1 + \frac{E_F}{E_g}\left(\frac{G}{E_F}\right)^2\sqrt{1 - \frac{E_g}{4E_F}}\right]^2} \tag{A.33}$$

is used, where E_F is the Fermi energy, ω_p the plasma frequency, and E_g is a band gap parameter determined by the $G \to 0$ limit

$$E_g = \frac{\hbar\omega_p}{\sqrt{\epsilon(0) - 1}} \tag{A.34}$$

This will screen the bare local ion potential according to

$$V_\alpha^L(\vec{G}) = \frac{V_\alpha^L(\vec{G})}{\epsilon(G; E_g)} \tag{A.35}$$

Screening of the nonlocal potential is included through the use of Sham and Ziman's screened self-consistent potential[52]. With $q=|\vec{K_2}-\vec{K_1}|$, this can be approximated as

$$I(\vec{K_1},\vec{K_2}) = \frac{4\pi e^2}{\Omega_\alpha q^2}\frac{(1-f(q))}{\epsilon(q;E_g)}\sum_{K_1<K_F}\frac{\left[V_\alpha^{NL}+(V_\alpha^{NL})^*\right]}{E(K_1)-E(K_2)} \tag{A.36}$$

or

$$I(\vec{K_1},\vec{K_2}) = -\frac{8\pi m^*}{\Omega_\alpha q^2}\frac{(1-f(q))}{\epsilon(q;E_g)}\frac{8\pi}{\Omega_\alpha}\sum_{l=0}^{1}(2l+1)(A_l-A_2)R_l^2H_l, \tag{A.37}$$

where $m^*=\frac{m_{eff}}{m_e}$, and the relation $\frac{m_e}{\hbar^2}=\frac{1}{a_o e^2}=\frac{1}{e^2}$in a.u. is used. Also the K_l are given by

$$H_l = \frac{2\Omega_a}{(2\pi)^3}\int_{K_1<k_F}\frac{2\left[K_1 j_{l+1}(K_1R_l)j_l(K_2R_l)-K_2 j_{l+1}(K_2R_l)j_l(K_1R_l)\right]P_l(\cos\Theta_{\vec{K_1},\vec{K_2}})d\vec{K_1}}{\left(K_1^2-K_2^2\right)^2} \tag{A.38}$$

and the screened exchange term factor, including the scattering wavevector $k_s=\frac{2k_F}{\pi}$ is

$$f(q) = \frac{q^2}{2\left(q^2+k_F^2+k_s^2\right)} \tag{A.39}$$

A.6 Fourier Transform of the Complete Atomic Pseudopotential

The screened atomic pseudopotential can thus be represented as

$$V_\alpha(\vec{k}+\vec{G_1},\vec{k}+\vec{G_2}) = \frac{V_\alpha^L(\vec{G_2}-\vec{G_1})}{\epsilon(\vec{G_2}-\vec{G_1}))}+I(\vec{k}+\vec{G_1},\vec{k}+\vec{G_2})+V_\alpha^{NL}(\vec{k}+\vec{G_1},\vec{k}+\vec{G_2}). \tag{A.40}$$

The total bare local potential V_α^L includes the contributions from the local ion, correlation, and orthogonality hole potentials. The result is

$$V_\alpha^L(G) = \frac{-8\pi Z}{\Omega_\alpha G^2}\left[\left(1 - \frac{A_l R}{Z}\right)\cos(GR) + \frac{A_l}{ZG}\sin(GR)\right] + \left[\frac{4\pi Ec}{\Omega_c G^3} - \frac{-24\pi Z\alpha}{\Omega_\alpha G^3 R_c^3}\right][\sin(GR_c) - GR\cos(GR_c)] \quad \text{(A.41)}$$

where $G = |\vec{G}_2 - \vec{G}_1|$.

BIBLIOGRAPHY

[1] P. Collins, M. S. Arnold, P. Avouris, Science **292**, 706 (2001).

[2] W. J. Choyke, D. R. Hamilton, and L. Patrick, Phys. Rev. **A133**, 1163 (1964).

[3] W. H. Backes, P. A. Bobbert, and W. van Haeringen, Phys. Rev. B **49**, 7564 (1994).

[4] P. G. Neudeck, J. Electron Mater. **24**, 283 (1995).

[5] Z. Dilli, *Silicon Carbide Power Devices* (M.Sc. Thesis, University of Maryland, 2001).

[6] G. T. Heydt and B. J. Skromme, Mat. Res. Soc. Symp. Proc. **483**, 3 (1999).

[7] R. W. Erickson, *Fundamentals of Power Electronics* (Chapman and Hall, New York, 1997).

[8] P. R. Chalker, Thin Solid Films **343**, 616 (1999).

[9] J. W Palmour, R. F. Davis, H. S. Kong, S. F. Corcoran, and D. F. Griffis, J. Electrochem. Soc. **136**, 502 (1989).

[10] E. Bellotti, *Advance modeling of wide band gap semiconductor materials and devices* (Ph.D Disseration, Georgia Institude of Technology, 1999).

[11] N. S. Saks and A. K. Agarwal, Appl. Phys. Lett. **77**, 3281 (2000).

[12] L. Lipkin, M. Das, and J. Palmour, Mat. Res. Soc. Symp. Proc. **640**, H3.1.1 (2001).

[13] H. Matsunami, T. Kimoto and H. Yano, Mat. Res. Soc. Symp. Proc. **640**, H3.4.1 (2001).

[14] S. K. Powell, N. Goldsman, J. M. McGarrity, J. Bernstein, C. J. Scozzie, and A. Lelis, J. Appl. Phys. **92**, 4053 (2002).

[15] J. N. Shenoy, M. K. Das, J. A. Cooper, M. R. Melloch, and J. W. Palmour, J. Appl. Phys. **79**, 3042 (1996).

[16] H. Yano, T. Hirao, T. Kimoto, and H. Matsunami, Appl. Phys. Lett. **81**, 4772 (2002).

[17] H. Yano, T. Kimoto, and H. Matsunami, Appl. Phys. Lett. **81**, 301 (2002).

[18] C. Raynaud, J. L. Autran, B. Balland, G. Guillot, C. Jaussaud, and T. Billion, J. Appl. Phys. **76**, 993 (1994).

[19] A. K. Agarwal, J. B. Casady, L. B. Rowland, W. F. Valek, M. H. White, and C. D. Brandt, IEEE Electron Device Lett., **18**, 586 (1997).

[20] M. Bhatnagar and B. B. Baliga, IEEE Trans. Electron Devices, **40**, 645 (1993).

[21] S. Iijima, Nature (London) **354**, 56 (1991).

[22] R. Saito, M.S. Dresselhaus, and G. Dresselhaus, *Physical properties of carbon nanotubes* (Imperial College Press, London 1998).

[23] J. Li, C. Papadopoulos, and J.M. Xu, Nature (London) **402**, 253 (1999).

[24] W.Z. Li, J.G. Wen, and Z.F. Ren, Appl. Phys. Lett. **79**, 1879 (2001).

[25] R.S. Lee, H.J. Kim, J.E. Fischer, A. Thess, and R.E. Smalley, Nature (London) **388**, 255 (1997).

[26] L. Grigorian, G.U. Sumanasekera, A.L. Loper, S. Fang, J.L. Allen, and P.C. Eklund, Phys. Rev. B **58**, R4195 (1998).

[27] Z. Yao, C.L. Kane, and C. Dekker, Phys. Rev. Lett. **84**, 2941 (2000).

[28] J. Hone, M. Whitney, C. Piskoti, and A. Zettl, Phys. Rev. B **59**, R2514 (1999).

[29] A. Bachtold, P. Hadley, T. Nakanishi, and C. Dekker, Science **294**, 1317 (2001).

[30] P. L. McEuen, M. S. Fuhrer and H. Park, IEEE Trans. Nano. **1**, 78 (2002).

[31] B.M Kim, T. Durkop, T. Brintlinger, E. Cobas and M. S. Fuhrer, Third IEEE Conf. on Nanotech., (2003).

[32] G. Pennington and N. Goldsman, Phys. Rev. B **64**, 45104 (2001).

[33] G. Pennington and N. Goldsman, Phys. Rev. B **86**, 45426 (2003).

[34] G. Pennington and N. Goldsman, IEICE Trans. Electron. **E86-C**, 372 (2003).

[35] A. Akturk, G. Pennington and N. Goldsman, Third IEEE Conf. on Nanotech., 24 (2003).

[36] T. Kurosawa, *Proc. Internat. Conf. Phys. Semicond.*, Kyoto; J. Phys. Soc. Japan, Suppl. **21**, 424 (1966).

[37] W. Fawcett, A. D. Boardman, and S. Swain, J. Phys. Chem. Soldis, **31**, 1963 (1970).

[38] C. Jacoboni and P. Lugli, *The Monte Carlo Method for Semiconductor Device Simulation* (Springer-Verlag Wien, New York 1989).

[39] J. F. Tang, *Theoretical Studies of High Field, High Energy Transport in Gallium Arsenide, Silicon and Heterostructures'* (Ph.D Thesis, University of Illinois, 1983).

[40] J. Singh, *Physics of Semiconductors and their Heterostructures* (McGraw-Hill, New York 1993).

[41] H. Shichijo, J. Y. Tang, J. Bude, and D. Yoder, in *Monte Carlo Device Simulation: Full Band and Beyond*, edited by K. Hess (Kluwer Academic, Boston, 1991), p. 285.

[42] W. R. L. Lambrecht and B. Segall, Phys. Rev. B **52**, R2249 (1995).

[43] M. L. Cohen and J. R. Chelikowsky, *Electronic Structure and Optical Properties of Semiconductors* (Springer-Verlag, New York, 1988).

[44] T. K. Bergstresser and Marvin L. Cohen, Phys. Rev. **164**, 1069 (1967).

[45] L. A. Hemstreet and C. Y. Fong, Phys. Rev. B **6**, 1464 (1972).

[46] E. Bellotti, H. Nilsson, and K. F. Brennan, J. Appl. Phys. **85**, 3211 (1998).

[47] H. Aourag, B. Djelouli, A. Hazzab, and B. Khelifa, Mater. Chem. Phys. **39**, 34 (1994).

[48] W. J. Choyke and L. Patrick, Phys. Rev. **187**, 1041 (1969).

[49] L. Patrick and W. J. Choyke, Phys. Rev. **186**, 775 (1969).

[50] I. V. Abarenkov and V. Heine, Phil. Mag. **12**, 529 (1965).

[51] A. O. E. Animalu and V. Heine, Phil. Mag. **12**, 1249 (1965).

[52] A. O. E. Animalu, Proc. Roy. Soc. A **294**, 376 (1966).

[53] R. W. Shaw, Phys. Rev.**174** 769 (1968).

[54] J. C. Phillips and L. Kleinman Phys. Rev. **116** 287 (1959).

[55] L. J. Sham, Proc. Roy. Soc. A **283**, 33 (1965).

[56] D. R. Penn, Phys. Rev.**128** 2093 (1962).

[57] J. C. Phillips,*Covalent Bonding in Crystals, Molecules, and Polymers* (The University of Chicago Press, Chicago 1969).

[58] M. L. Cohen and V. Heine, Solid State Phys. **24**, 37 (1970).

[59] D. Brust, Phys. Rev. **134**, A1337 (1964).

[60] Marvin L. Cohen and T. K. Bergstresser, Phys. Rev. **141**, 789 (1966).

[61] L. A. Hemstreet, C. Y. Fong, and Marvin L. Cohen, Phys. Rev. B **2**, 2054 (1970).

[62] D. R. Masovic, F. R. Vukajlovic, and S. Zekovic, J. Phys. C **16**, 6731 (1983).

[63] F. J. Himpsel, J. A. Knapp, J. A. van Vechten, and D. E. Eastman, Phys. Rev. B **20**, 624 (1979).

[64] F. J. Himpsel, J. F. van der Veen, and D. E. Eastman, Phys. Rev. B **22**, 1967 (1980).

[65] E. O. Kane, Phys. Rev. **146**, 558 (1966).

[66] F. Aymerich, R. Meloni, and G. Mula, Phys. Rev. B **15**, 3980 (1976).

[67] J. C. Phillips, Rev. Mod. Phys. **42**, 317 (1970).

[68] A. Garcia and M. L. Cohen, Phys. Rev. B **47**, 4212 (1992).

[69] P. Käckell, B. Wenzien, and F. Bechstedt, Phys. Rev. B **50**, 17037 (1994).

[70] A. Bauer et al., Phys. Rev. **57**, 2647 (1998).

[71] R. Kaplan and R. J. Wagner, Solid State Communications **55**, 67 (1985).

[72] W. R. L. Lambrecht and B. Segall, Phys. Stat. Sol. B **202**, 5 (1997).

[73] N. T. Son et al., Appl. Phys. Lett. **66**, 1074 (1995).

[74] C. H. Park, B. Cheong, K. Lee, and K. J. Chang, Phys. Rev. B **49**, 4485 (1993).

[75] L. Patrick, Phys. Rev. B **5**, 2198 (1972).

[76] D. M. Hofman, D. Volm, M. Drechsler, and B.K. Meyer, Appl. Phys. Lett. **66**, 1074 (1995).

[77] J. L*ü*ning, S. Eisebitt, J. E. Rubensson, C. Ellmers, and W. Everhardt, Phys. Rev. B **59**, 10573 (1998).

[78] B. Adolph, K. Tenelsen, V. I. Gavrilenko, and F. Bechstedt, Phys. Rev. B **55**, 1422 (1996).

[79] M. Fischetti, and S. Laux, Phys. Rev. B **38**, 9721 (1988).

[80] H. Nilsson et al., J. Appl. Phys. **86**, 965 (1999).

[81] L. J. Rauberheimer and G. Gilat, Phys. Rev. **157**, 586 (1967).

[82] J. Bardeen and W. Shockley, Phys. Rev. **80**, 72 (1950).

[83] D. K. Ferry, Phys. Rev. B **14**, 1605 (1976).

[84] C. Moglestue, *Monte Carlo Simulation of Semiconductor Devices* (Chapman and Hall, London, 1993).

[85] K. Tsukioka, D. Vasileska, and D. K. Ferry, Physica B **185**, 466 (1993).

[86] M. Lundstrom, *Fundamentals of Carrier Transport* (Addison-Wesley, New York, 1990).

[87] R. Mickevicius, and J. Zhao, J. Appl. Phy. **83**, 3161 (1998).

[88] H. Nilsson, U. Sannemo, and C. S. Petersson, J. Appl. Phys. **80**, 3365 (1996).

[89] W. Schaffer et al., Mat. Res. Soc. Symp. Proc. **339**, 595 (1994).

[90] I. Khan, and J. Cooper, IEEE Trans. Elec. Dev. **47**, 269 (2000).

[91] T. Ando, A. B. Fowler, and F. Stern, Rev. Mod. Phys. **54**, 437 (1982).

[92] F. Stern and W. E. Howard, Phys. Rev. **163**, 816 (1967).

[93] F. Stern, Phys. Rev. B **5**, 4891 (1972).

[94] T. Ouisse, J. Appl. Phys. **75**, 2092 (1993).

[95] L. Patrick, Phys. Rev. B **5**, 2198 (1972).

[96] I. Shalish, I. B. Altfeder, and V. Narayanamurti, Phys. Rev. B **65**, 73104 (2002).

[97] B. Wenzien, P. Kaeckell, F. Bechstedt, and G. Cappellini, Phys. Rev. B **52**, 10897 (1995).

[98] C. Persson, and U. Lindefelt, Phys. Rev. B **54**, 10257 (1996).

[99] W. R. L. Lambrecht and B. Segall, Phys. Rev. B **52**, R2249 (1995).

[100] T. Ando, Phys. Rev. B **13**, 3468 (1976).

[101] G. Pensl, M. Bassler, F. Ciobanu, V. Afanas'ev, H. Yano, T. Kimoto, and H. Matsunami,Mat. Res. Soc. Symp. Proc. **640**, H3.2.1 (2001).

[102] K. Ueno, R. Asai, and T. Tsuji, IEEE Electron Device Lett. **19**, 244 (1998).

[103] R. Schorner, P. friedrichs, D. Peters, and D. Stephani, IEEE Electron Device Lett. **20**, 241 (1999).

[104] E. Bano, C. Banc, T. Ouisse, and S. Scharnholz, Solid State Electron. **44**, 63 (2000).

[105] H. Matsunami, T. Kimoto, and H. Yano, Mat. Res. Soc. Symp. Proc. **640**, H3.4.1 (2001).

[106] B.K. Ridley, *Quantum processes in semiconductors* (Oxford University Press, Oxford 1982).

[107] P. J. Price, Ann. Phys. **133**, 217 (1981).

[108] L.J. Sham, J.M. Ziman, in *Solid State Physics*, edited by F. Seitz and D. Turnbull (Academic Press, New York 1963), Vol. 15, p. 223.

[109] P. K. Basu, J. Appl. Phys. **48**, 350 (1976).

[110] K. Yokoyama and K. Hess, Phys. Rev. B **33**, 5595 (1986).

[111] W. Fawcett, A. D. Boardman, and S. Swain, J. Phys. Chem. Sol. **31**, 1963 (1970).

[112] S. M. Goodnick and P. Lugli, Phys. Rev. B **15**, 2578 (1988).

[113] F. Gamiz, J. A. Lopez-Villanueva, J. A. Jimenez-Tejada, I. Melchor, and A. Palma, J. Appl. Phys. **75**, 924 (1994).

[114] S. Yamakawa, H. Ueno, K Taniguchi, C. Hamaguchi, K. Miyatsuji, K, Masaki, U. Ravaioli, J. Appl. Phys. **79**, 911 (1996).

[115] F. Gamiz, M. V. Fischetti, J. Appl. Phys. **89**, 5478 (2001).

[116] R. S. Muller and T. I. Kamins, *Device Electronics for Integrated Circuits* (Wiley and Sons, New York, 1986).

[117] S. M. Sze, *Physics of Semiconductor Devices* (Wiley and Sons, New York, 1981).

[118] S. Harada, R. Kosugi, J. Senzaki, S. Suzuki, W. J. Cho, K. Fukuda, and K. Arai, Mat. Res. Soc. Symp. Proc. **640**, H5.37.1 (2001).

[119] R. Martel *et al.*, Appl. Phys. Lett. **73**, 2447 (1998).

[120] S.J. Tans, A.R.M. Verschueuren, and C. Dekker, Nature (London) **393**, 49 (1998).

[121] P.G. Collins, A. Zettl, H. Bando, A. Thess, and R.E. Smalley, Science **278**, 100 (1997).

[122] Z. Yao, H.W.C. Postma, L. Balents, and C. Dekker, Nature (London) **402**, 273 (1999).

[123] M.S. Fuhrer *et. al.*, Science **288**, 494 (2000).

[124] C. Papadopoulos, A. Rakitin, J. Li, A.S. Vedeneev, and J.M. Xu, Phys. Rev. Lett. **85**, 3476 (2000).

[125] A.A. Odintsov, Phys. Rev. Lett. **85**, 150 (2000).

[126] F. Léonard and J. Tersoff, Phys. Rev. Lett. **85**, 4767 (2000).

[127] J. Kim, J. Lee, H. Oh, K. Yoo, and J. Kim, Phys. Rev. B **64**, R16140 (2001).

[128] S.L. Wang, N. Goldsman, Q. Lin, and J. Frey, Solid State Electronics **36**, 833 (1993).

[129] M.V. Fischetti, and S.E. Laux, Phys. Rev. B **38**, 9721 (1988).

[130] A. Spinelli, A. Benvenuti, and A. Pacelli, IEEE Trans. Electron Devices **45**, 1342 (1998).

[131] C.K. Huang, and N. Goldsman, in *Proceedings of the 2001 International Conference on Simulation of Semiconductor Processes and Devices*, edited by D. Tsoukalas and C. Tsamis (Springer Wien, New York 2001), p 148.

[132] S.J. Tans, M.H. Devoret, H. Dai, A. Thess, R.E. Smalley, L.J. Geerligs, and C. Dekker, Nature (London) **386**, 474 (1997).

[133] J.W.G. Wildöer, L.C. Venema, A.G. Rinzler, R.E. Smalley, and C. Dekker, Nature (London) **391**, 59 (1998).

[134] T.W. Odom, J.L. Huang, P. Kim, and C.M. Lieber, Nature (London) **391**, 62 (1998).

[135] M. Ouyang, J.L. Huang, and C.M. Lieber, Phys. Rev. Lett. **88**, 66804 (2002).

[136] P.E. Lammert and V.H. Crespi, Phys. Rev. B **61**, 7308 (1998).

[137] D. Sánchez-Portal, E. Artacho, and J.M. Soler, Phys. Rev. B **59**, 12678 (1999).

[138] G. Pennington and N. Goldsman, in *Proceedings of the 2001 International Semiconductor Device Research Symposium*, p. 310.

[139] M. Damnjanović, I. Milošević, T. Vuković, and R. Sredanović, Phys. Rev. B **60**, 2728 (1999).

[140] L. Yang, M.P. Anantram, J. Han, and J.P. Lu, Phys. Rev. B **60**, 13874 (1999).

[141] R. Heyd, A. Charlier, and E. McRae, Phys. Rev. B **55**, 6820 (1997).

[142] Verissimo-Alves et al., Phys. Rev. lett. **86**, 3372 (2001).

[143] T. Hertel and G. Moos, Phy. Rev. Lett. **84**, 5002 (2000).

[144] S. Briggs and J.P. Leburton, Phys. Rev. B **38**, 8163 (1988).

[145] S. Briggs, B.A. Mason, and J.P. Leburton, Phys. Rev. B **40**, 12001 (1989).

[146] Z. Yao, C. L. Kane, C. Dekker, Phs. Rev. Lett. **84**, 2941-2944 (2000).

[147] J. Y. Park, S. Rosenblatt, Y. Yaish, V. Sazonova, H. Ustunel, S. Braig, *to be published*, Cond. Mat. Archive 0309641, (2003).

[148] N. Ashcroft and N. Mermin, *Solid State Physics* (Holt, Rinehart, and Winston, 1976).

[149] S. Briggs and J.P. Leburton, Phys. Rev. B **39**, 8025 (1989).

[150] D.E. Soule, Phys. Rev. **112**, 698 (1958).

[151] B.K. Ridley and T.B. Watkins, Proc. Phys. Soc. (London) **78**, 293 (1961).

[152] C. Hilsum, Proc. IRE **50**, 185 (1962).

[153] K. Sugihara, Phys. Rev. B **28**, 2157 (1983).

[154] J.B. Gunn, Solid-State Commun. **1**, 88 (1963).

[155] M. Shur, *Physics of semiconducting devices* (Prentice-Hall, New Jersey 1990).

[156] T. Nakanishi, A. Bachtold, and C. Dekker, Phys. Rev. B **66**, 73307 (2002).

[157] Ph. Avouris, R. Martel, V. Derycke, J. Appenzeller, Physica B **323**, 6 (2002).